

Modelling of Fission Gas Behaviour in High Burnup Nuclear Fuel

THÈSE N° 4084 (2008)

PRÉSENTÉE LE 3 JUILLET 2008

À LA FACULTE SCIENCES DE BASE

LABORATOIRE DE PHYSIQUE DES RÉACTEURS ET DE COMPORTEMENT DES SYSTÈMES

PROGRAMME DOCTORAL EN ENERGIE

ÉCOLE POLYTECHNIQUE FÉDÉRALE DE LAUSANNE

POUR L'OBTENTION DU GRADE DE DOCTEUR ÈS SCIENCES

PAR

Paul BLAIR

Master in physics, University of York, Heslington York, Royaume-Uni
et de nationalité britannique

acceptée sur proposition du jury:

Prof. H. B. Püttgen, président du jury

Prof. R. Chawla, directeur de thèse

Dr Y. Guérin, rapporteur

Dr C. Hellwig, rapporteur

Dr A. Romano, rapporteur



ÉCOLE POLYTECHNIQUE
FÉDÉRALE DE LAUSANNE

Suisse
2008

"There is nothing like looking, if you want to find something.
You certainly usually find something, if you look,
but it is not always quite the something you were after."
J.R.R. Tolkien

For my family

Abstract

The safe and economic operation of nuclear power plants (NPPs) requires that the behaviour and performance of the fuel can be calculated reliably over its expected lifetime. This requires highly developed codes that treat the nuclear fuel in a general manner and which take into account the large number of influences on fuel behaviour, e.g. thermal, mechanical, chemical, etc. Although many mature fuel performance codes are in active use, there are still significant incentives to improve their predictive capability. One particular aspect is related to the strong trend of NPP operators to try and extend discharge burnups beyond current licensing limits.

With increasing burnup, more and more fission events impact the material characteristics of the fuel, as well as the cladding, and significant restructuring can be observed in the fuel. At local burnups in excess of 60–75 MWd/kgU, the microstructure of nuclear fuel pellets differs markedly from the as-fabricated structure. This “high burnup structure” (HBS) is characterised by three principal features: (1) low matrix xenon concentration, (2) sub-micron grains and (3) a high volume fraction of micrometer-sized pores. The peculiar features of the HBS have resulted in a significant effort to understand the consequences for fuel performance and safety. In particular there is the concern that the large retention of fission gas within the HBS could lead to significant gas release at high burnups, either through the degradation of thermal conductivity or through direct release.

While for the normal fuel microstructure numerous models, investigations and codes exist, only a few models for simulating fission gas behaviour in the HBS have been developed. Consequently, in this context, it is fair to say that reliable mechanistic models are largely missing today. In line with this situation the present doctoral work has focussed on the development and evaluation of HBS fission gas transport models, with a view to improve upon the current gap in fuel performance modelling. In particular two features of the HBS have been focussed on, viz. the equilibrium xenon concentration in the matrix of the HBS in UO₂ fuel pellets, and the growth of the HBS porosity and its effect on fission gas release.

In a first step a steady-state fission gas model has been developed to examine the importance of grain boundary diffusion for the gas dynamics in the HBS. With this model it was possible to simulate the ≈ 0.2 wt% experimentally observed xenon concentration under certain conditions, viz. fast grain boundary diffusion and a reduced grain diffusion coefficient. A sensitivity study has been conducted for the principal parameters of the model and it has been shown that the value of the grain boundary diffusion coefficient is not important for diffusion coefficient ratios in excess of $\sim 10^4$. Within this grain boundary diffusion saturation regime the model exhibits a high sensitivity to principally three other parameters: the grain diffusion coefficient, the bubble number density and the re-resolution rate coefficient. In spite of such sensitivity it has been shown that the model can reproduce the observed HBS xenon depletion with the assumption that grain boundary diffusion of fission gas is significantly faster than lattice diffusion. In particular the results from this study have demonstrated that the release of produced gas from the grains to the HBS porosity corresponds to a dynamic equilibrium, providing a justification for the typical modelling approach used in HBS modelling, viz. fast transport to the porosity, which from a fuel performance modelling point of view largely simplifies the calculations.

In a second step, a model describing the evolution of the HBS porosity under annealing conditions has been developed. The model was applied to a high burnup fuel annealing experiment to

assess its predictions against measurements. Reasonable agreement was found with respect to the experimental release in the temperature range where the release mechanism was originally interpreted to be due to volume diffusion of the gaseous fission products. In contrast to the original analysis, the developed model interprets the release mechanism as being due to pore growth, coalescence and, ultimately, venting. The model results for annealing conditions have been compared with available PIE data and this comparison has indicated that, for burnups examined to date, most of the fission gas is expected to be retained within the HBS porosity.

The model of porosity growth and venting developed for annealing conditions has then been extended to take into account the effect of irradiation on the defect population and accumulation of fission gas in the HBS porosity. The power history of a high burnup fuel rod from a Swiss NPP was used to model the local behaviour of the HBS and good agreement was found between the calculation of porosity growth and results from open literature. A comparison between the calculated local gas release was found to be consistent with both the observations from the annealing calculations and measurements performed on the same fuel rod using Laser Ablation Inductively Coupled Plasma Mass Spectrometry (LA-ICP-MS).

To provide a more comprehensive analysis of the model predictions, a gas release correlation for calculating the release due to pore venting has been developed from the stand-alone in-pile modelling of porosity growth and this was implemented into the fuel performance code TRANSURANUS. The examined high burnup rod was modelled using the thus extended TRANSURANUS code so that the integral behaviour (rather than just the local HBS behaviour) could be calculated.

The subsequent fuel performance analysis has revealed that venting from the HBS has a small effect on the integral fission gas release with the release increasing towards the pellet periphery. The principal effect of the HBS for the considered high-burnup irradiation is the presence of the high porosity, which increases the fuel centre temperatures and therefore the fission gas release from the centre of the rod. For the base case analysis 22 % of the integral fission gas was found to be released. However, this is less than the quantity measured by rod puncturing.

To address this discrepancy several sensitivity studies have been performed to investigate as to where the additional fission gas release originates, specifically the fuel centre and/or the HBS zones in the pellet periphery. It has been shown from this sensitivity analysis that extra release from just one of these regions is unlikely to account for the discrepancy between measured and calculated fission gas release. It is more likely that the uncertainties for each of the individual regions, when considered together, could account for the observed integral release. In particular the presence of an athermal gas release from within the HBS has been explored in detail and it has been shown that, while significant release could occur, there is still significant retention. Previous examinations of fuel behaviour have assumed little to no release in the HBS; however it is clear from this work that at burnups as high as considered currently, the gas release does have a significant component coming from the pellet periphery.

Keywords: Nuclear Power Plants, Nuclear Fuel, Mechanistic Modelling, Fission Gas Release, High Burnup Structure, Diffusion, Porosity Growth, Sensitivity Study.

Résumé

Une exploitation sûre et économique des centrales nucléaires exige une connaissance approfondie du comportement du combustible, ainsi qu'une bonne prédiction de ses performances, sur toute sa durée de vie. Ceci nécessite le développement de codes de calcul qui considèrent le combustible dans son ensemble et qui tiennent compte des influences multiples, notamment thermiques, mécaniques et chimiques, sur son comportement. Bien que de nombreux codes de calcul aient fait leurs preuves dans ce domaine, il subsiste néanmoins de fortes motivations pour améliorer leur capacité de prédiction, en particulier en raison de l'actuelle tendance des exploitants de centrales nucléaires à augmenter les taux de combustion et à repousser les limites imposées par les autorités de sûreté.

L'endommagement par les fissions, qui augmente avec les taux de combustion, altère les caractéristiques du combustible et des gaines, et engendre une restructuration du combustible. Dans la gamme supérieure des taux de combustion locaux, au-delà de 60–75 MWd/kgU, on observe un changement microstructural important dans les pastilles de combustible par rapport à leur état vierge. Cette « high burnup structure » (HBS) est caractérisée par trois aspects importants: (1) une faible concentration du xénon dans la matrice (2) la présence de grains sub-microniques (3) et une fraction volumique élevée de pores microniques. Ces aspects particuliers ont suscité un important effort de la communauté nucléaire pour comprendre l'influence de cette HBS sur la sûreté et sur le comportement du combustible. En particulier la rétention importante de gaz de fission dans la HBS a amené à considérer le risque d'un relâchement élevé de ces gaz aux forts taux de combustion, engendré soit par une baisse de la conductivité thermique, soit par un relâchement direct.

Tandis qu'il existe de nombreuses études et des modèles prédisant le comportement des gaz de fission dans le combustible à microstructure normale, le cas de la HBS n'a été que très peu abordé. On constate un manque de modèles mécanistes fiables dans ce domaine. En conséquence, nous nous proposons de développer et d'évaluer des modèles de transport de gaz de fission dans la HBS afin de combler ce manque dans la modélisation actuelle du comportement du combustible nucléaire. Plus particulièrement, nous nous focalisons sur deux aspects de la HBS : d'une part la concentration d'équilibre du xénon dans la matrice de la HBS, d'autre part la croissance de la porosité et son influence sur le relâchement des gaz de fission.

Dans une première étape, un modèle stationnaire est développé pour le gaz de fission afin d'examiner l'importance de la diffusion aux joints de grain sur le comportement dynamique des gaz dans la HBS. A l'aide de ce modèle, il est possible de simuler correctement la concentration du xénon (≈ 0.2 wt%) observée expérimentalement sous certaines conditions, à savoir une diffusion rapide aux joints de grain et un faible coefficient de diffusion dans les grains. Une étude de sensibilité, menée pour les paramètres les plus importants du modèle, démontre que la valeur du coefficient de diffusion intergranulaire n'a plus d'importance lorsque les rapports des coefficients de diffusion excèdent $\sim 10^4$. A l'intérieur de ce régime de saturation de la diffusion aux joints de grain, ce modèle est particulièrement sensible à trois autres paramètres : le coefficient de la diffusion intragranulaire, la densité du nombre de bulles et le coefficient du taux de re-solution. Malgré cette sensibilité, on démontre que le modèle peut les mesures du xénon, dans l'hypothèse où la diffusion de gaz de fission est beaucoup plus rapide aux joints de grain que dans la matrice. Plus particulièrement, les résultats de cette étude démontrent que le transfert de gaz, depuis les grains vers les pores de la HBS, correspond à un équilibre dynamique. Cela justifie l'approche de la modélisation typiquement utilisée dans le cas de la HBS, c'est-à-dire un transfert rapide vers les pores, ce qui simplifie fortement les calculs de comportement du combustible.

Dans une deuxième étape, un modèle est développé qui décrit l'évolution de la porosité de la HBS dans les conditions d'un recuit thermique. Pour valider ce modèle, les résultats de simulation sont comparés aux mesures réalisées dans un essai de recuit sur un combustible irradié à fort taux de combustion. Un accord correct a été trouvé entre les taux de relâchement de gaz calculé et mesuré, dans une gamme de température où, auparavant, le mécanisme de relâchement était attribué à la diffusion volumique des atomes de gaz. A la différence des l'analyses antérieures, le modèle développé ici explique le mécanisme

de relâchement comme résultant de la croissance et de la coalescence des pores, puis de l'échappement de leur gaz. Les résultats de calcul pour les conditions du recuit ont été comparés aux données disponibles issues des examens post-irradiation (PIE). Il ressort de cette analyse que pour les taux de combustion examinés jusqu'ici l'essentiel des gaz de fission seraient retenus dans les pores de la HBS.

Le modèle de croissance de pores et de relâchement du gaz développé pour les conditions de recuit est ensuite étendu pour inclure les effets de l'irradiation sur la population des défauts et sur l'accumulation de gaz de fission dans les pores de la HBS. L'historique d'irradiation d'un crayon combustible à taux de combustion très élevé, provenant d'une centrale nucléaire suisse, est utilisé pour modéliser le comportement local de la HBS, et un accord satisfaisant est trouvé entre les résultats calculés de la croissance de la porosité et ceux provenant de la littérature. Le calcul de la quantité de gaz relâché localement est en accord, aussi bien avec les observations faites lors des calculs de recuit qu'avec les mesures réalisées sur le même crayon combustible à l'aide de LA-ICP-MS (« Laser Ablation Inductively Coupled Plasma Mass Spectroscopy »).

Afin de fournir une analyse plus complète des prévisions de ce modèle, une corrélation permettant de calculer la quantité de gaz relâché par échappement hors des pores est développée à partir de la modélisation autonome de la croissance de la porosité sous irradiation. Cette corrélation est ensuite intégrée dans le code de comportement du combustible TRANSURANUS. Le crayon combustible examiné est modélisé à l'aide de la version modifiée du code TRANSURANUS afin de simuler le comportement intégral du combustible (au lieu du comportement local de la HBS uniquement).

L'analyse du comportement du combustible ainsi menée montre que le relâchement hors des pores de la HBS a relativement peu d'impact sur le relâchement intégral de gaz de fission, bien que le relâchement de gaz augmente lorsqu'on s'approche de la zone périphérique de pastille. L'influence principale de la HBS, dans le cadre de cette irradiation à fort taux de combustion, provient essentiellement de la porosité élevée qui augmente la température et donc le relâchement de gaz au centre du combustible. Pour le calcul de référence, 22 % du gaz de fission est relâché globalement. Néanmoins, cette valeur est inférieure à la quantité mesurée lors du perçage du crayon.

Pour résoudre ce désaccord entre le calcul et l'expérience, plusieurs études de sensibilité sont été menées afin d'identifier la source du gaz supplémentaire : centre du combustible et/ou zones HBS en périphérie. Ces études de sensibilité montrent qu'aucune de ces zones ne peut être responsable à elle seule de tout l'écart entre le calcul et l'expérience. C'est plus probablement le cumul des incertitudes de calcul sur toutes les zones, qui mène à cet écart entre calcul et mesure. Plus particulièrement, le relâchement athermique de gaz à partir de la HBS a été examiné en détail et on montre que même si une quantité importante du gaz a pu être relâchée, une fraction significative reste néanmoins retenue. Les analyses précédentes du comportement de combustible avaient fait l'hypothèse d'un relâchement négligeable du gaz hors de la HBS ; ce travail, en revanche, démontre clairement que dans le cas des taux de combustion aussi élevés que ceux traités ici, la contribution provenant des zones périphériques de pastille de combustible constitue une part significative du relâchement global des gaz.

Mots clé : Centrales nucléaires, Combustible nucléaire, Modélisation mécaniste, Relâchement de gaz de fission, HBS (« high burnup structure »), Diffusion, Croissance de la porosité, Etude de sensibilité

Contents

Contents	v
List of Figures	ix
List of Tables	xv
List of Abbreviations	xvii
Nomenclature	xix
1 Introduction	1
1.1 Background	2
1.1.1 Fission gas	2
1.1.2 High burnup structure	5
1.2 Research objectives and stages	6
1.3 Thesis outline	7
2 State of the art	11
2.1 Fission gas production, migration and release	11
2.1.1 Production	11
2.1.2 Recoil & knock-out	13
2.1.3 Lattice diffusion	15
2.1.4 Grain boundary diffusion	20
2.1.5 Trapping	22
2.2 The high burnup structure	28
2.2.1 Characteristics	30
2.2.2 Fuel performance	33
3 A steady state fission gas model for the HBS	43
3.1 Introduction	43
3.2 Model definition	45

3.2.1	Rate equations for a 1-dimensional system of grains and grain boundaries	47
3.2.2	Discretisation	50
3.2.3	Solution scheme and averaged gas concentration	52
3.2.4	Parameter values	53
3.3	Effect of grain boundary diffusion	55
3.4	Sensitivity to model parameters	56
3.4.1	Equilibrium concentrations at parameter value limits	56
3.4.2	Sensitivity with respect to the principal parameters	57
3.5	Conclusions	60
4	Growth of the high burnup structure porosity under annealing conditions	65
4.1	Introduction	65
4.2	Theoretical model development	66
4.2.1	Single pore growth	66
4.2.2	Growth of a pore population	68
4.3	Results	75
4.3.1	Model behaviour under static temperature conditions	75
4.3.2	Application to an annealing test	77
4.4	Discussion	82
4.5	Conclusions	84
5	Porosity growth and fission gas release at high burnup under in-pile conditions	89
5.1	Introduction	89
5.2	Extension of annealing model to in-pile conditions	90
5.2.1	Irradiation induced point defect population	90
5.2.2	Fission gas accumulation in the HBS porosity	92
5.3	Stand-alone modelling of a real irradiation history	93
5.3.1	Fuel and irradiation characteristics	93
5.3.2	Results	99
5.4	Integration of the model into a fuel performance code	102
5.4.1	Framework for HBS modelling	102
5.4.2	Development of a gas release correlation from the stand-alone modelling .	104
5.5	Integral modelling of a real irradiation history	108
5.5.1	Results for the base case	108
5.5.2	Effect of temperature on integral fission gas release	109
5.5.3	Athermal fission gas release from the pellet periphery	113
5.5.4	Effect of changes in the surface-to-volume ratio	119

5.5.5	Effects of other uncertainties	120
5.6	Summary	123
6	Conclusions and recommendations for future work	129
6.1	Summary	129
6.2	Main achievements	130
6.3	Recommendations for future work	134
6.4	Concluding remarks	135
A	Percolation theory	137
B	Gauss–Seidel method	141
B.1	Mathematical formulation	141
B.2	Algorithm	142
C	Derivation of equation for finding the equilibrium grain boundary bubble radius	143
C.1	Critical number of atoms per bubble for growth	143
C.2	Calculation of the equilibrium radius	144
D	Root finding	145
D.1	Bisection	145
D.2	Newton–Raphson method with derivatives	146
E	TRANSURANUS–PSI fission gas release model and the HBS	149
E.1	The TRANSURANUS–PSI fission gas release model (SPHERE)	149
E.2	Extension of TRANSURANUS–PSI for the HBS	152
	Acknowledgements	157
	CURRICULUM VITÆ	159

List of Figures

1.1	Schematic of a fuel rod.	1
1.2	Average bundle discharge burnup (in GWd/tU) at a Swiss BWR NPP.	2
1.3	Fission product yields as a function of mass number for ^{235}U , ^{233}U and ^{239}Pu [2].	3
2.1	Cumulative yields for fission product mass chains from thermal fission of ^{235}U , ^{239}Pu and ^{241}Pu . Figure 1 from [1]	12
2.2	Energy distribution of fission fragments from thermal fission of ^{235}U . [2]	13
2.3	Schematic of fission gas release by recoil and knock-out.	14
2.4	Measured release to birth ratios in the Halden IFA-504 assembly using 30 bar argon sweep gas. The dotted line shows the reduction in the fuel-clad gap during the experiment. Figure 29 from [1].	15
2.5	Thermal diffusion coefficient as a function of $1/\text{Temperature}$ for the Arrhenius parameters given in table 2.2.	17
2.6	Variation of D_{gr}^{Xe} for UO_2 powders as found by Lindner and Matzke [12]	18
2.7	Turnbull's three term diffusion coefficient as a function of temperature for a mass rating of 25 W/gU.	19
2.8	Estimation of the grain boundary diffusion coefficient by considering morphological relaxation and bubble growth of the grain boundaries. The estimates were calculated by fitting the model to available in-pile data of inter-granular bubble behaviour. Figure 14 from [21].	22
2.9	TEM images of intra-granular bubbles. Figure 2 from [23].	23
2.10	Development of grain boundary porosity with irradiation time. Figures 2–4 from [21].	25
2.11	Schematic of an isolated lenticular grain boundary bubble. R_{gbb}^s is the radius of the circular projection on the grain face, while R_{gbb}^e is the radius of curvature of the cross-section.	26
2.12	SEM of the fuel microstructure as a function of both burnup and irradiation temperature [41].	29
2.13	Variation of the matrix xenon concentration as a function of local burnup as measured by EPMA. Figure 4 from [43].	31
2.14	Change in the grain size distribution as a function of local burnup [48].	32
2.15	Variation of the porosity and number density with local burnup [48].	33
2.16	Variation of the porosity distribution at different radial positions [48].	34

2.17	3D-reconstruction of the porosity at the pellet rim of an LWR fuel pellet with average burnup 100 GWd/tM [37].	35
3.1	Schematic of the geometrical setup and transport processes (1)–(4) used in the current model. (1) Volume diffusion from grain to both grain boundary phases, (2) Trapping of free grain boundary gas to the trapped grain boundary phase, (3) Re-solution of both grain boundary phases to the grain phase, (4) Grain boundary diffusion of the free grain boundary phase to adjacent grain boundary volumes.	46
3.2	Schematic of the idealised grain boundary with width δ_{gb} and cross-sectional area A_{gb}	50
3.3	Schematic illustrating the discretisation of the 1-D region between two HBS pores separated by a distance l_{p-p}	51
3.4	Variation of the averaged xenon concentration with the diffusion coefficient ratio for different bubble density values. The grey area corresponds to the range of average concentrations seen in EPMA measurements of the HBS.	55
3.5	Variation of the averaged xenon concentration with the grain diffusion coefficient for different values of the diffusion coefficient ratio. The grey area corresponds to the range of average concentrations seen in EPMA measurements of the HBS.	57
3.6	Variation of the averaged xenon concentration with the re-solution rate. The grey area corresponds to the range of average concentrations seen in EPMA measurements of the HBS.	59
3.7	Required range of values of key parameters for producing an approx. 0.2 wt% average xenon concentration (diffusion coefficient ratio fixed at 5×10^4).	60
4.1	The three allowed first-order interactions between the closed porosity, vented porosity and the free surface, viz. (a) Coalescence of two closed pores, (b) Venting of a closed pore through intersection with the free surface and (c) Venting of a closed pore and coalescence with a vented pore.	70
4.2	Venn diagram illustrating the relationships between the compound interactions.	71
4.3	Variation of the porosity as a function of time for a range of temperatures from 1300–1800 K.	75
4.4	Variation of the fractional release and interaction probabilities as a function of time.	76
4.5	Evolution of the porosity for a range of surface-to-volume ratios at a static temperature of 1400 K.	77
4.6	Temperature and gas release histories in the Hiernaut and Ronchi experiment [28]	78
4.7	Rate of change of the temperature and the fractional release in the Hiernaut and Ronchi experiment [28]	79
4.8	Calculated fractional release using the temperature history of Hiernaut and Ronchi [28] for a range of stoichiometry deviations from $x = 0.001$ to $x = 0.005$	80
4.9	Calculated fractional release using the temperature history of Hiernaut and Ronchi [28] for a range of values of the surface-to-volume ratio.	80
4.10	Calculated fractional release using the temperature history of Hiernaut and Ronchi [28] for several assumed locations of the matrix xenon gas.	82

4.11	Comparison between the reduction in the number density and the increasing gas release from the porosity.	83
4.12	Variation of porosity and gas release as a function of number density for static temperatures and the temperature history from Hiernaut and Ronchi [28].	84
5.1	Collated scanning electron microscopy (SEM) picture of the high burnup fuel surface. At the upper edge is the fuel cladding and periphery of the fuel. The bottom edge is the centre of the fuel pellet. The HBS, transition zone and normal structure regions of the fuel radius are indicated as determined during PIE. Figure 5.4 from [10]	94
5.2	Scanning electron microscopy (SEM) images of the high burnup fuel surface. The left figure 5.2(a) shows the un-restructured fuel at the center of the fuel pellet. Figure 5.2(b) shows the HBS fuel and the presence of bonding between the fuel and the cladding. SEM images from [10].	95
5.3	Schematic illustrating the radial discretisation of an axial slice within TRANSURANUS.	96
5.4	Fission rate density at the pellet periphery and pellet average accross the pellet as calculated by TRANSURANUS.	97
5.5	Radial variation in the local burnup at end of life as calculated by TRANSURANUS. Also illustrated are the widths of the microstructure zones (normal structure, transition zone and HBS) as determined during PIE by electron probe microanalysis (EPMA) and SEM.	98
5.6	Temperature history for a high burnup fuel rod at the pellet periphery as calculated by TRANSURANUS.	98
5.7	Calculated pore number densities for the real fuel irradiation compared with data from Spino <i>et al.</i> [12].	100
5.8	Calculated porosity for the real fuel irradiation compared with data from Spino <i>et al.</i> [12].	100
5.9	Calculated local fission gas concentrations remaining in the HBS porosity and released along with the fractional local gas release from the HBS porosity.	101
5.10	Variation of the volume fraction of HBS as a function of local burnup for several different values of ΔB according to the correlation specified by equations 5.10 and 5.13.	104
5.11	Radial variation of the volume fraction of HBS at the end-of-life of a real high-burnup fuel irradiation. The microstructure regions, i.e. normal structure, transition zone and HBS, observed during PIE by EPMA and SEM are also indicated.	105
5.12	Fit to the absolute concentration of gas released.	106
5.13	Correlation describing the growth of the porosity.	107
5.14	Absolute gas release as a function of porosity calculated with the stand-alone in-pile model. Here the quantities of gas released at porosities of 14 % and 18 % are indicated.	108
5.15	Integral fission gas release and fuel/cladding temperatures for the base case. The gray area indicates the region where the measured fission gas release lies.	109
5.16	Radial distribution of fission gas release at end of life (EOL) for the base case.	110

5.17	Integral fission gas release as a function of reduced gap conductivity. The reduced gap conductivity is implemented for the entire power history of the rod. The gray area indicates the region where the measured fission gas release lies.	111
5.18	Gap width throughout irradiation as a function of the gap conductivity factor at an axial position ≈ 3046 mm from the end of the fuel rod.	111
5.19	Radial distribution of fission gas release at end of life as a function of reduced gap conductivity. The reduced gap conductivity is implemented for the entire power history of the rod.	112
5.20	Evolution of the calculated gap over-pressure throughout irradiation, the Halden clad lift-off initiation threshold and the measured overpressure from PIE.	113
5.21	Fuel centre, surface and clad inner temperatures and the integral fission gas release. The gray area indicates the region where the measured fission gas release lies.	114
5.22	Concentrations of created and released fission gas as a function of the radius for an additional athermal release from the HBS.	115
5.23	Time dependence of the pin outer pressure and fast neutron flux with and without the alterations to force gap closure.	116
5.24	Integral fission gas release, the fuel centre temperature, fuel surface temperature and the cladding inner temperature. The gray area indicates the region where the measured fission gas release lies.	116
5.25	Radial distribution of fission gas release at EOL for the slice taken at a position of ≈ 3000 mm from the end of the fuel rod.	117
5.26	Radial distribution of the athermal contribution to the pellet periphery release to take into account HBS volumes present in the transition zone.	119
5.27	Integral fission gas release at different surface-to-volume ratios. The gray area indicates the region where the measured fission gas release lies.	120
5.28	Radial distribution of fission gas release at EOL at a position ≈ 3046 mm from the rod end for several different values of the surface to volume ratio.	121
5.29	Schematic diagrams of adjustments made to the radial fission gas release profile to estimate the effects of other general uncertainties.	122
A.1	Percolation lattices for site and bond percolation. Figures 3a and 4a from [6].	137
D.1	Schematic showing the progression of the Newton-Raphson method for finding the root of a function of a single variable.	147
E.1	Schematic showing how a fuel rod is discretised in the SPHERE fission gas release model (a) axially and (b) radially.	150
E.2	Schematic illustrating the TRANSURANUS radial discretisation scheme for an axial slice.	150
E.3	A schematic of the processes considered in the PSI fission gas model showing the fission gas locations and the transport processes in the fuel grains and the grain boundaries.	151
E.4	Variation of the volume fraction of HBS as a function of local burnup for several different values of ΔB according to the correlation specified by equations E.2 and E.5.	154

E.5	A flowchart for the PSI HBS extension and its interaction with the PSI FGR model.	154
-----	---	-----

List of Tables

2.1	Cumulative produced atoms per fission of the stable fission gases from the fissile isotopes ^{235}U , ^{239}Pu and ^{241}Pu [1]	12
2.2	Values of the Arrhenius diffusion parameters from open literature	16
2.3	Precursor factors for some short-lived Xe & Kr isotopes	20
2.4	Cabri REP-Na tests with commercial PWR fuel rods (UO_2)	36
2.5	Cabri REP-Na tests with commercial PWR fuel rods (MOX)	36
2.6	Conditions for NSRR RIA tests of MOX and BWR (UO_2)	37
3.1	Summary of the processes and the gas phases which they affect	46
3.2	Nomenclature for the various transport processes and the different grain phases .	47
3.3	Nominal parameter values (corresponding to an averaged xenon concentration of ~ 0.2 wt %), along with parameter limits from open literature and the corresponding impact on gas concentrations	54
4.1	Interactions and their effect on the variables describing the state of the porosity (closed & vented) and the gas release.	73
4.2	Initial conditions for the model	74
5.1	In-pile porosity growth model parameters.	93
5.2	As-fabricated fuel rod specifications for the selected fuel rod	93
5.3	PIE Results	96
5.4	In-pile steady-state porosity growth model initial conditions.	99
5.5	Coefficients for the 5 th order polynomial fit to the gas release.	106
5.6	Coefficients for the 5 th order polynomial fit to the porosity.	107
5.7	Terms for the gas release correlation given by equation 5.17 for the porosity interval from 14% to 18%.	107
5.8	Coefficients for the 5 th order polynomial fits to the absolute gas release (see equation 5.17) at different surface-to-volume ratios	119
5.9	Increase in pellet average fission gas when taking into account increased release from several regions across the pellet radius	122

List of Abbreviations

BWR	Boiling Water Reactor
EPMA	Electron Probe Microanalysis
FBR	Fast Breeder Reactor
HBRP	High Burnup Rim Project
HBS	High Burnup Structure
HRP	OECD–Halden Reactor Project (Norway)
IFA	Instrumented Fuel Assembly
JAERI	Japan Atomic Energy Research Institute
KJMA	Kolmogorov–Johnson–Mehl–Avrami
LA-ICP-MS	Laser Ablation Inductively Coupled Plasma Mass Spectrometry
LWR	Light Water Reactor
MOX	Mixed OXide fuel, specifically a mixture of UO_2 and PuO_2
NPP	Nuclear Power Plant
NSRR	Japanese Nuclear Safety Research Reactor
ODE	Ordinary Differential Equation
OECD	Organisation for Economic Cooperation and Development
O/M	Oxygen to Metal ratio
PCMI	Pellet–Clad Mechanical Interaction
PDE	Partial Differential Equation
PIE	Post Irradiation Examination
PSI	Paul Scherrer Institute
PWR	Pressurised Water Reactor
RED	Radiation Enhanced Diffusion
RIA	Reactivity Initiated Accident
SEM	Scanning Electron Microscope
SIMS	Secondary Ion Mass Spectrometry
TD	Theoretical Density
TEM	Transmission Electron Microscope
XRF	X-Ray Fluorescence

Nomenclature

Physical constants

k_B	Boltzmann constant ($1.38066 \times 10^{-23} \text{ J K}^{-1}$)
m_{Xe}	Atomic mass of a xenon atom ($2.18 \times 10^{-25} \text{ kg}$)
N_A	Avogadro's number ($6.0221415 \times 10^{23} \text{ mol}^{-1}$)
ω_{Xe}	Van der Waal constant for xenon ($8.5 \times 10^{-29} \text{ m}^3/\text{atom}$)
Ω	Volume of a UO_2 cell ($4.09 \times 10^{-29} \text{ m}^3$)

Variables

a_U	Radiation enhanced diffusion constant for uranium (m^5)
$a_{v,i}$	Radiation enhanced diffusion constant for vacancies and interstitials (m^5)
A_{gb}	Cross-sectional area of the grain boundary (m^2)
A_{gr}	Surface area of a UO_2 grain (m^2)
B	Local burnup (MWd/kg)
B_0	Local burnup at which the microstructure starts to transform from a normal microstructure to HBS (MWd/kg)
ΔB	Burnup increment to complete the transition from normal microstructure to HBS (MWd/kg)
c_i	Concentration of interstitials (m^{-3})
c_{bulk}^i	Bulk interstitial concentration (m^{-3})
c_{grb}^{fg}	Concentration of gas in the intra-granular bubbles (m^{-3})
c_v	Concentration of vacancies (m^{-3})
c_{bulk}^v	Bulk vacancy concentration (m^{-3})
c_{cp}^{fg}	Concentration of fission gas in the closed porosity (m^{-3})
c_{cp}^{xe}	Concentration of xenon in the closed porosity (m^{-3})
c_p^{fg}	Concentration of fission gas in pores (m^{-3})
c_{gbf}^{fg}	Concentration of fission gas on the grain boundary that has not yet been trapped by inter-granular bubbles (m^{-3})
c_{gbb}^{fg}	Concentration of fission gas in inter-granular bubbles (m^{-3})
$c_{gbb}^{fg} \Big _{sat}$	Concentration of fission gas in inter-granular bubbles at inter-linkage (m^{-3})
c_{gr}^{fg}	Concentration of fission gas in a grain (m^{-3})
C_{irr}^i	Fractional concentration of irradiation induced interstitials (-)
C_{eq}^{io}	Fractional concentration of thermal equilibrium oxygen interstitials (-)

C_{eq}^{iu}	Fractional concentration of thermal equilibrium uranium interstitials (-)
c_{rel}^{fg}	Concentration of released fission gas (m^{-3})
c_U	Concentration of uranium atoms in the fuel (m^{-3})
C_{irr}^v	Fractional concentration of irradiation induced vacancies (-)
C_{eq}^{vo}	Fractional concentration of thermal equilibrium oxygen vacancies (-)
C_{eq}^{vu}	Fractional concentration of uranium vacancies (-)
$\langle c_{gr}^{Xe} \rangle_{vol}$	Average xenon concentration in the UO_2 grains (m^{-3})
$\langle c_{gr}^{Xe} \rangle_{wt}$	Average xenon concentration in the UO_2 grains (wt%)
D_0^{Xe}	Diffusion coefficient pre-exponential for xenon (m^2s^{-1})
D_0^{fg}	Diffusion coefficient pre-exponential for fission gas (m^2s^{-1})
$D_0^{v,i}$	Diffusion coefficient pre-exponential for vacancies and interstitials (m^2s^{-1})
$D_{1,2,3}^{fg}$	Terms for Turnbolls three term fission gas diffusion coefficient correlation (m^2s^{-1})
$(D_{gr}^{fg})^*$	Effective fission gas diffusion coefficient (m^2s^{-1})
D_{gb}^{fg}	Fission gas diffusion coefficient in the grain boundary (m^2s^{-1})
$D_{gr}^{fp}(i)$	Diffusion coefficient in UO_2 of fission product i (m^2s^{-1})
D_{gr}^i	Interstitial diffusion coefficient ($\text{m}^2 \text{ s}^{-1}$)
D_{RED}^U	Radiation enhanced diffusion coefficient (m^2s^{-1})
D_{gr}^{Xe}	Xenon diffusion coefficient in UO_2 (m^2s^{-1})
D_{gr}^v	Vacancy diffusion coefficient ($\text{m}^2 \text{ s}^{-1}$)
$D_{RED}^{v,i}$	Radiation enhanced diffusion coefficient for vacancies and interstitials respectively (m^2s^{-1})
D_{gr}^U	Self diffusion coefficient of uranium (m^2s^{-1})
$D_{irr}^{v,i}$	Diffusion coefficient of vacancies and interstitials under irradiation (m^2s^{-1})
\dot{f}	Fission rate (fissions s^{-1})
\dot{F}	Fission rate density (fissions $\text{m}^{-3} \text{ s}^{-1}$)
\dot{F}_{ref}	Reference fission rate density at a linear heat rate of 20 kW/m (fissions $\text{m}^{-3} \text{ s}^{-1}$)
F_{HBS}	Local volume fraction of HBS in the microstructure (-)
$[FGR(r)]_{redist}^{HBS}$	Re-distributed fission gas release from the HBS volumes at radius r in the fuel pellet (-)
$[FGR(r)]_{redist}$	Re-distributed fission gas release at radius r in the fuel pellet (-)
$[FGR(r)]_{redist}^{NS}$	Fission gas release from the normal microstructure at radius r in the fuel pellet (-)
$\Delta \langle FGR \rangle$	Increase in pellet average fission gas release (-)
ΔG_{Fo}	Formation energy of an oxygen Frenkel defect (eV/atom)
ΔG_{Fu}	Formation energy of a uranium Frenkel defect (eV/atom)
ΔG_s	Formation energy of a Schottky defect (eV/atom)
h_{pellet}	Pellet height (m)
$\Delta H_{v,i}$	Diffusion enthalpy for vacancies and interstitials respectively (eV/atom)
ΔH_{fg}	Diffusion enthalpy for fission gas (eV/atom)
ΔH_{Xe}	Diffusion enthalpy for xenon (eV/atom)
J_{recoil}^i	Rate of release due to recoil for isotope i (s^{-1})

J_{prod}^{gr}	Rate of production of fission gas per grain (s^{-1})
J_{ld}^{gbb}	Rate at which fission gas enters inter-granular bubbles due to volume diffusion from the grain to grain boundary (s^{-1})
J_{ld}^{gbf}	Rate at which fission gas enters the free grain boundary gas phase due to volume diffusion from the grain to grain boundary (s^{-1})
J_{res}^{gbb}	Rate of re-resolution for the trapped grain boundary gas phase (s^{-1})
J_{res}^{gbf}	Rate of re-resolution for the free grain boundary gas phase (s^{-1})
J_{tr}^{gbb}	Rate of trapping of gas in the free grain boundary gas phase (s^{-1})
J_{tr}^{grb}	Capture rate of fission gas in intra-granular bubbles in UO_2 (s^{-1})
k_{res}	Re-resolution rate coefficient (s^{-1})
k_{res}^{ref}	Reference re-resolution rate coefficient at a fission rate density \dot{F}_{ref} (s^{-1})
k_{grtr}	Rate constant for intra-granular trapping in UO_2 (s^{-1})
k_{ld}	Rate coefficient for volume diffusion (s^{-1})
k_{res}	Re-resolution rate coefficient (s^{-1})
k_{gbtr}	Rate coefficient for trapping of fission gas in inter-granular bubbles (s^{-1})
k_{gbd}	Rate coefficient for grain boundary diffusion ($m^4 s^{-1}$)
$k_{rec}^{v,i}$	Rate coefficient for recombination of Frenkel pairs (s^{-1})
l_f	Range of a fission fragment (m)
l_{p-p}	Average separation of HBS Pores (m)
l_{rec}	Recombination length (m)
n_{cp}	Number density of closed pores (m^{-3})
n_{gbb}	Areal number density of inter-granular bubbles (m^{-2})
n_{grb}	Number density of intra-granular bubbles in UO_2 (m^{-3})
n_p	Pore number density (m^{-3})
n_{vp}	Number density of vented pores (m^{-3})
N_v	Number of vacancies (-)
$N_b^{fg} \Big _{crit}$	Critical number of atoms in a single inter-granular bubble for growth to occur (-)
N_p^{fg}	Number of fission gas atoms in a single pore (-)
N_{cz}	Number of coarse radial zones in a TRANSURANUS calculation (-)
$N_{rel}^{fg}(r)$	Quantity of fission gas released at a radius r in the fuel pellet (-)
$N_{crea}^{fg}(r)$	Quantity of fission gas created at a radius r in the fuel pellet (-)
N_b^{fg}	Number of atoms of fission gas in a single grain boundary bubble (-)
$N_b^{fg} \Big _{crit}^{tot}$	Total amount of a gas in the grain boundary bubbles required to maintain mechanical equilibrium (-)
$N_b^{fg} \Big _{tot}$	Total amount of a gas on the grain boundary in grain boundary bubbles (-)
$N_p^{fg} \Big _{tot}$	Total amount of a gas in the porosity (-)
p_h	Hydrostatic pressure (Pa)
p_p	Internal gas pressure in a pore (Pa)
p_{gbb}	Internal gas pressure in a inter-granular bubble (Pa)
p_{grb}	Internal gas pressure in a intra-granular bubble (Pa)
P	Fractional porosity (-)
P_{cp}	Fractional porosity of the closed pores (-)

P_{vp}	Fractional porosity of the vented pores (-)
R_{booth}	Radius of the Booth equivalent sphere (m)
R_{gbb}	Radius of inter-granular bubbles (m)
R_{gr}^{HBS}	Radius of a HBS grain (m)
R_{gr}^{NS}	Radius of a normal structure grain (m)
$\left[\frac{R}{B}\right]_{knock-on}^i$	Release to birth ratio due to the knock-on process (-)
$\left[\frac{R}{B}\right]_{ld}^i$	Release to birth ratio of short lived fission gas isotopes due to lattice diffusion (-)
R_{grb}	Radius of an intra-granular bubble in UO_2 (m)
R_{gbb}^e	Radius of curvature of a lenticular inter-granular bubble perpendicular to the grain boundary of UO_2 (m)
R_{gbb}^s	Radius of curvature of a lenticular inter-granular bubble for a circular projection on the grain face of UO_2 (m)
R_p	Radius of a pore (m)
R_{pellet}	Fuel pellet radius (m)
R_{gr}	Grain radius (m)
R_{cp}	Radius of a closed pore (m)
R_{vp}	Radius of a vented pore (m)
S_1^*	Total cross-section for any compound interaction involving two closed pores (-)
S_2^*	Total cross-section for any compound interaction involving a closed pore and a vented pore (-)
S_3^*	Total cross-section for any compound interaction involving a closed pore and the open surface (-)
S_1	Cross-section for the interaction of a closed pore with another closed pore (-)
S_2	Cross-section for the interaction of a closed pore with another vented pore (-)
S_3	Cross-section for the interaction of a closed pore with open surface (-)
S_{12}	Cross-section for the interaction of a closed pore, closed pore and a vented pore (-)
S_{13}	Cross-section for the interaction of a closed pore, closed pore and the open surface (-)
S_{23}	Cross-section for the interaction of a closed pore, a vented pore and the open surface (-)
S_{123}	Cross-section for the interaction of a closed pore, closed pore, a vented pore and the open surface (-)
$\frac{S}{V}$	Surface to volume ratio (m^{-1})
$\left.\frac{S}{V}\right _{geom}$	Geometrical surface to volume ratio for the fuel (m^{-1})
$\left.\frac{S}{V}\right _{grain}$	Surface to volume ratio of a grain (m^{-1})
$\left.\frac{S}{V}\right _{total}$	Total surface to volume ratio for the fuel, taking into account porosity and cracks (m^{-1})
t	Time (secs)
T_C	Temperature ($^{\circ}C$)
T_K	Temperature (K)

V_{chip}	Volume of inter-granular bubble removed when a fission fragment intersects with the bubble (m^3)
V_{gr}^{HBS}	Volume of a HBS grain (m^3)
V_{gb}^{HBS}	Volume of the grain boundary for a single HBS grain (m^3)
V_{gbb}	Volume of an inter-granular bubble (m^3)
V_{defect}	Volume of a defect (m^3)
V_p	Volume of a pore (m^3)
V_{fuel}	Fuel volume (m^3)
V_{gb}	Volume of the grain boundary surrounding a single grain (m^3)
Y_i	Total cumulative yield for isotope i (-)
Y_{fg}	Total cumulative yield of xenon and krypton (-)
z_s	Number of stable Frenkel pairs per fission event (-)
z_u	Number of uranium atoms emitted per escaping fission fragment (-)
η	Recombination constant (m^{-2})
α	Grain boundary to grain diffusion coefficient ratio (-)
ν_i	Precursor factor for short lived fission gas isotopes (-)
δ_{gb}	Width of a grain boundary in UO_2 (m)
δ_{dl}	Width of the diffusion layer on the grain boundary (m)
γ_{fs}	UO_2 -gas specific surface energy for fission gas bubbles in UO_2 (J m^{-2})
λ_i	Decay constant of fission product i (s^{-1})
ϕ	Areal fractional coverage of a grain face by inter-granular bubbles (m^{-2})
ρ_f	Density of UO_2 (kg m^{-3})
θ	Semi-dihedral angle between the grain boundary and the bubble surface (50°)

Chapter 1

Introduction

Science is a great game. It is inspiring and refreshing. The playing field is the universe itself.

- Isidor Isaac Rabi

Nuclear power has experienced constant growth in the past twenty years and currently accounts for $\sim 16\%$ of the global electricity generating capacity. Although this figure has remained stable, global electricity production has increased indicating that growth in nuclear power has matched the rate of growth in global electricity production [1]. Approximately 85 % of the current nuclear generated electricity comes from light water reactors (LWRs)¹, i.e. reactors where water is used to remove the heat generated by the fuel pins and to moderate the neutrons. Most of these LWRs rely upon UO_2 enriched to 3–5 wt% ^{235}U , and, in some cases, a mixture of UO_2 and PuO_2 (MOX) as fuel. The fuel is made in the form of cylindrical ceramic fuel pellets that are stacked within a metallic cladding material (see Fig 1.1).

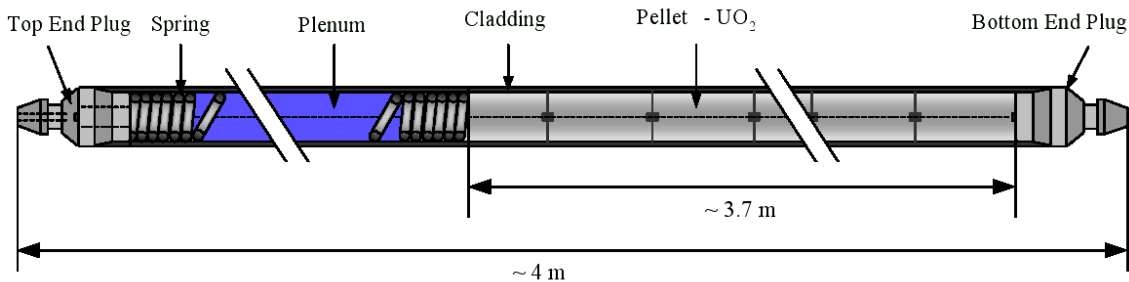


Figure 1.1. Schematic of a fuel rod.

The safe and economic operation of nuclear fuel requires that the behaviour and fuel performance can be calculated reliably for the expected lifetime of the fuel rod. This requires highly developed codes that treat the fuel in a general manner and which take into account the large number of influences on fuel behaviour, e.g. thermal, mechanical, chemical, etc. The nuclear utilities and safety authorities utilise fuel performance modelling as a cost-effective method of examining fuel

¹There are two broad categories of LWRs, viz. pressurised water reactors (PWRs) in which the primary coolant remains sub-cooled and boiling water reactors (BWRs) in which it exits the reactor core as a 2-phase mixture.

behaviour and defining conservative safety limits for operation. In turn, the predictions of such codes are regularly validated against data produced by post irradiation examination (PIE) and in-pile experiments in research reactors.

Although many mature fuel performance codes are in active use and development, there are still significant incentives to improve their predictive capability. One particular aspect that has been focused on in recent years is the possibility of extending discharge burnups² beyond current licensing limits. The motivation for increasing the discharge burnup is primarily centred on the improved economics of extracting more power from a given fuel rod, and a corresponding trend has been observed in nuclear power plants (NPPs) worldwide (e.g. see figure 1.2). The Swiss nuclear utilities (PWRs in particular) have pursued this path actively and, as a result, burnups at the pellet-level of up to 76 GWd/tU (both for UO₂ and MOX fuel) may be licensed in Switzerland.

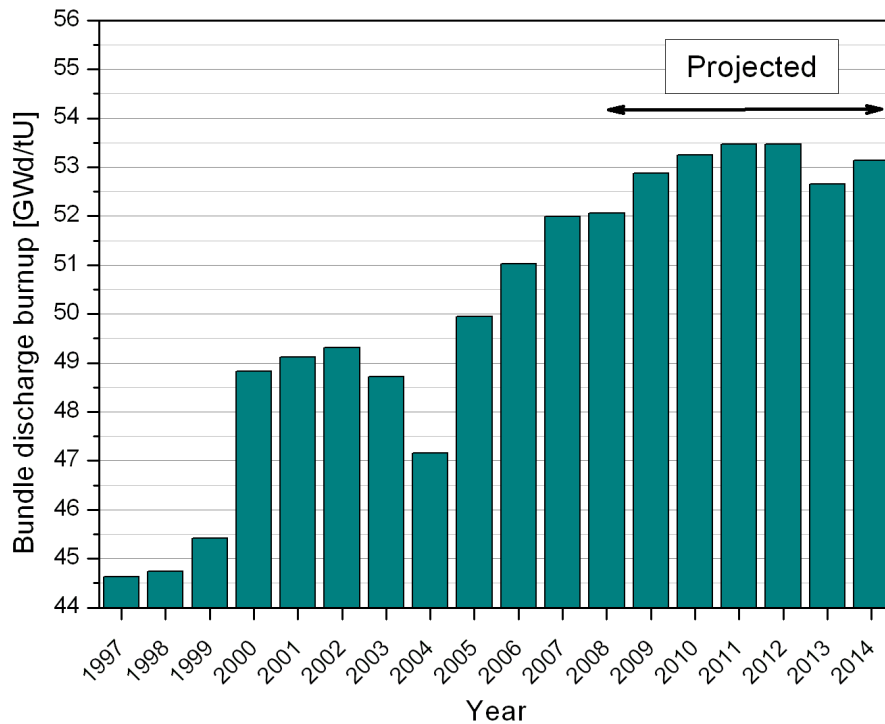


Figure 1.2. Average bundle discharge burnup (in GWd/tU) at a Swiss BWR NPP.

1.1 Background

1.1.1 Fission gas

With increasing burnup, more and more fission events impact the material characteristics of the fuel, as well as the cladding, and significant restructuring can be observed in the fuel. The fission

²The burnup of nuclear fuel is a measure of the energy produced per unit mass of either fuel or the uranium and plutonium content.

process not only generates heat in the fuel rod, it also produces a wide range of fission products³ (see Fig 1.3) that affect the microstructural characteristics of the fuel. Of particular note are the inert gas elements xenon and krypton (generally referred to as fission gas), which account for $\sim 13\%$ of all fission products. The release of fission gas from the fuel has the primary effect of increasing the inner pressure of the fuel pin and, consequently, is considered as one limiting factor for the discharge burnup of a fuel rod. A secondary effect of gas release can occur at low burnups, when the pellet-clad gap is open. The additional mixing with the pre-existing fill gas⁴ degrades the thermal conductivity of the gas-filled gap, thus increasing the fuel temperature. The transport of fission gas in the pellet is primarily diffusional and, consequently, significant release of fission gas can cause a feedback loop between rising temperatures and release, eventually causing cladding failure.

Although significant fission gas release can have detrimental effects, so does substantial retention. The retention of fission products in the fuel matrix causes swelling of the fuel pellet, and this swelling can enhance the pellet-clad mechanical interaction (PCMI) at high burnups potentially leading to fuel failure during power transients. Hence, the quantity and location of the fission gas is important when evaluating fuel performance and the corresponding safety margins for both normal operation and transient conditions.

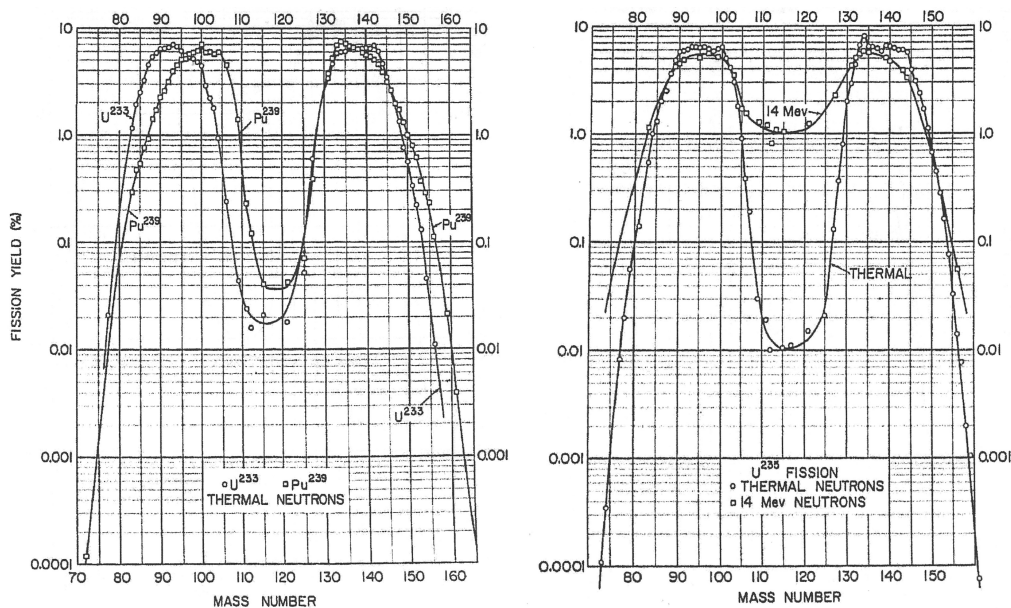


Figure 1.3. Fission product yields as a function of mass number for ^{235}U , ^{233}U and ^{239}Pu [2].

Today, the basic principles for fission gas behaviour in the normal fuel structure are largely known and implemented in fuel performance codes with various degrees of detail. One generally distinguishes two steps in most mechanistic fission gas models: fission gas transport in a fuel grain to the grain boundary and fission gas release from the grain boundaries to the free volume in the rod. The behaviour of fission gas during the intra-granular diffusion process is typically

³These fission products initially have considerable kinetic energy and consequently they cause primary and secondary damage to the surrounding material. The fission products are referred to as fission fragments until this initial kinetic energy is used up, at which point they are simply referred to as fission products.

⁴This is typically helium.

separated into several individual processes:

- Single atom diffusion within the fuel matrix.
- The nucleation of fission gas bubbles.
- Irradiation induced re-resolution of the fission gas bubbles by fission fragments and accompanying thermal spikes.
- Trapping in as-fabricated pores.

Upon creation, fission gas atoms migrate to the grain boundaries due to a concentration gradient resulting from the sink-like nature of the grain boundaries. However, a population of nm-size fission gas bubbles is created a small time after the start of irradiation. These bubbles act as traps and increase in size by absorbing vacancies and diffusing fission gas atoms. At the same time, fission fragments/thermal spikes destroy the bubbles and disperse the gas atoms and vacancies into the surrounding matrix, a process referred to as re-resolution. This competition leads to an equilibrium number density of bubbles forming in the grain structure. The saturation of bubbles within the matrix was originally shown by Speight [3] to occur very quickly and has been observed in some early experimental observations [4]. Fission gas can also be trapped in as-fabricated pores. Due to the larger size of the pores, they cannot normally be destroyed by fission fragments, i.e. re-resolution is not a significant effect.

Fission gas behaviour on the grain boundaries has, for some time, been modeled in one of two different ways, i.e.

1. By considering the grain boundary as a high-diffusivity path resulting in fast diffusion to the inter-granular bubbles or the plenum.
2. By considering the grain boundary as a perfect trap with the fission gas immediately trapped in grain boundary bubbles.

Several approaches have been developed in an attempt to provide better models for the behaviour of grain boundary gas. In particular, the recent trend has been to model the grain boundary bubbles as imperfect sinks by considering a small re-resolution of fission gas into the first few layers of the grain near the grain boundary. In some fission gas models, e.g. the Paul Scherrer Institute (PSI) SPHERE fission gas model, the re-resolution of grain boundary gas acts to build up a small “concentration wall” inside the grain close to the grain boundaries [5].

After a certain amount of time a population of grain boundary bubbles exists on the grain faces and edges. Eventually these bubbles grow to such an extent that they combine or “inter-link” producing a tunnel network of bubbles. This is typically considered the point at which the gas is released to the plenum. The interconnection process is reversible and highly susceptible to the temperature and local stresses in the fuel. The most common treatment of this process in fission gas models is to wait until the fission gas in the grain boundary bubbles has exceeded a threshold concentration and then allow release to take place [6]. However, this treatment relies

upon the assumptions that the gas is ideal and the bubble is in mechanical equilibrium. In order to address these significant simplifications, several mechanistic kinetic models have been developed to describe the gas behaviour without these assumptions [7, 8, 9].

As the fission gas in the matrix and in grain boundary bubbles can contribute significantly to fuel swelling, a number of models take this into account in an explicit manner. Other models try to cope with this problem with simple, fission gas independent, burnup dependent swelling models. If gaseous swelling is to be taken into account mechanistically, the fission gas model must be detailed enough to predict the location of the fission gas at every stage (i.e. dissolved in the matrix, in as-fabricated pores, in intragranular bubbles, on the grain boundaries, in grain boundary bubbles, and released).

1.1.2 High burnup structure

In recent years, the aspect of greatest interest for UO_2 fuel has been the formation of the so-called high burnup structure (HBS) and, in particular, the consequences for fuel behaviour. The first observations of the HBS were reported as early as 1963 by Bleiberg *et al.* [10]. They observed that, when the local burnup reaches 75 MWd/kgU, a significant decrease in the grain size can be seen at the periphery of fuel pellets in comparison with the as-fabricated state. Since then there has been a significant effort to characterise the HBS and understand the formation mechanism. This has led to the identification of three principle features:

1. A change in the grain size distribution from an average grain size of $\sim 10\ \mu\text{m}$ to $\sim 0.1\ \mu\text{m}$.
2. A large depletion of fission gas in the grains, specifically xenon, to a burnup independent value of $\sim 0.2\ \text{wt}\%$ Xe (as measured by electron probe microanalysis, EPMA).
3. The creation of large faceted pores (size $\sim 1\ \mu\text{m}$), with a porosity that increases continuously with local burnup. It is generally considered that most of the gas not present in the fuel matrix is contained within these pores.

There is now a general consensus that the HBS is formed when fuel is irradiated to high burnups (60–75 GWd/tHM local burnup) at low temperatures, i.e. lower than 1100–1200 °C. It is also clear that the transition is independent of the fuel type or irradiation history. At the threshold burnup, the first isolated spots of HBS, surrounded by unrestructured fuel, are formed. At a local burnup of $\sim 120\ \text{GWd/tHM}$, 100 % of the local fuel volume has transformed. Unrestructured fuel and fully developed HBS are separated by a transition zone. Across this transition zone, the fraction of HBS in the fuel increases from 0 % to 100 %.

Identification of the peculiar features of the HBS has led to a significant effort to understand the consequences for fuel performance and safety. There are two particular concerns: (1) the large retention of fission gas within the HBS, which could lead to the possibility for significant gas release at high burnups either through the degradation of thermal conductivity or direct release, and (2) the behaviour during operational transients and design basis accidents. Due to the burnups currently being achieved in reactors and the desirability of even higher discharge

burnups, several experimental programmes have been developed to investigate the fuel behaviour under reactivity initiated accident (RIA) scenarios. These programmes were initiated in order to review the existing licensing limits, which have been derived from experimental databases obtained for fuel with moderate burnup, and to eventually develop new ones allowing better defined margins for fuel safety at high burnups. Two of the biggest such programmes are the CABRI REP-Na tests, which ran between 1993 and 1998 [11], and the Japanese Nuclear Safety Research Reactor (NSRR) tests [12, 13], which started in 1989 and continues to produce results. These test programmes were started with the intention to look specifically at the behaviour of high burnup commercial fuel (UO_2 and MOX) under a series of different RIA conditions, with special attention given to early clad loading caused by the interaction between the fuel pellets and the cladding (PCMI). In the case of the NSRR programme, the initial tests used fresh fuel; however, since 1989, the programme has focused on pre-irradiated fuel experiments. In both programmes, a number of key observations have been made:

- Cladding failures occurring at lower than expected peak fuel enthalpy.
- Hydride spots and blisters on the failed cladding often associated with the failure.
- A large fission gas release ($\sim 20\%$).
- Grain separation due to fission gas swelling.

The last two points underline the importance of accurate fuel performance calculations for a reliable analysis of accident scenarios.

While for the normal structure numerous models, investigations and codes exist, only a few models for simulating fission gas behaviour in the HBS have been developed. Consequently, in this context, it is fair to say that reliable mechanistic models are largely missing today. The potential for a large release of fission gas from the porosity of the HBS is important enough for the accurate determination of the fission gas behaviour, porosity growth and any accompanying release to be a principal feature in evaluating safety margins and corresponding fuel performance at high burnups. In particular, the quantity and location of the fission gas prior to design basis accident situations is of special interest in this context. This provides the principal motivation for the present research, viz. to develop and evaluate models based upon normal structure models of fission gas transport, which are applicable to the HBS with a view to improve upon the current gap in fuel performance modelling.

1.2 Research objectives and stages

The goals of the present research correspond to its four principal stages. These are listed below along with the individual steps involved for each stage.

1. Modelling fission gas diffusion in the HBS:

- Develop a one-dimensional steady-state fission gas model, including grain boundary diffusion, for the fuel region between two HBS pores. Here, particular emphasis is placed on the geometrical characteristics (e.g. porosity, grain size) of the HBS rather than changes in earlier well established mechanisms for fission gas transport.
 - Examine the effect that grain boundary diffusion has upon the equilibrium xenon concentration.
 - Perform a sensitivity analysis to elucidate the effect of model parameters that are not accurately specified in literature and determine which of these parameters are the most significant for the model.
 - Determine the range of values of the significant parameters for which the calculated equilibrium xenon concentrations match the values reported in literature.
2. Simulation of defect transport and fission gas release under annealing conditions.
- Develop a continuum model to describe the growth, coalescence and venting of the HBS porosity during annealing conditions.
 - Evaluate the model behaviour with respect to the principal parameters.
 - Simulate an annealing test performed on a HBS fuel sample and compare with the experimental data.
3. Simulation of defect transport and fission gas release under irradiation.
- Extend the annealing porosity model to include the effect of irradiation.
 - Calculate the behaviour for a real irradiation history, specifically a fuel rod from a Swiss NPP.
 - From the model results, develop correlations for fission gas release and porosity growth as a function of the local burnup.
4. Integration of the new model into a fuel performance code.
- Implement the correlations developed from the stand-alone porosity model into the fission gas release subroutines of the fuel performance code TRANSURANUS.
 - Carry out the fuel performance calculation for the Swiss NPP fuel rod using the improved TRANSURANUS code.
 - Compare the model predictions from the fuel performance calculation with the post irradiation examination results.

1.3 Thesis outline

As sketched above, the principal aspects of the research presented in this thesis are: (i) the development of models to evaluate the impact of the HBS on the fission gas behaviour in nuclear fuel under annealing and irradiation conditions (chapters 3 and 4), and (ii) the validation and

analysis of the impact of the HBS on the fuel performance using a correlation based approach in the fuel performance code TRANSURANUS (chapter 5).

Chapter 2 presents a background survey of fission gas transport mechanisms and of the HBS. This includes the diffusion of fission gas within the normal structure, the effect of trapping by intra-granular and inter-granular bubbles, irradiation-induced re-solution effects, trapping by the porosity and grain boundary diffusion. The HBS is additionally reviewed from the point of view of both the present state of knowledge about the transition from normal structure and the fuel performance behaviour after the transformation is complete.

Chapter 3 focuses on the development and analysis of a one-dimensional fission gas model describing the steady-state concentrations of xenon within the fuel microstructure. The calculated equilibrium matrix xenon content is compared with the observed depletion in the fuel matrix and a sensitivity study is presented evaluating the behaviour of the model with respect to parameters that are not well defined in open literature.

Chapter 4 presents the development of models describing porosity growth for annealing conditions. A gas release model is developed that takes into account the growth of pores, interaction with the open surface and higher order compound interactions. A sensitivity analysis is presented evaluating the effect of parameters such as temperature and the surface-to-volume ratio on the fission gas release under static temperatures. The model is then applied to a high burnup LWR UO₂ annealing experiment to assess its predictions in comparison with the measurements. Implications of the results from the annealing case for in-pile behaviour are also discussed.

Chapter 5 concerns the extension of the annealing porosity growth model to in-pile conditions. The in-pile model is first used to calculate the local porosity growth and fission gas release in the HBS using the power history of a particular high burnup fuel rod from a Swiss NPP. The results are then compared with the post irradiation examination results from open literature. From the analysis of the irradiation behaviour, correlations describing the evolution of the porosity and fission gas release are developed. These correlations are then implemented into the fuel performance code TRANSURANUS. The code is then used to model the real-life irradiation of a complete high-burnup fuel rod and evaluate the consequences for fuel performance.

Chapter 6 presents conclusions from the research, and recommendations are made for avenues of future work.

Bibliography

- [1] International Atomic Energy Agency. *IAEA (International Atomic Energy Agency) Annual report for 2005*, 2005.
- [2] S. Katcoff. Fission-product yields from neutron-induced fission. *Nucleonics.*, 18(11):201–208, 1960.
- [3] M. V. Speight. A calculation on the migration of fission gas in material exhibiting precipitation and re-solution of gas atoms under irradiation. *Nucl. Sci. Eng.*, 37:180–185, 1969.
- [4] J.A. Turnbull. Distribution of intragranular fission gas bubbles in UO_2 during irradiation. *J. Nucl. Mater.*, 38(2):203, 1971.
- [5] H. Wallin, L.Å. Nordström, and Ch. Hellwig. Fission gas model of the fuel code SPHERE-3. In *Proceedings of the IAEA/NEA/CEA International Seminar on Fission Gas behaviour in Water Reactor Fuels*, pages 391–406, Cadarache, France, September 2000.
- [6] R.J. White and M.O. Tucker. A new fission-gas release model. *J. Nucl. Mater.*, 118:1–38, 1983.
- [7] T. Kogai. Modelling of fission gas release and gaseous swelling of light water reactor fuels. *J. Nucl. Mater.*, 244:131–140, 1997.
- [8] P. Van Uffelen. *Contribution to the Modelling of Fission Gas Release in Light Water Reactor Fuel*. PhD thesis, l’Université de Liège, 2002.
- [9] G. Khvostov, A. Medvedev, and S. Bogatyr. The dynamic model of grain boundary processes in high burn-up LWR fuel and it’s application in analysis by the START-3 code. In *Proceedings of the International Conference on WWER Fuel Performance, Modelling and Experimental Support*, Albena-Varna, Bulgaria, September 2003.
- [10] M.L. Bleiberg, R.M. Berman, and B. Lustman. Effects of high burn-up on oxide ceramic fuels. In *Proceedings of the Symposium on Radiation Damage in Solids and Reactor Materials*, pages 319–428, Vienna, August 1963. IAEA.
- [11] F. Schmitz and J. Papin. High burn-up effects on fuel behaviour under accident conditions: The tests CABRI REP-Na. *J. Nucl. Mater.*, 270:55–64, 1999.
- [12] T. Nakamura, T. Sasjima, H. Fuketa, and K. Ishikima. Fission gas induced cladding deformation of LWR fuel rods under reactivity initiated accident conditions. *J. Nucl. Sci. Technol.*, 33(12):924–935, 1996.
- [13] T. Fuketa, H. Sasajima, Y. Mori, and K. Ishijima. Fuel failure and fission gas release in high burnup PWR fuels under RIA conditions. *J. Nucl. Mater.*, 248:249–256, 1997.

Chapter 2

State of the art

Among the myriad phenomena that occur simultaneously in a nuclear fuel element under irradiation, none has so frustrated the designer, so challenged the experimentalist, or so intrigued the theorist as the behavior of the fission products xenon and krypton.

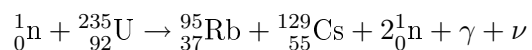
- D. R. Olander

2.1 Fission gas production, migration and release

Fission gas production, migration and release in nuclear fuel has been studied since the earliest days of nuclear energy. At this time metallic fuels were in use and the early interest in fission gas release was mostly due to the large swelling they exhibited and the potential cladding damage due to enhanced gap pressure induced by the fission gas release. At that time theoretical analyses of fission gas behavior were quite simple, as was necessary for reactors in which fission density, burnup, and fuel temperatures were too low to produce the wide variety of mechanisms that are now recognized as occurring in modern highly rated fuels. This section brings together the current state of knowledge surrounding the migration of fission gas.

2.1.1 Production

A typical example of a neutron-induced fission reaction for thermal neutron energies is:



The two daughter fission products in general are not uniquely determined, rather there is a distribution of masses (see figure 1.3). The isotopes produced directly are generally short-lived, radioactive and typically decay via gamma or beta emission. Because the predominant decay process is beta and/or gamma the decay process does not change the mass number. In general the fission products undergo multiple decays involving several nuclides of the same mass number. These decay chains result in an additional production of fission products in addition to the direct

production from fission. The cumulative yield¹ of a fission product is the sum of the yield from direct fission and all the decay chains contributing to the nuclide in question. Figure 2.1 shows the cumulative yield for the principal fissile isotopes, ^{235}U , ^{239}Pu and ^{241}Pu ².

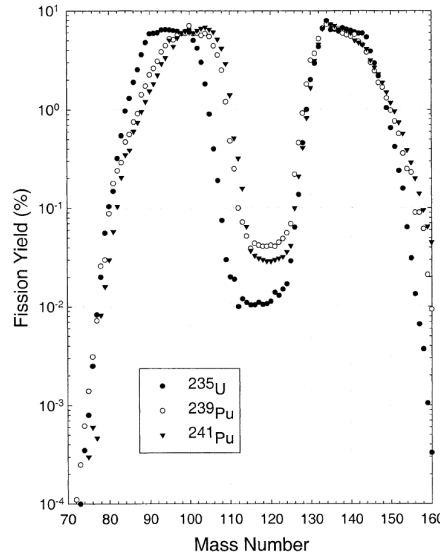


Figure 2.1. Cumulative yields for fission product mass chains from thermal fission of ^{235}U , ^{239}Pu and ^{241}Pu . Figure 1 from [1]

The stable xenon ($A=131\text{--}136$) and krypton ($A=83\text{--}86$) isotopes, generally referred to as fission gases, are close to the top of the peaks in the mass distribution (see figure 2.1) and consequently they comprise a significant proportion of the fission products. Table 2.1 lists the cumulative yields for the stable xenon and krypton isotopes.

Table 2.1. Cumulative produced atoms per fission of the stable fission gases from the fissile isotopes ^{235}U , ^{239}Pu and ^{241}Pu [1]

Isotope	Cumulative yields [%]		
	^{235}U	^{239}Pu	^{241}Pu
^{83}Kr	0.55	0.29	0.20
^{84}Kr	1.01	0.47	0.35
^{85}Kr	0.29	0.13	0.09
^{86}Kr	1.20	0.77	0.61
Total Kr	3.05	1.66	1.25
^{131}Xe	2.89	3.87	3.07
^{132}Xe	4.27	5.26	4.08
^{134}Xe	7.75	7.56	7.60
^{136}Xe	6.27	6.94	6.71
Total Xe	21.21	23.63	21.46

¹Sometimes referred to as the chain yield

² ^{239}Pu is generated from neutron absorption in ^{238}U , which for most commercial LWR fuels constitutes the bulk of the uranium inventory. ^{241}Pu results from successive neutron captures in ^{239}Pu .

Table 2.1 illustrates important points regarding the quantity of generated xenon and krypton. First, $\sim 13\%$ of the fission products are gaseous with krypton only making up $\approx 5\text{--}15\%$ of these. Secondly the xenon total yields are relatively invariant with the particular fissile isotope. The same is not true of krypton and, because of this and the build up of ^{239}Pu and ^{241}Pu in the periphery of the fuel pellet³, the Xe/Kr ratio can typically be used to indicate where the origin of the fission gas release lies. Generally, the rate of production of the fission gases in a unit volume of fuel is $\dot{F}Y_{fg}$, where \dot{F} is the fission rate density and Y_{fg} is the total cumulative yield of xenon and krypton.

2.1.2 Recoil & knock-out

When the two fission products are initially produced the coulomb repulsion drives them apart. Released they carry, as kinetic energy, the major part of the fission energy, at which point they are referred to as fission fragments. The energy distribution (see figure 2.2) is related to the fission product mass distribution [2]. This initial kinetic energy is slowly expended through electronic interactions with the material until the fission fragment comes to rest, typically $\sim 10\text{ }\mu\text{m}$ from it's formation, and becomes known as a fission product once again.

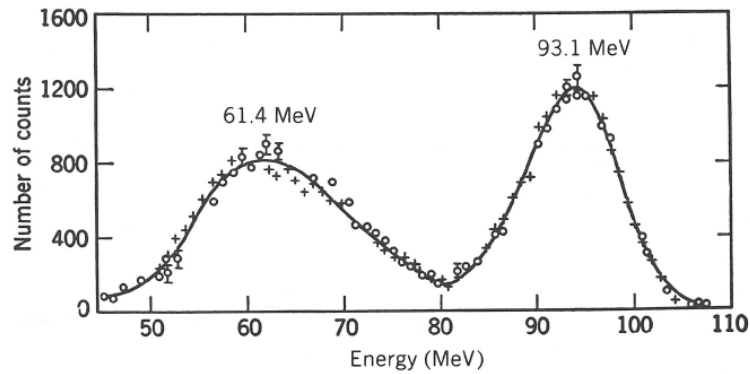


Figure 2.2. Energy distribution of fission fragments from thermal fission of ^{235}U . [2]

If the fission fragment is created sufficiently close to the fuel surface (i.e. $< 6\text{--}7\text{ }\mu\text{m}$) the fission fragment can be directly released (see figure 2.3). In addition to this direct release of fission fragments by recoil there is the higher order effect of knock-outs. In passing through the material the fission fragment can occasionally make elastic collisions with the nuclei of atoms in the lattice. The primary knock-on could be the uranium or oxygen atoms that make up stoichiometric UO_2 , but occasionally a fission product residing in the lattice may also be struck by the fission fragment. This primary knock-on may or may not have enough energy imparted to it to allow it to be released. If released it is referred to as a knock-out; if it is not released then it can transfer its energy to other atoms in the lattice by elastic collisions. These are known as secondary knock-ons, which in turn can strike other atoms, and so on to higher orders of knock-ons. This process creates a cascade of knock-ons some of which may escape if they are produced at a

³This occurs largely because the neutron flux is highest in the outer regions of the fuel pellet and so the plutonium distribution is sharply peaked in the pellet periphery with an exponential reduction further along the pellet radius.

distance less than their mean range. Figure 2.3 shows a schematic of the recoil and knock-out processes.

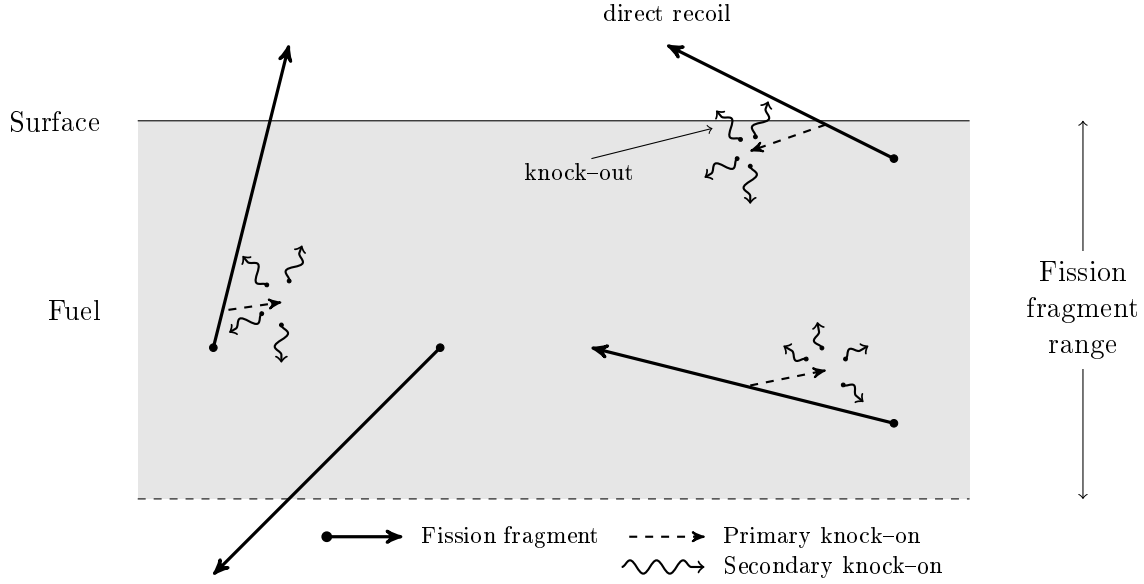


Figure 2.3. Schematic of fission gas release by recoil and knock-out.

Release by recoil is an athermal mechanism that is dependent on the fission rate, \dot{f} (fissions per second), and is independent of the half-life for the radioactive species:

$$J_{recoil}^i = \frac{1}{4} Y_i \dot{f} l_f \left(\frac{S}{V} \right)_{geom} \quad (2.1)$$

where J_{recoil}^i is the rate of release by recoil, Y_i is the cumulative yield for isotope i , l_f is the range of the fission fragment and $(S/V)_{geom}$ is the geometrical surface to volume ratio for the fuel.

In the case of knock-ons, Olander [3] has evaluated the release-to-birth ratio⁴, $[R/B]_i^{knock-on}$, as:

$$\left[\frac{R}{B} \right]_i^{knock-on} = \frac{z_u l_f \dot{F}}{4 c_U \lambda_i} \left(\frac{S}{V} \right)_{total} \quad (2.2)$$

where z_u is the number of uranium atoms emitted per escaping fission fragment, l_f is the range of the fission fragment, \dot{F} is the fission rate density, c_U is the concentration of uranium atoms in the fuel, λ_i is the radioactive decay constant of fission product of type i , $(S/V)_{total}$ is the total surface to volume ratio of the fuel. The total surface to volume ratio differs from the geometrical surface to volume ratio referred to in equation 2.1 as it takes into account the contribution from the porosity and cracks, which are only significant for the knock-on process as the corresponding atom has a smaller kinetic energy and is therefore likely to be trapped at these features.

In general the recoil and knock-on processes are only of significance at temperatures below

⁴This is generally defined as the number of atoms released divided by the number of atoms created.

1000 °C where thermal processes are not dominant, and even here absolute release is generally negligible for stable fission gas in comparison with other release modes. However, in the case of the short-lived fission products the recoil component can dominate the release. Equations 2.1 and 2.2 illustrate that recoil is independent of the decay constant, while there is an inverse dependence (i.e. $\propto \lambda_i^{-1}$) with the decay constant for knock-outs. Consequently the contribution of knock-outs to the total release is negligible in comparison with recoil for the short-lived fission products. A significant number of measurements of the half-life independent release have been performed at the OECD Halden Reactor Project (HRP), utilising the online gas flow system [1]. Figure 2.4 shows the measurements of the fractional release for an experiment in the Halden reactor (IFA-504), which show fractional release values of $2 - 4 \times 10^{-5}$ for the shorter lived isotopes⁵.

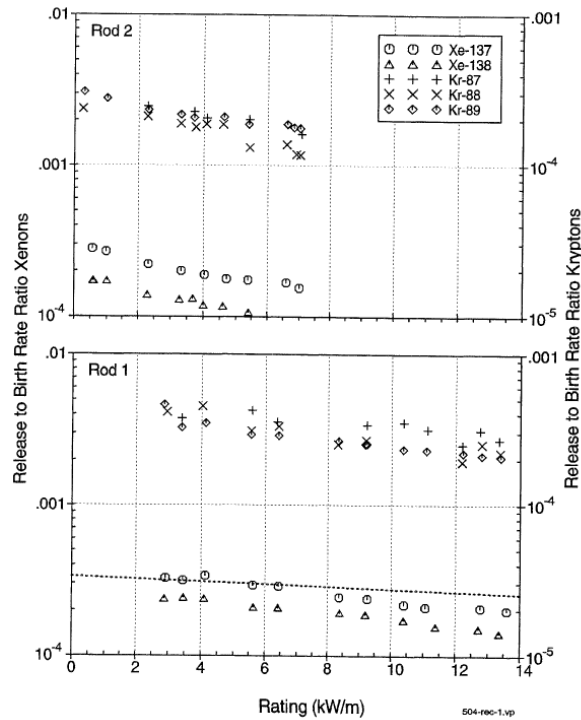


Figure 2.4. Measured release to birth ratios in the Halden IFA-504 assembly using 30 bar argon sweep gas. The dotted line shows the reduction in the fuel-clad gap during the experiment. Figure 29 from [1].

2.1.3 Lattice diffusion

The release of fission gas by recoil and/or knock-ons typically contributes little to the global fission gas release seen in-pile. The first step considered for significant release of fission gas from the fuel is single atom diffusion through the crystal lattice. Mechanisms for the transport of single xenon and krypton atoms have been studied by a variety of different authors, using a combination of out-of-pile experiments [4] (e.g. post-irradiation annealing, ion-implantation) and ab-initio calculations [5, 6, 7, 8]. Jackson *et al.* [5] have studied the equilibrium sites and postulated a

⁵The knock-out component is inversely proportional to the decay constant and consequently the short lived fission products have a larger contribution of the recoil component to the fractional release

migration pathway for a defective $\text{UO}_{2\pm x}$ ⁶ lattice. For hypostoichiometric and stoichiometric UO_2 it was found from the calculations that the neutral UO_2 tri-vacancy site was the preferred site, while for hyperstoichiometry the charged tri-vacancy, tetra-vacancy and a simple cation vacancy are all possible. For migration it was found that the most likely mechanism was the migration of a neutral tri-vacancy to a xenon atom at which point the xenon atom moves from one tri-vacancy to the other. These results agree with the channelling and ion-implantation experiments performed by Matzke *et al.* [4].

The migration of xenon and krypton can be treated using diffusion theory and consequently a large body of work exists concerning the diffusion coefficient of xenon (and krypton) in UO_2 , for in-pile conditions. However, there are several different factors that influence the in-pile diffusion coefficient, and these change the diffusion coefficient from a pure Arrhenius relationship into something more complicated. We summarise the various contributions and effects here.

Thermal diffusion

Although there has been considerable effort in determining the thermal diffusion coefficient of xenon in UO_2 there is still considerable variation in the available data. In general the thermal diffusion coefficient should be expected to follow the Arrhenius law, i.e.:

$$D_{gr}^{Xe} = D_0^{Xe} \exp\left(\frac{-\Delta H_{Xe}}{k_B T_K}\right) \quad (2.3)$$

The single atom diffusion coefficient is, in general, rather poorly characterised. A number of different studies have been performed over the years to determine the Arrhenius pre-exponential, D_0^{Xe} , and the diffusion enthalpy ΔH_{Xe} [4, 9, 10, 11]. Table 2.2 shows the values for the parameters from some of these studies, and figure 2.5 shows the resulting Arrhenius curves.

Table 2.2. Values of the Arrhenius diffusion parameters from open literature

Diffusion coefficient pre-factor, D_0^{Xe} [m^2s^{-1}]	Diffusion enthalpy, ΔH_{Xe} [eV/atom]	Experimental technique	Reference
5.0×10^{-6} – 5.0×10^{-2}	3.9	Ion implantation and annealing	[9]
5.0×10^{-5}	3.9	Ion implantation and annealing	[4]
7.6×10^{-10}	3.0	In-situ measurements with gas flow rig	[10]
2.1×10^{-8}	3.9	Annealing of irradiated fuel	[11]

The results from Matzke [4] and Miekley [9] should be generally representative of fission gas atoms in the absence of trapping by intra-granular bubbles. In spite of this a number of authors use the intrinsic diffusion coefficient as specified by Turnbull *et al.* [10]. The parameters given by Turnbull *et al.* are somewhat in contrast to both the data from Matzke and Miekley and as a result there has been some suggestion that the measurements are skewed by the trapping of ^{85}Kr in the intra-granular bubbles.

⁶Here x is the deviation from stoichiometry and can be calculated as $|\frac{O}{U} - 2|$.

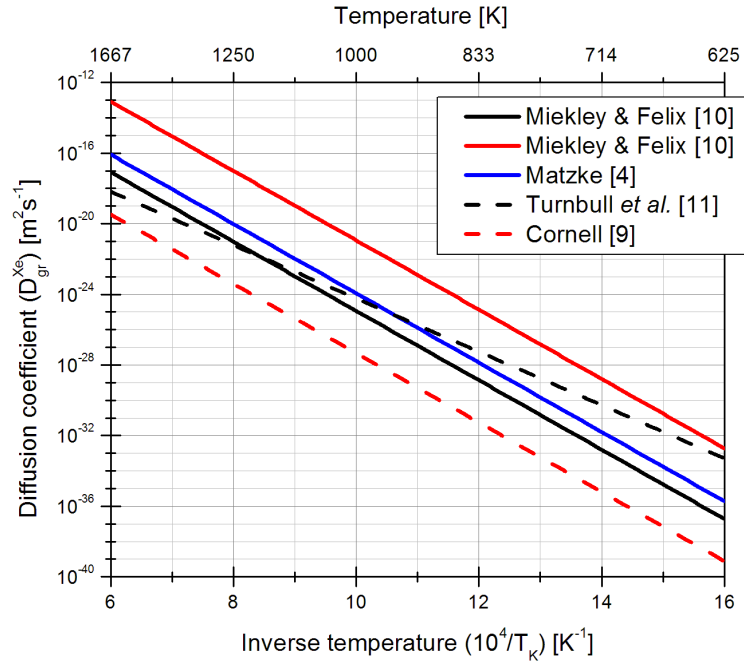


Figure 2.5. Thermal diffusion coefficient as a function of $1/\text{Temperature}$ for the Arrhenius parameters given in table 2.2.

Effect of burnup

A fission event produces two fission products that create impurity atoms in the fuel lattice. This chemical doping causes changes in the defect structure of the fuel, changing the equilibrium sites for xenon and krypton. These impurities have differences in their oxidation states causing the average stoichiometry to rise as a function of burnup. Lindner and Matzke [12] have previously shown that the diffusion coefficient increases with the oxygen-to-metal ratio (O/M) as can be seen in figure 2.6. Consequently we might expect that any variation in stoichiometry with burnup will affect the diffusion coefficient. Nicoll *et al.* [8] have also shown that the diffusion coefficient is sensitive to the specific site that the xenon atoms occupy and in addition that the preferential sites are influenced by both stoichiometry and the xenon concentration. However, in spite of the studies indicating an effect of stoichiometry on the diffusion coefficient of xenon and krypton, this author is not aware of any fission gas release models currently utilising a stoichiometry dependent diffusion coefficient.

In addition to chemical effects, fission events also induce radiation damage within the lattice increasing the concentration of defects. The interaction of fission gas atoms with this radiation damage acts to both retard (trapping in intra-granular bubbles) and speed up diffusion (resolution, radiation enhanced diffusion). These effects are treated in more detail in the following sections.

Radiation enhanced diffusion

The effect of electronic interactions between a fission fragment and the surrounding fuel matrix causes the fission fragment to slow down. During the final stages of the fragment coming to a

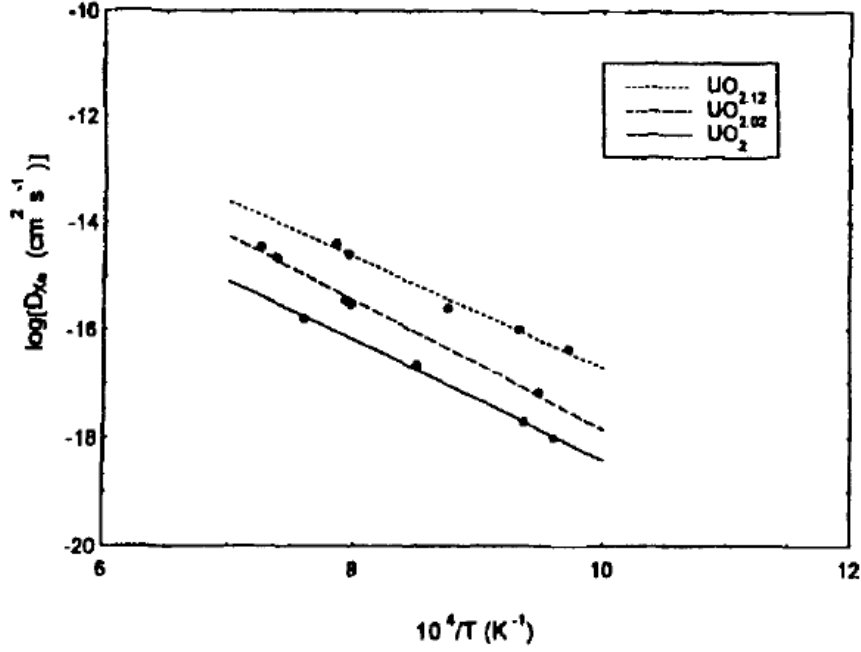


Figure 2.6. Variation of D_{gr}^{Xe} for UO_2 powders as found by Lindner and Matzke [12]

stop fission spikes and tracks are observed to occur. These spikes are typically $7\text{ }\mu\text{m}$ in length and produce approximately 10^4 uranium Frenkel pairs almost instantaneously. The fission spike causes significant temperature gradients along the axis of the spike resulting in the separation of vacancies and interstitials. This leads to an athermal-radiation enhanced diffusion and the destruction of nm intra-granular fission gas bubbles.

Radiation enhanced diffusion is also observed for uranium self-diffusion at low temperatures. Assuming that the fission spike has a similar effect, i.e. mixing, on the surrounding atoms, the values for uranium self-diffusion will also apply to fission gas. For uranium self-diffusion it has been shown [13] that the athermal contribution to the diffusion coefficient, D_{RED}^U , is proportional to the fission rate density, \dot{F} :

$$D_{RED}^U = a_U \times \dot{F} \quad (2.4)$$

where $a_U = 1.2 \times 10^{-39} \text{ m}^5$ for UO_2 . In the case of uranium self-diffusion we find that the transition from thermally activated to radiation enhanced diffusion occurs at a temperature of $1000\text{ }^\circ\text{C}$. However, for xenon we have in general that $D_{gr}^{Xe} > D_{gr}^U$, which results in a lower temperature for the transition. As a consequence the xenon radiation-enhanced diffusion should only be apparent at low temperatures, i.e. in the periphery of the fuel pellets where recoil and knock-out also play a role. Turnbull *et al.* [10] have examined the release of gas from both single and poly-crystal UO_2 under irradiation. The athermal contribution of the radiation enhanced diffusion is clearly observed at lower temperatures. However at intermediate temperatures ($1000\text{--}1400\text{ }^\circ\text{C}$), where thermally activated diffusion is expected to dominate, there is an apparent effect of irradiation on the diffusion that affects the enthalpy in comparison with the thermal-activation diffusion coefficient. This has been attributed to the enhancement of diffusion of both thermal

and irradiation induced vacancies.

Turnbull *et al.* have modelled the effect of irradiation on the diffusion coefficient by considering a three-term diffusion coefficient:

$$D_{gr}^{fg} = D_1^{fg} + D_2^{fg} + D_3^{fg} \quad (2.5)$$

where:

$$\begin{aligned} D_1^{fg} &= 7.6 \times 10^{-10} \exp\left(\frac{-35000}{T_K}\right) \\ D_2^{fg} &= 1.41 \times 10^{-19} \sqrt{\dot{F}} \exp\left(\frac{-13800}{T_K}\right) \\ D_3^{fg} &= 2 \times 10^{-40} \dot{F} \end{aligned}$$

Here D_1^{fg} represents the thermally activated diffusion, D_2^{fg} represents the effect of the thermal and irradiation uranium vacancies on the diffusion coefficient, and D_3^{fg} represents the athermal radiation enhanced diffusion. Figure 2.7 shows the three term diffusion coefficient specified in equation 2.5.

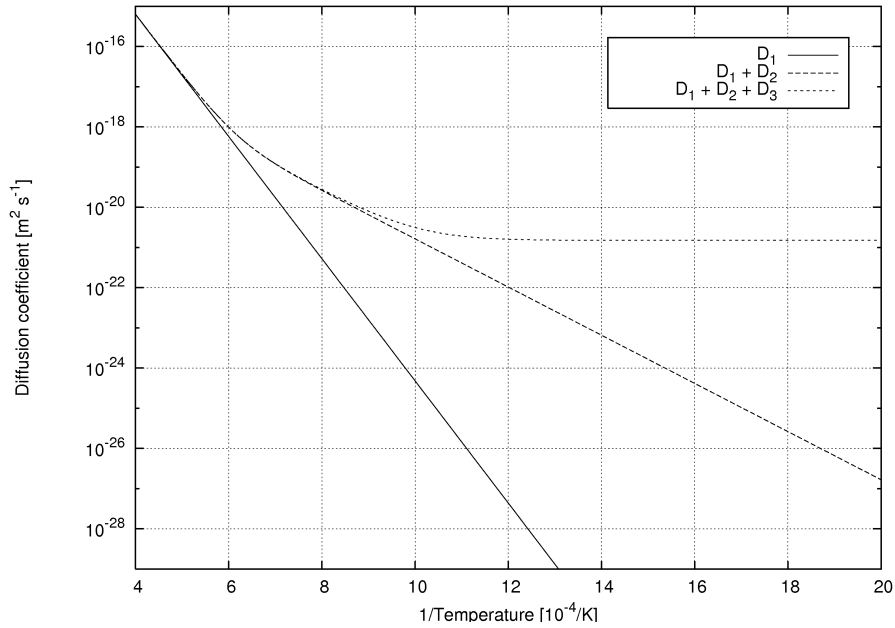


Figure 2.7. Turnbull's three term diffusion coefficient as a function of temperature for a mass rating of 25 W/gU.

Effect of precursors

Xenon and krypton are not usually directly produced but rather result from the β -decay of other fission products. In the case of krypton the precursor is bromine and it is considered that bromine diffuses approximately 20–30 times faster than krypton [10]. This fast diffusion followed by decay produces an enhancement to the observed diffusion of xenon and krypton. For most isotopes this is normally taken into account by incorporating it into an effective diffusion coefficient. However,

in the case of short-lived fission gas isotopes complications can arise where the precursor has a comparable or significantly longer half-life in comparison with the daughter isotope, or if the diffusion coefficient of the precursor is significantly larger (e.g. iodine diffuses significantly faster than Xe [10]). Friskney and Speight [14] have considered the effect of a general decay chain on the effective diffusivity of the short-lived fission gases. In general we have that for a chain of m decaying fission products, each with a diffusion coefficient $D_{gr}^{fp}(j)$ and a decay constant λ_i , the fractional release $\left[\frac{R}{B}\right]_{ld}^j$ (for small releases) from a homogenous sphere of radius R_{Booth} is:

$$\left[\frac{R}{B}\right]_{ld}^j = \sum_{j=1}^m \left[\frac{3}{\gamma_j} \left(\coth \gamma_j - \frac{1}{\gamma_j} \right) \prod_{k=1, k \neq j}^m \left(\frac{1}{1 - \frac{\gamma_j^2}{\gamma_k^2}} \right) \right] \text{ where } \gamma_j = R_{Booth} \sqrt{\frac{\lambda_i}{D_{gr}^{fp}(j)}} \quad (2.6)$$

For cases where there is a single precursor, the fractional release of the nuclide with decay constant λ_i and diffusion coefficient D_{gr}^i follows the following equation:

$$\left[\frac{R}{B}\right]_{ld}^i = \frac{S}{V} \sqrt{\frac{\nu_i D_{gr}^i}{\lambda_i}} \quad (2.7)$$

where S/V is the surface to volume ratio and ν_i is the precursor factor. Table 2.3 shows several examples of precursor factors.

Table 2.3. Precursor factors for some short-lived Xe & Kr isotopes

Isotope	Decay constant, λ_i (s^{-1})	Precursor factor, ν_i
^{133}Xe	1.53×10^{-6}	1.25
^{85m}Kr	4.30×10^{-5}	1.31
^{87}Kr	1.52×10^{-4}	1.25
^{135m}Xe	7.38×10^{-4}	23.50
^{137}Xe	3.02×10^{-3}	1.07

The value of the surface to volume ratio is generally used to describe the microstructural state of the fuel. For fresh, trace irradiated fuel⁷ the surface to volume ratio has values in the range $\sim 2 \times 10^3 - 10^4 \text{ m}^{-1}$, corresponding to the as-fabricated porosity and cracks in the fuel. If we consider the situation where all the grains, i.e. diffusion to the grain boundaries constitutes release, then the value can be as high as $5 \times 10^5 \text{ m}^{-1}$. In reality values this high are rarely seen in measurements, rather the effect of grain boundary tunnels (see section 2.1.5), while not completely covering the grain boundaries, can produce values of the surface to volume ratio up to 10^5 m^{-1} .

2.1.4 Grain boundary diffusion

It is generally accepted that grain boundary diffusion in a polycrystalline material is significantly more rapid than in the bulk [15]. This is primarily due to the atomic jump frequency on a grain

⁷Trace irradiated fuel refers to fuel that has been subjected to a low dose of irradiation.

boundary being significantly larger than the jump frequency of the lattice atoms. In most cases the dominant jump mechanism in the grain boundary appears to be a vacancy mechanism.

Several authors have attributed various processes occurring in nuclear fuel to grain boundary diffusion, e.g. creep [16], oxygen migration [17] and dispersion of plutonium [18]. For fission gas migration in grain boundaries the opinion is divided. Some authors suggest that it is a highly diffusive pathway for release of fission gas; however most current models dispense with this and consider the gas atoms to be immobile and release to primarily occur due to inter-granular bubble interconnection. One case where grain boundary diffusion is still of potential significance is in trace irradiated fuels as there are few traps to impede the fission gas migrating through the grain boundaries. Consequently several authors have advocated models utilising grain boundary diffusion for trace-irradiated fuel [19].

Olander and Van Uffelen [20] performed calculations to answer the question of whether grain boundary diffusion is a significant mechanism and under which circumstances this may be so. The distance a gas atom can migrate in a grain boundary populated by perfectly absorbing traps was calculated for parameters typical of fuel irradiated in excess of 20 MWd/kgU. It was observed that a Xe atom will be trapped after a migration distance less than or equal to the typical grain size. As a consequence, the release of fission gas via grain boundaries at intermediate and higher burnups is not considered as a significant release mechanism. In a second analysis Olander and Van Uffelen considered the release from trace-irradiated fuel where there are few inter-granular traps. The calculated releases indicated that the release from trace-irradiated specimens involved more than simple lattice diffusion through the free surface. The results are consistent with a two-stage release mechanism of lattice and grain boundary diffusion with no grain boundary traps.

Data concerning the grain boundary diffusion coefficient of xenon in UO_2 is normally determined indirectly from other measurable processes. Olander and Van Uffelen [20] used the trace-irradiation model described earlier to fit the grain boundary diffusion coefficient to xenon release data. They found that at a temperature of 1773 K the value of the grain boundary diffusivity was $D_{gb}^{fg} = 1.6 \times 10^{-14} \text{ m}^2 \text{ s}^{-1}$. However, estimates at other temperatures are hampered by the range of data for the diffusion coefficient in the matrix. Here they considered the effects of both low and high estimates for the grain diffusion coefficient and found that the difference between the two derived correlations was entirely controlled by the difference between the two grain diffusion coefficients.

White [21] has performed a comprehensive analysis of the behaviour of inter-granular bubbles and from this has derived estimates for the grain boundary diffusion coefficient. Figure 2.8 shows the result of fitting a model of morphological relaxation and growth of grain boundary bubbles to available in-pile test data.

Although the absolute values of the diffusivity determined by White are significantly lower than those determined by Reynold and Burton [16], the diffusion enthalpy of both data sets are close. White has attributed the discrepancy in the absolute value to the analytical methods used in the calculation of the bubble growth. However, if we compare the value derived by Olander and Van Uffelen at 1773 K with the results from White we find that for the two results to match

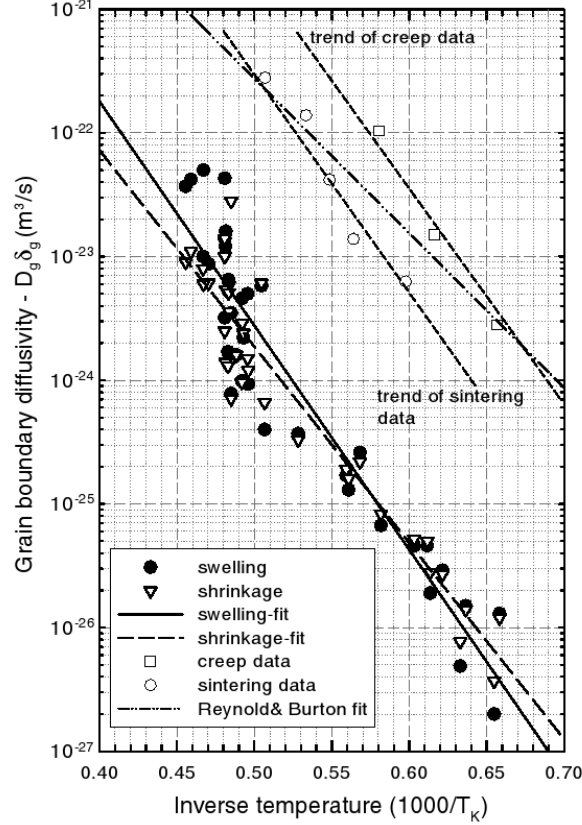


Figure 2.8. Estimation of the grain boundary diffusion coefficient by considering morphological relaxation and bubble growth of the grain boundaries. The estimates were calculated by fitting the model to available in-pile data of inter-granular bubble behaviour. Figure 14 from [21].

we require a grain boundary of width $\delta_{gb} = 0.125 \text{ \AA}$. This could be entirely due to problems in fitting such data when the value of the grain diffusion coefficient has considerable uncertainty in it.

2.1.5 Trapping

Intra-granular trapping

The migration of fission gas through the fuel lattice is more complicated than simple diffusion. Transmission electron microscopy (TEM) of nuclear fuel reveals a population of nanometre size bubbles within the grains that stabilises early in irradiation to a bubble size of a few nanometres and bubble densities of 10^{23} – 10^{24} m^{-3} [22]. Figure 2.9 illustrates a typical TEM image of intra-granular bubbles.

There are two particular theories on how these bubbles are nucleated, viz. homogenous and heterogeneous nucleation. Nucleation refers to the formation of clusters of fission gas atoms (~ 2 – 4 atoms) that are stable enough to grow into observable bubbles. If the clusters form by the random migration of fission gas atoms then this is referred to as homogenous nucleation. Alternatively, if they form on natural (e.g. dislocations, defects) or radiation induced imperfections (e.g. vacancy clusters) then the formation is referred to as heterogeneous nucleation. Turnbull [24] has observed that the bubbles appear to lie in straight tracks, which has led to the suggestion that

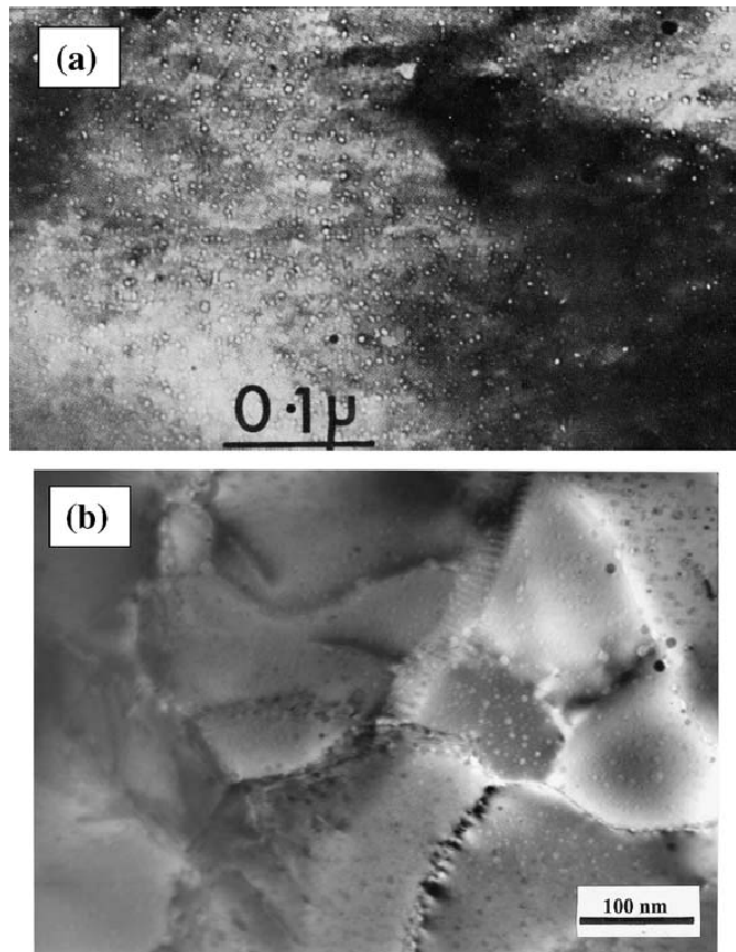


Figure 2.9. TEM images of intra-granular bubbles. Figure 2 from [23].

the bubbles are nucleated by fission fragments, i.e. in the wake of fission spikes. However, there are key objections to this. First, not all TEM images show aligned bubbles. Secondly if a fission fragment has the dual role of destroying (via re-solution, see later in this section) and nucleating bubbles then it is likely that the re-solution process simply generates a locally high concentration of fission gas atoms which then nucleate. The net result is that the same gas atoms make up the newly nucleated intra-granular bubbles. In spite of this objection Olander and Wongsawaeng [23] have recently performed calculations for separate models of re-solution and nucleation. They found that heterogeneous nucleation fits the observed TEM data for intra-granular bubbles, but cannot accurately reproduce their size. However the homogenous model also suffers from the problem that uncertainties in its parameters are far too large to draw meaningful conclusions from the available experimental data.

Although the specific mechanism of nucleation is still an issue for research, it is clear that traps such as intra-granular bubbles are highly efficient, and if left unchecked would grow via diffusion limited capture of the migrating fission gas, and retard the gas release. Speight [25] has observed that the presence of fission fragments acts to return the trapped fission gas atoms into solution with the matrix. This process of irradiation induced re-solution causes the stabilisation of the bubble population limiting it to nm-sized bubbles.

The trapping of fission gas in intra-granular bubbles is typically described in terms of rate theory,

where the reactions of the fission gas and the bubbles are treated in terms of phenomenological rate equations. The capture rate (J_{tr}^{grb}) of fission gas in the intra-granular bubbles of size R_{grb} is proportional to both the bubble density (n_{grb}) and the fission gas concentration in the grain c_{gr}^{fg} , i.e.:

$$J_{tr}^{grb} = k_{grtr} c_{gr}^{fg} n_{grb} \quad (2.8)$$

Here k_{grtr} is the rate constant for intra-granular trapping, which for the case of a diffusion limited trapping at a perfect spherical sink is $k_{grtr} = 4\pi R_{grb} D_{gr}^{fg}$ [26]. As was mentioned earlier the stabilisation of the intra-granular traps occurs relatively quickly in-pile, i.e. the rates of capture and re-resolution have to balance:

$$k_{grtr} c_{gr}^{fg} n_{grb} = k_{res} c_{grb}^{fg} \quad (2.9)$$

Here k_{res} corresponds to the re-resolution rate and c_{grb}^{fg} is the concentration of gas in the bubbles. As a consequence of the fast saturation (or stabilisation) of the intra-granular bubbles [25], many models define an effective diffusion coefficient:

$$(D_{gr}^{fg})^* = D_{gr}^{fg} \frac{k_{res}}{k_{res} + k_{grtr} n_{grb}} \quad (2.10)$$

Here the total concentration of gas atoms ($c_{gr}^{fg} + c_{grb}^{fg}$) is treated as if it is diffusing at a reduced rate.

Inter-granular trapping

One of the key determinants in the balance between release and retention of fission gases is the dynamics of grain boundary bubble development⁸. Most models of fission gas behaviour on the grain boundaries have, for some time, been modeled in one of two different ways, i.e.

1. By considering the grain boundary as a high-diffusivity path resulting in fast diffusion to the inter-granular pores or the plenum.
2. By considering the grain boundary as a perfect trap with the fission gas immediately trapped in grain boundary bubbles.

Point 1 has been shown by Olander and Van Uffelen [20] to only be significant for trace irradiated fuel (see section 2.1.4). Consequently most approaches that have been developed in an attempt to provide better models for the behaviour of grain boundary gas have focussed more on point 2. As a consequence of the large number of post irradiation examinations (PIEs) conducted over the past 40 years a detailed description of the stages of development of the grain boundary bubbles is available:

- In low burnup fuel there are large numbers of small lenticular bubbles on the faces of the fuel grains.

⁸Also referred to as inter-granular bubbles.

- As the burnup increases these bubbles grow while their numbers decrease due to coalescence.
- The coalescence process allows the presence of elongated bubbles, which as burnup increases results in a connection with the grain edges⁹ and this can lead to the development of partial tunnel networks of grain edge bubbles to the fuel exterior through which fission gas may be released.
- In a final stage all the bubbles, grain edge and grain face inter-link and at this point all the gas arriving at the grain boundaries will be released.

Figure 2.10 illustrates the development of the grain boundary porosity with increasing burnup.

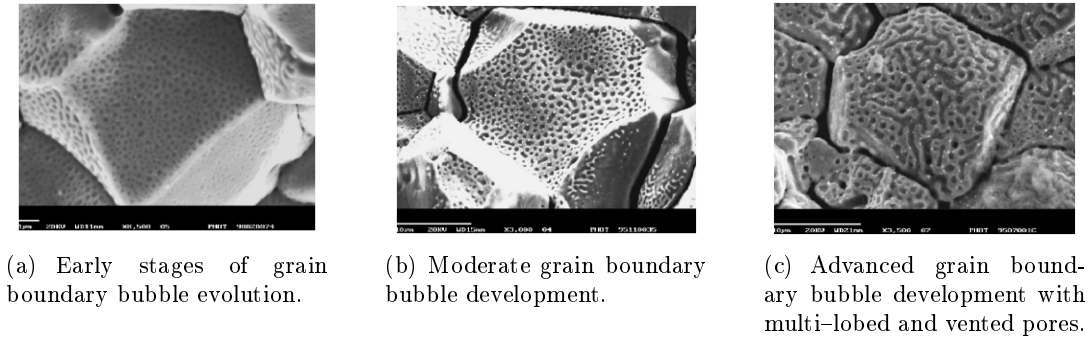


Figure 2.10. Development of grain boundary porosity with irradiation time. Figures 2–4 from [21].

Early in the irradiation large numbers of small ($\sim 1\text{nm}$) grain boundary bubbles appear on the grain faces. White [21] has measured the areal bubble densities at this stage and found values from 0.04 to 40 bubbles per μm^2 . The upper value is most likely close to the value of the nucleation bubble density. Comparison with bubble densities observed in the grain structure suggests that if the intra-granular bubbles are uniformly distributed then the growth of bubbles immediately adjacent to the grain boundary will cause the growing bubble to become a newly nucleated grain boundary bubble. Upon considering the typical bubble densities observed in the grain of 10^{23} – 10^{24}m^{-3} and then considering a layer of thickness equal to the intra-granular bubble diameter the limits for the newly nucleating grain boundary bubbles can be calculated. Upon doing this White found that the predicted areal density ranges between 50–500 μm^{-2} , with the lower limit matching reasonably well with the upper limit of the observations in lightly irradiated fuel.

The newly formed grain boundary bubbles have a lenticular shape with a circular projection. Figure 2.11 illustrates the schematic of a typical isolated grain boundary bubble when viewing the grain face (plan view) and when looking at the bubble cross-section.

The growth of porosity of any type is governed by the competition between the bubble internal pressure p_{gbb} , capillarity and the surrounding hydrostatic pressure p_h in the fuel. Mechanical

⁹This is where three grains meet.

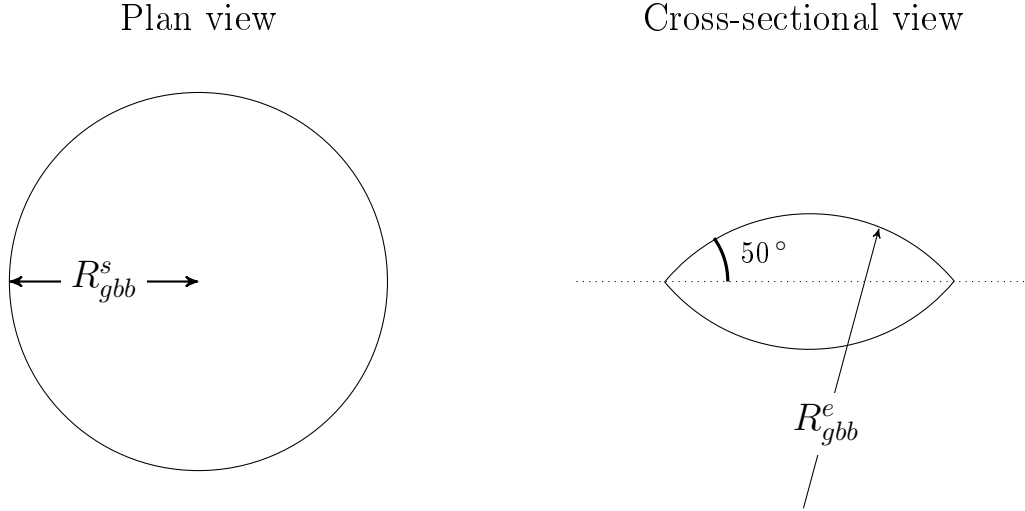


Figure 2.11. Schematic of an isolated lenticular grain boundary bubble. R_{gbb}^s is the radius of the circular projection on the grain face, while R_{gbb}^e is the radius of curvature of the cross-section.

equilibrium requires that these forces, balance i.e.:

$$p_{gbb} - p_h - \frac{2\gamma_{fs}}{R_{gbb}^e} = 0 \quad (2.11)$$

where $2\gamma_{fs}/R_{gbb}^e$ is the bubble capillarity, γ_{fs} is the UO_2 -gas specific surface energy and R_{gbb}^e is the radius of curvature of the spherical interface between the gas and the solid. The specific surface energy has a value of 1 J/m^2 and because of this lenticular bubbles form with a semi-dihedral angle of 50° [27].

In general cavity growth/shrinkage occurs when there is a departure from mechanical equilibrium, e.g. over-pressurisation, at which point the cavity acts as a vacancy sink/source in order to return to the equilibrium state. In general the grain face bubbles are over-pressurised and equilibrium can only be restored by absorbing vacancies. Speight and Beere [28] have introduced a revised version of the Hull and Rimmer [29] approach to calculating the growth of the cavities. According to Speight and Beere the rate of absorption/emission for a bubble with circular projection is given by:

$$\frac{dN_v}{dt} = \frac{2\pi D_{gb}^{fg} \delta_{dl}}{k_B T_K S} \left(p_h + p_{gbb} - \frac{2\gamma_{fs} \sin \theta}{R_{gbb}^s} \right) \quad (2.12)$$

where:

$$S = -\frac{1}{4} ((3 - \phi)(1 - \phi) + 2 \ln(\phi))$$

Here N_v is the number of vacancies, D_{gb}^{fg} is the grain boundary diffusivity δ_{dl} is the width of the diffusion layer on the grain boundary, p_h is the externally applied pressure and ϕ is the areal fractional coverage of the grain face by the bubbles. Equation 2.12 is generally applicable provided the parameter S is defined in terms of fractional coverage rather than the bubble radii.

In addition to the growth/shrinkage of bubbles via vacancy absorption/emission, irradiation induced re-resolution has been considered to affect the size of the grain boundary bubbles. Speight [25]

has argued that because of the sink-like nature of the grain boundary at temperatures of 1400 °C fuel with grains of size 5 μm should have all its gas residing on the grain boundary after only 3 days of irradiation. It was suggested that because large releases of gas are not observed a irradiation re-solution might instead be providing a back-flux of gas from the grain boundary into the grains. As a consequence of this observation the grain boundary bubbles have been modelled by a number of authors [30] as imperfect sinks by considering a small re-solution of fission gas to the first few layers of the grain near the grain boundary. Some fission gas models also build up a “concentration wall” inside the grain close to the grain boundaries [31]. Several objections have been made to this suggestion [1]. First the re-solution effect is of primary importance at low temperatures where the low diffusivity does not overwhelm the relatively small re-solution rate. The original argument for a re-solution process is based upon much higher temperatures where re-solution would be swamped by the diffusional release. In addition although the fractional release from the grain to the grain boundary would be near 100 % the quantity of gas generated within 3 days of irradiation falls far short of that required for inter-linked grain boundary bubbles to form.

A common alternative to the grain boundary re-solution model proposed by Speight is to consider the fission fragments as “chipping” away gas from the grain boundary bubbles without destroying them completely [1]. The model considers that each collision removes a chip volume, V_{chip} from the bubble and that this volume decreases with temperature. Considering the chip as a sphere of volume V_{chip} the radius of the chip is $\sim 15\text{--}20$ nm at the highest temperatures, decreasing to 1 nm at 800–1000 °C. Given that the grain boundary bubbles are typically of much greater volume than the intra-granular bubbles, (where irradiation induced re-solution certainly plays a role), the bubbles are no longer destroyed.

The most common treatment of the inter-linkage of the grain boundary bubbles is to wait until the fission gas in the grain boundary bubbles has exceeded a threshold concentration and then allow release to take place. White and Tucker [32] calculated this saturation concentration for non-spherical grain boundary bubbles:

$$c_{gbb}^{fg}|_{sat} = \frac{4R_{gbb}^e f(\theta)}{3k_B T_K \sin(\theta^2)} \phi \left[\left(\frac{2\gamma_{fs}}{R_{gbb}^e} \right) + p_h \right] \quad (2.13)$$

where R_{gbb}^e is the radius of curvature for grain face bubbles, 2θ is the dihedral angle between grain boundary and bubble surface, γ_{fs} is the free surface energy ($\sim 1 \text{ J m}^{-2}$), p_h is the hydrostatic pressure of surrounding bulk material and ϕ is the fraction of the grain face occupied by grain boundary bubbles at interconnection, with $f(\theta) = 1 - \frac{3}{2} \cos(\theta) + \frac{1}{2} \cos^3(\theta)$.

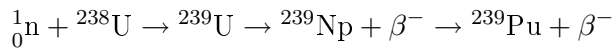
However, this treatment relies upon the assumptions that the gas is ideal and the bubble is in mechanical equilibrium. Because these are significant simplifications, several mechanistic kinetic models have been developed to describe the gas behaviour [21, 33, 34] without these assumptions. Some of the models consider the limiting factor in the inter-linkage process to be the grain edges, whilst others consider it to be the grain faces. The White model [21] is one of the more comprehensive models in this class; growth, coalescence and venting are all taken into account. This model is based upon extensive empirical observations of the development of

the grain boundary bubbles and its predictions of the geometrical parameters of the grain face bubbles closely match experimental data. However, the coalescence model predicts complete inter-linkage at areal surface fractions as low as 30–40 %, which is in disagreement with the theoretical value of 50 %.

The inter-linkage process has also been examined with percolation theory. Some early papers have addressed the issue of bubble and pore inter-linkage [35, 36] and more recently [37] percolation theory has been applied to pore interlinkage within the high burnup structure (see section 2.2.2). However, all the models presented so far are based on a stand-alone approach with simplified geometry (e.g. cubic grain structure) and were made to demonstrate the potential of this method rather than to be included in a fully fledged fission gas model. The major challenge this implementation would face will be the mathematical definition of the geometry needed to take into account the statistical effects of the real fuel structure. Another approach to the inter-linkage phase has been introduced by Noirot *et al.* [38]. Their model takes into account the tunnel radius in the inter-linked state via the variable “inter-linked tunnel length per unit volume”. This variable replaces the grain boundary gas concentration upon inter-linkage, i.e. the gas in the grain boundary bubbles is transferred to the inter-linked tunnel. The inter-linked tunnel length per unit volume is assumed to be constant but the tunnel radius can vary and, therefore, so can the pressure.

2.2 The high burnup structure

The strong resonance absorption of neutrons in ^{238}U leads to the production of ^{239}Pu via the beta decay of ^{239}Np , i.e.



Consequently, for fuel pellets the plutonium distribution is sharply peaked at the pellet periphery with an exponential reduction along the pellet radius. The high plutonium production in the rim of the pellets results in a burnup enhancement that is approximately 2–3 times (depending on the neutron spectrum) the pellet average burnup. It is in this region of the pellet that a transformation in the microstructure in comparison with the as-fabricated state can typically be observed in nuclear fuel pellets. This “high burnup structure” (HBS) was first observed in the 1950’s in the uranium bearing fuel of naval reactors. Experiments with this type of fuel gave several observations about this new microstructure:

- The appearance of large pores which were clearly visible with optical microscopy.
- An enhanced plasticity of the material.
- Enhanced swelling and crack healing.
- An apparent amorphisation of the microstructure as seen in X-ray diffraction.

In the late 1980’s there was a renewed interest in the material properties of the HBS due to the introduction of 4–5 cycle irradiations in nuclear power plants (NPPs). Since then there has been

a concerted effort to characterise and understand the physics behind the transformation of the microstructure.

It was initially thought that the enhancement of the plutonium concentration in the rim was the cause of the microstructural change. This has since been shown to be incorrect. Walker *et al.* [39] performed a series of Electron probe microanalysis (EPMA) studies on high burnup fuel and found that the HBS zone extended much further into the fuel than would be accounted for by the plutonium concentration distribution. However the extent of the restructured zone was found to be representative of the burnup profile in the fuel pellets, leading to the conclusion that the restructuring is a function of the local burnup, not plutonium concentration. In addition Walker *et al.* found that there was a limiting temperature of 1100–1200 °C beyond which the HBS would not form. These results have since been supported by a wide range of studies [40, 41] on high burnup fuel. Of particular note is the results from the High Burnup Rim Project (HBRP) [40]. The HBRP was initiated to identify both the conditions for the formation of the HBS and its properties once the transformation has been completed. The project irradiated highly enriched (≈ 25 wt% ^{235}U) UO_2 discs that were sandwiched between molybdenum discs to ensure near isothermal temperatures and burnups in the fuel. This arrangement allowed a range of burnups and temperatures to be examined. The results (see figure 2.12) showed that the transformation to HBS occurs at about a local burnup of approximately 55–82 MWd/kgU and below a temperature of 1100 ± 100 °C. These investigations have led to a general consensus that the HBS forms for local burnups in excess of 60 MWd/kgU and at temperatures below 1100 °C.

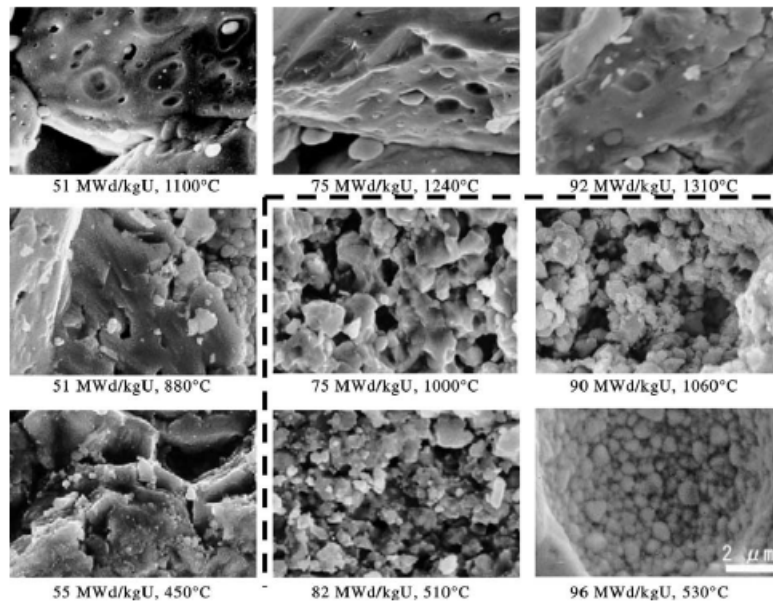


Figure 2.12. SEM of the fuel microstructure as a function of both burnup and irradiation temperature [41].

Due to these limits the fully formed HBS does not extend throughout the entire pellet, in part because of the increase in temperature towards the pellet centre. Although the threshold for restructuring is ~ 60 MWd/kgU the complete transformation at a particular radial point is not complete until the local burnup reaches ~ 120 MWd/kg. Consequently the un-restructured fuel

and HBS are typically separated by a transition zone where the fraction of HBS increases from 0 % to 100 %.

2.2.1 Characteristics

In the past decade there has been much focus on the characterisation of the HBS as a function of burnup. This has led to the identification of three microstructural features that are typical of the HBS:

1. A change in the grain size distribution from an average grain size of $\sim 10 \mu\text{m}$ to $\sim 0.1 \mu\text{m}$.
2. A large depletion of fission gas in the grains, specifically xenon, to a burnup independent value of $\sim 0.2 \text{ wt\% Xe}$ (as measured by EPMA).
3. The creation of large faceted pores (size $\sim 1 \mu\text{m}$) with a porosity that increases continuously with local burnup. It is generally considered that most of the gas not present in the fuel matrix is contained within these pores.

Xenon depletion

The first principle feature of the HBS is the depletion of xenon from the matrix. The primary method for examining elemental concentrations in nuclear fuel is EPMA, in which characteristic X-rays are used to determine the quantity and concentration of isotopes within the material. To date this methodology has been the most widely employed for examining the quantity of xenon in high burnup nuclear fuel. Walker *et al.* [39, 42] showed that as a function of local burnup there is a distinct pattern to the xenon concentration (see figure 2.13), i.e.:

- At burnups below $\sim 60\text{--}75 \text{ MWd/kgU}$ the xenon concentration varies linearly with burnup reaching $\sim 1 \text{ wt\%}$ at 60 MWd/kgU .
- For burnups between $\sim 60\text{--}120 \text{ MWd/kgU}$ the xenon concentration drops sharply reaching a value of 0.2 wt\% at $\sim 120 \text{ MWd/kgU}$.
- Above $\sim 120 \text{ MWd/kgU}$ the xenon concentration is constant with a value of 0.2 wt\% .

These three stages are attributed by most authors to the three zones of the fuel, i.e. un-restructured, transition and HBS zones. In the transition zone, the measurements seen in figure 2.13 show quite a wide degree of scatter. Several authors have tried to address this issue by introducing models which deal with the effects that temperature and grain size have on the HBS threshold; however there is little consistent data providing a trend with respect to these variables. An alternative possibility that has been proposed by some authors is that because of the mixture of normal structure and HBS in the measurement there will inevitably be scatter in the EPMA data.

While the large amount of data available points to a constant matrix concentration in the HBS, several authors have suggested that there is a further slower depletion after the HBS

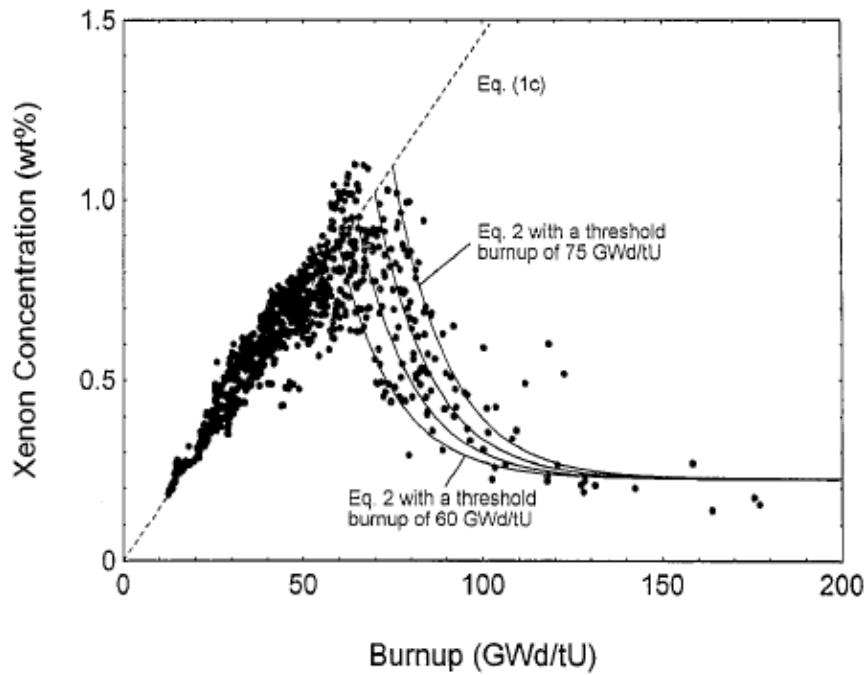


Figure 2.13. Variation of the matrix xenon concentration as a function of local burnup as measured by EPMA. Figure 4 from [43].

has formed [44]. In order to address how the xenon concentration is maintained at such a low value, Bremier *et al.* [45] performed a series of calculations based upon the simple Booth model for gas release. They found that for reasonable values of the system parameters the 0.2 wt% stable value could be achieved. However this simplified modelling did not take into account the effect of trapping on the grain boundary, nor the effect of grain boundary diffusion. Moreover the effect of the reduction in pore-pore separation was not explicitly taken into account when considering the xenon concentration on the grain boundary. In spite of this, it is clear that the xenon concentration remains low in the HBS, inevitably leading to the question of where the excess gas is located, a point which will be addressed later.

Grain size

As was noted earlier, one of the HBS features that was first noticed was the lack of an optically definable grain structure. Typically the grain radius reduces from the as-fabricated value ($\sim 10 \mu\text{m}$) to an average grain radius of $\sim 0.1 \mu\text{m}$. SEM and TEM observations [41, 46] have shown that the HBS grains, in comparison to the un-restructured grains, have a much lower concentration of irradiation defects (point defects, dislocation loops, etc), matrix gas and gas bubbles. In spite of this there are significant differences between adjacent grains, since the intragranular gas bubble density varies depending on which particular grain you observe.

One point of contention which has yet to be resolved is the lattice orientation between neighbouring sub-grains. Electron diffraction patterns of the sub-divided grains in the HBS have shown contradictory results with respect to this issue. In some studies no preferred lattice orientation has been found, indicating that the new sub-grains have high-angle grain boundaries with a

random orientation [47]. However other papers report small-angle grain boundaries [46].

The distribution of grain size in the HBS is approximately constant with burnup. Recent studies [48] have however shown a broadening of the grain size distribution within the transition zone (see figure 2.14). This has been attributed to the effect of the increased local temperature induced by the increasing porosity in the outer regions of the HBS.

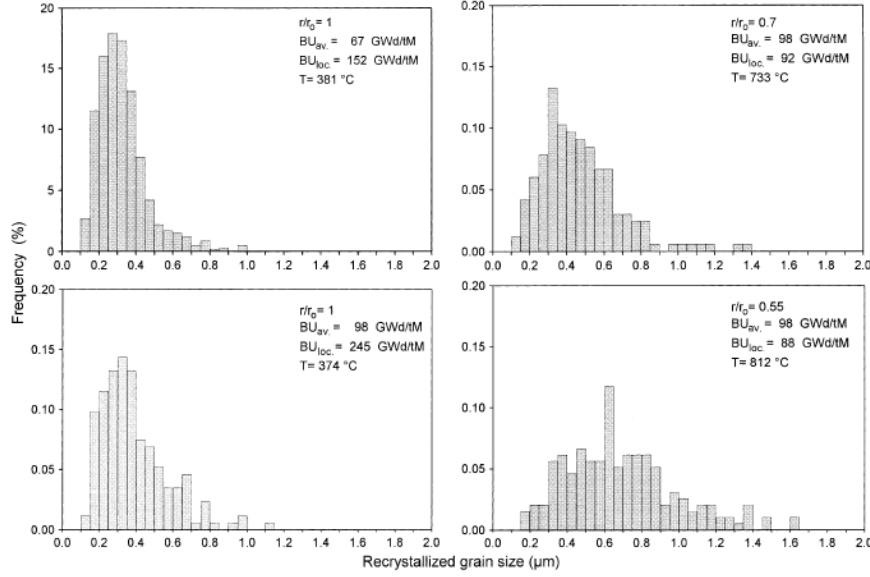


Figure 2.14. Change in the grain size distribution as a function of local burnup [48].

Porosity

Spino *et al.* [48, 49] have performed a number of different characterisations of the stereological parameters of the HBS, and in particular the porosity, up to local burnups of ~ 250 MWd/kgU. They found that, in the highest burnup region of the fuel, there is a change in the porosity growth behaviour. Below ~ 100 MWd/kgU both the porosity and pore number density are increasing with burnup (see figure 2.15). However after this point the number density starts to decrease and the porosity grows at a slower rate (~ 0.6 % per 10 MWd/kgU).

Spino *et al.* note that this growth rate is remarkably close to the matrix-gas swelling rate in high burnup fuels [48], given that the depletion of xenon from the matrix is complete by ~ 120 MWd/kgU (see figure 2.13). Moreover it is apparent that the volume increase attributable to fission gases would be in the form of the porosity, which may be consistent with the matrix-gas swelling rate mentioned earlier. This pore-size increase, in concomitance with pore-number density, is consistent with either coalescence or Ostwald ripening. In the latter case the larger pores grow at the expense of the smaller pores, which eventually disappear. It was noted that the rate at which the porosity grows ($\sim t^{0.4}$) and the rate of decrease in the number density ($\sim t^{-1.0}$) suggest that the Ostwald ripening process is indeed active. However there is also evidence that coalescence may also be active. As part of the same characterisation, the distribution of pores as a function of pellet radius was examined (see figure 2.16). It is clear from this analysis that

in periphery of the fuel the distribution changes to a bimodal distribution, which is indicative of coalescence type behaviour. In general a coarsening of the porosity distribution has the potential to generate interlinked channels within the HBS, introducing the possibility that the gas contained within the porosity might be released at a later stage. This will be discussed in some more detail in section 2.2.2.

2.2.2 Fuel performance

Fission gas release

At the same time at which the HBS restructuring was observed an increase in the fission gas release from discharged fuel rods was identified (e.g. see [50]). Initially it was considered that the significant growth of the porosity was an indication of an enhancement in the mobility of the fission gas, meaning that a new fission gas release process was operative in the HBS. This was initially supported by the EPMA results showing the depletion in the xenon concentration;

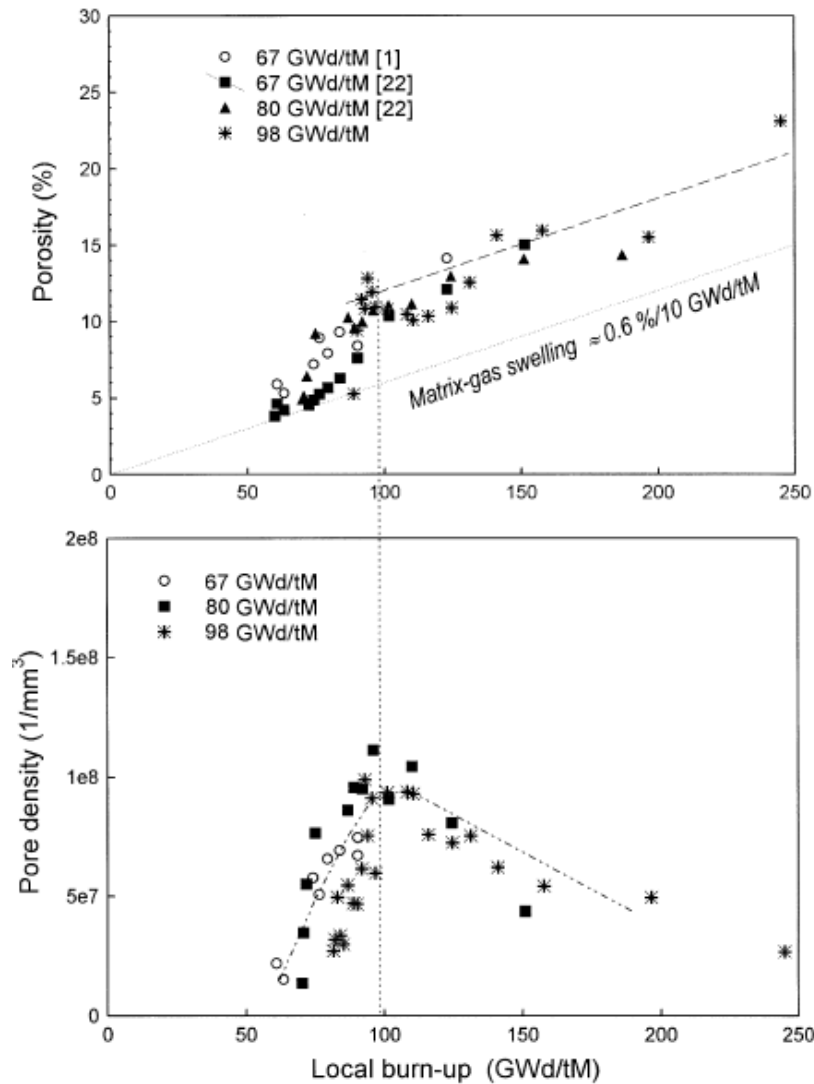


Figure 2.15. Variation of the porosity and number density with local burnup [48].

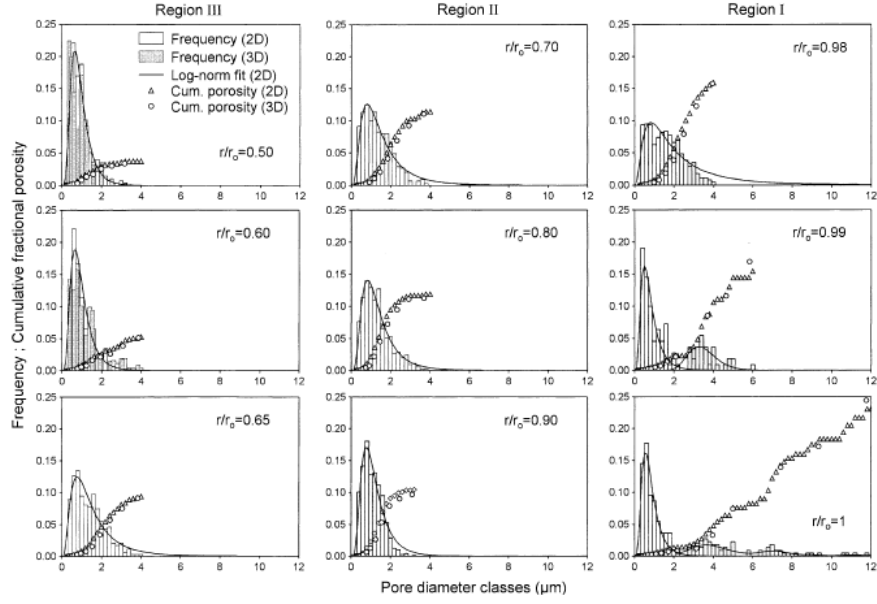


Figure 2.16. Variation of the porosity distribution at different radial positions [48].

however, further examinations using X-Ray Fluorescence (XRF) [51] showed no reduction in the xenon concentration. XRF typically measures both the xenon in the large pores and the matrix concentration whereas EPMA measures the matrix concentration. In opposition to the idea of a new fission gas release process operating in the rim, Brémier and Walker [45] calculated the effective diffusion coefficient of xenon needed to maintain the steady 0.2 wt% xenon concentration in the matrix. They found that the low depletion can be accounted for by the established fission gas transport processes and that the porosity is the most likely repository of the “released” fission gas. In a further study, Noirot *et al.* [38] have analysed data from the CABRI tests, and concluded that the contribution of the “rim” to released fission gas during reactivity initiated accidents (RIAs) is low (see the following section). Three of the CABRI test rods were subjected to isotopic examination and it was concluded that most of the gas is released from the more central regions of the pellet. This point has since been further evaluated by Desranges *et al.* using Secondary Ion Mass Spectrometry (SIMS) and EPMA [52]. They found that under transient conditions a sample of burnup 67 GWd/tM did not release a significant quantity of gas from the HBS, in agreement with the results of Noirot *et al.*.

Overall the consensus from most studies is that the excess gas resides within the porosity and that it is this that drives the porosity growth seen in the HBS. However, Bernard *et al.* [53] and Koo *et al.* [54] have postulated that the HBS porosity slowly evolves towards an open system, potentially inducing a substantial release of fission gas. This was challenged by Spino *et al.* [37] who examined the state of the HBS porosity using a 3D pore reconstruction technique (see figure 2.17) that showed that even up to high porosity ($\approx 25\%$) there was little evidence of pore interconnection.

As a consequence of these studies the current consensus is that the HBS contributes little to no release in the fuel for discharge burnups reached so far. However, there is limited data available of the exact quantity of gas in the HBS porosity, and as a result the existence of any gas release

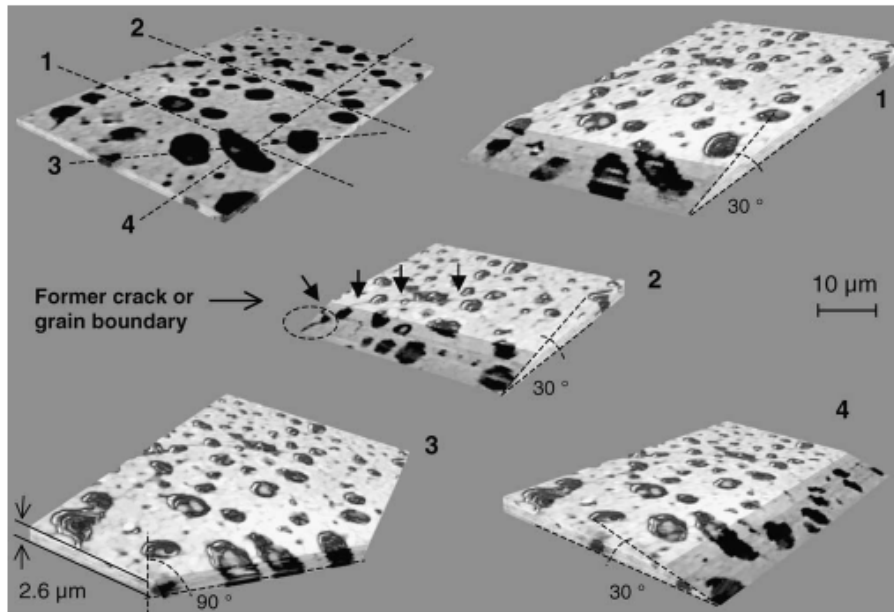


Figure 2.17. 3D-reconstruction of the porosity at the pellet rim of an LWR fuel pellet with average burnup 100 GWd/tM [37].

is still a partially open question.

Transient conditions

One particular concern regarding the HBS is the behaviour during design based accidents and in particular under RIA conditions. Several experimental programs have been initiated to investigate the corresponding fuel behaviour. Two of the biggest such programs are the CABRI REP-Na tests, which ran between 1993 and 1998, and the Japanese Nuclear Safety Research Reactor (NSRR) second-phase tests, which started in 1989 and continue to produce results.

The CABRI-REP (PWR fuel) test programme was started in 1993 with the intention to look specifically at the behaviour of high burnup fuel under RIA conditions with special attention to early clad loading caused by pellet-clad mechanical interaction (PCMI). UO_2 and MOX commercial fuel rods were subjected to the tests with parameters and results as shown in tables 2.4, 2.5 and 2.6. The most notable analysis of the data that came out from the CABRI programme was that of Schmitz and Papin [55]. These authors concluded that the fuel failure enthalpy reduces with burnup to a considerable extent, and the observations of the REP-Na1 test underline that this, in combination with oxide spalling and blisters, can cause failure at an unacceptably low failure enthalpy. It was suggested that the fuel failures could be attributed to the swelling, and therefore cladding loading, due to the extra intra-granular gas found in the HBS. However it should be noted that the cladding material used in the REP-Na1 test is obsolete and not prototypical of the current standard. Evidence for fission gas swelling being an important factor in the clad loading comes from the REP-Na5 and REP-Na2 experiments where grain separation was observed after the tests. This was identified as evidence for grain fragmentation in PWR fuel and for fission gas enhanced PCMI loading. This view was reiterated by Lemoine [56] with two specific loading mechanisms in mind, viz.:

- High gas pressure early in the transient causing fuel swelling which in turn can cause failure in brittle claddings. In high burnup MOX fuel the sudden increase in the available fission gas was observed to cause failure in sound claddings at the enthalpy level of 120 cal/g (REP-Na7).
- In the latter half of the pulse the grain boundary gases can expand and therefore contribute to the clad loading.

Table 2.4. Cabri REP-Na tests with commercial PWR fuel rods (UO₂)

	REP-Na1	REP-Na2	REP-Na3	REP-Na4	REP-Na5	REP-Na8	REP-Na10	REP-Na11
Initial Enrichment (%)	4.5	6.85	4.5	4.5	4.5	4.5	4.5	-
Max Burnup (GWd/t)	64	33	53	62	64	60	62	63
Energy Deposition (J/g) ^a	460	882	502	397	439	444	448	440
Pulse Width (ms)	9.5	9.5	9.5	64	9	75	31	31
Peak Fuel Enthalpy (J/g)	481	879	523	414	481	461	461	-
Fission Gas Release (%)	N/A ^b	5.54	13.7	8.3	15.1	N/A ^c	N/A ^d	-
Failure Mode	Brittle type, fuel dispersal	No failure	No failure	No failure	No failure	Failure, no fuel dispersal	Failure, no fuel dispersal	No failure

^a At 0.4 seconds except for REP-Na4 which was at 1.2 seconds.

^b Rod failed early at H=125 J/g.

^c Rod failed at H=343 J/g.

^d Rod failed at H=331 J/g.

Table 2.5. Cabri REP-Na tests with commercial PWR fuel rods (MOX)

	REP-Na9	REP-Na6	REP-Na7	REP-Na12
No. Cycles	2	3	4	5
Max Burnup (GWd/t)	28	47	55	65
Energy Deposition (J/g)	825 (0.5 secs)	527 (0.66 secs)	523 (0.48 secs)	440
Pulse Width (ms)	34	35	40	62
Peak Fuel Enthalpy (J/g)	879	619	502	-
Fission Gas Release (%)	34	21.6	Fuel Dispersal	-
Failure Mode	No failure	No failure	Failure	No failure

In MOX, fuel swelling will be restricted because of the higher volume fraction of HBS in comparison with UO₂ fuel due to the Pu clusters commonly observed in heterogeneous MOX. The

REP-Na7 test provides some evidence for extra loading in MOX fuel with a failure at 502 J/g without any hydride blisters.

The NSRR programme was instigated by the Japan Atomic Energy Research Institute (JAERI) to investigate the behaviour of fuels during RIA. Initially the programme focused on fresh fuel; however, since 1989, the programme has focused on pre-irradiated fuel experiments and has established a large experimental base for the corresponding fuel behaviour.

Table 2.6. Conditions for NSRR RIA tests of MOX and BWR (UO₂)

Fuel Rod	Burnup (MWd/kg)	Inserted Reactivity (\$)	Pulse half width (ms)	Peak fuel enthalpy (J/g)
ATR-1	20	3.2	6.5	335
ATR-2	20	4.0	5.2	461
ATR-3	20	4.5	4.7	502
ATR-4	20	4.6	4.5	586
FK-1	45	4.6	4.4	544
FK-2	41	3.2	6.5	293
FK-3	45	4.6	4.4	607

Observations similar to those made in CABRI have also been made in the NSRR programme. In one set of tests [57], BWR, PWR and highly enriched short rods, with burnups between 13 and 42.1 GWd/tU, were pulse irradiated. Larger cladding hoop deformation and fission gas release were observed for these rods in comparison with the fresh fuel rods. Nakamura *et al.* [57] explained these observations with a model in which inter-granular gas is pressurised during the power pulse, causing grain boundary separation and extra cladding stress. The model also assumes that the gases do not leave the fuel until the later parts of the pulse. The results seem to reproduce the data from the NSRR tests reasonably well. Similar observations have also been noted by Fuketa *et al.* [58], viz. larger fission gas release ($\leq 22.7\%$) with grain separation also present. However, calculations with the code FRAPCON-2 suggested that the total available gas on the grain boundaries and in the HBS is less than that released. This leads to the view that at least some of the gas must be coming from the central regions of the fuel, which agrees with the calculations of Noirot *et al.* [38]. The failure modes for the tests also illustrated that the existence of hydrides has a significant effect on the cladding and is a factor in the observed cladding failures. This is in accordance with the results from the CABRI tests.

More recently, Nakamura *et al.* [59] reported the results of RIA tests on BWR rods pre-irradiated to 56–61 GWd/tU. PIE showed that the failures were similar to those observed in high burnup PWR tests, i.e. embrittled cladding, hydride precipitation and blisters, with PCMI leading to failure. The fission gas release was similar to that observed in PWR fuel rods, viz. ~ 9.6 –17% depending on the peak fuel enthalpy. It was commented that most of the plastic deformation of the cladding seemed to be due to the fission gas behaviour in the latter half of the pulse. Fission gas release was also seen to correlate very well with the peak fuel enthalpy, although no dependence upon burnup was noted.

Bibliography

- [1] R.J. White. Fission gas release. Technical Report HWR-632, OECD Halden Reactor Project, Halden, Norway, October 2000.
- [2] J.L. Fowler and L. Rosen. Energy distribution of the fragments resulting from the fission of U-235 and Th-232 by slow and by fast neutrons. *Phys. Rev.*, 72:926, 1947.
- [3] D. R. Olander. *Fundamental aspects of nuclear reactor fuel elements*. Energy research and development administration, 1976.
- [4] H. J. Matzke. Gas release mechanisms in UO_2 – a critical review. *Radiat. Eff. Defect. S.*, 53:219–242, 1980.
- [5] R.A. Jackson and C.R.A. Catlow. Trapping and solution of fission Xe in UO_2 . *J. Nucl. Mater.*, 127:161–166, 1985.
- [6] C.R.A. Catlow. Theory of fission gas migration in UO_2 . *Radiat. Eff. Defect. S.*, 53:127–132, 1980.
- [7] C.R.A. Catlow and R. W. Grimes. The charge state of Xe in UO_2 . *J. Nucl. Mater.*, 165:313–314, 1989.
- [8] S. Nicoll, H. J. Matzke, and C. R. A. Catlow. A computational study of the effect of Xe concentration on the behaviour of single Xe atoms in UO_2 . *J. Nucl. Mater.*, 226:51–57, 1995.
- [9] W. Miekeley and F.W. Felix. Effect of stoichiometry on diffusion of xenon in UO_2 . *J. Nucl. Mater.*, 42:297–306, 1972.
- [10] J. A. Turnbull, C. A. Friskney, J. R. Findlay, F. A. Johnson, and A. J. Walter. The diffusion coefficients of gaseous and volatile species during the irradiation of uranium dioxide. *J. Nucl. Mater.*, 107:168–184, 1982.
- [11] R.M. Cornell. Electron microscope examination of matrix fission-gas bubbles in irradiated uranium dioxide. *J. Nucl. Mater.*, 38:319, 1971.
- [12] R. Lindner and H.J. Matzke. Diffusion von Xe-133 in Uranoxyd verschiedenen Sauerstoffgehaltes. *Z. Naturforsch. Pt. A.*, 14:582–584, 1959.
- [13] H. J. Matzke. Fission gases in nuclear fuels. *Ann. Chim. France.*, 14:133–147, 1989.
- [14] C. A. Friskney and M. V. Speight. A calculation on the in-pile diffusional release of fission products forming a general decay chain. *J. Nucl. Mater.*, 62:89–64, 1976.
- [15] Y. Mishin and Chr. Herzig. Grain boundary diffusion: recent progress and future research. *Mat. Sci. Eng. A-Struct.*, 260:55–71, 1999.
- [16] G. L. Reynolds and B. Burton. Grain-boundary diffusion in uranium dioxide: The correlation between sintering and creep and a reinterpretation of creep mechanism. *J. Nucl. Mater.*, 82:22–25, 1979.

- [17] K. Une and S. Kashibe. Corrosion behavior of irradiated oxide fuel pellets in high temperature water. *J. Nucl. Mater.*, 232(2-3):240–247, September 1996.
- [18] G. R. Chilton and J. Edwards. The solid-state diffusion of plutonium in uranium dioxide. *J. Nucl. Mater.*, 78(1):182–191, November 1978.
- [19] J. A. Turnbull and C. A. Friskney. The release of fission products from nuclear fuel during irradiation by both lattice and grain boundary diffusion. *J. Nucl. Mater.*, 58:31–38, 1975.
- [20] D. R. Olander and P. Van Uffelen. On the role of grain boundary diffusion in fission gas release. *J. Nucl. Mater.*, 288:137–147, 2001.
- [21] R. J. White. The development of grain-face porosity in irradiated oxide fuel. *J. Nucl. Mater.*, 325:61–77, 2004.
- [22] C. Baker. The fission gas bubble distribution in uranium dioxide from high temperature irradiated SGHWR fuel pins. *J. Nucl. Mater.*, 66:283, 1977.
- [23] D. R. Olander and D. Wongsawaeng. Re-resolution of fission gas - A review: Part I. Intragranular bubbles. *J. Nucl. Mater.*, 354:94–109, 2006.
- [24] J.A. Turnbull. Distribution of intragranular fission gas bubbles in UO_2 during irradiation. *J. Nucl. Mater.*, 38(2):203, 1971.
- [25] M. V. Speight. A calculation on the migration of fission gas in material exhibiting precipitation and re-resolution of gas atoms under irradiation. *Nucl. Sci. Eng.*, 37:180–185, 1969.
- [26] Y. H. Kalnin and E. A. Kotomin. A comparison of the effective medium and modified Smoluchowski equations for the reaction rate of the diffusion-controlled reactions. *J. Nucl. Mater.*, 232:253–255, 1996.
- [27] G. L. Reynolds, W. Beere, and P.T. Sawbridge. *J. Nucl. Mater.*, 41:112, 1971.
- [28] M. V. Speight and W. Beere. Vacancy potential and void growth on grain boundaries. *Met. Sci.*, 9:190–191, 1975.
- [29] D. Hull and D. E. Rimmer. The growth of grain boundary voids under stress. *Philos. Mag.*, 4:673, 1959.
- [30] J. Rest. The effect of irradiation-induced gas-atom re-resolution on grain boundary bubble growth. *J. Nucl. Mater.*, 321:305–312, 2003.
- [31] H. Wallin, L.Å. Nordström, and Ch. Hellwig. Fission gas model of the fuel code SPHERE-3. In *Proceedings of the IAEA/NEA/CEA International Seminar on Fission Gas behaviour in Water Reactor Fuels*, pages 391–406, Cadarache, France, September 2000.
- [32] R.J. White and M.O. Tucker. A new fission-gas release model. *J. Nucl. Mater.*, 118:1–38, 1983.
- [33] P. Van Uffelen. *Contribution to the Modelling of Fission Gas Release in Light Water Reactor Fuel*. PhD thesis, l’Université de Liège, 2002.

-
- [34] T. Kogai. Modelling of fission gas release and gaseous swelling of light water reactor fuels. *J. Nucl. Mater.*, 244:131–140, 1997.
- [35] A. R. Massih. Percolation model for bubble interlinkage in ceramic nuclear fuels. *J. Nucl. Mater.*, 119:116–118, 1983.
- [36] H.C. Kim and G.S. Cho. A hexagonal percolation model for zone-dependent pore interlinkage fraction and its application to the prediction of fission gas release. *Ann. Nucl. Energy.*, 23:1445–1457, 1996.
- [37] J. Spino, D. Papaioannou, and J.-P. Glatz. Comments on the threshold porosity for fission gas release in high burn-up fuels. *J. Nucl. Mater.*, 328:67–70, 2004.
- [38] L. Noirot, Ph. Garcia, and C. Struzik. A mechanistic fission gas behaviour model for UO_2 and MOX fuels. In *Proceedings of the IAEA/NEA/CEA International Seminar on Fission Gas behaviour in Water Reactor Fuels*, Cadarache, France, September 2000.
- [39] C. T. Walker, T. Kameyama, S. Kitajima, and M. Kinoshita. Concerning the microstructure changes that occur at the surface of UO_2 pellets on irradiation to high burnup. *J. Nucl. Mater.*, 188:73–79, 1992.
- [40] High burnup effects programme final report. Technical Report DOE/NE/34046-1.
- [41] T. Sonoda, M. Kinoshita, I. L. F. Ray, T. Wiss, H. Thiele, D. Pellottiero, V. V. Rondinella, and H. J. Matzke. Transmission electron microscopy observation on irradiation induced microstructural evolution in high burn-up UO_2 disk fuel. *Nucl. Instrum. Meth. B.*, 191:622–628, 2002.
- [42] C. T. Walker. Assessment of radial extent and completion of recrystallisation in high burn-up UO_2 nuclear fuel by EPMA. *J. Nucl. Mater.*, 275:56–62, 1999.
- [43] K. Lassman, C. T. Walker, J. van de Laar, and F. Lindström. Modelling the high burnup UO_2 structure in LWR fuel. *J. Nucl. Mater.*, 226:1–8, 1995.
- [44] J. Noirot, L. Desgranges, and J. Lamontagne. Detailed characterisations of high burn-up structure in oxide fuels. *J. Nucl. Mater.*, *in press*.
- [45] S. Bremier and C. T. Walker. Radiation-enhanced diffusion and fission gas release from recrystallised grains in high burn-up UO_2 nuclear fuel. *Radiat. Eff. Defect. S.*, 157:311–322, 2002.
- [46] K. Nogita and K. Une. High resolution TEM of high burnup UO_2 fuel. *J. Nucl. Mater.*, 250:244–249, 1997.
- [47] K. Nogita and K. Une. Irradiation induced recrystallization in high burnup UO_2 fuel. *J. Nucl. Mater.*, 226:302–310, 1995.
- [48] J. Spino, A. D. Stalios, H. Santa Cruz, and D. Baron. Stereological evolution of the rim structure in PWR-fuels at prolonged irradiation: Dependencies with burn-up and temperature. *J. Nucl. Mater.*, 354:66–84, 2006.

- [49] J. Spino, K. Vennix, and M. Coquerelle. Detailed characterisation of the rim microstructure in PWR fuels in the burn-up range 40-67 GWd/tM. *J. Nucl. Mater.*, 231:179–190, 1996.
- [50] R. Manzel, M. Coquerelle, and M.R. Billaux. Fuel rod behaviour at extended burnup. In *ANS Topical Meeting on Light Water Reactor Fuel Performance*, April 1994.
- [51] J.O. Barner, M.E. Cunningham, M.D. Freshley, and D.D. Lanning. Relationship between microstructure and fission gas release in high burnup UO_2 fuel with emphasis on the rim region. In *ENS International Topical meeting on LWR fuel performance*, apr 1991.
- [52] L. Desgranges, C. Valot, B. Pasquet, J. Lamontagne, T. Blay, and I. Roure. A method for the quantification of total xenon concentration in irradiated nuclear fuel with SIMS and EPMA. *Nucl. Instrum. Meth. B.*, 266:147–154, 2008.
- [53] L. C. Bernard and E. Bonnaud. Finite volume method for fission gas release modeling. *J. Nucl. Mater.*, 244:75–84, 1997.
- [54] Y-H. Koo, J-Y. Oh, B-H. Lee, and D-S. Sohn. Three-dimensional simulation of threshold porosity for fission gas release in the rim region of LWR UO_2 fuel. *J. Nucl. Mater.*, 321(2-3):249–255, 2003.
- [55] F. Schmitz and J. Papin. High burn-up effects on fuel behaviour under accident conditions: The tests CABRI REP-Na. *J. Nucl. Mater.*, 270:55–64, 1999.
- [56] F. Lemoine. High burnup fuel behaviour related to fission gas effects under reactivity initiated accidents (RIA) conditions. *J. Nucl. Mater.*, 248:238–248, 1997.
- [57] T. Nakamura, T. Sasjima, H. Fuketa, and K. Ishikima. Fission gas induced cladding deformation of LWR fuel rods under reactivity initiated accident conditions. *J. Nucl. Sci. Technol.*, 33(12):924–935, 1996.
- [58] T. Fuketa, H. Sasajima, Y. Mori, and K. Ishijima. Fuel failure and fission gas release in high burnup PWR fuels under RIA conditions. *J. Nucl. Mater.*, 248:249–256, 1997.
- [59] T. Nakamura, K. Kusagaya, and T. Fuketa. High-burnup BWR fuel behaviour under simulated reactivity-initiated accident conditions. *Nucl. Technol.*, 138:246–259, 2001.

Chapter 3

A steady state fission gas model for the HBS

We want to deal with reality here ... well, at least we try to.

- Aida El-Khadra

3.1 Introduction

The behaviour of fission gas in the high burnup structure (HBS) is one of the key points often addressed when considering the fuel performance of high burnup fuel. A number of studies (both experimental and calculational) [1, 2, 3] have added to the consensus that the HBS retains most, if not all, of the generated fission gas (see section 2.2.2). Although the consequences of fission gas release are generally believed to be mitigated for the HBS, the distribution of the retained fission gas within the HBS can have a degrading effect on the fuel performance in both steady-state and transient conditions. For example, several studies [4, 5, 6] of fuel behaviour during reactivity initiated accident (RIA) type transients have indicated that the swelling of the inter-granular porosity during transient conditions (driven by the inner fission gas pressure) plays an important role in fuel rod failures. As a consequence the distribution of fission gas within the HBS is important.

The large number of electron probe microanalysis (EPMA) investigations of the HBS have conclusively demonstrated the invariance of the intra-granular xenon concentration with burnup (~ 0.2 wt%) within the HBS (see section 2.2.1 for more details). When considering the fission gas behaviour in the HBS it should be kept in mind that in the normal fuel structure EPMA measurements record a steadily increasing xenon concentration with burnup (see figure 2.13). This difference is a clear indication of a shift in the importance of one or more fission gas transport processes, resulting in a balance between the production of fission gas in the HBS grains and the flux to the grain boundaries. Concomitant with the HBS xenon depletion is a marked growth in the HBS porosity (see section 2.2.1 for details). Walker *et al.* [7] have demonstrated that the EPMA signals for HBS pores are consistent with the presence of a large quantity of xenon, implying that there is a steady flow of both vacancies and fission gas to the porosity. This

in part justifies the conventional approach in modelling fission gas behaviour in the HBS, i.e. the generated fission gas is immediately placed in the porosity. The typical modelling approach implicitly assumes that the transport to the porosity is arbitrarily fast, which begs the question as to which migration mechanism (or mechanisms) are being implicitly assumed.

The role of grain boundary diffusion in the HBS is of particular interest in this context due to the large concentration of grain boundaries in comparison with un-restructured fuel. In the normal fuel structure, grain boundary diffusion is only significant for trace irradiated fuel when the trapping probability on the grain boundary is low due to the absence of grain boundary bubbles. Later in life, the trapping probability on the grain boundaries increases due to inter-granular bubble nucleation and growth. Consequently, the diffusion length (i.e. the distance traveled by a fission gas atom before it is trapped in an inter-granular bubble) is $\sim 6\ \mu\text{m}$, i.e. comparable to the width of a grain face [8]. For un-restructured fuel the short diffusion length in comparison with grain size justifies the non-importance placed upon grain boundary diffusion at medium burnups. In the HBS the situation changes dramatically:

1. The grain boundary surface to grain volume ratio increases considerably (~ 100 times) due to the reduced grain size.
2. The pore separation decreases due to the increased porosity.

The increase in the concentration of the grain boundaries enhances the importance of the grain boundary transport mechanisms, and the reduction in pore separation acts to reduce the effectiveness of the bubble trapping. Spino *et al.* [9] have determined that the average pore separation after transformation to HBS is no greater than $1.5\ \mu\text{m}$, and consequently is much smaller than the average migration distance of fission gas on the grain boundary, as determined by Van Uffelen and Olander [8]. As a consequence, the impact of fission gas migration and trapping on the grain boundary has the potential to play an important role in the dynamics of fission gas migration within the HBS. While the reduction in pore separation should reduce the grain boundary trapping efficiency, to this author's knowledge no evidence, experimental or calculational has been presented that the effect of grain boundary diffusion is significant for the equilibrium xenon concentration in the matrix. This presents three questions that need to be addressed:

1. Is it possible to reach a dynamic equilibrium in the matrix xenon concentrations of the HBS using known processes of fission gas transport?
2. How important is grain boundary diffusion to the HBS equilibrium concentration?
3. Are there any limitations on fission gas parameters?

In order to address these questions we have developed a one-dimensional, steady-state, two-stage fission gas model that describes the transport from sub-micron sized grains to micrometer pores via grain boundary diffusion. Specifically, intra-granular and inter-granular diffusion are considered. The gas can be trapped in nanometer-sized bubbles at the grain boundary and resolved back to the sub-micron grains. Inter-granular bubbles are assumed to be at equilibrium

but are allowed to grow when a departure from the nucleation phase occurs. Therefore, the fission gas transport mechanisms are essentially the same as for normal fuel with the addition of grain boundary diffusion.

The model is applied to light water reactor (LWR) UO_2 fuel at the moderate temperatures found in the rim to determine the averaged xenon concentration. For the HBS the measured xenon depletion is ~ 0.2 wt% and it is calculated with respect to this value that we compare the results from the calculations. The model contains several parameters for which the relative importance is not well established a priori, and consequently we evaluate the sensitivity of the calculated average concentration with respect to these parameters and determine the parameter limits to achieve the observed xenon concentration.

3.2 Model definition

Fission gas release models for low to moderate burnups typically consider the three basic processes of fission gas migration: volume diffusion within the fuel matrix including the precipitation of single atoms into intra-granular bubbles, re-solution of gas atoms back into solution, precipitation and growth (and shrinkage/destruction) of grain boundary gas bubbles and inter-linkage of grain boundary bubbles resulting in release to the pin free volume. Within each of these processes there are usually several different sub-processes acting on different phases of the gas, e.g. irradiation induced re-solution that affects the shrinkage of grain boundary gas bubbles (see section 2.1 for details). For most fission gas release models up to five separate phases are considered in calculating the distribution of gas within the normal fuel structure, i.e. gas within the matrix, gas trapped in intra-granular bubbles, gas trapped within grain boundary bubbles, grain boundary gas that is free to diffuse (the last two comprising the grain boundary phases) and gas that is released to the rod free volume.

In the model developed here we consider the fuel volume lying between two HBS pores, which act as perfect sinks, separated by an average distance, l_{p-p} . The fuel volume between the two pores consists of spherical fuel grains of uniform volume V_{gr}^{HBS} with a grain boundary of volume V_{gb}^{HBS} . Within the fuel volume considered we treat three gas phases:

- Gas residing within the HBS grains with a concentration c_{gr}^{fg} , i.e. dissolved in the matrix.
- Gas residing within the inter-granular bubbles with a concentration c_{gbb}^{fg} .
- Gas residing within the grain boundary that has not yet been trapped by the inter-granular bubble population, with a concentration c_{gbf}^{fg} .

Each concentration is a function of the position between the two pores only, e.g. $c_{gr}^{fg}(x)$. Furthermore the concentrations are calculated relative to the local volume, viz. the two grain boundary phases are calculated with respect to the local grain boundary volume while the grain concentration is considered with respect to the local grain volume. For each of the phases there are various processes that move the fission gas from one phase to another. For the grain phase the primary transport process is volume diffusion; however there is additionally a contribution due

to re-resolution of gas from the grain boundary phases into the grains. The transport processes for the grain boundary gas phases are a combination of several phenomena: grain boundary diffusion, re-resolution and grain boundary trapping. Both the trapping and grain boundary diffusion processes only act upon the free grain boundary gas phase. Figure 3.1 and table 3.1 describe the idealised system .

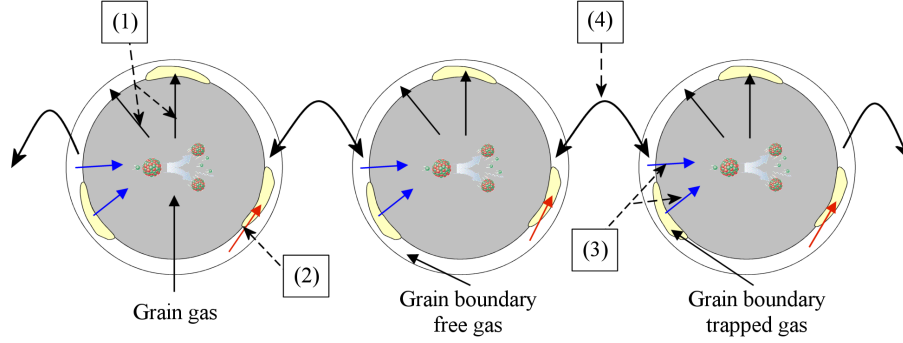


Figure 3.1. Schematic of the geometrical setup and transport processes (1)–(4) used in the current model. (1) Volume diffusion from grain to both grain boundary phases, (2) Trapping of free grain boundary gas to the trapped grain boundary phase, (3) Re-resolution of both grain boundary phases to the grain phase, (4) Grain boundary diffusion of the free grain boundary phase to adjacent grain boundary volumes.

Table 3.1. Summary of the processes and the gas phases which they affect

Transport process	Transported from	Transported to
Volume diffusion	Gas in the grain	Grain boundary gas (trapped & free)
Re-resolution	Grain boundary gas (trapped & free)	Gas in the grain
Grain boundary trapping	Free grain boundary gas	Trapped grain boundary gas
Grain boundary diffusion	Free grain boundary gas is transported along the grain boundary	

In addition to the transport processes there are three principal assumptions:

1. Gas release from the HBS is not considered.
2. The large HBS pores form perfect sinks for the diffusing fission gas.
3. The grain boundary bubbles are in a nucleation phase and do not undergo significant growth.

Assumptions 1 and 2 are in accordance with the general consensus that most of the gas is retained in the HBS pores. Therefore a possible release mechanism via the HBS pores is not considered here. The restructuring of the fuel microstructure results in a large number of newly formed grain boundaries. Assumption 3 essentially implies that the state of the grain boundary bubbles is the same as that in low burnup fuel, i.e. a high areal bubble density (n_{gbb}) of nanometer-sized bubbles (radius R_{gbb}), and that there is little change in the state of the grain boundary bubbles. There have been some observations of such a state in high burnup fuel [10], reinforcing this assumption.

3.2.1 Rate equations for a 1-dimensional system of grains and grain boundaries

We first consider the governing rate equations for a 1-dimensional system of grains and grain boundaries in the absence of the HBS porosity. In general the rate of change of each gas phase i can be described as the summation of the accumulation rates for each process j affecting that gas phase, i.e.:

$$\frac{\partial N_i^{fg}}{\partial t} = \sum_j J_j^i \quad (3.1)$$

The rates can be represented by a rate coefficient (k_j) describing the process (j) and a function of the local concentrations, local concentration gradients and higher order derivatives¹, i.e.

$$J_j^i = k_j f \left(N_1^{fg} \dots N_N^{fg}, \frac{dc_1^{fg}}{dx} \dots \frac{dc_N^{fg}}{dx}, \frac{d^2 c_1^{fg}}{dx^2} \dots \frac{d^2 c_N^{fg}}{dx^2} \right) \quad (3.2)$$

For the present model we consider five processes affecting the local concentrations, viz. production of fission gas, volume diffusion, grain boundary trapping, re-solution of grain boundary gas and grain boundary diffusion. Each process and the associated rate is specified in the following sections (see table 3.2 for the notation used for each process).

Table 3.2. Nomenclature for the various transport processes and the different grain phases

j:	prod	=	Production
	ld	=	Volume diffusion
	res	=	Re-solution
	tr	=	Trapping of free grain boundary gas
	gbd	=	Grain boundary diffusion
i:	gr	=	Grain phase
	gbb	=	Trapped grain boundary phase
	gbf	=	Free grain boundary phase

Fission gas production

We can define the rate of production of fission gas atoms per HBS grain, J_{prod}^{gr} , as the product of the local fission rate density (\dot{F}), the chain yield for the stable fission gases (Y_{fg}) and the total local volume of the grains (V_{gr}^{HBS}), i.e.

$$J_{prod}^{gr} = Y_{fg} \dot{F} V_{gr}^{HBS} \quad (3.3)$$

Volume diffusion

The present model approximates the grains of the HBS as spheres of size R_{gr}^{HBS} in accordance with the Booth equivalent sphere model [11, 12]. When the diffusion coefficient is independent of

¹In practice derivatives of orders greater than 2 are rarely considered

both the concentration and position (i.e. there is no anisotropy), the local rate of change in the fission gas concentration due to diffusion can be calculated using the following partial differential equation (PDE):

$$\frac{\partial c}{\partial t} = D \nabla^2 c \quad (3.4)$$

If we consider steady-state conditions, i.e. $\partial c / \partial t = 0$ then equation 3.4 simply reduces to Fick's 1st law:

$$F = -D \frac{dc}{dr} \quad (3.5)$$

where F is the flux of a diffusing substance, r is the space coordinate normal to the cross-sectional area and D is the diffusion coefficient. Consequently, using this relation, the rate of change in the number of atoms in the grain phase can be calculated as:

$$J_{ld}^{gr} = -4\pi (R_{gr}^{HBS})^2 D_{gr}^{fg} \left. \frac{dc_{gr}^{fg}}{dr} \right|_{r=R_{gr}^{HBS}} \quad (3.6)$$

$$= k_{ld} \left. \frac{dc_{gr}^{fg}}{dr} \right|_{r=R_{gr}^{HBS}} \quad (3.7)$$

where k_{ld} is the volume diffusion rate coefficient and is given by $k_{ld} = -4\pi (R_{gr}^{HBS})^2 D_{gr}^{fg}$. Although equation 3.6 describes the rate of change for the grain phase, the gas in the grain boundary exists in two separate phases. Consequently the flux of gas to the two grain boundary phases depends upon the surface coverage of the trapped grain boundary gas phase, ϕ . The effect of the grain boundary traps reduces the cross-sectional area proportionally with the trap surface fraction. Therefore the rates at which gas enters the trapped grain boundary gas, J_{ld}^{gbb} , and the free grain boundary gas, J_{ld}^{gbf} , are given by:

$$J_{ld}^{gbb} = \phi k_{ld} \left. \frac{\partial c_{gr}^{fg}}{\partial r} \right|_{r=R_{gr}^{HBS}} \quad (3.8)$$

$$J_{ld}^{gbf} = (1 - \phi) k_{ld} \left. \frac{\partial c_{gr}^{fg}}{\partial r} \right|_{r=R_{gr}^{HBS}} \quad (3.9)$$

It should be noted that the summation of J_{ld}^{gbb} and J_{ld}^{gbf} is clearly equivalent to equation 3.6, as is required for mass balance.

Re-solution

The re-solution terms for the trapped and free gas phases, and the rate of trapping of the free phase, are calculated using the formulation used by Van Uffelen [13], viz.

$$J_{res}^k = k_{res}^{ref} \frac{\dot{F}}{\dot{F}_{ref}} c_k^{fg} V_{gb}^{HBS} \quad (3.10)$$

$$= k_{res} c_k^{fg} V_{gb}^{HBS} \quad (3.11)$$

where the subscript k represents the grain-boundary free and trapped phases, and V_{gb}^{HBS} is the volume associated with the grain boundary. The re-solution rate coefficient, k_{res} , is given by $k_{res} = k_{res}^{ref} \frac{\dot{F}}{\dot{F}_{ref}}$. k_{res}^{ref} is the reference re-solution rate coefficient at a reference fission rate density \dot{F}_{ref} . The reference re-solution rate normally refers to the value at a reference fission rate density corresponding to a linear heat rate of 20 kW/m.

Grain boundary trapping

The trapping rate is calculated using:

$$J_{tr}^{gbb} = k_{gbtr} c_{gbf}^{fg} V_{gb}^{HBS} \quad (3.12)$$

where k_{gbtr} is the trapping rate coefficient. The trapping rate coefficient itself is a function of several variables, e.g. bubble density and radius. Using the expression for the trapping coefficient derived by Van Uffelen [13] one has:

$$k_{gbtr} = \frac{1}{R_{gbb}^2} \left(\frac{8D_{gb}^{fg} \phi(1-\phi)}{(1-\phi)(\phi-3) - 2 \ln \phi} \right) \quad (3.13)$$

Grain boundary diffusion

The model considers an idealised grain boundary with a circular cross-section of radius δ_{gb} and area $A_{gb} = \pi \delta_{gb}^2$. Figure 3.2 shows a schematic of the grain boundary. The diffusion of fission gas within the grain boundary is considered to be one-dimensional. Considering, as depicted, an element of grain boundary volume of length dx and cross-sectional area A_{gb} , the rate at which the fission gas leaves the volume through faces 1 & 2 is, according to Fick's law (equation 3.5):

$$J_{gbd}^{gbf} = -D_{gb}^{fg} A_{gb} \frac{dc_{gbf}^{fg}}{dx} \quad (3.14)$$

$$= k_{gbd} \frac{dc_{gbf}^{fg}}{dx} \quad (3.15)$$

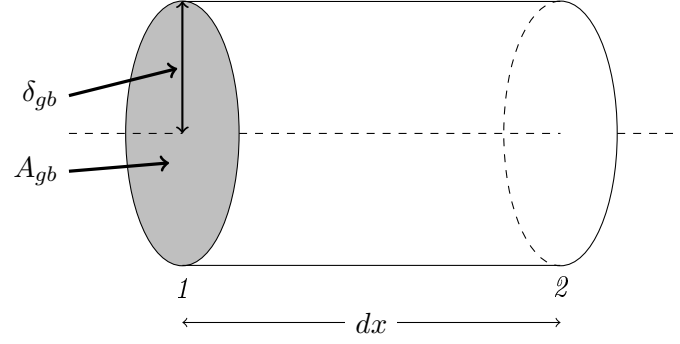


Figure 3.2. Schematic of the idealised grain boundary with width δ_{gb} and cross-sectional area A_{gb} .

Generalised rate equations

Substituting these rates into equation 3.1 for each gas phase we obtain a set of simultaneous equations that are continuous in space:

$$0 = Y_{fg}\dot{F}V_{gr}^{HBS} - k_{ld} \left. \frac{dc_{gr}^{fg}}{dr} \right|_{r=R_{gr}^{HBS}} + k_{res}V_{gb} \left(c_{gbb}^{fg} + c_{gbf}^{fg} \right) \quad (3.16)$$

$$0 = k_{ld}\phi \left. \frac{dc_{gr}^{fg}}{dr} \right|_{r=R_{gr}^{HBS}} - k_{res}V_{gb}c_{gbb}^{fg} + k_{gbtr}V_{gb}c_{gbf}^{fg} \quad (3.17)$$

$$0 = k_{ld}(1 - \phi) \left. \frac{dc_{gr}^{fg}}{dr} \right|_{r=R_{gr}^{HBS}} - k_{res}V_{gb}c_{gbf}^{fg} - k_{gbtr}V_{gb}c_{gbf}^{fg} - k_{gbd} \frac{dc_{gbf}^{fg}}{dx} \quad (3.18)$$

Boundary conditions

Equations 3.16– 3.18 describe the steady state equations to be solved for an infinite 1-D array of grains and grain boundaries. However our system is closed at either end by HBS pores. Consequently the HBS pores provide boundary conditions for these equations, viz. the gas concentration at the surface of the pore is considered to be negligible, i.e.:

$$c_{gbf}^{fg} = \begin{cases} 0 & \text{for } x = 0 \\ 0 & \text{for } x = l_{p-p} \end{cases} \quad (3.19)$$

This is in accordance with the assumption that once the gas enters the porosity it does not leave again, neither via diffusion nor re-resolution back to the grain phase.

3.2.2 Discretisation

With the addition of the boundary conditions 3.19 and equations 3.16– 3.18 we have a complete equation set describing the steady state concentrations in our system. We discretise the space between the two pores such that the separation dx between any two nodes is $2R_{gr}^{HBS}$. Figure 3.3 illustrates the discretisation scheme.

With the exception of the diffusional fluxes, each term can be rewritten in terms of the nodal

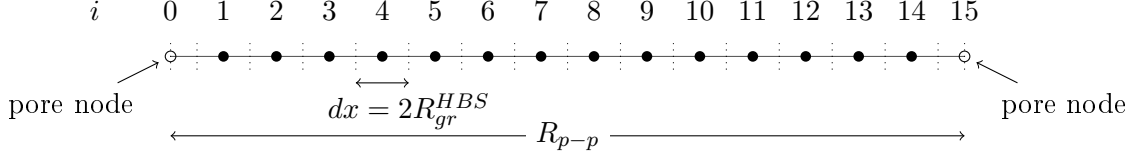


Figure 3.3. Schematic illustrating the discretisation of the 1-D region between two HBS pores separated by a distance l_{p-p} .

number, i , e.g. $c_{gbf}^{fg}(x) \rightarrow c_{gbf}^{fg}(i)$. For the diffusional fluxes the situation is not as simple. Instead we rewrite the concentration derivatives using finite differences. Equation 3.7 represents the diffusional transport of fission gas atoms from the grain to the porosity. From the point of view of diffusion we can consider the grain boundary as being a perfect sink, i.e. there is no “back” diffusion into the grains². In general we can write:

$$\frac{dc_{gr}^{fg}(i)}{dr} = \frac{c_{gb}^{fg}(i+1) - c_{gr}^{fg}(i)}{R_{gr}^{HBS}} \quad (3.20)$$

With the perfect sink boundary condition this becomes:

$$\frac{dc_{gr}^{fg}(i)}{dr} = \frac{-c_{gr}^{fg}(i)}{R_{gr}^{HBS}} \quad (3.21)$$

Substituting equation 3.21 into 3.7 we find:

$$-k_{ld} \left. \frac{dc_{gr}^{fg}}{dr} \right|_{r=R_{gr}^{HBS}} = -k_{ld} \left(\frac{-c_{gr}^{fg}(i)}{R_{gr}^{HBS}} \right) \quad (3.22)$$

Similarly for the grain boundary diffusion term in equation 3.18 we can represent the derivative as a finite difference. However, in the case of grain boundary diffusion we take a slightly different approach. Figure 3.2 shows a schematic of a section of our grain boundary. We consider the flux of gas through the cross-sectional surfaces 1 and 2 to the adjacent nodes at $i-1$ and $i+1$ respectively. The gradients in these directions can be represented as:

$$\left. \frac{dc_{gbf}^{fg}(i)}{dx} \right|_1 = \frac{c_{gbf}^{fg}(i-1) - c_{gbf}^{fg}(i)}{2R_{gr}^{HBS}} \quad (3.23)$$

$$\left. \frac{dc_{gbf}^{fg}(i)}{dx} \right|_2 = \frac{c_{gbf}^{fg}(i+1) - c_{gbf}^{fg}(i)}{2R_{gr}^{HBS}} \quad (3.24)$$

Substituting 3.23 and 3.24 into expression 3.15 we can calculate the grain boundary diffusion

²Of course the re-solution process acts to counter this diffusional transport. However we have taken this into account separately as another process and so does not need to be considered here.

transport at node i :

$$k_{gbd} \frac{dc_{gbf}^{fg}}{dx} = k_{gbd} \left(\frac{\left(c_{gbf}^{fg}(i+1) + c_{gbf}^{fg}(i-1) - 2c_{gbf}^{fg}(i) \right)}{2R_{gb}^{HBS}} \right) \quad (3.25)$$

While these expressions apply generally for all nodes, the boundary conditions specified in 3.19 fix the concentrations at $i = 0$ and $i = N$. Consequently we do not calculate the concentrations at these points and merely fit the free grain boundary gas concentration to the boundary conditions. If we now substitute equations 3.25 and 3.22 into expressions 3.16–3.18 we obtain our discretised equation system:

$$0 = Y_{fg} \dot{F} V_{gr}^{HBS} - k_{ld} \left(\frac{-c_{gr}^{fg}(i)}{R_{gr}^{HBS}} \right) + k_{res} V_{gb} \left(c_{gbb}^{fg}(i) + c_{gbf}^{fg}(i) \right) \quad (3.26)$$

$$0 = k_{ld} \phi \left(\frac{-c_{gr}^{fg}(i)}{R_{gr}^{HBS}} \right) - k_{res} V_{gb} c_{gbb}^{fg}(i) + k_{gbtr} V_{gb} c_{gbf}^{fg}(i) \quad (3.27)$$

$$0 = k_{ld}(1 - \phi) \left(\frac{-c_{gr}^{fg}(i)}{R_{gr}^{HBS}} \right) - k_{res} V_{gb} c_{gbf}^{fg}(i) - k_{gbtr} V_{gb} c_{gbf}^{fg}(i) - k_{gbd} \left(\frac{\left(c_{gbf}^{fg}(i+1) + c_{gbf}^{fg}(i-1) - 2c_{gbf}^{fg}(i) \right)}{2R_{gb}^{HBS}} \right) \quad (3.28)$$

3.2.3 Solution scheme and averaged gas concentration

The system of equations (equations. 3.26– 3.28) is solved iteratively using the Gauss-Seidel method (see appendix B), yielding the equilibrium concentrations for the three gas phases.

The output of the calculations is a detailed profile of the gas concentrations between the pores for each of the three phases: grain gas, free grain boundary gas and trapped grain boundary gas. However the experimental information obtained from the EPMA analysis that is commonly performed on high burnup fuel is not that detailed. As a consequence an averaged xenon concentration is calculated to compare with EPMA results. This is done by summing the number of atoms for each phase to produce a total amount of xenon in the system and then dividing by the fuel volume,

$$\langle c_{gr}^{fg} \rangle_{vol} = \frac{V_{gb}^{HBS} \sum_i \left(c_{gbf}^{fg}(i) + c_{gbb}^{fg}(i) \right) + V_{gr}^{HBS} \sum_i c_{gr}^{fg}(i)}{\sum_i V_{gr}^{HBS}} \quad (3.29)$$

which is in units of atoms m^{-3} . Equivalently in wt%:

$$\langle c_{gr}^{fg} \rangle = \frac{100m_{xe}}{\rho_f N_A} \left[\frac{V_{gb}^{HBS} \sum_i (c_{gbf}^{fg}(i) + c_{gbb}^{fg}(i)) + V_{gr}^{HBS} \sum_i c_{gr}^{fg}(i)}{\sum_i V_{gr}^{HBS}} \right] \quad (3.30)$$

where m_{xe} is the atomic mass for xenon, ρ_f is the density of the fuel and N_A is Avogadro's number.

Steady-state bubble growth modification

Although there is an implicit assumption in the model that the bubbles are in a nucleating phase, equations describing a basic growth process are introduced in order to gauge how valid this initial assumption is in the context of the model. The condition under which a bubble must start to grow can be evaluated by balancing the bubble pressure and the effect of surface tension, yielding the critical number of trapped atoms per node for growth to occur:

$$N_b^{fg} \Big|_{crit}^{tot} = \frac{2\gamma_{fs}}{R_{gbb}} \left[\frac{V_{gbb} n_{gbb} A_{gr}}{k_B T_K + \omega_{Xe} \frac{2\gamma_{fs}}{R_{gbb}}} \right] \text{ for } p_h << \frac{2\gamma_{fs}}{R_{gbb}} \quad (3.31)$$

where:

γ_{fs} = surface tension of the bubble

R_{gbb} = bubble radius of curvature

V_{gbb} = bubble volume

n_{gbb} = bubble number density

A_{gr} = grain surface area

k_B = Boltzmann constant

p_h = hydrostatic pressure

T_K = temperature

ω_{Xe} = Van der Waal constant for xenon

If the number of trapped atoms for a given node during the calculation is greater than the critical number of atoms given by equation (11) then a new radius is calculated and used further. This condition is considered throughout the iterative solution of the main equations. Appendices C and D provide more details concerning the calculation of the equilibrium bubble radius.

3.2.4 Parameter values

The nominal values used for the model parameters are listed in table 3.3 along with the corresponding range of values found in open literature. Some of the nominal parameter values correspond to specific characterisations of the HBS (e.g. grain size and pore separation) and as

such have been set with the corresponding reported values [2, 3, 9, 10, 14, 15, 16]. However, there are other parameters that have not been measured for the HBS (e.g. nucleating bubble density). In this case the values used for the normal fuel structure are used.

Table 3.3. Nominal parameter values (corresponding to an averaged xenon concentration of ~ 0.2 wt %), along with parameter limits from open literature and the corresponding impact on gas concentrations

Parameter	Nominal value	Parameter limits from open literature	Corresponding xenon concentration range / wt%
Volume diffusion coefficient, D_{gr}^{fg}	$5.3 \times 10^{-22} \text{ m}^2 \text{ s}^{-1}$	10^{-24} – $10^{-20} \text{ m}^2 \text{ s}^{-1}$	46.1 – 6.7×10^{-3}
Bubble number density, n_{gbb}	10^{12} m^{-2}	10^{11} – 10^{13} m^{-2}	0.16 – 0.54
Reference re-solution rate coefficient, k_{res}^{ref}	$2 \times 10^{-6} \text{ s}^{-1}$	10^{-7} – 10^{-4} s^{-1}	0.16 – 2.1
Diffusion coefficient ratio, $\alpha = D_{gb}^{fg} / D_{UO_2}^{fg}$	5×10^4	10^3 – 10^6	2.1 – 0.13
Pore separation, l_{p-p}	$3.0 \text{ } \mu\text{m}$	1.2 – $4.2 \text{ } \mu\text{m}$	0.13 – 0.20
Grain radius, R_{gr}^{HBS}	$0.15 \text{ } \mu\text{m}$	0.05 – $0.3 \text{ } \mu\text{m}$	1.7×10^{-2} – 0.73
Pellet average fission rate density, \dot{F}	$6 \times 10^{18} \text{ m}^{-3} \text{ s}^{-1}$	10^{18} – $10^{19} \text{ m}^{-3} \text{ s}^{-1}$	5.7×10^{-2} – 0.23
Peaking factor	3	1–4	8.5×10^{-2} – 0.20
Initial Bubble radius of curvature, R_{gbb}	2 nm	1–10 nm	0.16 – 0.17
Trapping rate coefficient, k_{gbtr}^a	$3.4 \times 10^{-5} \text{ s}^{-1}^b$	2.47×10^{-6} – $7.78 \times 10^{-4} \text{ s}^{-1}^c$	-
Temperature	600 K	-	-
Grain boundary radius, δ_{gb}	0.5 nm	-	-

^a The trapping rate coefficient here is the initial value calculated from the initial grain boundary bubble radius and bubble number density. We additionally assume that the diffusion coefficient ratio takes a value of $\alpha = 5 \times 10^4$.

^b This value corresponds to the nominal value for the initial grain boundary bubble radius and bubble number density for a diffusion coefficient ratio of $\alpha = 5 \times 10^4$.

^c These values correspond to the parameter limits of the initial grain boundary bubble radius and bubble number density for a diffusion coefficient ratio of $\alpha = 5 \times 10^4$.

It is clear that certain parameter values carry considerable uncertainty. However, in the interest of establishing a starting point, we have used a “nominal parameter set” (the “base case”) such that the calculated averaged xenon concentration is close to the measured EPMA concentration (~ 0.2 wt%), while staying within the parameter ranges specified in the literature. It should be pointed out that while the value of the volume diffusion coefficient for xenon has been measured, no such data exist for the grain boundary diffusion coefficient. (It should be mentioned that our model uses a diffusion coefficient ratio to calculate the grain boundary diffusion coefficient; see table 3.3).

3.3 Effect of grain boundary diffusion

Figure 3.4 shows the effects of the variation of both the diffusion coefficient ratio and the bubble density.

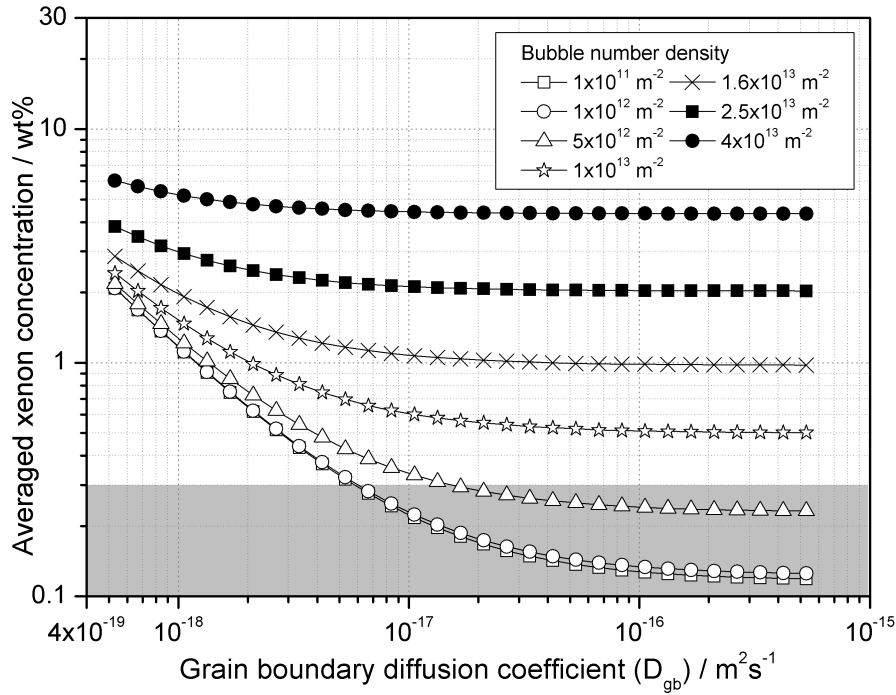


Figure 3.4. Variation of the averaged xenon concentration with the diffusion coefficient ratio for different bubble density values. The grey area corresponds to the range of average concentrations seen in EPMA measurements of the HBS.

As can be seen the averaged xenon concentration saturates for high values of the diffusion coefficient ratio ($\alpha > 100$). Since the grain boundary diffusion coefficient increases with the diffusion coefficient ratio the effective diffusion distance on the grain boundary also increases, until a certain diffusion distance beyond which the specific value for the coefficient does not matter any more. Within this saturation regime it is clear that the bubble density has the dominant influence on the absolute value of the averaged xenon concentration: if the bubble density is increased from 10^{11} to $4 \times 10^{13} \text{ m}^{-2}$ then the averaged xenon concentration markedly increases from ~ 0.1 to $\sim 6 \text{ wt}\%$. However, at lower bubble densities ($< 10^{12} \text{ m}^{-2}$), there is a second saturation effect. This behaviour is another aspect of the increasing effective diffusion distance, primarily because the reduction in trapping strength enhances the grain boundary diffusion process. At lower diffusion coefficient ratios, i.e. as the grain boundary diffusion coefficient approaches the volume diffusion coefficient, there is a considerable increase in the averaged xenon concentration. It should be commented though that the saturation concentration, i.e. for a diffusion coefficient ratio above $\sim 10^4$, is dependent on the absolute value of the volume diffusion coefficient. In spite of this it is a clear conclusion of figure 3.4 that for the current model to achieve the $\sim 0.2 \text{ wt}\%$ averaged xenon concentration the nucleating bubble density needs to be low and the grain boundary diffusion coefficient should be high (for the case of the nominal volume diffusion coefficient).

3.4 Sensitivity to model parameters

3.4.1 Equilibrium concentrations at parameter value limits

As an initial assessment of the impact of the large uncertainties in the model parameters, the values of the averaged xenon concentration corresponding to the open–literature parameter limits have been calculated and are shown in the last column of table 3.3. The calculations were performed by setting the parameter of interest to the upper and lower limits while retaining the nominal values for the remaining parameters.

It is clear from table 3.3 that the volume diffusion coefficient has the largest effect on the averaged xenon concentrations with ~ 7 orders of magnitude variation for a volume diffusion coefficient range of 10^{-24} to $10^{-20} \text{ m}^2\text{s}^{-1}$. With such a large variation in concentrations, the accuracy of measurements for the volume diffusion coefficient at low temperatures is clearly important. Unfortunately, the available experimental data is the least accurate in this range and absolute values for the diffusion coefficient vary wildly. For example the Turnbull three term diffusion coefficient [17] at a temperature of 673 K and mass rating of 25 W/gU is $\sim 10^{-21} \text{ m}^2\text{s}^{-1}$, while the correlation derived by Matzke [18] gives $\sim 10^{-25} \text{ m}^2\text{s}^{-1}$. Clearly the current variations in correlations and measurements at low temperatures are much too large to provide any reliable choice for the nominal value.

Although the volume diffusion coefficient is the most sensitive parameter in the model the other parameters do clearly affect the averaged xenon concentration as well. However, in almost every case, the variation at the parameter limits is less than two orders of magnitude over the entire parameter range. This is particularly interesting in the case of the geometrical parameters, indicating a remarkable insensitivity to the HBS–specific geometry parameters, viz. pore separation and grain radius. For the pore separation, the averaged xenon concentrations fall exactly within the experimental errors for the measured xenon concentration, even for pore separations as high as $4.2 \mu\text{m}$. This range of pore separations covers the observed values for the HBS and as a consequence there is little sensitivity to the radial variation of porosity as reported for high burnup fuel samples. For the grain radius it is clear that there is an increase in concentration with grain size, which might be of some concern given that the measured xenon concentration in the HBS zone is generally found to be constant. However it should be noted that a grain radius distribution develops in the HBS zone [9], and thus the upper and lower limits should contribute less to the average concentration than the average grain radius of $0.15 \mu\text{m}$. To confirm this, a simple Monte Carlo calculation was performed to reproduce the experimentally observed HBS grain distribution. The introduction of a grain distribution was found to increase the averaged xenon concentration by less than twice the nominal value.

Another point of interest is the variation of the averaged xenon concentration with the pellet averaged fission rate density. The selected range of 10^{18} – $10^{19} \text{ m}^{-3}\text{s}^{-1}$ corresponds approximately to pellet–average linear heat rates of 2 kW/m and 17 kW/m respectively. The variation over the entire range is relatively small, i.e. less than an order of magnitude. More importantly, one would expect to have average linear heat rates of at least 10 kW/m at steady state, which reduces this range even further.

Although the model was implemented with the assumption that bubble growth kinetics is not an important factor for the averaged xenon concentration, a simple equilibrium bubble growth model has been considered (see section 3.2.3). Consequently, the sensitivity with respect to the starting bubble radius was investigated. Typically, a nucleating bubble is expected to have a radius on the order of nanometres. As can be seen from table 3.3, varying the initial bubble radius from 1 to 10 nm, even when considering bubble growth, does not significantly affect the averaged xenon concentration. In fact the observed increase is entirely within the experimental uncertainties in xenon concentration measurements.

3.4.2 Sensitivity with respect to the principal parameters

The sensitivity of the averaged xenon concentration has been examined in greater detail for four parameters: 1) the grain boundary and 2) volume diffusion coefficients, 3) the re-resolution rate coefficient and 4) the bubble number density. These parameters are of particular interest because they are the principal ones that affect the four mass transfer processes in the model, i.e. grain and grain boundary diffusion, grain boundary bubble re-resolution and trapping. To examine the effects of these parameters, several two-parameter variations were performed with the remaining model parameters fixed at their nominal values in each case.

In figure 3.5 the variation of the averaged xenon concentration with volume diffusion coefficient and the diffusion coefficient ratio can be seen.

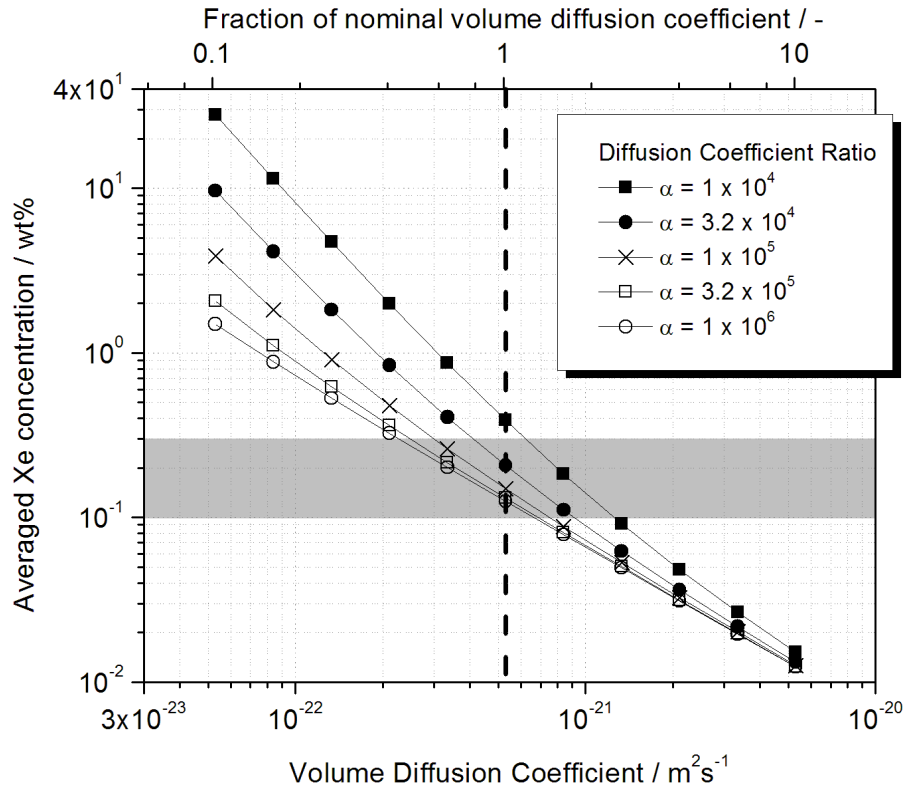


Figure 3.5. Variation of the averaged xenon concentration with the grain diffusion coefficient for different values of the diffusion coefficient ratio. The grey area corresponds to the range of average concentrations seen in EPMA measurements of the HBS.

In the previous section, the range of average concentration values with respect to the volume diffusion coefficient limits was observed to be very large. In fact it can be seen from figure 3.5 that the variation between the two limits is also a function of the diffusion coefficient ratio. For example, for a diffusion coefficient ratio of 10^6 the change in average concentration between volume diffusion coefficient values of $\sim 5 \times 10^{-23} \text{ m}^2 \text{ s}^{-1}$ and $\sim 5 \times 10^{-21} \text{ m}^2 \text{ s}^{-1}$ is approximately a factor of 100, while for the low diffusion coefficient ratio of 10^4 this increases to a factor of $\approx 4 \times 10^3$. This behaviour is consistent with the expected high gas concentrations for low values of both grain boundary and volume diffusion coefficients. In this respect, it is abundantly clear that the model is highly dependent on the absolute values of both coefficients. These observations reinforce the previous statement that reliable conclusions can only be made if the diffusion coefficients are known more accurately than at present. In spite of this we can say that for the current model to achieve the observed 0.2 wt% concentration we require a diffusion coefficient that is approximately an order of magnitude lower than the value given by the Turnbull diffusion coefficient. A similar conclusion was obtained by Br  mier and Walker [19] for the simple Booth sphere calculation they performed to predict the observed HBS xenon depletion of $\sim 0.2\text{--}0.3$ wt%.

Figure 3.6 illustrates the dependence on both the re-solution rate and the bubble density. It shows two separate behaviours with respect to the re-solution rate. At high re-solution rates there is little variation in the averaged xenon concentration with respect to the bubble density; this is contrary to the behaviour displayed at low re-solution rates where there is also saturation in the effect of the bubble density (for $n_{gb} < 10^{12} \text{ m}^{-2}$). The two different regimes can be understood by considering that, although the averaged xenon concentration is calculated using the grain and grain boundary concentrations, the principal contribution comes from the grain concentration. Moreover, because the model considers a steady-state regime, the resulting flux balance ensures that if the total re-solution flux increases then there is a corresponding increase in the grain concentration. There are therefore two fluxes in this case which contribute to the increase in the averaged xenon concentration, viz. 1) the re-solution flux from the free gas to the grain and 2) the re-solution flux from the trapped gas to the grain.

The definition of the re-solution flux depends upon the local gas concentrations (from both free and trapped phases). The free gas re-solution flux is linearly dependent on the re-solution coefficient. However, the trapped gas concentration depends on how much gas is available for trapping, i.e. how much free gas there is (equation 3.12). So, when the re-solution coefficient is high, the re-solution of free gas from the grain boundary yields a reduced free gas concentration on the grain boundary. Consequently, the trapping flux and the trapped gas concentration are lower, leading to a reduction in the re-solution flux from the trapped gas as well. The ultimate consequence of these coupled phenomena is that at high re-solution coefficients the linear behaviour of the free gas re-solution flux is the main determining factor for the averaged xenon concentration. Secondly, because the free gas re-solution behaviour is only governed by equation 3.11 there is no bubble density dependence.

At low re-solution coefficients the behaviour is reverse, i.e. the low re-solution flux from the free gas produces a high trapped gas concentration and therefore a high trapped gas re-solution flux, which dominates the overall xenon concentration behaviour. There are two principal differences in this case though:

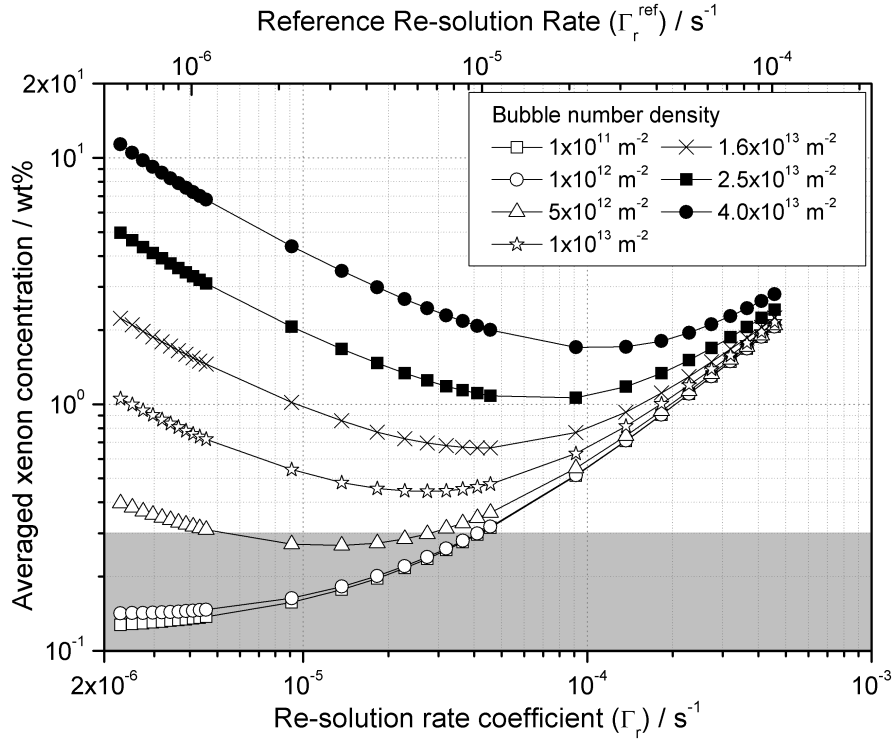


Figure 3.6. Variation of the averaged xenon concentration with the re-solution rate. The grey area corresponds to the range of average concentrations seen in EPMA measurements of the HBS.

1. The trapping rate has a bubble density dependence and hence the trapped gas concentration will also have a dependence. This results in a trapped gas re-solution flux (and therefore an averaged xenon concentration) that is also bubble-density dependent.
2. The re-solution flux from the trapped gas is inversely proportional to the re-solution coefficient because the trapped gas concentration is dependent on the amount of free gas available for trapping.

Because of the multi-variable nature of the current model it is obvious that different parameter combinations will lead to different averaged concentrations. Figure 3.7 illustrates the range of values of the three principal parameters, over which the model produces an averaged xenon concentration of ~ 0.2 wt%. In this figure the diffusion coefficient ratio has been placed in the saturation regime, $\alpha = 5 \times 10^4$, i.e. the grain boundary diffusion is high enough that the fission gas is immediately transported to the HBS-pores.

As expected, Figure 3.7 exhibits most of the features that have been commented on previously, viz.

- There is a lower sensitivity to the bubble density at high re-solution rates; this however develops strongly when the re-solution rate is reduced.
- The range of the required volume diffusion coefficient (for attaining ~ 0.2 wt%) is well within the anticipated uncertainty on parameter values. However it does mean that an accurate determination of diffusion coefficients is crucial to finally validate this modelling approach.

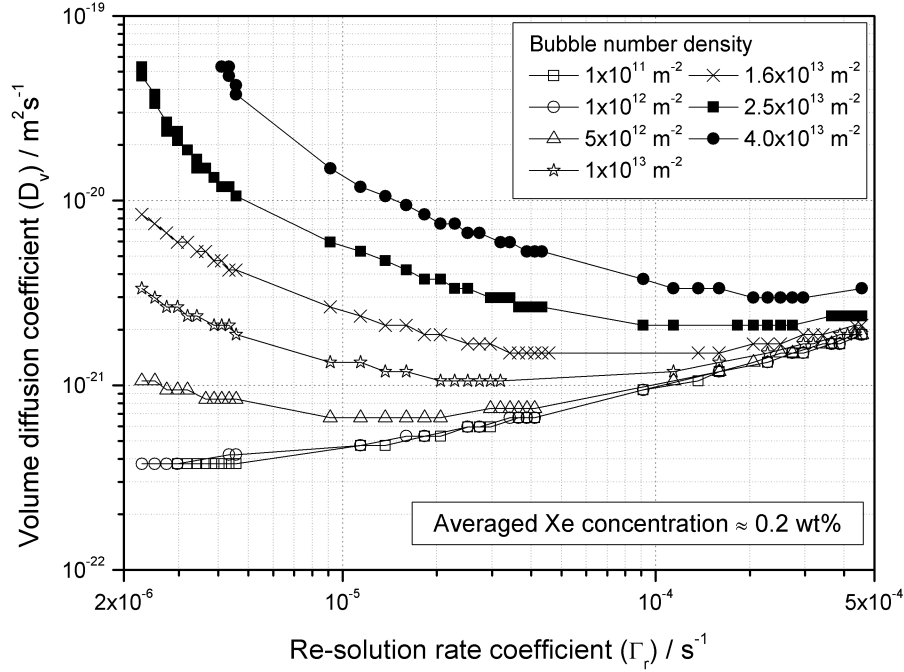


Figure 3.7. Required range of values of key parameters for producing an approx. 0.2 wt% average xenon concentration (diffusion coefficient ratio fixed at 5×10^4).

3.5 Conclusions

A steady-state fission gas model has been developed to examine the importance of grain boundary diffusion for the gas dynamics in the HBS. A stable solution was achieved for the set of parameters used in common fission gas models combined with parameter values specific to the HBS. With the current model it is possible to approximately simulate the 0.2 wt% experimentally observed xenon concentration under certain conditions, viz. fast grain boundary diffusion and a reduced volume diffusion coefficient. The sensitivity study has shown that the value of the grain boundary diffusion coefficient is not important for diffusion coefficient ratios above $\sim 10^4$. However, in the limit of “slow” grain boundary diffusion a sizeable effect on the calculated xenon depletion value is obtained. Within the grain boundary diffusion saturation regime the current model exhibits a high sensitivity to three principal parameters: the volume diffusion coefficient, the bubble number density and the re-resolution rate coefficient. The more detailed examination of the sensitivity with respect to these parameters has shown that:

1. There is a secondary saturation observed in variation of the averaged xenon concentration with respect to the bubble density at bubble densities below 10^{13} m^{-2} .
2. The volume diffusion coefficient is the crucial parameter in the model due to its high sensitivity and because most of the gas contributing to the averaged xenon concentration is in the grains.
3. If the re-resolution rate is high then the sensitivity to the bubble density is severely reduced, whereas at lower re-resolution rates the sensitivity is important. However, the bubble density saturation is still apparent at low re-resolution rates.

All of these observations are seen in figure 3.7, which illustrates the necessary combination of these parameters for the 0.2 wt% concentration. It is clear from this “locus” plot that at low re-solution rates all three parameters are of relevance. Of particular significance is the relatively small range of required values for the volume diffusion coefficient. In spite of the uncertainties in the input parameters it is clear that this model can reproduce the observed HBS xenon depletion with the assumption that grain boundary diffusion of fission gas is significantly faster than volume diffusion. Moreover, it is clear that the reduction of geometrical characteristics such as pore separation and grain size facilitates the maintenance of the xenon depletion. The fact that this can be maintained without considering a new transport process is an indication that gas transport within the HBS is similar to that found in normal structure. In particular this model demonstrates that the release of produced gas from the grains to the HBS porosity corresponds to a dynamic equilibrium which provides a justification for the typical modelling approach used in HBS fuel performance modelling, viz. fast transport to the porosity. From a fuel performance modelling point of view this simplifies the calculations enormously. However, the question then remains, what happens to the gas once it is in the porosity? This question is addressed in the next chapter by introducing a model that describes the effect of the accumulation of fission gas in the porosity.

Bibliography

- [1] J. Spino, A. D. Stalios, H. Santa Cruz, and D. Baron. Stereological evolution of the rim structure in PWR-fuels at prolonged irradiation: Dependencies with burn-up and temperature. *J. Nucl. Mater.*, 354:66–84, 2006.
- [2] J. Spino, D. Papaioannou, and J.-P. Glatz. Comments on the threshold porosity for fission gas release in high burn-up fuels. *J. Nucl. Mater.*, 328:67–70, 2004.
- [3] L. Noirot, Ph. Garcia, and C. Struzik. A mechanistic fission gas behaviour model for UO_2 and MOX fuels. In *Proceedings of the IAEA/NEA/CEA International Seminar on Fission Gas behaviour in Water Reactor Fuels*, Cadarache, France, September 2000.
- [4] T. Fuketa, H. Sasajima, Y. Mori, and K. Ishijima. Fuel failure and fission gas release in high burnup PWR fuels under RIA conditions. *J. Nucl. Mater.*, 248:249–256, 1997.
- [5] F. Schmitz and J. Papin. High burn-up effects on fuel behaviour under accident conditions: The tests CABRI REP-Na. *J. Nucl. Mater.*, 270:55–64, 1999.
- [6] High burnup effects programme final report. Technical Report DOE/NE/34046-1.
- [7] C. T. Walker, T. Kameyama, S. Kitajima, and M. Kinoshita. Concerning the microstructure changes that occur at the surface of UO_2 pellets on irradiation to high burnup. *J. Nucl. Mater.*, 188:73–79, 1992.
- [8] D. R. Olander and P. Van Uffelen. On the role of grain boundary diffusion in fission gas release. *J. Nucl. Mater.*, 288:137–147, 2001.
- [9] J. Spino, K. Vennix, and M. Coquerelle. Detailed characterisation of the rim microstructure in PWR fuels in the burn-up range 40-67 GWd/tM. *J. Nucl. Mater.*, 231:179–190, 1996.
- [10] T. Sonoda, M. Kinoshita, I. L. F. Ray, T. Wiss, H. Thiele, D. Pellottiero, V. V. Rondinella, and H. J. Matzke. Transmission electron microscopy observation on irradiation induced microstructural evolution in high burn-up UO_2 disk fuel. *Nucl. Instrum. Meth. B.*, 191:622–628, 2002.
- [11] A. H. Booth. A method of calculating fission gas diffusion from UO_2 fuel and its application to the X-2-F loop test. Technical Report CRDC-721, Atomic Energy of Canada Limited, Chalk River, Ontario, Canada, 1957.
- [12] A. H. Booth. A suggested method for calculating the diffusion of radioactive rare gas fission products from UO_2 fuel elements and a discussion of proposed in-reactor experiments that may be used to test its validity. Technical Report DCI-27, Atomic Energy of Canada Limited, Chalk River, Ontario, Canada, 1957.
- [13] P. Van Uffelen. *Contribution to the Modelling of Fission Gas Release in Light Water Reactor Fuel*. PhD thesis, l’Université de Liège, 2002.
- [14] R. Manzel and C. T. Walker. EPMA and SEM of fuel samples from PWR rods with an average burn-up of around 100 MWd/kgHM. *J. Nucl. Mater.*, 301:170–182, 2002.

- [15] J. Spino and D. Papaioannou. Lattice parameter changes associated with the rim-structure formation in high burn-up UO_2 fuels by micro X-ray diffraction. *J. Nucl. Mater.*, 281:146–162, 2000.
- [16] N. Lozano, L. Desgranges, D. Aymes, and J. C. Niepce. High magnification SEM observation for two types of granularity in a high burnup PWR fuel rim. *J. Nucl. Mater.*, 257:78–87, 1998.
- [17] J.A. Turnbull, R. J. White, and C. Wise. IAEA Technical Committee meeting on Water Reactor Fuel Element Computer Modelling in Steady-state. Technical Report T1-TC-659, IAEA, 1998.
- [18] H. J. Matzke. Gas release mechanisms in UO_2 – a critical review. *Radiat. Eff. Defect. S.*, 53:219–242, 1980.
- [19] S. Bremier and C. T. Walker. Radiation-enhanced diffusion and fission gas release from recrystallised grains in high burn-up UO_2 nuclear fuel. *Radiat. Eff. Defect. S.*, 157:311–322, 2002.

Chapter 4

Growth of the high burnup structure porosity under annealing conditions

As far as the laws of mathematics refer to reality, they are not certain; and as far as they are certain, they do not refer to reality.

- Albert Einstein

4.1 Introduction

The evolution of the high burnup structure (HBS) porosity is considered a key point when evaluating the retention capabilities of fission gas within the HBS. The porosity is widely recognised as the primary location of most of the unreleased fission gas. Consequently, there has been much effort in characterising the stereological parameters of HBS porosity [1, 2] (see section 2.2.1 for details) and the consequences for fuel performance, e.g. thermal conductivity degradation [3, 4] and fission gas release [5, 6, 7, 8, 9, 10], during steady-state and transient conditions. As a result the evolution of porosity in the HBS needs to be evaluated in order to adequately assess fuel performance and safety.

Annealing experiments provide a way to examine the HBS behaviour under laboratory conditions, where temperatures are well characterised and the release of fission products can be monitored on-line. This provides a good opportunity for verification of models of pore growth and fission product behaviour within the HBS. In spite of this, the literature on mechanistic models addressing the growth of the HBS porosity [11, 12, 13, 14] and the effect on fission gas release, particularly under annealing conditions, is scarce.

In this chapter we develop a gas release model that takes into account the growth of pores, interaction with the open surface and higher order compound interactions. The developed model is generally applicable to annealing and in-pile conditions; however, in each case the source of lattice defects differs. Here we only consider annealing conditions (in-pile conditions are addressed in chapter 5), and as such we only use the thermal equilibrium vacancy and interstitial population for the defects. This chapter is organised as follows. The next section presents the

theoretical development of the model, starting from the basic equations for pore growth and then moving to the effect of compound interactions. In section 4.3.1 we perform a sensitivity analysis to study the effect of parameters such as temperature and the surface-to-volume ratio on the fission gas release at constant temperatures. In section 4.3.2 the model is applied to a high burnup light water reactor (LWR) UO_2 annealing experiment to assess its predictions in comparison with the measurements. Finally, in sections 4.4 and 4.5 a summary of the conclusions and the implications for in-pile behaviour are presented.

4.2 Theoretical model development

4.2.1 Single pore growth

Pore growth/shrinkage occurs when there is a departure from mechanical equilibrium, e.g. pore over/under-pressurisation. Mechanical equilibrium occurs when the sum of all the forces acting on the pore is equal to zero, which for the case of a pore of size R_p in UO_2 can be expressed as:

$$p_p = \frac{2\gamma_{fs}}{R_p} - p_h \quad (4.1)$$

where p_p is the internal gas pressure in the pore, γ_{fs} is the surface energy and p_h is the hydrostatic pressure. The maintenance of mechanical equilibrium¹ is controlled by a flux of defects to the pore providing the additional volume needed for relaxation of over-pressurisation due to the in-flux of fission gas atoms. In majority of existing models the mechanical equilibrium state is used to calculate the pore size evolution; however, for pore growth to occur this condition cannot hold, rather we have:

$$p_p \neq \frac{2\gamma_{fs}}{R_p} - p_h \quad (4.2)$$

Under these conditions the more general and applicable expression for the rate of accumulation of vacancies by a pore of size R_p is:

$$\frac{dc_v}{dt} = 4\pi R_p (D_{gr}^v \Delta c_v - D_{gr}^i \Delta c_i) \quad (4.3)$$

where $c_{v,i}$ is the concentration of vacancies and interstitials, $\Delta c_{v,i}$ is the gradient of vacancies/interstitials, $D_{gr}^{v,i}$ is the vacancy and interstitial diffusion coefficient. If we consider that each defect contributes (or removes) a volume V_{defect} to (or from) the pore then the rate of change of the pore radius is given by:

$$\frac{dR_p}{dt} = \frac{V_{defect}}{R_p} (D_{gr}^v \Delta c_v - D_{gr}^i \Delta c_i) \quad (4.4)$$

The gradient of the point defects can be calculated by considering the difference between the defect concentration in the bulk and at the pore surface. For a pore with an over-pressure of

¹Also referred to as the capillarity condition

$\Delta p = p_p - 2\gamma_{fs}/R_p + p_h$ this difference can be written as:

$$\Delta c_{v,i} = c_{bulk}^{v,i} \left(1 - \exp \left(\pm \frac{V_{defect} \Delta p}{k_B T_K} \right) \right) \quad (4.5)$$

where $c_{bulk}^{v,i}$ is the bulk defect concentration, k_B is the Boltzmann constant and T_K is the local temperature. It should also be noted that for vacancies the argument in the exponential is positive while for interstitials it is negative.

The local pore pressure is often calculated using the ideal gas law; however this relies upon the assumption that there are no inter-molecular forces and that interactions between the gas atoms undergo purely elastic collisions with the pore boundary. A more appropriate equation of state is the Van der Waals equation of state, viz:

$$p_p \left(\frac{4}{3} \pi R_p^3 - \omega_{Xe} N_p^{fg} \right) = N_p^{fg} k_B T_K \quad (4.6)$$

where ω_{Xe} is the Van der Waals constant for Xe gas ($\sim 8.5 \times 10^{-29} \text{ m}^3/\text{atom}$).

Under annealing conditions the defect concentrations are entirely dependent on the formation of thermal equilibrium defects. Griesmeyer *et al.* [15] have derived the thermal equilibrium point defect population from the defect formation energies, charge balance and lattice site conservation within $\text{UO}_{2\pm x}$, viz.

$$C_{eq}^{vu} (C_{eq}^{vo})^2 = \exp(-\Delta G_s/kT) \equiv K_s \quad (4.7)$$

$$C_{eq}^{vo} C_{eq}^{io} = \exp(-\Delta G_{Fo}/kT) \equiv K_{Fo} \quad (4.8)$$

$$C_{eq}^{vu} C_{eq}^{iu} = \exp(-\Delta G_{Fu}/kT) \equiv K_{Fu} \quad (4.9)$$

$$0 = \frac{K_{Fu}}{K_s} (C_{eq}^{vo})^4 + (C_{eq}^{vo})^3 + \frac{1}{2} x (C_{eq}^{vo})^2 - \frac{1}{2} K_{Fo} (C_{eq}^{vo}) - K_s \quad (4.10)$$

Here, the fractional concentration C is defined as the fraction of the matrix volume taken up by the defects² and the subscripts u, o, v and i stand for uranium, oxygen, vacancies and interstitials, respectively. The formation energies of a Schottky defect (ΔG_s), an oxygen Frenkel defect (ΔG_{Fo}) and a uranium Frenkel defect (ΔG_{Fu}) are taken as 6.4 eV/atom, 3.1 eV/atom and 9.5 eV/atom, in accordance with Griesmeyer *et al.* [15]. The limiting factor for porosity growth is the diffusion of the slowest species, which in the case of UO_2 is the metallic defect population, i.e. uranium [15]. Consequently, upon substituting equation 4.5 into 4.4 and considering the thermal equilibrium metallic defect population, we find that equation 4.4 can be written as:

$$\frac{dR_p}{dt} = \frac{1}{R_p} \left(D_{gr}^v C_{eq}^{vu} \left(1 - \exp \left(\frac{V_{defect} \Delta p}{k_B T_K} \right) \right) - D_{gr}^i C_{eq}^{iu} \left(1 - \exp \left(-\frac{V_{defect} \Delta p}{k_B T_K} \right) \right) \right) \quad (4.11)$$

²The fractional concentration is related to the volumetric concentration by $C = c \times V_{defect}$

4.2.2 Growth of a pore population

Although equations 4.6, 4.7- 4.10 and 4.11 adequately describe the growth/shrinkage of a single pore, the UO_2 fuel microstructure contains a pore population³ with a distribution of sizes. Most characterisations of the porosity use two integral quantities to describe the state of the pores: fractional porosity (P) defined as the fraction of the fuel volume taken up by pores, and number density (n_p) defined as the number of pores per unit volume of fuel. Here the average pore radius can be calculated by considering that these two quantities are related as follows:

$$P = \frac{4}{3}\pi R_p^3 n_p \quad (4.12)$$

so that

$$R_p = \sqrt[3]{\frac{3}{4\pi} \frac{P}{n_p}} \quad (4.13)$$

The average pore pressure can be calculated using the Van der Waals equation of state (equation 4.6) upon considering that the total volume of the porosity V_p^{tot} resides within a volume of fuel V_{fuel} , i.e.:

$$\frac{p_p}{V_{fuel}} \left(V_p^{tot} - \omega_{Xe} N_p^{fg} \right) = \frac{N_p^{fg} k_B T_K}{V_{fuel}} \quad (4.14)$$

and therefore:

$$p_p (P - \omega_{Xe} c_p^{fg}) = c_p^{fg} k_B T_K \quad (4.15)$$

In an infinite medium with large separations between pores these expressions would suffice to describe the porosity growth. However, reality is not so kind! There are two additional features that also need to be taken into account:

- The presence of a free surface.
- Compound interactions between pores and also with the free surface.

The presence of a free surface is important because it allows the production of so-called vented pores, i.e. pores that have released their gas to the free volume. White [16] has examined the behaviour of grain face bubbles in UO_2 during coalescence and venting to the grain edges. It was noted that the areal fractional coverage⁴ never reaches the theoretical estimate for grain face saturation, i.e. $\pi/4$. The presence of boundaries (in this case the grain edges) has the effect that the system is not closed and consequently any grain face bubble within a certain range of the grain edge will intersect and vent after a certain period of growth. This depletes the grain face of bubbles and as a result limits the maximum areal coverage reached. Similarly,

³From here on the population of pores is simply referred to as porosity.

⁴This is analogous to the fractional porosity and is defined as the ratio of total area taken up by grain face bubbles to the area of the grain face.

it has been argued that the HBS porosity should not exhibit gas release until high values of the porosity [11]. These arguments are based upon percolation theory calculations and use the percolation threshold (see appendix A) as the point at which significant venting of the porosity occurs. However, this threshold relies upon the assumption of both an infinite medium and the absence of pore shrinkage after venting. In the first case it is clear that once a bubble intersects with the open surface release will occur. Therefore initiation of release from the porosity does not solely depend on the appearance of compound pore clusters as the percolation argument requires. Moreover if we examine equation 4.11 then we can see that under conditions where there is no longer any gas in a pore to resist the capillarity effect, the accumulation of interstitials and the emission of vacancies will affect the size of the pore. Consequently an analysis of pore behaviour with the free surface taken into account is necessary to effectively evaluate release from the HBS porosity.

The presence of compound interactions between pores coarsens the porosity distribution allowing larger pore sizes than could be achieved with pure growth. This has already been observed in the HBS [1, 2] and in studies of grain face bubbles [16]. A key indication of coarsening is the presence of a multi-peak porosity distribution. Spino *et al.* [1] have observed both bi-modal and tri-modal distributions at the pellet periphery indicating that coalescence is taking place. Furthermore Spino *et al.* have made the argument, using the colloid coagulation model of Chandrasekhar [17] and the hard-sphere packing calculations of Torquato [18], that coalescence should occur when the porosity exceeds $\approx 8-9\%$. A drop in the number density is observed in the HBS at approximately 100 MWd/kg at which point the porosity is $\approx 10\%$. This drop can only conceivably occur by two processes, coalescence and/or pore venting. It is reasonable to conclude that the presense of compound interactions is a necessary component in modelling the porosity behaviour.

Considering these points we introduce two types of porosity in the fuel: closed porosity and pores that have vented the contained fission gas (vented porosity). The state of these two porosity types can be characterised by a set of five time-dependent variables:

$$\begin{aligned} n_{cp} &= \text{Number density of closed pores } (m^{-3}) \\ C_{cp}^{fg} &= \text{Concentration of fission gas in the closed porosity } (m^{-3}) \\ P_{cp} &= \text{Porosity of the closed pores } (-) \\ n_{vp} &= \text{Number density of vented pores } (m^{-3}) \\ P_{vp} &= \text{Porosity of the vented pores } (-) \end{aligned}$$

where the subscripts *cp* and *vp* represent the closed and vented porosity respectively. These five variables only characterise the porosity and so we additionally specify the state of the open surface using a surface-to-volume ratio, S/V . The surface-to-volume ratio can take values between the geometrical surface-to-volume ratio of an intact pellet⁵ and that corresponding to complete grain separation, i.e. the surface-to-volume ratio of a grain⁶. Furthermore, the concentration of the

⁵Assuming the pellet is intact, i.e. no cracks, and can be approximated by a cylinder of radius R_{pellet} and depth h_{pellet} the geometrical surface-to-volume ratio is $(S/V)_{\text{geom}} = 2(R_{\text{pellet}} + h_{\text{pellet}})/R_{\text{pellet}}h_{\text{pellet}}$.

⁶For a monosized grain size distribution with grain radius R_{gr} the surface-to-volume ratio becomes $(S/V)_{\text{grain}} = 3/R_{gr}$

released fission gas (c_{rel}^{fg}) is calculated from the variation in the concentration of xenon in the closed porosity, (c_{cp}^{fg}).

Khvostov *et al.* [19] have developed a method for calculating the changes in grain boundary porosity and gas release using a macro cross-section approach. Here, compound interactions of the porosity with grain edges, vented bubbles and closed bubbles are considered and a set of differential cross-sections to describe the respective rates of change is introduced. We can apply this method to our system by considering the cross-sections for single interactions of a closed pore with the closed porosity, vented porosity and the free surface. Figure 4.1 illustrates the allowed first-order compound interactions in the current model.

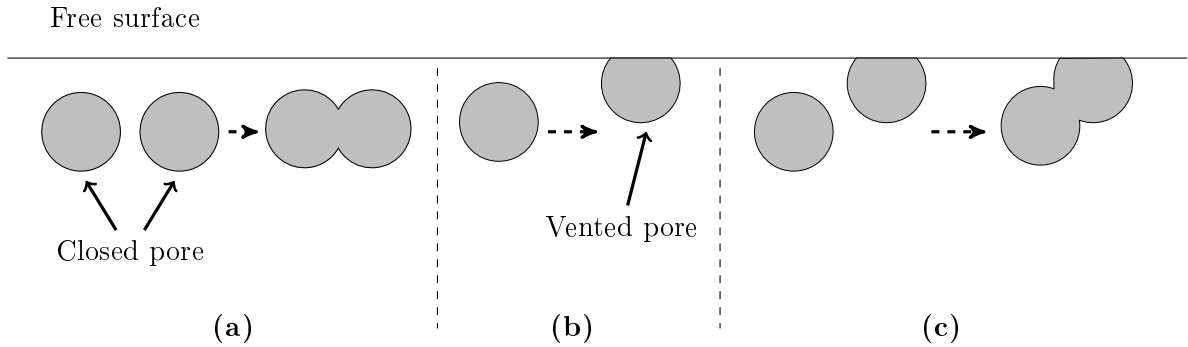


Figure 4.1. The three allowed first-order interactions between the closed porosity, vented porosity and the free surface, viz. (a) Coalescence of two closed pores, (b) Venting of a closed pore through intersection with the free surface and (c) Venting of a closed pore and coalescence with a vented pore.

For the interaction between a single closed pore and the closed porosity the cross-section depends on the average radius of the closed porosity, i.e.:

$$S_1^* = \frac{4}{3}\pi(2R_{cp})^3 n_{cp} \quad (4.16)$$

In the same way the cross-section for the interaction with the vented porosity can be calculated using the average radii of both the closed and vented porosity, i.e:

$$S_2^* = \frac{4}{3}\pi n_{vp} (R_{cp} + R_{vp})^3 \quad (4.17)$$

In the case of the interaction of a closed pore with the free surface only closed pores that are within a distance $2R_{cp}$ from the surface can interact with the free surface and consequently the fraction of pores available for venting (assuming they are distributed homogenously) can be written as:

$$S_3^* = 2R_{cp} (S/V) \quad (4.18)$$

The cross-section S_i^* is the total cross-section for any interaction, regardless of order, that involves the closed porosity and i . For example, S_1^* is the cross-section for coalescence (S_1). Similarly higher order interactions have a cross-section involving the closed porosity, e.g. S_{12} is the cross-section between two closed pores and a vented pore. Consequently to calculate the true

cross-sections we have to remove these extraneous contributions from S_i^* . Figure 4.2 illustrates how these can be derived from the equations 4.16– 4.18 using a set theory approach. The true cross-sections then become:

$$S_{123} = S_1^* S_2^* S_3^* \quad (4.19)$$

$$S_{12} = S_1^* S_2^* - S_{123} \quad (4.20)$$

$$S_{13} = S_1^* S_3^* - S_{123} \quad (4.21)$$

$$S_{23} = S_2^* S_3^* - S_{123} \quad (4.22)$$

$$S_1 = S_1^* - S_{12} - S_{13} - S_{123} \quad (4.23)$$

$$S_2 = S_2^* - S_{12} - S_{23} - S_{123} \quad (4.24)$$

$$S_3 = S_3^* - S_{13} - S_{23} - S_{123} \quad (4.25)$$

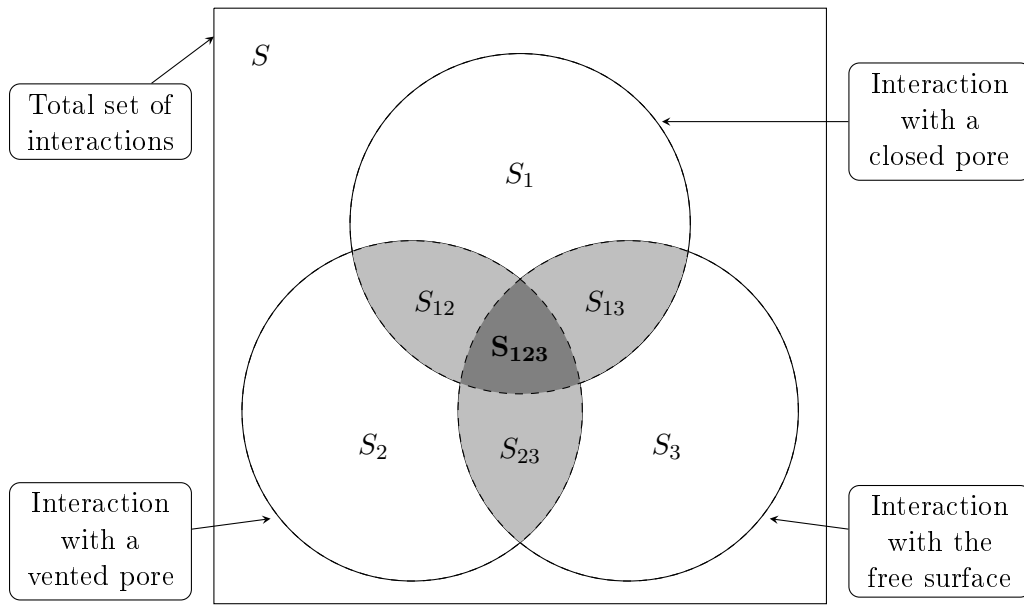


Figure 4.2. Venn diagram illustrating the relationships between the compound interactions.

Expressions 4.19– 4.25 describe the “probability” of a specific type of interaction occurring. For example, the expression for S_{12} gives the probability for the interaction of a closed pore with a closed pore and vented pore simultaneously. This scheme could be extended to describe an infinite number of compound interactions (i.e. 4, 5, 6 ...). However, it is expected that the cross-sections for the higher order interactions will be smaller than the lower order ones. Therefore only interactions up to third order are used here. In addition to equations 4.16– 4.25 we require

the derivatives⁷:

$$\frac{dS_1^*}{dt} = 32\pi R_{cp}^2 n_{cp} \frac{dR_{cp}}{dt} \quad (4.26)$$

$$\frac{dS_2^*}{dt} = 4\pi n_{vp} (R_{cp} + R_{vp})^2 \left(\frac{dR_{cp}}{dt} + \frac{dR_{vp}}{dt} \right) \quad (4.27)$$

$$\frac{dS_3^*}{dt} = 2 \frac{S}{V} \frac{dR_{cp}}{dt} \quad (4.28)$$

$$\frac{dS_{123}}{dt} = \frac{dS_1^*}{dt} S_2^* S_3^* + S_1^* \frac{dS_2^*}{dt} S_3^* + S_1^* S_2^* \frac{dS_3^*}{dt} \quad (4.29)$$

$$\frac{dS_{12}}{dt} = \frac{dS_1^*}{dt} S_2^* + S_1^* \frac{dS_2^*}{dt} - \frac{dS_{123}}{dt} \quad (4.30)$$

$$\frac{dS_{13}}{dt} = \frac{dS_1^*}{dt} S_3^* + S_1^* \frac{dS_3^*}{dt} - \frac{dS_{123}}{dt} \quad (4.31)$$

$$\frac{dS_{23}}{dt} = \frac{dS_2^*}{dt} S_3^* + S_2^* \frac{dS_3^*}{dt} - \frac{dS_{123}}{dt} \quad (4.32)$$

$$\frac{dS_1}{dt} = \frac{dS_1^*}{dt} - \frac{dS_{12}}{dt} - \frac{dS_{13}}{dt} - \frac{dS_{123}}{dt} \quad (4.33)$$

$$\frac{dS_2}{dt} = \frac{dS_2^*}{dt} - \frac{dS_{12}}{dt} - \frac{dS_{23}}{dt} - \frac{dS_{123}}{dt} \quad (4.34)$$

$$\frac{dS_3}{dt} = \frac{dS_3^*}{dt} - \frac{dS_{13}}{dt} - \frac{dS_{23}}{dt} - \frac{dS_{123}}{dt} \quad (4.35)$$

where the terms $dS_{ij(k)}/dt$ in equations 4.26 to 4.35 describe the differential probability for a closed pore interacting with objects i and j (and k). Table 4.1 shows each interaction and the effect it has on the number densities of the two porosities and the concentration of fission gas in the porosity.

Considering these interactions we can derive a set of ordinary differential equations (ODEs) describing the time evolution of the number densities and the gas in the closed porosity, i.e:

$$\frac{dn_{cp}}{dt} = -n_{cp} \left(\frac{1}{2} \frac{dS_1}{dt} + \frac{dS_2}{dt} + \frac{dS_3}{dt} + \frac{dS_{12}}{dt} + \frac{dS_{13}}{dt} + \frac{dS_{23}}{dt} + \frac{dS_{123}}{dt} \right) \quad (4.36)$$

$$\frac{dn_{vp}}{dt} = n_{cp} \left(\frac{dS_3}{dt} + \frac{1}{2} \frac{dS_{13}}{dt} \right) \quad (4.37)$$

$$\frac{dc_{cp}^{fg}}{dt} = -c_{cp}^{fg} \left(\frac{dS_2}{dt} + \frac{dS_3}{dt} + \frac{dS_{12}}{dt} + \frac{dS_{13}}{dt} + \frac{dS_{23}}{dt} + \frac{dS_{123}}{dt} \right) \quad (4.38)$$

Equation (4.36) automatically produces a reduction in the closed porosity number density, a situation that is seen in the HBS at local burnups in excess of ≈ 100 MWd/kg [1]. It is important to note this since the present model does not include the creation of HBS porosity and thus can only be applied to conditions where the number density is expected to decrease, e.g. annealing conditions or at ultra-high burnups. The evolution of the fractional porosities P_{cp} and P_{vp} is

⁷Here we consider the change in the cross-sections during a time corresponding to an infinitesimal increase in the radius when the pore number densities, i.e. n_{cp} and n_{vp} , are held constant.

Table 4.1. Interactions and their effect on the variables describing the state of the porosity (closed & vented) and the gas release.

Interaction ^a	Associated cross-section	Effect on variables ^b		
		n_{cp}	n_{vp}	c_{rel}^{fg}
$(cp) \leftrightarrow (cp)$	S_1	Reduces	No effect	None
$(cp) \leftrightarrow (vp)$	S_2	Reduces	No effect	Increases
$(cp) \leftrightarrow (fs)$	S_3	Reduces	Increases	Increases
$(cp) \leftrightarrow (cp) \leftrightarrow (vp)$	S_{12}	Reduces	No effect	Increases
$(cp) \leftrightarrow (cp) \leftrightarrow (fs)$	S_{13}	Reduces	Increases	Increases
$(cp) \leftrightarrow (vp) \leftrightarrow (fs)$	S_{23}	Reduces	No effect	Increases
$(cp) \leftrightarrow (cp) \leftrightarrow (vp) \leftrightarrow (fs)$	S_{123}	Reduces	No effect	Increases

^a Here (cp) represents the closed porosity, (vp) represents the vented porosity and (fs) represents the free surface. Therefore an interaction such as coalescence of two closed pores can be represented as $(cp) \leftrightarrow (cp)$.

^b Here n_{cp} is the number density of the closed porosity, n_{vp} is the number density of the vented porosity and c_{rel}^{fg} is the concentration of released gas.

determined by the derivative of equation 4.12, i.e.:

$$\frac{dP_p}{dt} = 4\pi R_p n_p \frac{dR_p}{dt} + \frac{P_p}{n_p} \frac{dC_p}{dt} \quad (4.39)$$

Therefore, applying equation 4.39 to the closed and vented fractional porosities, we have:

$$\frac{dP_{cp}}{dt} = 4\pi R_{cp} n_{cp} \frac{dR_{cp}}{dt} + \frac{P_{cp}}{n_{cp}} \frac{dn_{cp}}{dt} \quad (4.40)$$

$$\frac{dP_{vp}}{dt} = 4\pi R_{vp} n_{vp} \frac{dR_{vp}}{dt} + \frac{P_{vp}}{n_{vp}} \frac{dn_{vp}}{dt} \quad (4.41)$$

Furthermore we can derive the quantity of released gas by considering that the rate of change of gas in the porosity is a direct reflection of the increase in released gas⁸, i.e.:

$$\frac{dc_{rel}^{fg}}{dt} = c_{cp}^{fg} \left(\frac{dS_2}{dt} + \frac{dS_3}{dt} + \frac{dS_{12}}{dt} + \frac{dS_{13}}{dt} + \frac{dS_{23}}{dt} + \frac{dS_{123}}{dt} \right) \quad (4.42)$$

Equations 4.36– 4.42 are the principal equations that describe the evolution of the system. The equations form a set of coupled ODEs with fully time dependent parameters, i.e. the parameters are dependent on the solution of the equations. To solve these equations we use the ODE solver package SLSODE [20, 21]⁹. At each time step, the new solution is used to re-calculate the

⁸It should be noted that this is only valid for the annealing case as there is no flux of gas to the porosity. In the case where there is gas production in the fuel, i.e. in-pile conditions, a modification needs to be introduced to account for this (see chapter 5 for details).

⁹Although the ODE solver package used here is treated as a “black box” there are certain numerical considerations that should be taken into account when solving an equation set such as that presented here. As soon as one deals with more than one first-order differential equation, the possibility of a stiff set of equations arises. Stiffness occurs in a problem where there are two or more very different scales of the independent variable on which the dependent variables are changing. In general, when solving stiff equations with a non-stiff solver we are required to follow the variation in the solution on the shortest length scale to maintain stability of the solution. An alternative approach is to use implicit differencing and linearization e.g. *the semi-implicit Euler method*. Where this is not possible higher order methods such as *predictor-corrector methods* can be employed. When

differential macro cross-sections, the pore radii, the system porosity and concentrations, and finally the fission gas release. In addition, the equations 4.7 to 4.10 have to be solved to calculate the defect concentrations. This is done by finding the root (see appendix D) for equation 4.10 and then solving equations 4.7 to 4.9 in turn.

Table 4.2 gives the initial conditions for the model based upon available data for the HBS. In assigning values to the number density and porosity of the vented pores we have assumed that during irradiation the in-pile release due to pore venting was limited. Therefore, we have used small but finite values. The surface-to-volume ratio is an important parameter affecting the gas release behaviour. We can assign limiting values to the surface-to-volume ratio, specifically the fabrication surface-to-volume ratio of a fuel pellet (low S/V) [22] and open grain boundary porosity (high S/V) [23]. The OECD Halden Reactor Project (HRP) has performed measurements of the surface-to-volume ratio for a high burnup disk irradiation using the short lived xenon and krypton isotopes [24]. The measurements clearly indicate that the surface-to-volume ratio remains low ($\sim 10^4 \text{ m}^{-1}$) throughout the irradiation. Consequently, we have set the surface-to-volume ratio to this value. Obviously the surface-to-volume ratio may vary throughout a particular annealing experiment, in particular due to the venting of the porosity. By taking into account the vented pore population this contribution to the time dependence of the surface-to-volume ratio is indirectly accounted for.

Table 4.2. Initial conditions for the model

Variable	Symbol	Value	Reference
Concentration of gas in the closed porosity	c_{cp}^{fg}	1.3 wt% at 98 MWd/kgU	[25]
Porosity of the closed pores	P_{cp}	12%	[1]
Radius of a closed pore	R_{cp}	$0.6 \mu\text{m}$	^a
Concentration of released gas	c_{rel}^{fg}	0.0 m^{-3}	^a
Surface-to-volume ratio of open surface	S/V	10^4 m^{-1}	[22, 23, 24]

^a this work

using such methods one should be careful in specifying the desired accuracy of the solution. In the particular case of equations 4.36–4.42 we have set the relative tolerance to 10^{-4} , i.e. the solution at each time step should have an accuracy of 10^{-4} multiplied by the solution vector. One should be careful not to set the relative tolerance too small as this will considerably increase the computational cost and can cause a failure in convergence. This occurs because the desired accuracy informs the solver by how much it should reduce the step size to achieve this accuracy. If the accuracy is set too small then the step size will be reduced to such an extent that either the calculation becomes prohibitively expensive or the step size is reduced beyond the lower limit of the floating point accuracy, i.e. numerical underflow occurs. Another point is the specification of the Jacobian. Here we have employed a numerical calculation of the Jacobian rather than analytically specifying it. In cases where the equation set is simpler and an analytical Jacobian can be written, it is advisable to specify it using the analytical form.

4.3 Results

4.3.1 Model behaviour under static temperature conditions

As an initial assessment of the impact of the principle parameters on the model behaviour, a sensitivity study has been performed with respect to the annealing temperature and the surface-to-volume ratio of the technological open surface. In both cases we consider a steady-state temperature and keep the other variables and parameters fixed to the initial conditions given in table 4.2.

Figures 4.3 and 4.4(a) show the variation of the porosity and fractional release (i.e. the fraction of xenon released with respect to the initial gas inventory) with temperature, as a function of time for a range of temperatures from 1300 to 1800 K. There are two initial observations to make

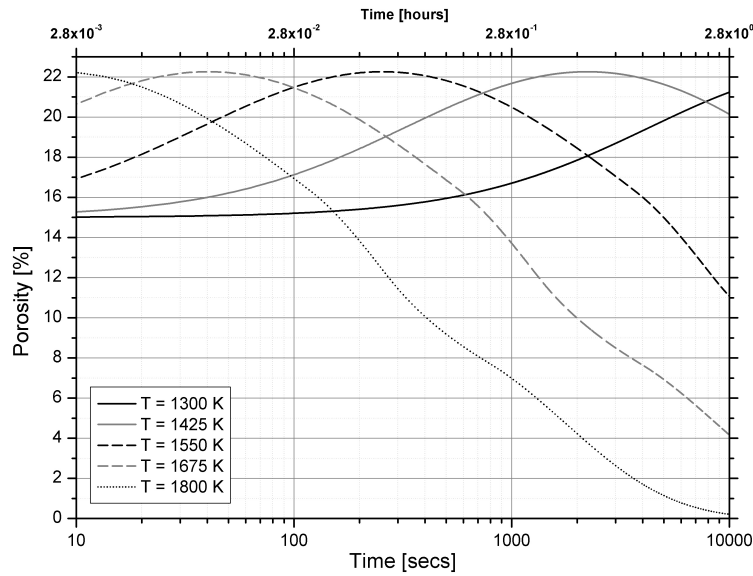
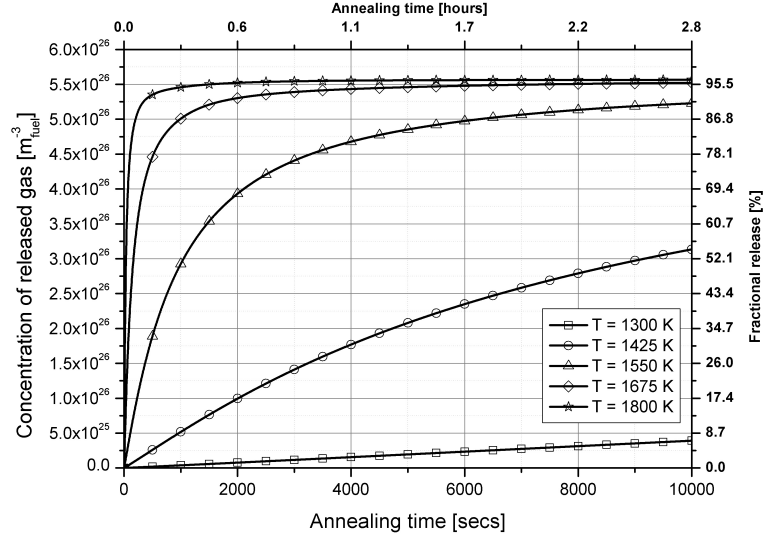
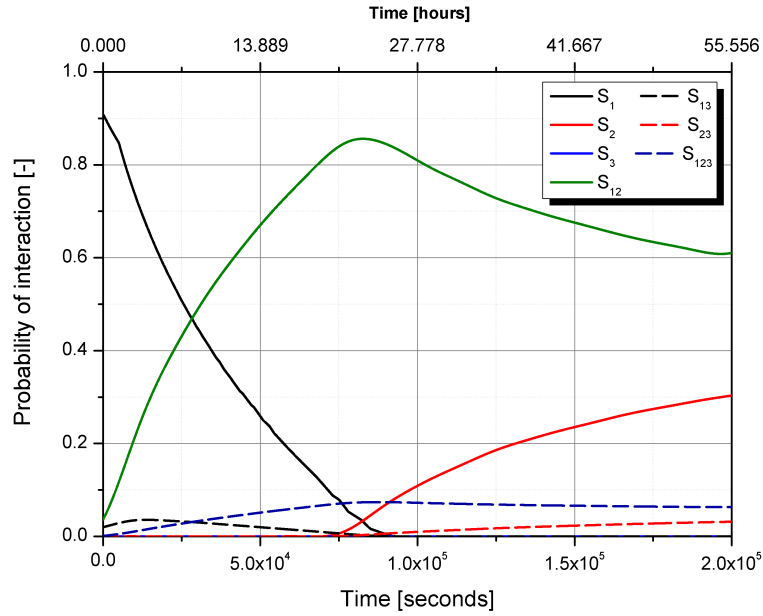


Figure 4.3. Variation of the porosity as a function of time for a range of temperatures from 1300–1800 K.

about figure 4.3: (1) the annealing time required to reach the maximum porosity is temperature dependent, (2) the maximum reachable porosity is temperature independent. The fact that the time to maximum porosity is temperature dependent is an important demonstration that the rate of pore growth and therefore of pore interactions is dependent upon the defect concentrations and the diffusion rate to the porosity. Figure 4.4(a) also illustrates this, in that the rate of gas release is temperature dependent. This of course should be expected as the rate of pore growth is determined by equation 4.11. Exactly the same behaviour can be seen when varying the stoichiometry as this also affects the defect concentrations (figures 1–3 in [26]) and consequently the pore growth rate (see equations 4.5 and 4.11). In addition, figure 4.4(a) illustrates that the gas release occurs continuously throughout the growth of the porosity instead of being controlled by a threshold porosity [11, 13, 27]. If we examine the fractional gas release at the point of maximum porosity we find that the value is ~ 20 – 23 % for the temperatures examined, indicating some level of invariance in the gas release once the maximum porosity has been released. The invariance with respect to the pore growth rate is also important as it indicates that the maximum



(a) Fractional release for range of temperatures from 1300–1800 K.



(b) Interaction probabilities at a static temperature of 1420 K.

Figure 4.4. Variation of the fractional release and interaction probabilities as a function of time.

porosity is only dependent on geometrical parameters. For the initial conditions of table 4.2 this maximum porosity is $\sim 22\%$. Figure 4.4(b) shows the changes in the interaction probabilities for annealing at a static temperature of 1420 K. It is seen that as annealing progresses interactions leading to release start to dominate over pore coalescence, with coalescence ultimately becoming less important than interactions with the vented pore population and the free surface.

Figure 4.5 shows the evolution of the porosity for a range of surface-to-volume ratios at a static temperature of 1400 K. The limits on this range correspond to those of the fabrication surface-to-volume ratio (low S/V) [22] and an open grain boundary porosity (high S/V) [23]. Figure 4.5 shows that the maximum value of the porosity increases as the surface-to-volume ratio decreases. Furthermore, the position of this maximum is also dependent on the value of the surface-to-volume ratio. By increasing the surface-to-volume ratio the point at which the

dominant interactions shift from coalescence to release is anticipated. This should be expected as the available surface area increases (or conversely the fuel volume bounded by the surface decreases), which makes interactions leading to release more probable.

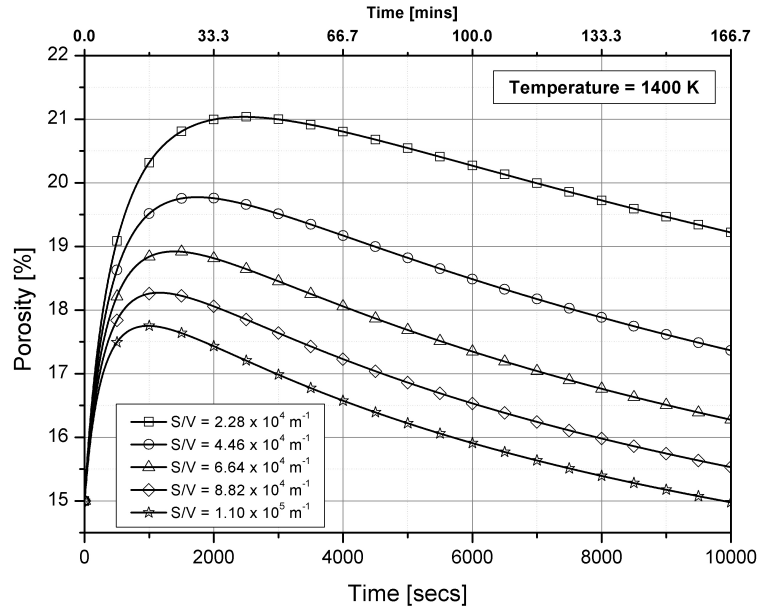


Figure 4.5. Evolution of the porosity for a range of surface-to-volume ratios at a static temperature of 1400 K.

4.3.2 Application to an annealing test

Several good examples of high burnup annealing experiments exist in open literature. Of particular note is the experiment reported by Hiernaut and Ronchi [28], in which a high-burnup fuel sample ($\approx 95 \text{ MWd/kgU}$ local burnup) was subjected to a rising temperature history (see figure 4.6) until it was completely vaporised.

Using a fitting model [29, 30] the authors interpreted that the release was due to three distinct processes, viz.: (1) grain boundary diffusion, (2) bulk volume diffusion and (3) vaporisation. Although (1) and (3) can be understood in terms of the already existing matrix and grain boundary gas, (2) is more problematic to interpret as it is widely accepted that most of the generated HBS fission gas is retained within the porosity. Considering that the original analysis suggested that 10 % of the gas inventory was contained within the grain boundary, then, with the measured $\approx 0.2 \text{ wt\%}$ matrix gas concentration [31, 32, 33], this analysis still leaves $\approx 70 \%$ of the fission gas within the HBS porosity. Furthermore, although the original analysis suggested that 10 % of the gas initially resided on the grain boundary, we have shown in chapter 3 that the grain boundary inventory could be significantly smaller while still maintaining the observed $\approx 0.2 \text{ wt\%}$ matrix gas concentration. Consequently, we do not currently consider the grain boundary in specifying the initial conditions for the gas inventory. This does not however detract from the fact that most of the gas is expected to reside within the porosity and that the release mechanism must take this into account.

In particular, there are two mechanisms that could be responsible for the release of the HBS

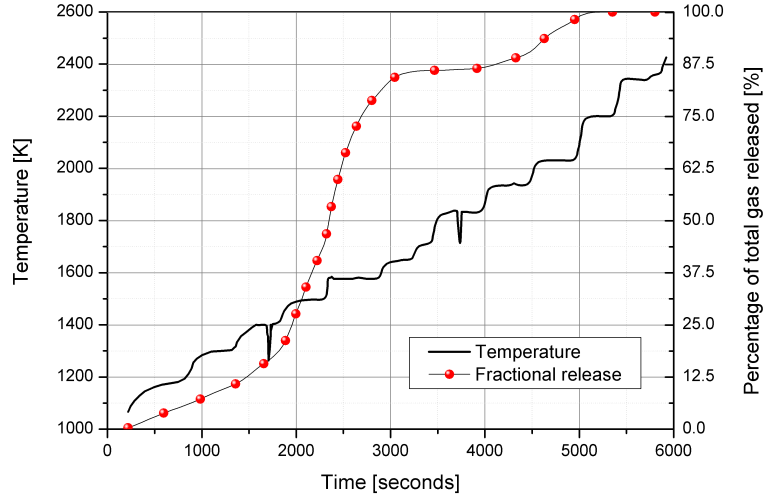


Figure 4.6. Temperature and gas release histories in the Hiernaut and Ronchi experiment [28]

porosity gas for this experiment: porosity growth and/or micro-cracking. Une *et al.* [34] recently performed a series of annealing experiments on high burnup UO_2 fuel to examine the fission gas release behaviour as a function of the heating rate. They found that, between heating rates of 0.4 and 90 K s^{-1} , there is a transition from pore growth release to micro-cracking assisted release. Figure 4.7 shows the derivative with respect to time of the temperature history of the Hiernaut and Ronchi [28] experiment. We can see that the heating rate increases to no more than 5 K s^{-1} . More recently Pontillon *et al.* [35] have reported that micro-cracking was observed in a 70 GWd/t UO_2 sample when subjected to simulated LOCA conditions. Specifically they found that a significant release of fission gas occurred at temperatures above 1000°C and micro-cracking was in fact observed. However it should be noted that while micro-cracking was observed there were also a significant number of pores remaining that were untouched by the generated cracks. While micro-cracking for this particular sample cannot be ruled out for the present experiment, we can consider that the second-stage gas release mechanism will have a contribution from the growth, coalescence and inter-linkage of the pores. As a result this experiment is an ideal candidate for testing the new porosity growth model.

In addition to the temperature history (figure 4.6) there are additional initial values that must be decided upon. Kinoshita *et al.* [25] reported that, for this particular experiment, the total amount of ^{85}Kr released from the sample was $79 \mu\text{g/gU}$. Assuming that the total fractional release of xenon (with respect to the total created) is the same as for ^{85}Kr , we can calculate the quantity of xenon in the sample from the amount of xenon created. This gives a quantity of 14.9 mg/gU , or equivalently 1.5 wt\% . We can then derive the expected xenon content in the porosity by taking into account that $\approx 0.2 \text{ wt\%}$ of this is retained within the matrix of the completely transformed fuel structure. Parameters such as porosity and pore radius are well characterised [1, 2] and are therefore fixed at the beginning of the calculation. However, the uranium vacancy diffusion coefficient is not so well determined in literature [36], with different authors quoting different correlations depending on the experiment. We can however set bounds

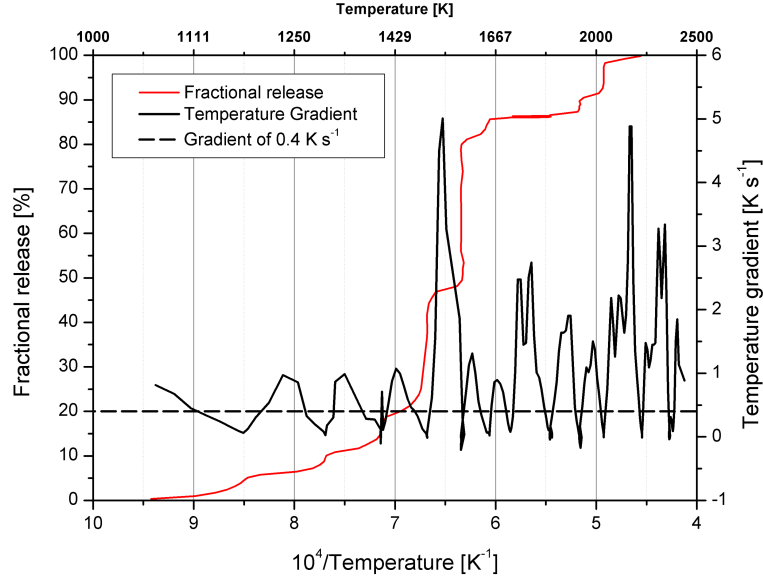


Figure 4.7. Rate of change of the temperature and the fractional release in the Hiernaut and Ronchi experiment [28]

on the diffusion enthalpy and then compare with the results from this experiment. With the exception of the diffusion coefficient, all the other parameters are set according to the initial conditions in table 4.2.

Kleykamp [37] examined the variation of the stoichiometry of UO_2 during irradiation and found that the pellet averaged deviation increases by ~ 0.001 per 10 MWd/kgU. For our particular case this gives a deviation of $x = 0.0098$. However it was also pointed out that because of oxygen diffusion into the cladding, the stoichiometric deviation at the pellet periphery is lower than the pellet average. We should therefore expect that such deviation will still be of the order of 10^{-3} with a deviation of no more than $x = 0.0098$. Thus, given the uncertainty in this parameter, several calculations have been performed to examine the model behaviour for a range of stoichiometric deviations with a fixed surface-to-volume ratio of 10^4 m^{-1} . Figure 4.8 shows the fractional release for a range of stoichiometry deviations from $x = 0.001$ to 0.005.

It is clear that the release profile is very sensitive to the absolute stoichiometry deviation, which is because the concentration of thermal equilibrium defects, and in particular the uranium vacancies, is sensitive to stoichiometry. In spite of this, we see that within this range we “straddle” the experimental results indicating that the considered range of stoichiometric deviations is reasonable. From the observed variation we find that a temperature averaged stoichiometry deviation of $\approx 3.5 \times 10^{-3}$ fits the experimental profile reasonably well. However, care should be taken in interpreting this fit as being an indication of hyper-stoichiometry of the HBS. For example the effect of the cladding can reduce the stoichiometry enough to push it to be hypo-stoichiometric. Walker *et al.* [38] have calculated the radial variation in the stoichiometry for a high burnup (100 MWd/kgHM) fuel pellet and concluded that the periphery of the pellet was slightly hypo-stoichiometric. It should be noted that the uncertainties in the derived O/M ratio reported by Walker *et al.* are within the range used in these calculations. In spite of this one should not rely upon this fit as a prediction of the stoichiometry deviation.

Figure 4.9 shows the amount of gas released as a function of the surface-to-volume ratio with a

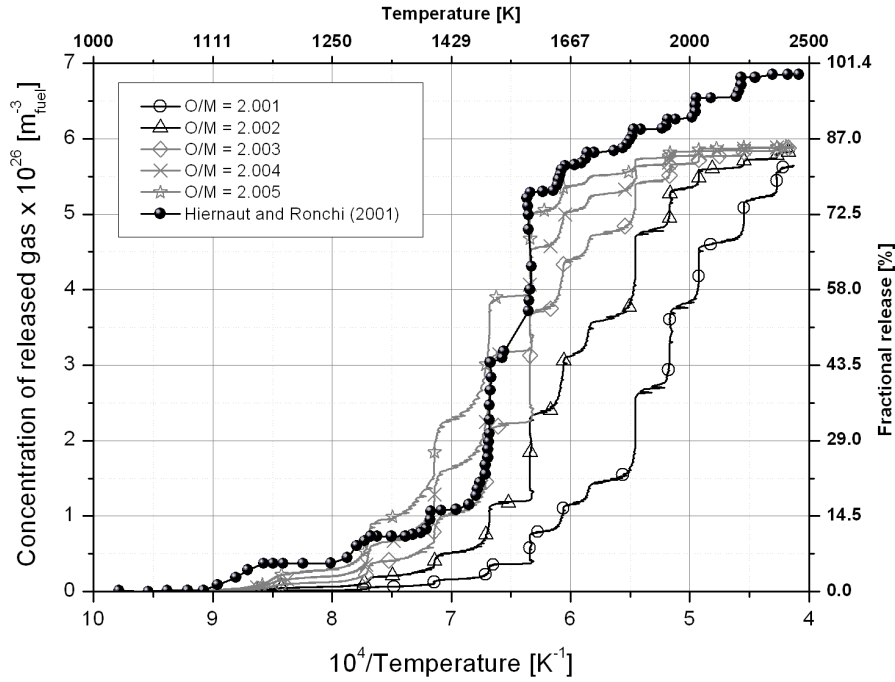


Figure 4.8. Calculated fractional release using the temperature history of Hiernaut and Ronchi [28] for a range of stoichiometry deviations from $x = 0.001$ to $x = 0.005$.

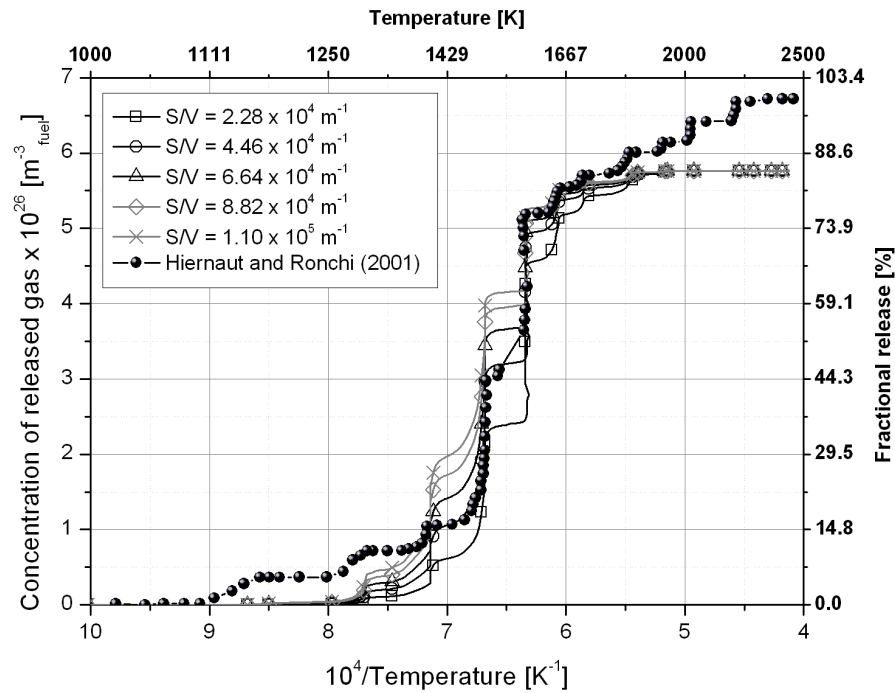


Figure 4.9. Calculated fractional release using the temperature history of Hiernaut and Ronchi [28] for a range of values of the surface-to-volume ratio.

stoichiometry deviation fixed to the best fit value of $\sim 3.5 \times 10^{-3}$ commented on earlier.

The surface-to-volume ratio is a controlling parameter for the maximum reachable porosity. It was also pointed out in section 4.3.1 that the quantity of gas released prior to the maximum porosity is significant ($\sim 20\%$). However, based upon the results of the sensitivity analysis, this

would still leave a large amount of gas remaining in the porosity after the maximum porosity has been reached. Consequently, the influence of the surface-to-volume ratio on the point (in terms of time and temperature) at which the maximum porosity is achieved is important. This effect can be seen in figure 4.9, i.e. increasing the surface-to-volume ratio makes the onset of significant release happen at lower temperatures. It is interesting to note that the best fit for the data is found at surface-to-volume ratios between $\sim 2 \times 10^4 \text{ m}^{-1}$ and $\sim 10^5 \text{ m}^{-1}$. This is the typical range of values seen in low to medium burnup fuel before the grain boundary bubbles inter-link and form release pathways [22, 23].

Given the uncertainty surrounding the diffusion coefficient for vacancies within the normal fuel structure, let alone the high-burnup structure, we have calculated the release for a range of diffusion enthalpies from 2 eV to 3.3 eV. We have fixed the diffusion coefficient to a value of $9 \times 10^{-9} \text{ m}^2 \text{ s}^{-1}$ at a temperature of 1450 K, which is the approximate starting point of significant release from the fuel sample. The pre-exponential within the Arrhenius diffusion coefficient relationship (see section 2.1.3) can then be determined based on the enthalpy and this value. Upon doing this, we find that an enthalpy of $\sim 2.9 \text{ eV}$ shows the best agreement between the experimental and calculation results, in the temperature range that Hiernaut and Ronchi determined for yielding release by the volume diffusion of fission gas within the fuel matrix [28]. This is approximately the same as that determined in the experiment. This provides an alternative interpretation of the results, viz. that the release mechanism is due to porosity growth during annealing. In this case, the measured enthalpy would correspond to the diffusion enthalpy for vacancies instead of the xenon diffusion enthalpy.

The model presented here only considers the effect of porosity growth on gas release and as such cannot directly address the mode of release of the remaining matrix gas. Instead we have considered several different locations of the 0.2 wt% matrix xenon in the fuel microstructure: (1) the gas originally in the matrix is frozen and does not move, (2) the matrix gas releases to the open volume very early and (3) the matrix gas is trapped within the fuel porosity prior to the onset of release from the porosity. Given the uncertainty in the location and dynamics of the matrix fission gas, these different conditions provide bounding estimates for the gas release, and the experimental data should lie within these boundaries. Figure 4.10 shows the calculated release curve for these different approximations. It can be seen from the figure that, at the higher temperatures, where vaporisation/sublimation is expected to dominate, the experimental data is entirely bounded by the different approximations. Specifically, the release of gas via the porosity or via an unspecified low temperature mechanism over-predicts the gas release at high temperatures, while considering the gas as frozen under-predicts it. This indicates that the release of the matrix gas does not happen until sublimation/vaporisation occurs. This is in agreement with the post irradiation examination (PIE) performed by Hiernaut and Ronchi [28] after the fuel was annealed up to temperatures of 1300 K. The PIE showed that the intra-granular bubbles grew markedly during the course of annealing. A simple calculation, based on the total intragranular gas inventory (matrix and bubbles), the bubble number density [1] and the Van der Waals volume of a xenon atom, puts the quantity of gas in this phase at $\sim 0.203 \text{ wt\%}$. This corresponds to an increase in the bubble radius from ≈ 1.5 to $\approx 9.5 \text{ nm}$. Consequently, it is reasonable to expect that the matrix gas has been retained within the intragranular bubbles and

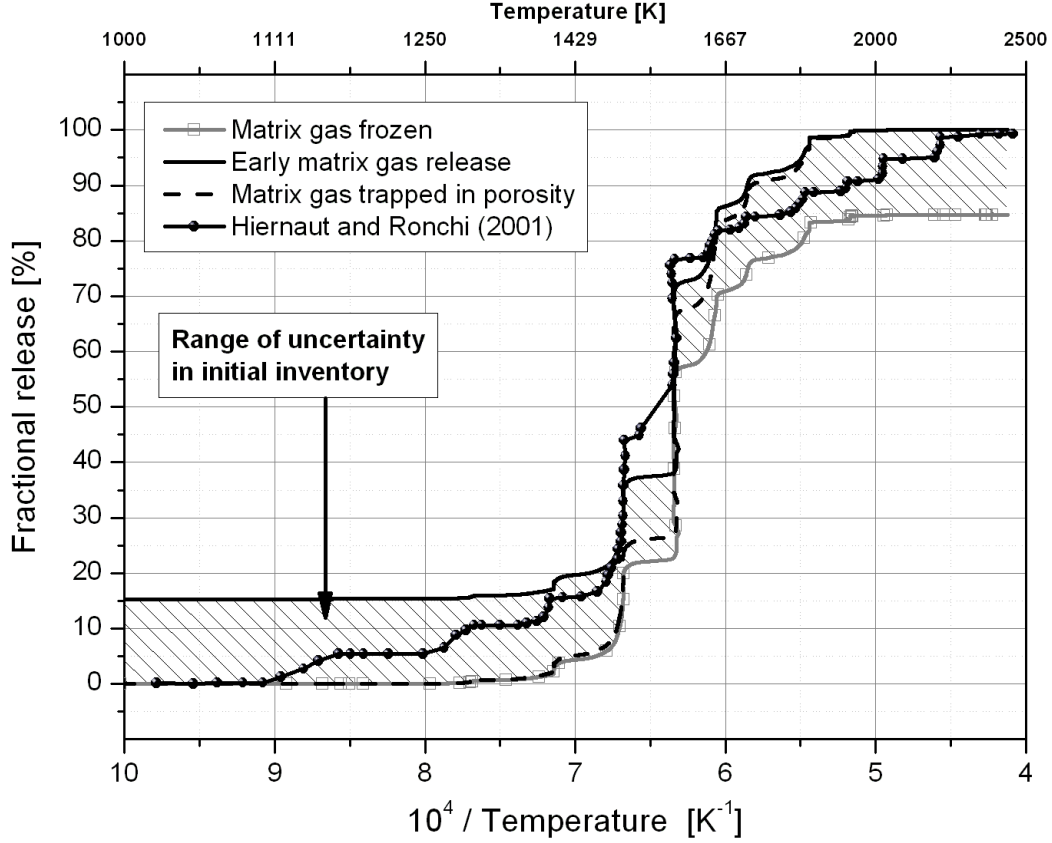


Figure 4.10. Calculated fractional release using the temperature history of Hiernaut and Ronchi [28] for several assumed locations of the matrix xenon gas.

is primarily released during the high temperature stages of annealing.

4.4 Discussion

Although the current model has only been applied to out-of-pile conditions, some implications can be drawn about fuel behaviour during in-pile irradiations. In particular, the variation of “state variables” such as the pore number density can be compared, since these specify the state of the porosity. Figure 4.11 shows the variation of the fractional pore number density¹⁰ and of the gas released from the porosity, for the Hiernaut and Ronchi experimental temperature history. The decrease in the calculated number density seen in figure 4.11 is consistent with results from the PIE of HBS samples with a local burnup in excess of ~ 100 MWd/kgU [1] (see figure 2.15). Figure 4.11 also clearly illustrates the correlation between the reduction in the pore number density and the release of gas from the HBS porosity. Our model predicts that we should expect some gas release in-pile if compound interactions are considered because the drop in the number density is partly due to pores venting to the free volume (cf. equations (4.38),(4.42)).

Figure 4.12 shows the variation of the porosity and fission gas release as a function of the number density for a range of constant temperatures (1300 to 1500 K), as also for the Hiernaut

¹⁰Here we define the fractional number density with respect to the initial number density, e.g. for the annealing case the fractional porosity at time t during annealing is $C_{cp}(t)/C_{cp}(t=0)$.

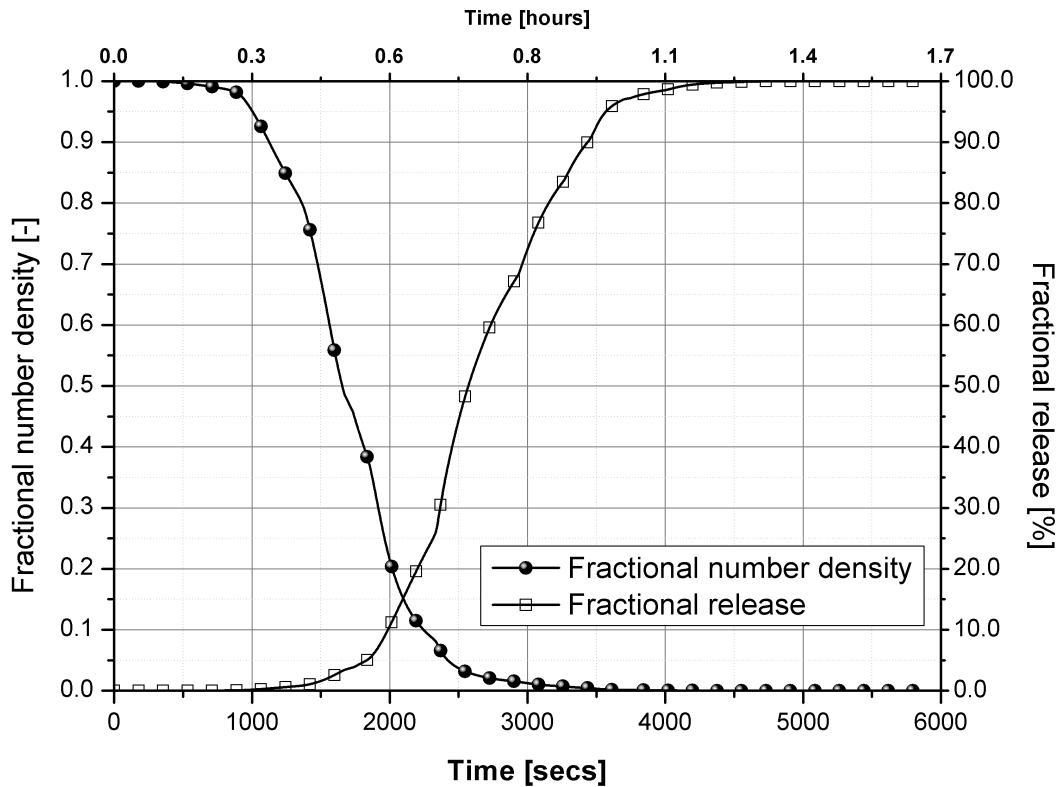


Figure 4.11. Comparison between the reduction in the number density and the increasing gas release from the porosity.

and Ronchi temperature history. The first point to emphasise is that the gas release and porosity behaviour is independent of the temperature and hence the rate of pore growth when considered with respect to the number density. Consequently the quantity of gas released can be related directly to the state of the porosity within our model. More importantly the gas release is a continuous process in contrast to other studies [11, 13, 27], which suggest that the release of gas from the HBS should only occur after a threshold porosity has been reached. We also see that the porosity grows until it reaches a maximum after which it decreases and that the point at which the maximum porosity is achieved occurs when the number density has dropped to 10 % of its starting value. At this point ~ 20 % of the gas within the porosity has been released, regardless of the growth rate. PIE results up to local burnups of ~ 250 MWd/kgU [1] indicate that the number density has not decreased to 10 % of the value at 100 MWd/kgU, suggesting that the maximum porosity has yet to occur. This is important as it implies that, while there should be some release (less than ~ 20 % of the gas in the porosity) due to pore growth and surface interactions, the majority of the gas is still retained. However, it should be noted that, because these observations are based on an out-of-pile experiment, the comparison can only provide a conservative estimate of the actual fission gas release. No account is taken of the fission gas accumulation in the HBS porosity, which will accelerate the porosity growth. Additionally, we might also expect parameters such as the stoichiometry and surface-to-volume ratio to vary through irradiation, which will also affect the time-scale of the release process. Nevertheless, the qualitative behaviour should remain the same, viz.:

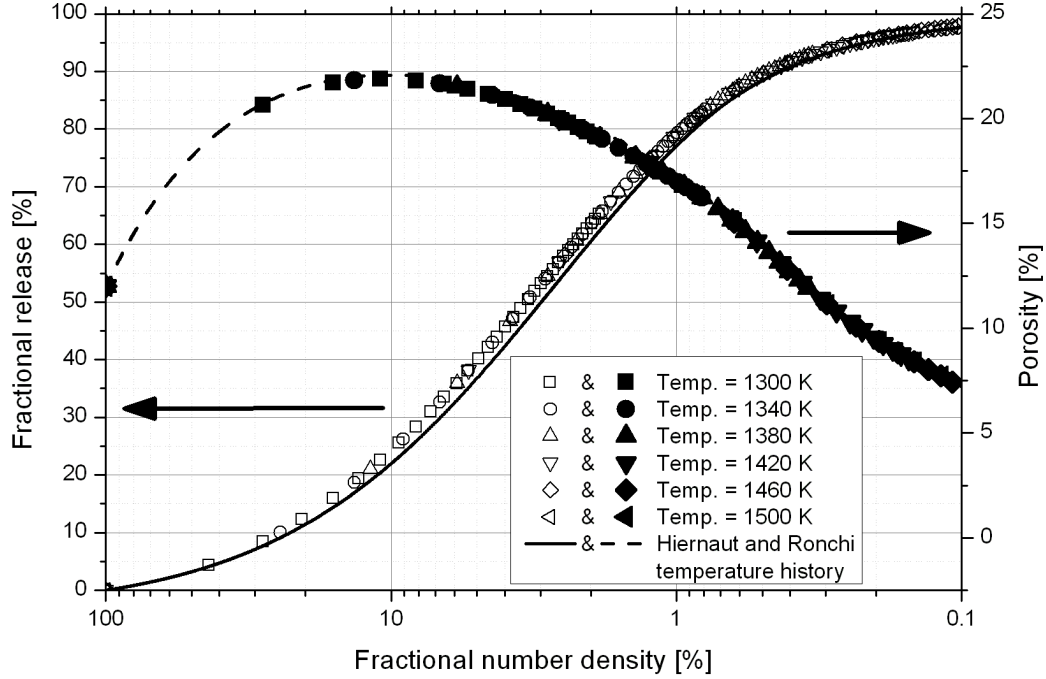


Figure 4.12. Variation of porosity and gas release as a function of number density for static temperatures and the temperature history from Hiernaut and Ronchi [28].

1. An increasing porosity up to a maximum (geometrically dependent) value, followed by a slower decrease.
2. A continuously decreasing number density.
3. A continuous fission gas release that starts once the number density starts to decrease.

4.5 Conclusions

A temperature dependent gas release model has been developed to examine the release due to porosity growth in the HBS under annealing conditions. A stable solution was achieved for LWR UO_2 fuel with typical stereological parameters for the HBS.

The model was applied to a high-burnup fuel annealing experiment to assess its predictions in comparison with experimental measurements. We find reasonable agreement with the experimental release measurements in the temperature range where the release mechanism was considered to be due to volume diffusion of the gaseous fission products. In contrast to the original analysis, our model interprets the release mechanism as being due to pore growth, coalescence and, ultimately, venting.

We find that the model predicts several qualitative features of the porosity evolution that are independent of the model parameters used, viz.:

- The porosity increases until it reaches a maximum value, after which it decreases at a slower rate.

- The number density continuously decreases.
- The gas release from the porosity is a continuous process and begins as soon as the number density starts to decrease.

A comparison of out-of-pile and in-pile release (with respect to porosity) indicates that, for burnups examined to date, the maximum porosity has yet to be reached. Consequently, most of the fission gas is expected to be retained within the HBS porosity. However, while this comparison is certainly conservative, the invariance in the features of the porosity evolution suggests that the main difference in-pile will simply be a time-scale change.

Bibliography

- [1] J. Spino, A. D. Stalios, H. Santa Cruz, and D. Baron. Stereological evolution of the rim structure in PWR-fuels at prolonged irradiation: Dependencies with burn-up and temperature. *J. Nucl. Mater.*, 354:66–84, 2006.
- [2] J. Spino, K. Vennix, and M. Coquerelle. Detailed characterisation of the rim microstructure in PWR fuels in the burn-up range 40-67 GWd/tM. *J. Nucl. Mater.*, 231:179–190, 1996.
- [3] C. Ronchi, M. Sheindlin, D. Staicu, and M. Kinoshita. Effect of burn-up on the thermal conductivity of uranium dioxide up to 100.000 MWd t⁻¹. *J. Nucl. Mater.*, 327:58–76, 2004.
- [4] B-H. Lee, Y-H. Koo, and D-S. Sohn. Rim characteristics and their effects on the thermal conductivity in high burnup UO₂ fuel. *J. Nucl. Sci. Technol.*, 38(1):45–52, 2001.
- [5] K. Lassman, C. T. Walker, J. van de Laar, and F. Lindström. Modelling the high burnup UO₂ structure in LWR fuel. *J. Nucl. Mater.*, 226:1–8, 1995.
- [6] J. Noirot, L. Desgranges, and P. Marimbeau. Contribution of the rim to the overall fission gas release; What do isotopic analyses reveal? In *Proceedings of the IAEA/NEA/CEA International Seminar on Fission Gas behaviour in Water Reactor Fuels*, September 2000.
- [7] S. Bremier and C. T. Walker. Radiation-enhanced diffusion and fission gas release from recrystallised grains in high burn-up UO₂ nuclear fuel. *Radiat. Eff. Defect. S.*, 157:311–322, 2002.
- [8] P. Losonen. Modelling intragranular fission gas release in irradiation sintered LWR UO₂ fuel. *J. Nucl. Mater.*, 304:29–49, 2002.
- [9] F. Schmitz and J. Papin. High burn-up effects on fuel behaviour under accident conditions: The tests CABRI REP-Na. *J. Nucl. Mater.*, 270:55–64, 1999.
- [10] T. Fuketa, H. Sasajima, Y. Mori, and K. Ishijima. Fuel failure and fission gas release in high burnup PWR fuels under RIA conditions. *J. Nucl. Mater.*, 248:249–256, 1997.
- [11] J. Spino, D. Papaioannou, and J.-P. Glatz. Comments on the threshold porosity for fission gas release in high burn-up fuels. *J. Nucl. Mater.*, 328:67–70, 2004.
- [12] Y-H. Koo, B-H. Lee, J-S. Cheon, and D-S. Sohn. Pore pressure and swelling in the rim region of LWR high burnup UO₂ fuel. *J. Nucl. Mater.*, 295:213–220, 2001.
- [13] Y-H. Koo, J-Y. Oh, B-H. Lee, and D-S. Sohn. Three-dimensional simulation of threshold porosity for fission gas release in the rim region of LWR UO₂ fuel. *J. Nucl. Mater.*, 321(2-3):249–255, 2003.
- [14] A. Romano, M. I. Horvath, and R. Restani. Evolution of porosity in the high-burnup fuel structure. *J. Nucl. Mater.*, 361(1):62–68, March 2007.
- [15] J. M. Griesmeyer, N. M. Ghoniem, and D. Okrent. A dynamic intragranular fission gas behavior model. *Nucl. Eng. Des.*, 55:69–95, 1979.

- [16] R. J. White. The development of grain-face porosity in irradiated oxide fuel. *J. Nucl. Mater.*, 325:61–77, 2004.
- [17] S. Chandrasekhar. Stochastic problems in physics and astronomy. *Rev. Mod. Phys.*, 15(1):0001–0089, 1943.
- [18] S. Torquato. Nearest-neighbour statistics for packings of hard spheres and disks. *Phys. Rev. E.*, 51(4):3170–3182, apr 1995.
- [19] G. Khvostov, A. Medvedev, and S. Bogatyr. The dynamic model of grain boundary processes in high burn-up LWR fuel and it's application in analysis by the START-3 code. In *Proceedings of the International Conference on WWER Fuel Performance, Modelling and Experimental Support*, Albena-Varna, Bulgaria, September 2003.
- [20] K. Radhakrishnan and A. C. Hindmarsh. Description and Use of LSODE, the Livermore Solver for Ordinary Differential Equations. Technical Report UCRL-ID-113855, Lawrence Livermore National Laboratory, December 1993.
- [21] A. C. Hindmarsh. *IMACS Transactions on Scientific Computation*, volume 1, pages 55–64. Elsevier, North-Holland, Amsterdam, 1983.
- [22] W. Dörr, H. Assmann, G. Maier, and J. Steven. Bestimmung der dichte, offenen porosität, porengrößenverteilung und spezifischen oberfläche von UO_2 -tabletten. *J. Nucl. Mater.*, 81:135, 1979.
- [23] J. A. Turnbull, C. A. Friskney, J. R. Findlay, F. A. Johnson, and A. J. Walter. The diffusion coefficients of gaseous and volatile species during the irradiation of uranium dioxide. *J. Nucl. Mater.*, 107:168–184, 1982.
- [24] T. Tverberg, M. Amaya, and J. Wright. The high burn-up disk irradiation test, IFA-655: Final report on the in-pile performance. In *Proceedings of the 2007 Enlarged Halden Programme Group Meeting*, mar 2007.
- [25] M. Kinoshita, T. Sonoda, S. Kitajima, A. Sasahara, T. Kameyama, T. Matasumura, E. Kolstad, V. V. Rondinella, C. Ronchi, J. P. Hiernaut, T. Wiss, F. Kinnart, J. Etjon, D. Papaioannou, and H. J. Matzke. High burnup rim project: (III) Properties of Rim-structured fuel. In *Proceedings of the 2004 International Meeting on LWR Fuel Performance*, Orlando, Florida, 2004.
- [26] J. M. Griesmeyer and N. M. Ghoniem. The response of fission gas bubbles to the dynamic behavior of point defects. *J. Nucl. Mater.*, 80:88–101, 1979.
- [27] L. C. Bernard and E. Bonnaud. Finite volume method for fission gas release modeling. *J. Nucl. Mater.*, 244:75–84, 1997.
- [28] J. P. Hiernaut and C. Ronchi. Fission gas release and volume diffusion enthalpy in UO_2 irradiated at low and high burnup. *J. Nucl. Mater.*, 294:39–44, 2001.

- [29] C. Syros, J. Sakellaridis, and C. Ronchi. Analytical solution of the radioactive volatile fission product release equation in the presence of precipitation and re-solution. *J. Nucl. Mater.*, 168:65–69, 1989.
- [30] F. Capone, J. P. Hiernaut, W. Martellenghi, and C. Ronchi. Mass spectrometric measurements of fission product effusion from irradiated light water reactor fuel. *Nucl. Sci. Eng.*, 124:436–454, 1996.
- [31] R. Manzel and C. T. Walker. EPMA and SEM of fuel samples from PWR rods with an average burn-up of around 100 MWd/kgHM. *J. Nucl. Mater.*, 301:170–182, 2002.
- [32] C. T. Walker. Assessment of radial extent and completion of recrystallisation in high burn-up UO_2 nuclear fuel by EPMA. *J. Nucl. Mater.*, 275:56–62, 1999.
- [33] J. Spino, D. Baron, M. Coquerelle, and A. D. Stalios. High burn-up rim structure: evidences that xenon-depletion, pore formation and grain subdivision start at different local burn-ups. *J. Nucl. Mater.*, 256:189–196, 1998.
- [34] K. Une, S. Kashibe, and A. Takagi. Fission gas release from high burnup UO_2 fuels under rapid heating conditions. *J. Nucl. Sci. Technol.*, 43(9):1161–1171, 2006.
- [35] Y. Pontillon, M.P. Ferroud-Plattet, D. Parrat, S. Ravel, G. Ducros, C. Struzik, I. Aubrun, G. Eminent, J. Lamontagne, J. Noirot, and A. Harrer. Experimental and theoretical investigation of fission gas release from UO_2 up to 70 GWd/t under simulated LOCA type conditions: The GASPARD program. In *Proceedings of the 2004 International Meeting on LWR Fuel Performance*, 2004.
- [36] H. J. Matzke. Atomic transport properties in UO_2 and mixed oxides $(\text{U,Pu})\text{O}_2$. *J. Chem. Soc. Farad. T. 2.*, 83:1121–1142, 1987.
- [37] H. Kleykamp. The chemical state of LWR high-power rods under irradiation. *J. Nucl. Mater.*, 84:109–117, 1979.
- [38] C. T. Walker, V. V. Rondinella, D. Papaioannou, S. Van. Winkel, W. Goll, and R. Manzel. On the oxidation state of UO_2 nuclear fuel at a burn-up of around 100 MWd/kgHM. *J. Nucl. Mater.*, 345:192–205, 2005.

Chapter 5

Porosity growth and fission gas release at high burnup under in-pile conditions

Physicists like to think that all you have to do is say, these are the conditions, now what happens next?

- R. P. Feynman

5.1 Introduction

In chapter 4 we developed a model to describe the porosity evolution and gas release within the high burnup structure (HBS) under annealing conditions. Although annealing conditions provide a number of advantages for investigating the HBS porosity, the calculation of the evolution during irradiation is of significant interest. We concluded from the calculations presented in the previous chapter that we would not expect more than 20 % of the local porosity inventory to be released for burnups examined so far. However, this analogy between the annealing calculations and in-pile data only provides a qualitative comparison at best. In reality the direct calculation of the in-pile behaviour is desirable both to evaluate the qualitative comparison made in chapter 4 and to directly calculate the contribution of the pellet periphery to the integral fission gas release.

As was pointed out in the previous chapter, the annealing model of porosity growth and compound interactions is generally applicable to both out-of-pile and in-pile conditions. While the equations governing the porosity growth are broadly the same, there are slight differences between the two cases. Firstly the presence of irradiation induced defects has to be accounted for, and in particular their evolution with a given power history has to be calculated. This evolution differs from the thermal equilibrium defects presented in chapter 4 in that the defect population can no longer be considered at equilibrium and so must be calculated by taking into account the time dependent processes affecting the defect concentration. In addition parameters such as the defect diffusion coefficients have to be adjusted to include the effect of irradiation. Finally, the accumulation of fission gas in the porosity during irradiation has also to be taken into account.

In this chapter we extend the model developed in chapter 4 to in-pile conditions. In contrast

to the model developed in chapter 4 the in-pile model takes into account the effect of irradiation induced defects to calculate the growth of the porosity under a time dependent power and temperature history. This chapter is organised as follows. The next section presents the theoretical development of the extension to in-pile conditions, starting from the model developed in chapter 4 and introducing extra terms specific to in-pile conditions. In section 5.3 we examine the local porosity and fission gas release behaviour under idealised steady state conditions and a power history of a particular high burnup fuel rod from a Swiss nuclear power plant (NPP). In section 5.4 we describe the development and implementation into the fuel performance code TRANSURANUS of two correlations that describe the evolution of the HBS and the gas release from the HBS porosity. Finally in section 5.5 we calculate the integral behaviour of the high burnup fuel rod from a Swiss NPP that was modelled in section 5.3 and evaluate the results in comparison with post irradiation examination (PIE) observations.

5.2 Extension of annealing model to in-pile conditions

Equations 4.36– 4.42 generally describe the evolution of the porosity. However, under irradiation we have to now consider two additional types of phenomena:

1. Evolution of the irradiation induced point defect population, effect of the irradiation defects on the pore growth rate, and the influence of radiation enhanced diffusion.
2. Transport of fission gas to the porosity.

5.2.1 Irradiation induced point defect population

In general we can divide the point defect population into two distinct classes: (1) thermal equilibrium defects that are temperature and stoichiometric dependent, and (2) irradiation induced defects that are dependent on the fission rate density. While both oxygen and uranium defects are produced in UO_2 , the limiting factor for porosity growth is the diffusion of the slowest species, which in the case of UO_2 is the uranium defect population [1]. Equations 4.7– 4.10 describe the equilibrium thermal defect population. Although thermally activated defects are constantly being created in the UO_2 lattice the irradiation induced defects are produced in a non-equilibrium fashion. The evolution of the irradiation defects is controlled by three principal processes:

1. Production of stable Frenkel pairs from the initial fission cascade.
2. Recombination of irradiation induced frenkel pairs, i.e. $v + i \rightarrow 0$.
3. Trapping at sinks present in the microstructure of the fuel, i.e. grain boundaries, dislocation structures, and the porosity.

To calculate the concentration of the irradiation induced defect population we can use the rate theory continuum model of Brailsford and Bullough [2]:

$$\frac{dC_{irr}^{v,i}}{dt} = \dot{F}z_s\Omega - \eta D_{gr}^i C_{irr}^v C_{irr}^i - \left. \frac{dC_{irr}^{v,i}}{dt} \right|_{sinks} \quad (5.1)$$

Here the subscripts v and i denote vacancies and interstitials respectively. Equation 5.1 describes the evolution of the fractional concentrations C_{irr}^v and C_{irr}^i , where processes 1–3 are operative. The first term, $\dot{F}z_s\Omega$, is the rate of production of stable¹ vacancy and interstitials. Here \dot{F} is the local fission rate density, z_s is the number of stable Frenkel pairs per fission event and Ω is the volume of a UO₂ cell ($4.09 \times 10^{-29} \text{ m}^3$). The second term, $\eta D_{gr}^i C_{irr}^v C_{irr}^i$, describes the recombination of the stable Frenkel pair population resulting from the initial fission cascade. In the parlance of rate theory we have the rate of change in the defect concentration due to Frenkel pair recombination as:

$$\frac{dC_{irr}^{v,i}}{dt} = k_{rec}^{v,i} C_{irr}^v C_{irr}^i \quad (5.2)$$

and

$$k_{irr}^{v,i} = \eta D_{gr}^i \quad (5.3)$$

Here the recombination constant $\eta = (4\pi l_{rec})/\Omega$, where l_{rec} is the recombination length (≈ 0.1 – 0.5 nm). It should be pointed out that in Frenkel pair recombination the rate is dependent on the diffusion behaviour of the interstitials and vacancies. Consequently recombination depends on the fastest moving species, which in this case is the uranium interstitials. For this reason the rate of constant for recombination depends on the interstitial diffusion coefficient as can be seen in equation 5.3.

The last term in equation 5.1, $dC_{irr}^{v,i}/dt|_{sinks}$, describes the accumulation of the defects at various sinks in the microstructure. In general this should include the effect of the grain boundaries, dislocation structures and the porosity. In our particular case, however, we disregard the dislocation contribution as the HBS exhibits a low concentration of dislocations after transformation from normal structure to HBS [3, 4, 5]. In addition we disregard the effect of the grain boundaries on the basis that vacancy diffusion is likely to be fast and consequently the diffusion of defects to the porosity can be adequately described by considering just the defect gradient to the porosity. Following Olander [6] we calculate this as:

$$\left. \frac{dC_{irr}^{v,i}}{dt} \right|_{pores} = 4\pi R_{cp} n_{cp} \left(D_{irr}^{v,i} C_{irr}^{v,i} \right) \quad (5.4)$$

where R_{cp} and n_{cp} are the average radius of the closed porosity and number density of the closed porosity.

¹The term stable here means that vacancy–interstitial pairs created close to each other immediately recombine and are excluded.

At low temperatures ($T_k < 1000$ K) the defect diffusion coefficients become athermal [7] and are linearly dependent on the fission rate density:

$$D_{RED}^{v,i} = a_{v,i} \times \dot{F} \quad (5.5)$$

where $a_{v,i}$ is the radiation enhanced diffusion constant for vacancies and interstitials and where $a_U = 1.2 \times 10^{-39} \text{ m}^5$ for uranium self-diffusion in UO_2 . Combining the athermal contribution with the thermally activated diffusion coefficients for the vacancies and interstitials we have:

$$D_{irr}^{v,i} = D_0^{v,i} \exp\left(\frac{\Delta H_{v,i}}{k_B T_k}\right) + a_{v,i} \dot{F} \quad (5.6)$$

where v and i denote the vacancy and interstitial respectively, $D_0^{v,i}$ is the diffusion coefficient pre-exponential, $\Delta H_{v,i}$ is the diffusion enthalpy, k_B is the Boltzmann constant and T_k is the temperature.

5.2.2 Fission gas accumulation in the HBS porosity

Previous experimental studies (see section 2.2.1) have demonstrated that a constant concentration of xenon (≈ 0.2 wt%) is achieved within the fuel matrix at high burnups (at local burnups in excess of 120 MWd/kg), i.e. a dynamic equilibrium has been achieved. We have demonstrated in chapter 3 that this dynamic equilibrium has the effect of balancing the flux between the generated gas and the trapping in the porosity under steady state conditions, i.e. at time scales longer than the diffusion time. In the annealing model presented in chapter 4 the rate of change in the porosity gas inventory was dependent on the rate at which pores vent to the external volume (see equations 4.37 and 4.38), i.e.

$$\frac{dc_{cp}^{fg}}{dt} = \frac{dc_{cp}^{fg}}{dt} \bigg|_{venting} \quad (5.7)$$

where dc_{cp}^{fg}/dt is the total rate of change of fission gas in the porosity, and $dc_{cp}^{fg}/dt \big|_{venting}$ is the rate of decrease in the fission gas due to pore venting. So we can take into account fission gas transport to the porosity by adding the production rate of fission gas, $dc_{cp}^{fg}/dt \big|_{prod}$, to equation 5.7, i.e.

$$\frac{dc_{cp}^{fg}}{dt} = \frac{dc_{cp}^{fg}}{dt} \bigg|_{venting} + \frac{dc_{cp}^{fg}}{dt} \bigg|_{prod} \quad (5.8)$$

where:

$$\frac{dc_{cp}^{fg}}{dt} \bigg|_{prod} = \dot{F} Y_{fg} \quad (5.9)$$

where \dot{F} is the local fission rate density and Y_{fg} is the cumulative yield of fission gas per fission. By including equation 5.1 for both the vacancies and interstitials in the equation set used in the

annealing model (equations 4.36– 4.42), and adding the fission gas release term (equation 5.9) to equation 4.38, we can calculate the behaviour of the porosity under irradiation. Table 5.1 lists the time invariant parameters used for this model.

Table 5.1. In-pile porosity growth model parameters.

Variable	Symbol	Value	Reference
Number of generated frenkel pairs per fission	z_s	1×10^5	[8]
Recombination length	l_{rec}	1×10^{-10} m	[9]
Diffusion enthalpy for vacancies	ΔH_v	2.4 eV	[8]
Diffusion enthalpy for interstitials	ΔH_i	2.0 eV	[7]
Diffusion pre-exponential for vacancies	D_0^v	$1 \times 10^{-7} \text{ m}^2 \text{ s}^{-1}$	[8]
Diffusion pre-exponential for interstitials	D_0^i	$1 \times 10^{-5} \text{ m}^2 \text{ s}^{-1}$	[7]
Athermal diffusion constant for vacancies	a_v	$1 \times 10^{-39} \text{ m}^5$	[7]
Athermal diffusion constant for interstitials	a_i	$1 \times 10^{-39} \text{ m}^5$	[7]
Surface to volume ratio of open surface	S/V	10^4 m^{-1}	^a

^a this work

5.3 Stand-alone modelling of a real irradiation history

5.3.1 Fuel and irradiation characteristics

Although calculating the in-pile behaviour of the porosity and gas release under ideal steady state conditions is of interest, the direct calculation of the HBS behaviour under real irradiation conditions is of greater significance for understanding the contribution of the HBS to fission gas release and the effect of the HBS on fuel performance at high rod-average burnups. We have selected a high burnup fuel rod that was irradiated to a rod average burnup of 105 GWd/tHM in a Swiss NPP for 10 annual cycles. Table 5.2 shows the as-fabricated characteristics of the fuel rod.

Table 5.2. As-fabricated fuel rod specifications for the selected fuel rod

Fuel Type	UO ₂
Enrichment	3.5 wt% ²³⁵ U
Rod length	3842 mm
Outer rod diameter	10.74 mm
Diametral gap width	190 μ m
Fuel pellet diameter	9.1 mm
Fuel density	10.4 g cm ⁻³
Fuel density	94.6 % TD

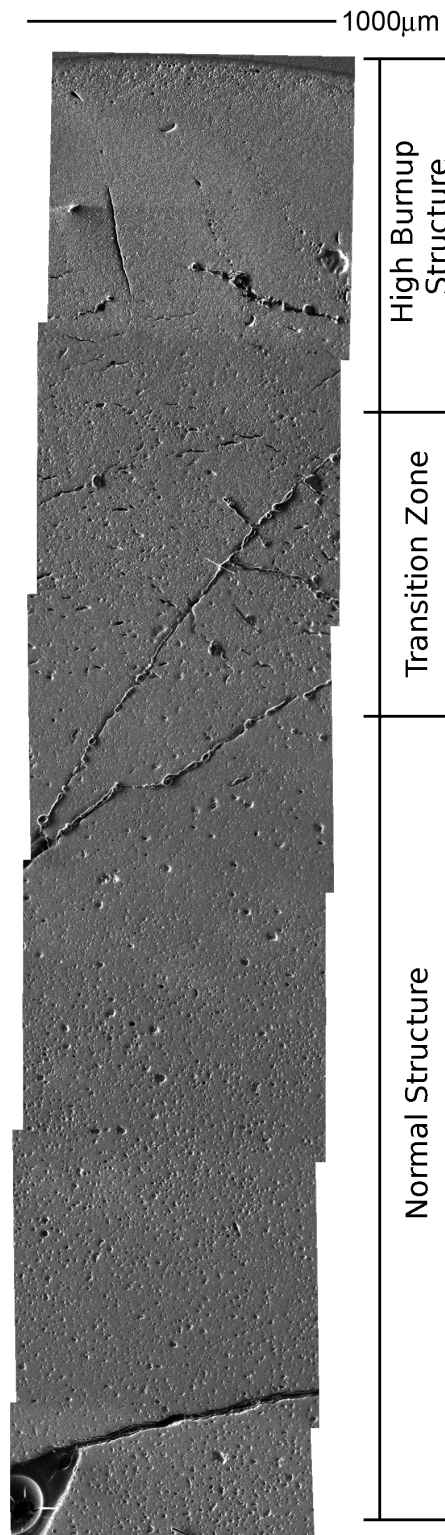


Figure 5.1. Collated scanning electron microscopy (SEM) picture of the high burnup fuel surface. At the upper edge is the fuel cladding and periphery of the fuel. The bottom edge is the centre of the fuel pellet. The HBS, transition zone and normal structure regions of the fuel radius are indicated as determined during PIE. Figure 5.4 from [10]

As part of the PIE campaign for this particular rod Scanning Electron Microscopy (SEM) was performed across a section taken at an axial position of 3046 mm from the bottom of the fuel rod. Figures 5.1 and 5.2 show some of the SEM micrographs of the examined fuel section. Figure 5.1 is a composite of several SEM micrographs taken across the slice with the observed microstructure regions indicated, i.e. normal structure, transition zone and the HBS. The fully transformed HBS extends ≈ 1 mm, from the pellet periphery followed by a transition zone of width 1 mm and then the normal structure extending until the center of the fuel rod. Figures 5.2(a) and 5.2(b) show the SEM micrographs for the fuel rod centre and rim region respectively.

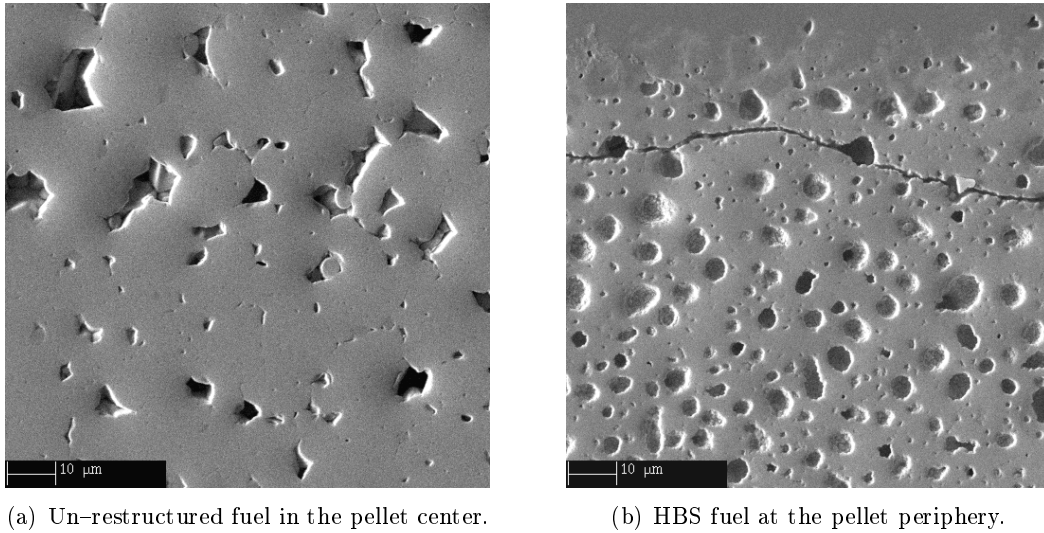


Figure 5.2. Scanning electron microscopy (SEM) images of the high burnup fuel surface. The left figure 5.2(a) shows the un-restructured fuel at the center of the fuel pellet. Figure 5.2(b) shows the HBS fuel and the presence of bonding between the fuel and the cladding. SEM images from [10].

There are several observations we can make regarding the microstructure at both the centre and in the rim region of the fuel rod. As can be seen in figure 5.2(a) there is little restructuring, specifically no columnar grain formation or pore migration. This is important as it places some limits on the fuel centre temperatures that would have occurred during irradiation. Columnar grain formation and pore migration only occurs when the fuel centre temperature (and consequently the radial temperature gradient) is high enough ($\sim 1600^\circ\text{C}$) to allow evaporation–condensation from one side of a pore to the other. The absence of such features in the micrographs from the centre of the fuel thus indicates that the temperatures in the centre did not rise above the temperatures required for restructuring for any significant length of time during the irradiation. In figure 5.2(b) we can clearly see the high HBS porosity with large pores very closely packed together. We can also see that the fuel pellet and the cladding have bonded and that inter-diffusion has occurred. Table 5.3 shows some selected results from the PIE. As can be seen this fuel rod achieved a very high burnup (105 GWd/tHMi), which to this author’s knowledge is the highest reported within open literature. The fission gas release measured by rod puncturing is also significant. Because of the high burnup achieved with this particular rod, and the high fission gas release, this irradiation is an ideal candidate to evaluate the model and to determine the most likely location for the high measured gas release.

Table 5.3. PIE Results

Rod average burnup	105 GWd/tHMi
Pellet average burnup at examined axial position ^a	120 GWd/tHMi
Burnup at pellet rim at examined axial position ^a	≈300 GWd/tHMi
Integral fission gas release	>35 %

^a The examined position was 3046 mm from the bottom of the fuel rod.

To calculate the behaviour of the HBS with the developed in-pile model, two particular time dependent parameters are required, viz. the local fuel temperature and the fission rate density. Obviously the temperature and power histories are not available purely from the PIE results and as such must be derived from calculation. The power history for the TRANSURANUS input was calculated using neutronics codes. However it should be noted that this calculation was complicated by the fact that, after the 4th cycle, the rod was placed into fresh fuel bundles several times to achieve this high burnup. Thus, the power history for the later cycles incorporates higher uncertainty. However, as was mentioned earlier, a rod average burnup of 105 GWd/tHM was experimentally measured during PIE and so the linear heat rate was adjusted during the last 6 cycles such that the TRANSURANUS calculated pellet average burn-up for the position examined during PIE corresponded to the measured value.

While neutronic codes were used to calculate the power history the fuel performance code TRANSURANUS was employed to calculate the local fission rate density and temperature as a function of the radius. TRANSURANUS considers the fuel pin to be axially symmetric and divides the fuel axially into a number of slices. Within each axial slice the fuel and cladding are divided into a number of coarse rings. Each coarse ring is further divided into finer rings, each of which is associated with a mesh point. At the boundary of adjacent coarse rings two mesh points with the same radial position exist. The number of fine mesh points in each coarse zone can take different values for each coarse zone allowing a finer discretisation to be specified in regions of special interest. Figure 5.3 illustrates the radial discretisation scheme in TRANSURANUS.

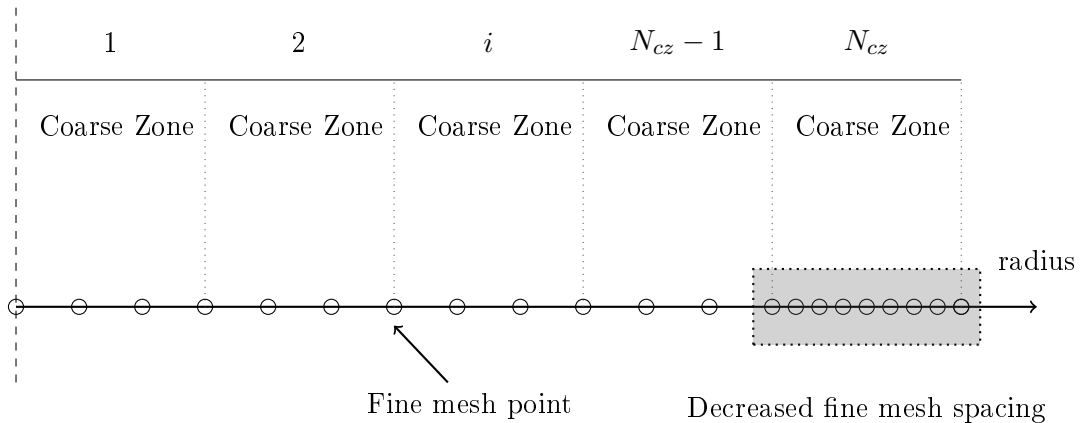


Figure 5.3. Schematic illustrating the radial discretisation of an axial slice within TRANSURANUS.

To calculate the local fission rate density and temperature in the HBS the fuel rod was discretised axially into 19 slices. The fuel radius was divided into 18 coarse zones with 3 fine mesh points

per coarse zone for coarse zones 1 to 15, 5 fine mesh points for coarse zone 16, 15 fine mesh points for coarse zone 17 and 20 fine mesh points for coarse zone 18. This scheme was chosen to mirror the sharp rise in burnup towards the pellet periphery.

Figures 5.4, 5.5 and 5.6 respectively show the TRANSURANUS results for the fission rate density (average and at the pellet periphery), the local burnup at the end of life, and the temperature history at the pellet periphery. Figure 5.5 also illustrates the widths of the microstructure zone (normal structure, transition zone and HBS) that were measured during PIE. For the local fission rate density and temperature at the pellet periphery we have taken the outermost node (coarse zone 18, fine mesh point 20) in the calculation (thickness= $13.76\text{ }\mu\text{m}$), primarily because this is the first region to transform from normal structure to HBS and consequently shows a much more evolved porosity state.

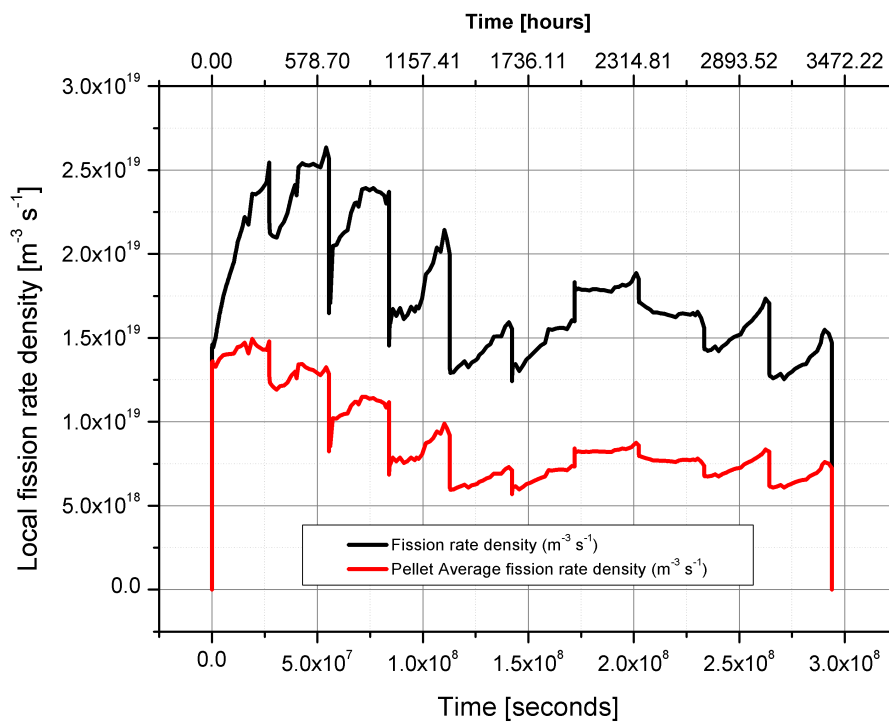


Figure 5.4. Fission rate density at the pellet periphery and pellet average across the pellet as calculated by TRANSURANUS.

It should be noted that (as in chapter 4) the present model does not include the creation of HBS porosity and thus can only be applied to conditions where the number density is expected to decrease, e.g. annealing conditions or at ultra-high burnups. Consequently we have taken the local fission rate density and temperature history from the point at which the local burnup in the outermost node exceeds 100 MWd/kg (see section 2.2.1) as an input for the stand-alone model.

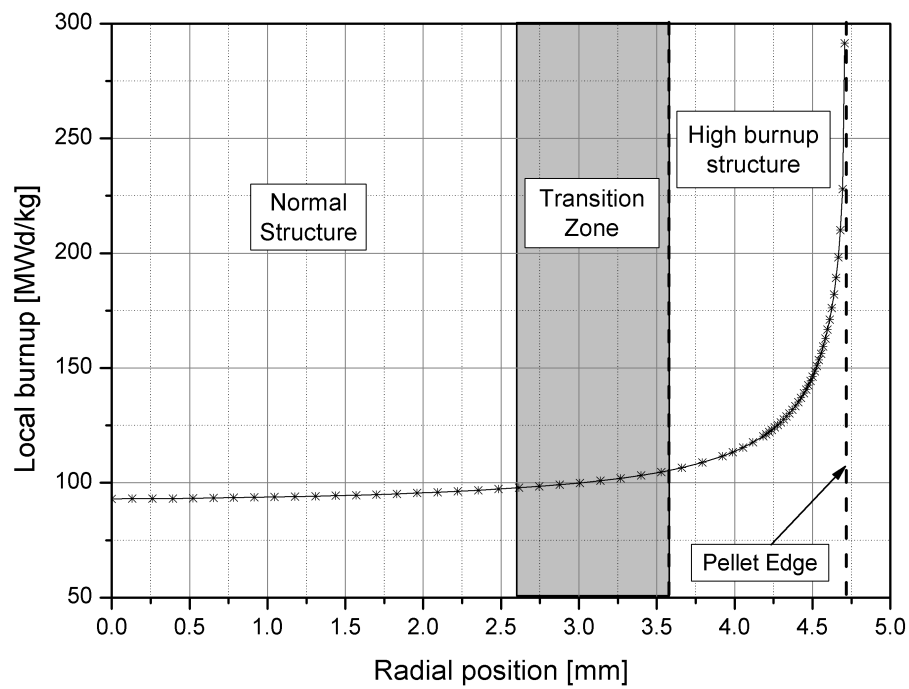


Figure 5.5. Radial variation in the local burnup at end of life as calculated by TRANSURANUS. Also illustrated are the widths of the microstructure zones (normal structure, transition zone and HBS) as determined during PIE by electron probe microanalysis (EPMA) and SEM.

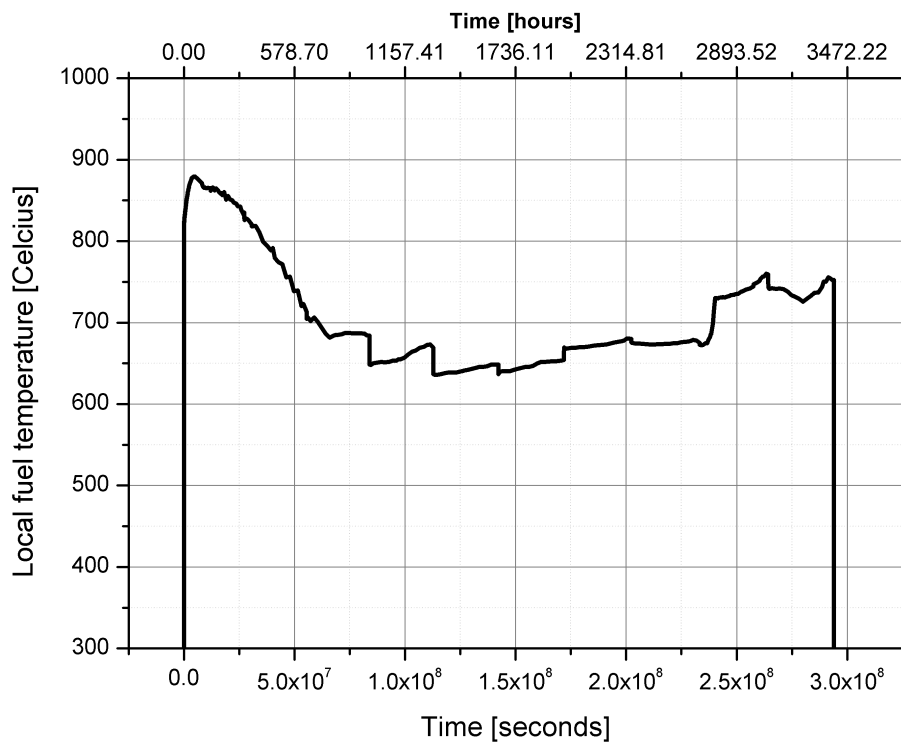


Figure 5.6. Temperature history for a high burnup fuel rod at the pellet periphery as calculated by TRANSURANUS.

5.3.2 Results

As an initial assessment of the behaviour of the model under in-pile conditions we consider the evolution of the porosity under steady-state conditions typical for the HBS in light water reactor (LWR) UO_2 fuel rods. We consider a steady-state temperature ($T_C = 600^\circ\text{C}$) and local fission rate density ($\dot{F} = 1 \times 10^{19} \text{ m}^{-3} \text{ s}^{-1}$) and calculate the evolution of the porosity and gas release in time. The initial conditions have been set according to the state of the porosity at a local burnup of 100 MWd/kg. Table 5.4 gives the initial conditions for the model at a starting local burnup of 100 MWd/kg based upon available data for the HBS.

Table 5.4. In-pile steady-state porosity growth model initial conditions.

Variable	Symbol	Value	Reference
Concentration of gas in the closed porosity	c_{cp}^{fg}	1.3 wt% at 98 MWd/kgU	[11]
Porosity of the closed pores	P_{cp}	12%	[12]
Radius of a closed pore	R_{cp}	$0.6 \mu\text{m}$	[12]
Concentration of released gas	c_{rel}^{fg}	0.0 m^{-3}	^a
Irradiation induced vacancy concentration	C_v	0.0	^a
Irradiation induced interstitial concentration	C_i	0.0	^a
Local burnup	B	100 MWd/kg	^a
Pore internal pressure	p_p	15.1 MPa at $T_K=293 \text{ K}$	^a
Pore overpressure	-	11.77 MPa at $T_K=293 \text{ K}$	^a

^a this work

Spino *et al.* [12] have previously established that after 100 MWd/kg there appears to be a linear increase of 0.6 % per 10 MWd/kg in the porosity. However, simply using the parameters specified in table 5.1 fails to reproduce the trend. The absence of one feature in the model that could explain this disparity is the absence of trapping at grain boundaries and dislocations.

Most calculations of defect evolution in the HBS, e.g. see [8] or [9], include a term for the trapping of defects at dislocations and grain boundaries. Examination of the HBS after transformation points to the newly formed grain boundaries of the sub-divided grains being a product of the cellular dislocation structure formed before the transition to the HBS [13]. Additionally it has been seen that the average distance between pores is $\sim 3 \mu\text{m}$ [14], illustrating that for defect transport to the porosity grain boundary trapping and transport must be considered. The absence of these features in the present model is a potential reason for the mis-match between experimentally observed and calculated porosity growth. However, we can include the effect of these missing processes by considering an effective athermal contribution to the vacancy diffusion coefficient. This is analogous to the use of an effective diffusion coefficient for Xe due to the presence of trapping inside the UO_2 grains. We have adjusted the athermal vacancy diffusion constant, a_v , such that we approximately match the trend observed by Spino *et al.* [12]. Doing this we find that a value of $a_v = 10^{-36} \text{ m}^5$ reproduces the observed porosity evolution.

Taking the fission rate density and temperature history discussed in the previous section, and using this as an input into the stand-alone model, we can calculate the porosity evolution and

the local gas release. Figures 5.7 and 5.8 respectively show the calculated pore number density and porosity as a function of the burnup after the transformation from normal structure to HBS.

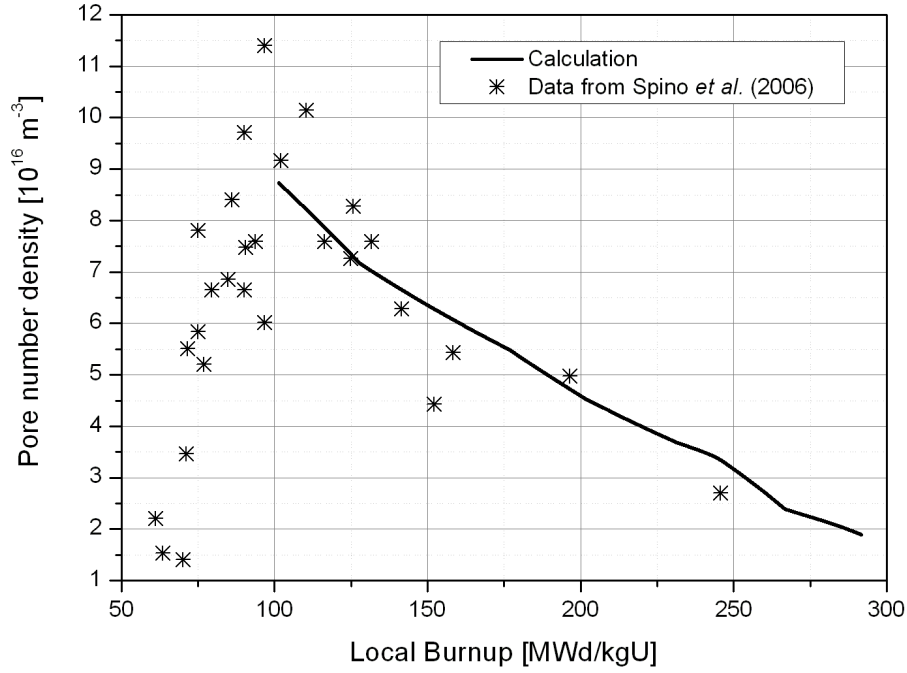


Figure 5.7. Calculated pore number densities for the real fuel irradiation compared with data from Spino *et al.* [12].

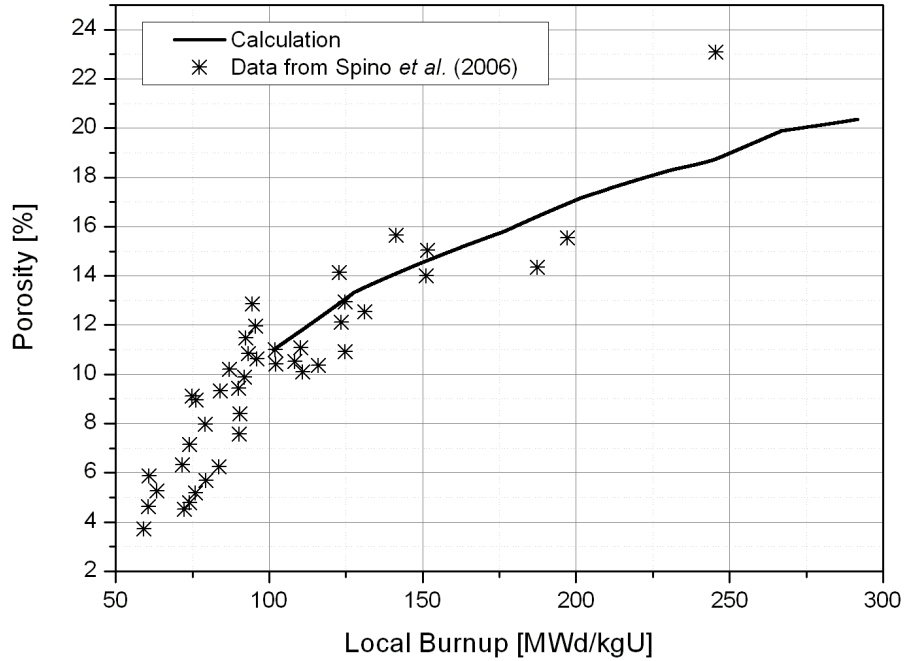


Figure 5.8. Calculated porosity for the real fuel irradiation compared with data from Spino *et al.* [12].

As can be seen there is good agreement between the calculated in-pile porosity evolution and the data from Spino *et al.* [12]. There is another point that can be made with respect to the porosity. In chapter 4 we commented that based upon results from the annealing calculation we

would expect no more than 20 % of the locally produced fission gas to have been released from the HBS porosity for the burnups examined so far in open literature. This assertion was made on the basis that the pore number density has not yet been seen to drop to 10 % of its value at ≈ 100 MWd/kg and consequently the maximum porosity has not yet been reached. Figures 5.7 and 5.8 also illustrate this behaviour, even though the burnup achieved is significantly higher than that observed in open literature so far. Figure 5.9 shows the calculated local fission gas release. It is clear from the calculated gas release that while there has been some release, it is

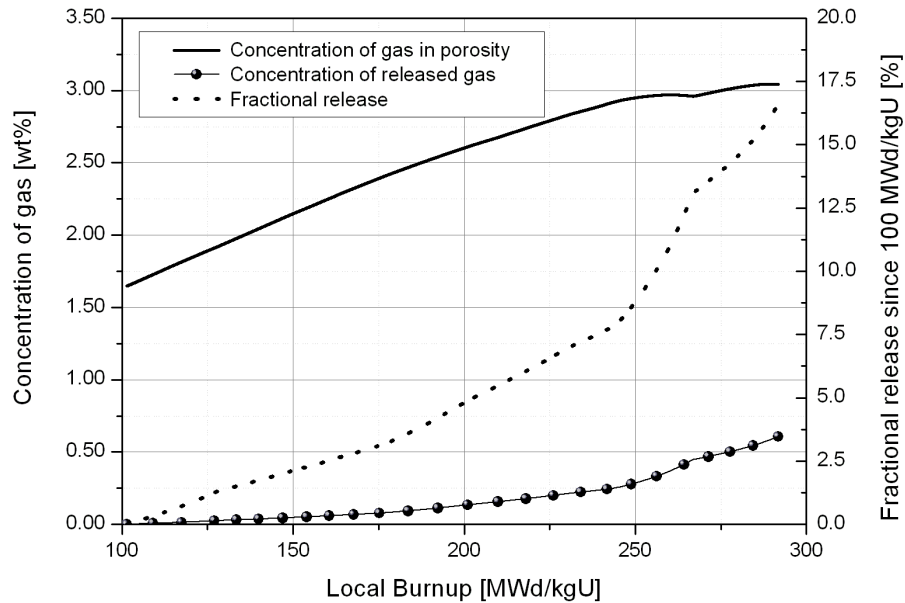


Figure 5.9. Calculated local fission gas concentrations remaining in the HBS porosity and released along with the fractional local gas release from the HBS porosity.

still less than 20 % of the initial inventory, in line with the previous observations during annealing about the relation between the porosity and gas release. As was commented in section 2.2.2 the prevailing consensus at the time of writing is that the release of gas from the HBS porosity is limited. Figure 5.9 reinforces this point of view, with one difference. Thus, while previous models maintain that release of gas from the HBS porosity is a threshold process and as a consequence one should expect little release, the model presented here suggests the alternative view that the gas release is in fact continuous but slow; specifically very high burnups need to be achieved before extensive release can occur. This is supported by the work of Manzel and Walker [15] and Horvath [10]. In the first case Manzel and Walker examined two high burnup rods (rod average burnups 89.5 MWd/kgHM and 97.8 MWd/kgHM) and concluded that at ultra-high burnups the HBS contribution to the integral gas release is minimal (~ 20 – 30 % local inventory). In addition Horvath [10] has measured the fission gas inventory in the HBS porosity using Laser Ablation Inductively Coupled Mass Spectrometry (LA-ICP-MS). Using the inventory and the measured matrix xenon concentration Horvath estimated the fission gas release to be $\sim 15 \pm 7$ %. Both studies are in agreement with the calculation presented here and consequently we can consider the estimate of local gas release to be reasonable.

5.4 Integration of the model into a fuel performance code

Although modelling the porosity behaviour and fission gas release using the stand-alone model is of interest for examining local quantities, the lack of data for the locally retained gas in the HBS porosity provides little opportunity for the validation of the gas release calculations. One way of comparing the model predictions with experimental results is to compare integral values, i.e. whole rod measurements of fission gas release. However, to do this the developed model needs to be integrated into a fuel performance code. This section describes the development of correlations describing the gas release and transformation from the normal microstructure to the HBS, and their implementation in a fuel performance code.

5.4.1 Framework for HBS modelling

The fuel behaviour code TRANSURANUS provides an ideal framework for fuel performance modelling, and in particular for the calculation of fission gas release. TRANSURANUS uses an empirical fission gas release model as standard [16]; however, in order to better understand the processes in fuel under irradiation, a more detailed fission gas release model, based on and describing the basic mechanisms in the fuel matrix, has previously been developed at the Paul Scherrer Institute (PSI) [17] and adapted for use in TRANSURANUS [18]. It considers several transport processes in the fuel grains and the grain boundaries, specifically,

- Single atom diffusion
- Grain and grain boundary trapping
- Irradiation-induced re-solution
- Grain boundary bubble inter-linkage.

The model is based on work by Speight [19], Turnbull [20], and White and Tucker [21]. Fission gas release occurs when the grain boundary bubbles cover the whole grain surface and interlink. To take into account the modified microstructure and fission gas distribution in the HBS, the PSI model was extended with respect to the HBS (see appendix E for a detailed description). The extended model divides the fuel radius into three zones, normal structure, transition zone and HBS. This transformation is calculated using a correlation describing the volume of HBS at each fine node point (see below for details). Within each zone the fission gas release is calculated using three different sub-models:

Normal structure: The PSI fission gas release model is applied.

Transition Zone: The fission gas concentration is redistributed such that in the HBS volumes the concentration in the grains is 0.2 wt% with the rest of the gas in the HBS porosity, while the normal structure fuel volume is untouched. In this zone the PSI fission gas release model is only applied to the normal structure volume fraction.

HBS: Here, as was shown in chapter 3, any generated gas is immediately transported to the HBS porosity. We have developed a correlation (see section 5.4.2) to describe the development of the porosity and release of the fission gas from the HBS porosity, and consequently the calculated gas release is subtracted from the gas that is transported to the porosity.

As was noted above the extended fission gas release model in TRANSURANUS takes into account the transition from the unrestructured fuel to the HBS, including the formation of the transition zone. To do this we have considered a correlation derived from that proposed by Kinoshita [22]. The correlation proposed by Kinoshita utilises a generic phenomenological description for the transformation of a microstructure called Kolmogorov–Johnson–Mehl–Avrami (KJMA) theory [23, 24, 25] to describe the transformation of the HBS. In the form presented by Kinoshita the local volume fraction of HBS in the microstructure, F_{HBS} , can be calculated as:

$$F_{HBS} = 1 - \exp \left(-k \left(\frac{B - B_0}{B_0} \right)^3 \right) \quad (5.10)$$

Here B is the local burnup in the fuel, B_0 is the local burnup at which the microstructure is transformed and k is the rate coefficient for the transformation. As was described in section 2.2.1 the transformation is generally accepted to be complete by a local burnup of ≈ 120 MWd/kg. However it should be noted that equation 5.10 only asymptotically approaches a complete transformation from normal structure to HBS, i.e.

$$\lim_{B \rightarrow \infty} F_{HBS} = 1 \quad (5.11)$$

As a consequence if we wish to divide the fuel radius into the three zones observable in high burnup fuel, i.e. normal structure, transition zone and HBS, then we require the transformation to HBS to be complete after a certain burnup increment, ΔB . To do this we consider that once there is a volume of normal structure equal to the volume of a HBS grain, we can no longer consider the volume of fuel to have any normal structure left. Consequently we can calculate the rate coefficient, k , that results in the volume fraction of normal structure equal to one HBS grain volume per normal structure grain volume after a burnup increment of ΔB , viz:

$$F_{HBS}|_{complete} = 1 - \left(\frac{R_{gr}^{HBS}}{R_{gr}^{NS}} \right)^3 \quad (5.12)$$

Here R_{gr}^{NS} is the radius of the unrestructured grain. We consider that at the point that equation 5.12 is satisfied we can essentially say that the transformation is complete, i.e. $F_{HBS} = 1$. Using this and assuming that the transformation requires a burnup increment ΔB to be complete, we can derive an expression for the rate coefficient, k :

$$k = \left(\frac{B_0}{\Delta B} \right)^3 \ln \left(\left(\frac{R_{gr}^{NS}}{R_{gr}^{HBS}} \right)^3 \right) \quad (5.13)$$

Using equations 5.10 and 5.13 we can calculate for a given burnup how much HBS exists locally. Figure 5.10 shows the correlation for a starting burnup, B_0 , of 60 MWd/kg, a normal structure

grain size of $R_{gr}^{NS} = 10 \mu\text{m}$, a HBS grain size of $R_{gr}^{HBS} = 0.1 \mu\text{m}$ and a several different values of the burnup increment required to complete the transformation, ΔB .

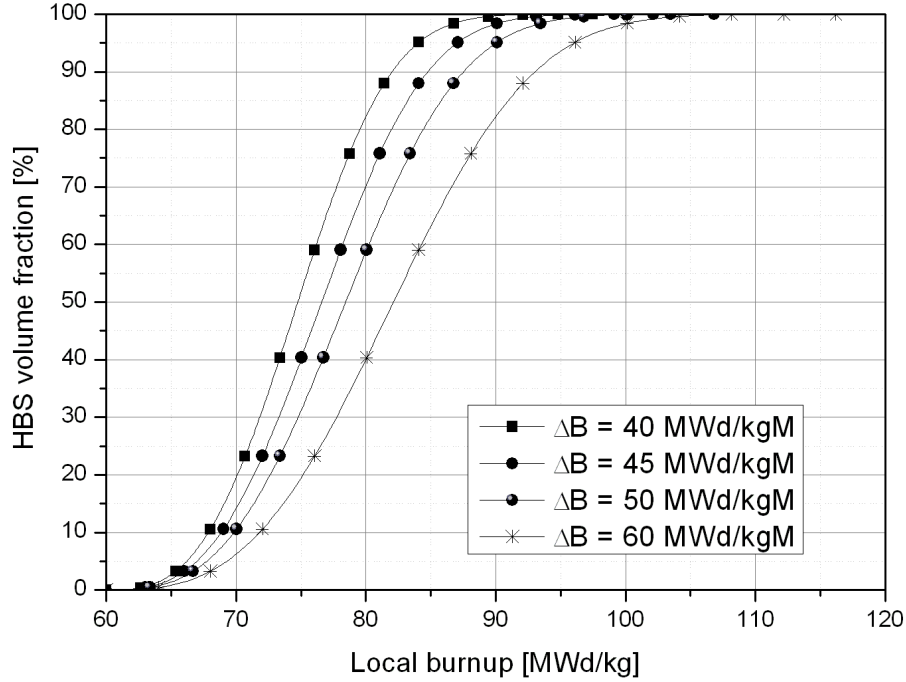


Figure 5.10. Variation of the volume fraction of HBS as a function of local burnup for several different values of ΔB according to the correlation specified by equations 5.10 and 5.13.

Figure 5.11 shows the volume fraction of HBS determined by this correlation for the fuel irradiation simulated in section 5.3. To compare with the situation seen in this real fuel rod TRANSURANUS was employed with this correlation integrated into the extended PSI-HBS fission gas release model. Figure 5.11 shows the fraction of HBS as a function of the radius as obtained by TRANSURANUS for the modelled experimental rod. Figure 5.11 also shows the widths of the various zones that were observed in PIE [10] by considering the EPMA measurements of caesium/xenon and the observation of the pore structure in SEM accross the radius of a fuel section taken at approximately 3046 mm from the rod bottom. Although there is some uncertainty in the zone widths it should be commented that the combination of SEM observations and the drop in caesium/xenon concentrations provide a reasonable indication of the location of each fuel microstructure type with an uncertainty in width of up to $100 \mu\text{m}$. Nevertheless figure 5.11 shows reasonable agreement between the predicted fraction of HBS and the observations from PIE.

5.4.2 Development of a gas release correlation from the stand-alone modelling

To develop the correlation for the gas release we consider the release as a function of porosity. This has been done with respect to the porosity instead of time as the gas release is a geometrically dependent quantity, i.e. the state of the porosity determines the fraction of pores that are interlinked (cf. percolation theory, see appendix A). Specifically we require the increment of gas

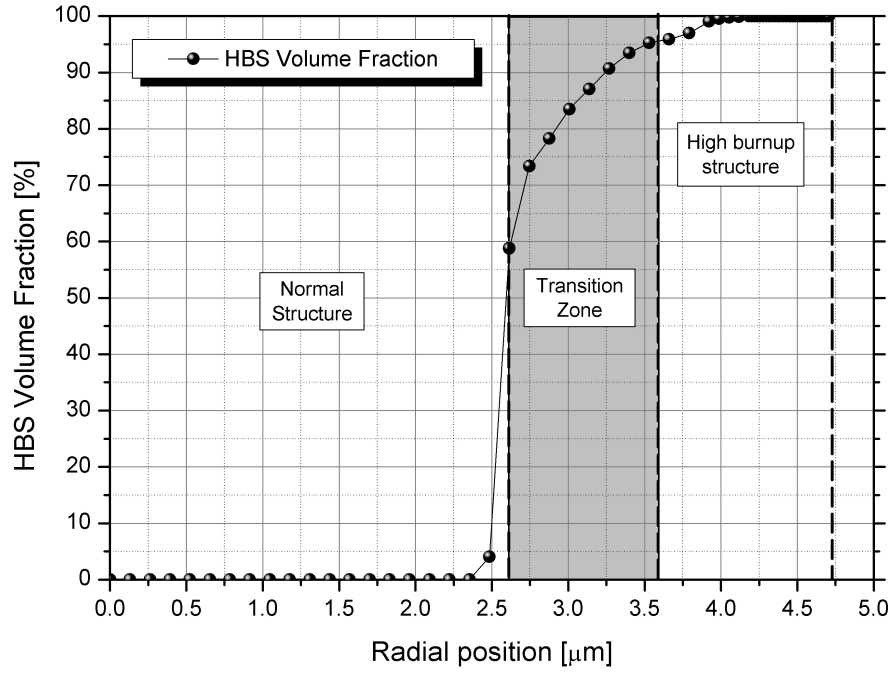


Figure 5.11. Radial variation of the volume fraction of HBS at the end-of-life of a real high-burnup fuel irradiation. The microstructure regions, i.e. normal structure, transition zone and HBS, observed during PIE by EPMA and SEM are also indicated.

release, dC_{fg}^{rel} , when the porosity changes from P_1 to P_2 . We consider a 5th order polynomial fit to the absolute concentration of gas release, i.e.

$$C_{fg}^{rel} = \sum_{i=0}^5 a_i P^i \quad (5.14)$$

Taking equation 5.14 we can derive the increment of release, dC_{fg}^{rel} , when the porosity changes from P_1 to P_2 as follows:

$$dC_{fg}^{rel} = C_{fg}^{rel} \Big|_{P_2} - C_{fg}^{rel} \Big|_{P_1} \quad (5.15)$$

$$dC_{fg}^{rel} = \left(\sum_{i=0}^5 a_i P_2^i \right) - \left(\sum_{i=0}^5 a_i P_1^i \right) \quad (5.16)$$

$$dC_{fg}^{rel} = \sum_{i=0}^5 a_i (P_2^i - P_1^i) \quad (5.17)$$

Figure 5.12 shows the 5th order polynomial fit (equation 5.14) and table 5.5 lists the fitting constants.

In addition to the correlation describing the gas release increment, we also require the porosity growth as a function of the local burnup. We consider a 5th order polynomial fit to the growth of the porosity as a function of burnup, i.e.

$$P_{cp} = \sum_{i=0}^5 b_i B^i \quad (5.18)$$

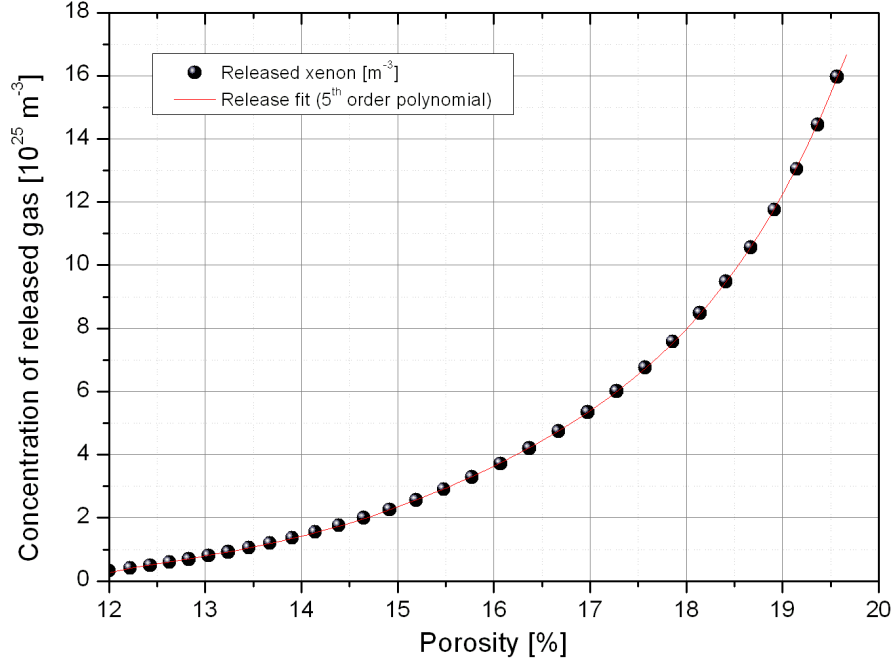


Figure 5.12. Fit to the absolute concentration of gas released.

Table 5.5. Coefficients for the 5th order polynomial fit to the gas release.

Coefficient	Value
a_0	-1.1806×10^{28}
a_1	4.0325×10^{29}
a_2	-5.4941×10^{30}
a_3	3.7319×10^{31}
a_4	-1.2647×10^{32}
a_5	1.7159×10^{32}

where the fitting parameters can be seen in table 5.6 and the correlation can be seen in figure 5.13.

Estimation of the error in the fit to the gas release

As a test of the accuracy of the correlation for the gas release we can calculate the incremental gas release using equation 5.17 and compare with the original calculation results. Figure 5.14 shows the gas release from the stand-alone calculation between a porosity of 14 % and 18 %.

The released gas concentration at porosities of 14 % and 18 % are $1.47 \times 10^{25} \text{ m}^{-3}$ and $8.02 \times 10^{25} \text{ m}^{-3}$ respectively. Consequently the incremental gas release from the calculation results, dC_{fg}^{rel} , is $6.55 \times 10^{25} \text{ m}^{-3}$. Looking at each term in equation 5.17 and calculating the predicted increment from the correlation we get the terms shown in table 5.7.

Using the terms shown in table 5.7 for the fit to the absolute gas release and calculating the

Table 5.6. Coefficients for the 5th order polynomial fit to the porosity.

Coefficient	Value
b_0	-0.21058×10^{-6}
b_1	6.71486×10^{-11}
b_2	-5.35583×10^{-11}
b_3	2.26830×10^{-16}
b_4	-4.68410×10^{-22}
b_5	3.71294×10^{-28}

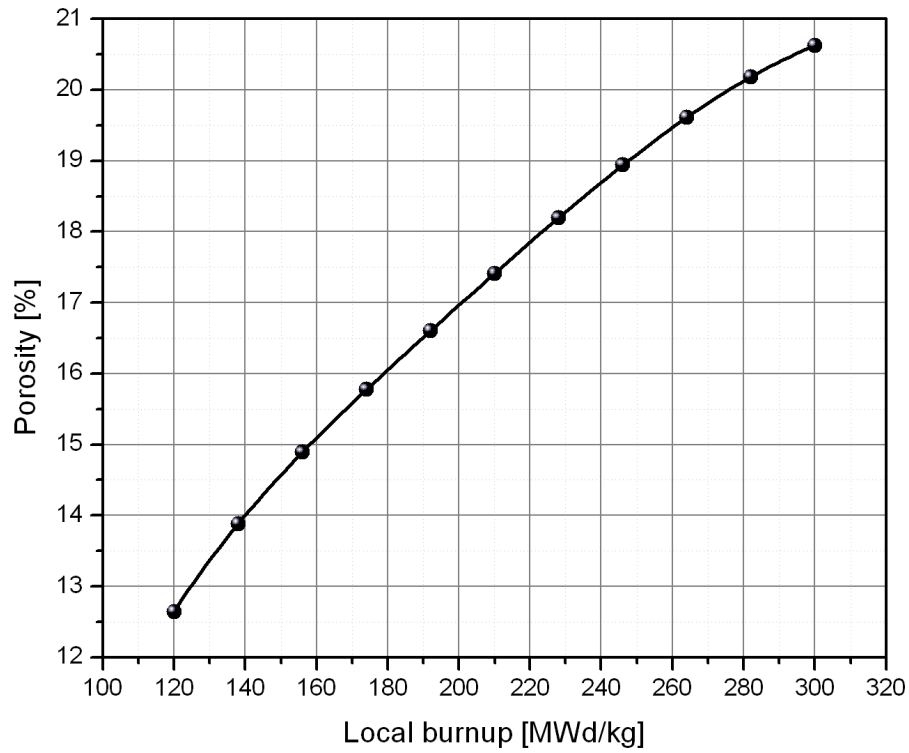


Figure 5.13. Correlation describing the growth of the porosity.

Table 5.7. Terms for the gas release correlation given by equation 5.17 for the porosity interval from 14% to 18%.

i	P_1^i	P_2^i	$P_2^i - P_1^i$	$a_i (P_2^i - P_1^i)$
0	1.0	1.0	0.0	0.0
1	0.14	0.18	0.04	1.613×10^{28}
2	0.0196	0.0324	0.0128	-7.032448×10^{28}
3	2.744×10^{-3}	5.832×10^{-3}	3.088×10^{-3}	$1.15241072 \times 10^{29}$
4	3.8416×10^{-4}	1.04976×10^{-3}	6.656×10^{-4}	$-8.4178432 \times 10^{28}$
5	5.37824×10^{-5}	1.889568×10^{-4}	1.351744×10^{-4}	$2.31945753 \times 10^{28}$
$\sum_{i=0}^5 a_i (P_2^i - P_1^i) =$				6.27353×10^{25}

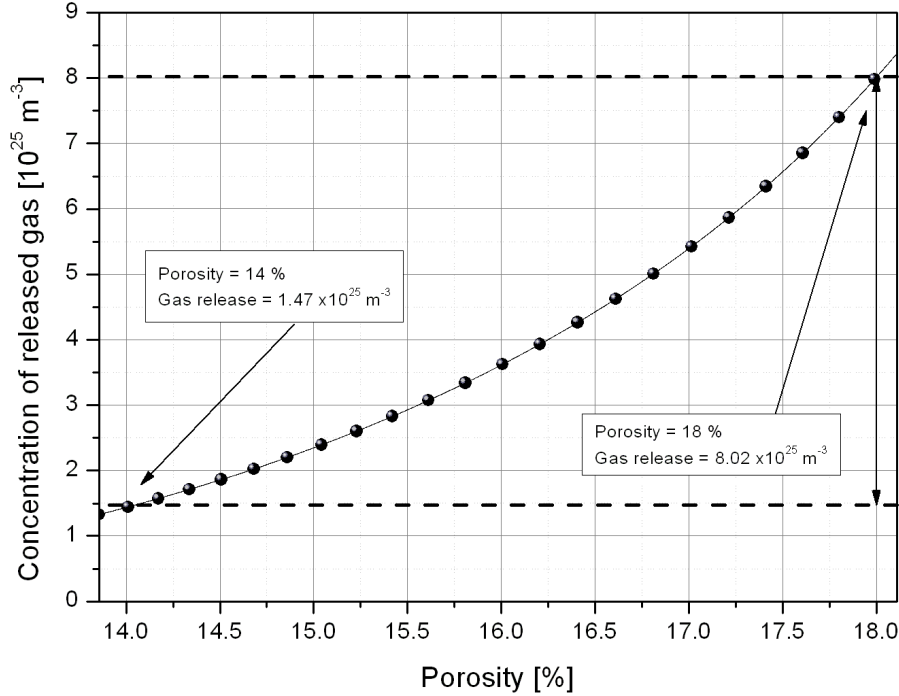


Figure 5.14. Absolute gas release as a function of porosity calculated with the stand-alone in-pile model. Here the quantities of gas released at porosities of 14 % and 18 % are indicated.

increment of release using equation 5.17 between porosities of 14 % and 18 % we get an estimated increment in the gas release of $6.27 \times 10^{25} \text{ m}^{-3}$. Comparing this with the calculation results we see that the fractional error is 4.2 %. Instead of fitting to the absolute gas release we could also perform the fit to the rate of gas release; however, upon doing this we find that the fractional error in the estimation of the gas release increment is 19.7 % in comparison with the original calculation result. This is not surprising as the calculation of the release increment from the release rate requires an integration that produces a 6th order polynomial. Consequently we might expect the error here to be higher when considering that the 5 % confidence limit is only applicable to the 5th order fit. Regardless of this we can safely use the correlation derived from the absolute release rate, i.e. equation 5.17, with the parameters specified in table 5.5.

The correlations described here have been implemented in TRANSURANUS by calculating the gas release quantity with respect to the local HBS porosity and then subtracting this amount from the local concentration of fission in the HBS porosity. See appendix E for more details about how the HBS is treated in the extended fission gas release model.

5.5 Integral modelling of a real irradiation history

5.5.1 Results for the base case

In order to evaluate the effect of porosity growth and venting on fission gas release for the real irradiation modelled in section 5.3, the HBS model implemented in TRANSURANUS was used to calculate the integral behaviour. We use the power history derived from the neutronic calculations of the irradiation (see section 5.3.1) and directly calculate the integral fission gas

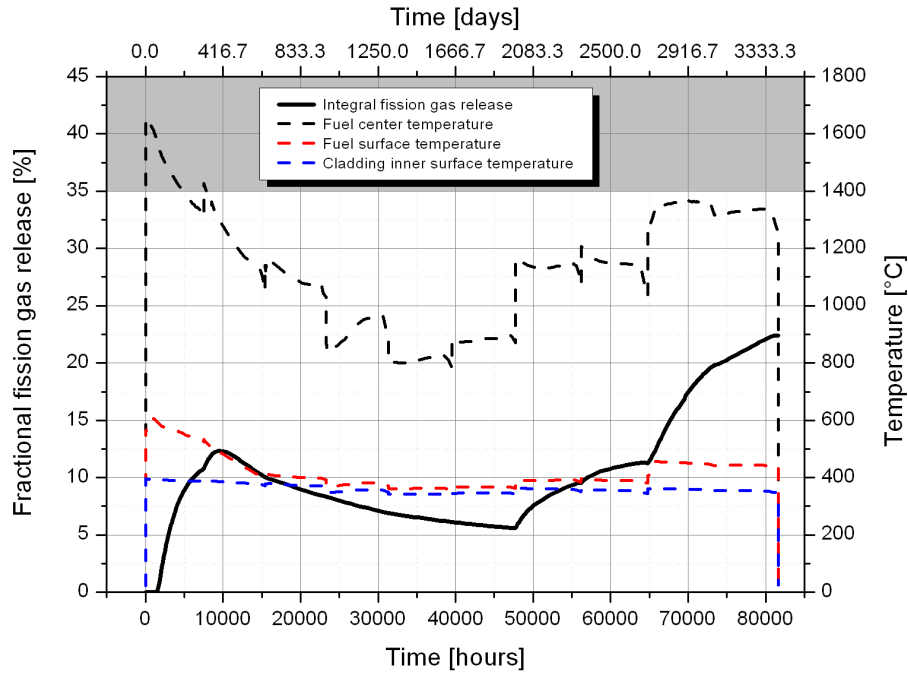


Figure 5.15. Integral fission gas release and fuel/cladding temperatures for the base case. The gray area indicates the region where the measured fission gas release lies.

release and fuel temperatures. In the following section this “straight” calculation is referred to as the “base case”. Figure 5.15 shows the evolution of the integral fission gas release and rod temperatures throughout the irradiation.

For this base case 22% of the integral fission gas is released. However, this is significantly below the fission gas release measured by rod puncturing. Figure 5.16 shows the end-of-life calculated radial distribution of fission gas release at an axial position ≈ 3046 mm from the bottom of the fuel rod. It can be seen that venting from the HBS has a small effect on the integral fission gas release with the HBS release increasing towards the pellet periphery, i.e. following the burnup profile at this axial position. The principle effect of the HBS on the gas release is the presence of the high porosity, which increases the fuel centre temperatures and therefore the fission gas release from the centre of the rod. It is clear from this that most of the released gas comes from the central regions of the fuel with the HBS regions only releasing 2 % of its inventory. This is in-line with the prevalent point of view to date, viz. the enhanced release of fission gas at high burnups is primarily due to higher release from the centre of the fuel rod [26, 27]. However, it is clear that for the base case there is a missing component of release. The question then arises as to where this comes from, the centre or the pellet periphery.

5.5.2 Effect of temperature on integral fission gas release

In order to address the discrepancy between the base case integral release and the results from rod puncturing we can consider several uncertainties that could account for the difference. In the first case the calculation of release from the central part of the fuel is dependent upon the accurate calculation of the fuel temperatures. Ideally one would like to compare the calculated temperatures with direct measurements; however, due to the particular conditions of this irradi-

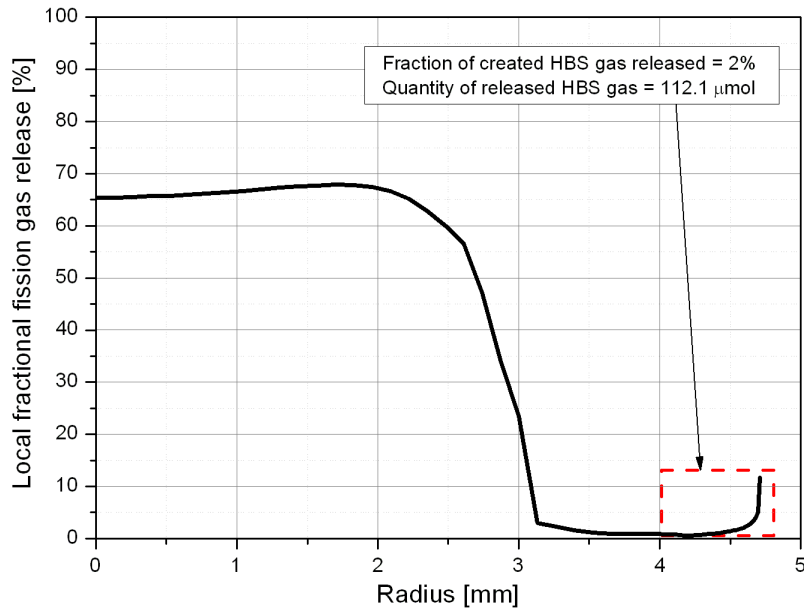


Figure 5.16. Radial distribution of fission gas release at end of life (EOL) for the base case.

ation these data are not available. Consequently we are reduced to examining the effect of fuel centre temperature on the integral gas release. One particular factor that affects the fuel centre temperature is the gap conductivity. By altering the gap conductivity one can influence the fuel temperatures, and in particular that at the centre of the fuel rod. In order to do this we have adjusted the gap conductivity by a constant factor. Figure 5.17 shows the integral release and fuel centre temperature as a function of time for several different factors of the gap conductivity.

At first glance figure 5.17 demonstrates that it is indeed possible to match the measured fission gas release by adjusting the temperatures in the fuel. Specifically a reduction in the standard TRANSURANUS correlation for gap conductivity by a factor of 0.4 produces an integral gas release that is consistent with the fission gas release measured using rod puncturing. However, one needs to examine the increase in fuel centre temperature corresponding to the gap conductivity factor that produces this “good match” to the measured integral fission gas release. The coincident increase in fuel temperature and fission gas release is a distinct indicator of thermal feedback, i.e. the increased fission gas release reduces the thermal conductivity further, which increases fuel centre temperature which results in more fission gas release, and so on. At a certain stage the increasing pressure causes clad lift-off, i.e. the gap between the cladding and the fuel re-opens.

Figure 5.18 shows the evolution of the gap width at a particular axial position of the rod (≈ 3046 mm from the bottom of the rod). As can be seen the gap between the fuel and cladding closes early on in the irradiation, which is a common feature of fuel behaviour and is due to the swelling of the pellet and creep-down of the cladding. However, for the gap conductivity factors observed to match the integral fission gas release measurement we can see that shortly before the end of the irradiation the gap re-opens due to cladding creep-out and this triggers a large

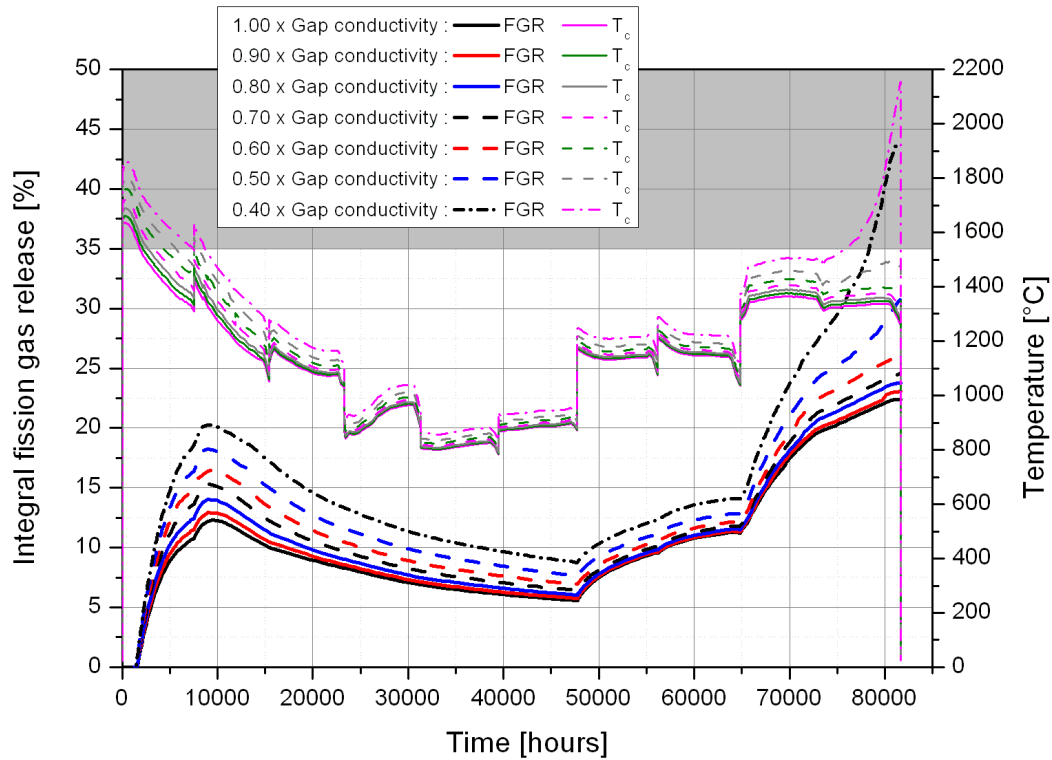


Figure 5.17. Integral fission gas release as a function of reduced gap conductivity. The reduced gap conductivity is implemented for the entire power history of the rod. The gray area indicates the region where the measured fission gas release lies.

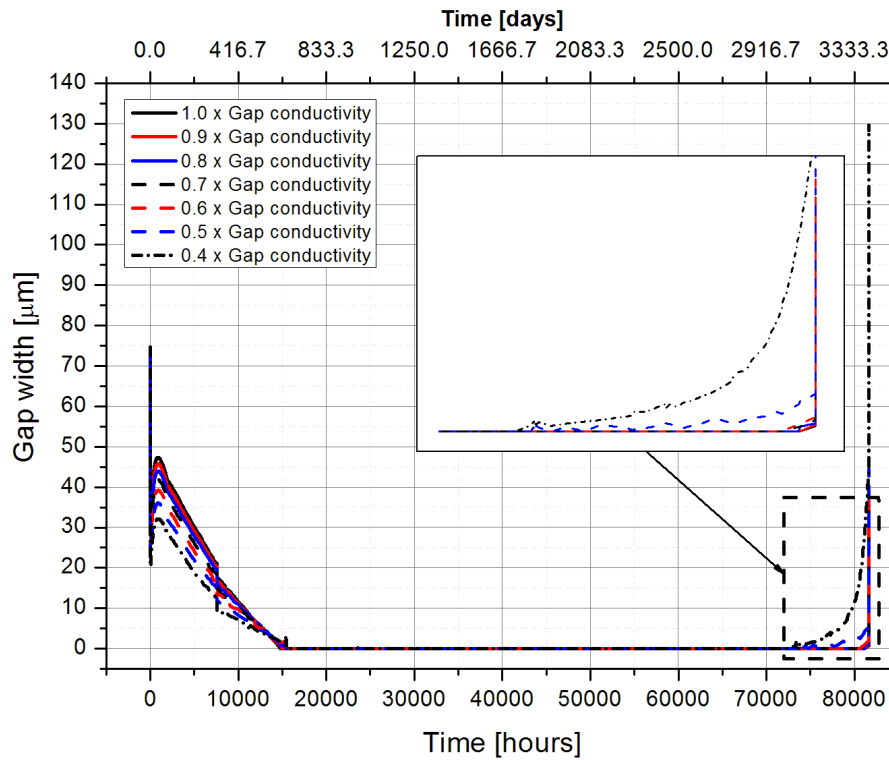


Figure 5.18. Gap width throughout irradiation as a function of the gap conductivity factor at an axial position ≈ 3046 mm from the end of the fuel rod.

thermal feedback effect. This points to clad lift-off being the reason for the high gas releases produced when altering the fuel temperature. Figure 5.19 shows the radial distribution of fission gas release at end-of-life.

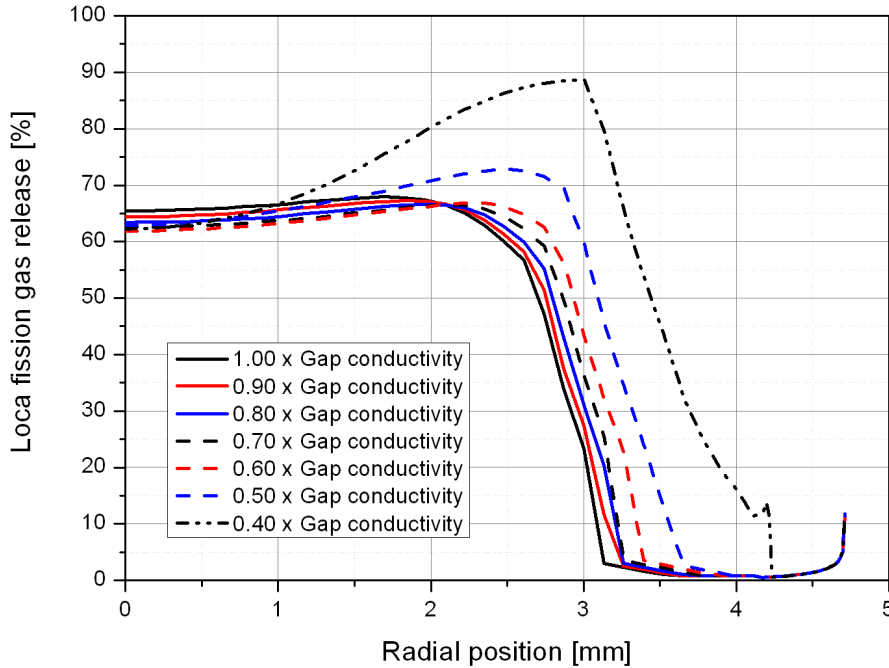


Figure 5.19. Radial distribution of fission gas release at end of life as a function of reduced gap conductivity. The reduced gap conductivity is implemented for the entire power history of the rod.

It can be clearly seen that most of the release comes from the central part of the fuel as would be expected with such high central temperatures. At these temperatures fuel restructuring should occur, specifically grain growth, pore migration and columnar grain formation [6]. However, grain growth was the only restructuring observed during PIE of the experimental rod, i.e. there was no observation of pore migration and columnar grain formation. Figures 5.1 and 5.2(a) clearly show that both columnar grains and pore migration were absent. Moreover, both ceramography and rod diameter measurements revealed no evidence of the gap opening, not even partial opening at the ends of the fuel rod. This is perhaps not so surprising as the fuel and clad had bonded to the point that it was difficult to distinguish the boundary between the pellet and cladding.

To further evaluate the possibility of cladding lift-off having taken place, we can compare the pin over-pressure with available data. The OECD Halden Reactor Project (HRP) has performed a series of tests on pressurised water reactor (PWR) fuel to determine the minimum overpressure, i.e. the difference between the internal gap pressure and the coolant pressure, such that clad lift-off is initiated [28]. This was done by increasing the rod internal pressure in steps by flowing argon gas through the fuel rod and measuring the fuel centre temperature and the fuel stack elongation. They found that a minimum overpressure of 150 bar was required to initiate lift-off but that the temperature effects were not noticeable until this was increased to 200 bar. Figure 5.20 shows the overpressure as calculated by TRANSURANUS for the experimental rod along with the 150-200 bar overpressure range seen in the Halden experiments.

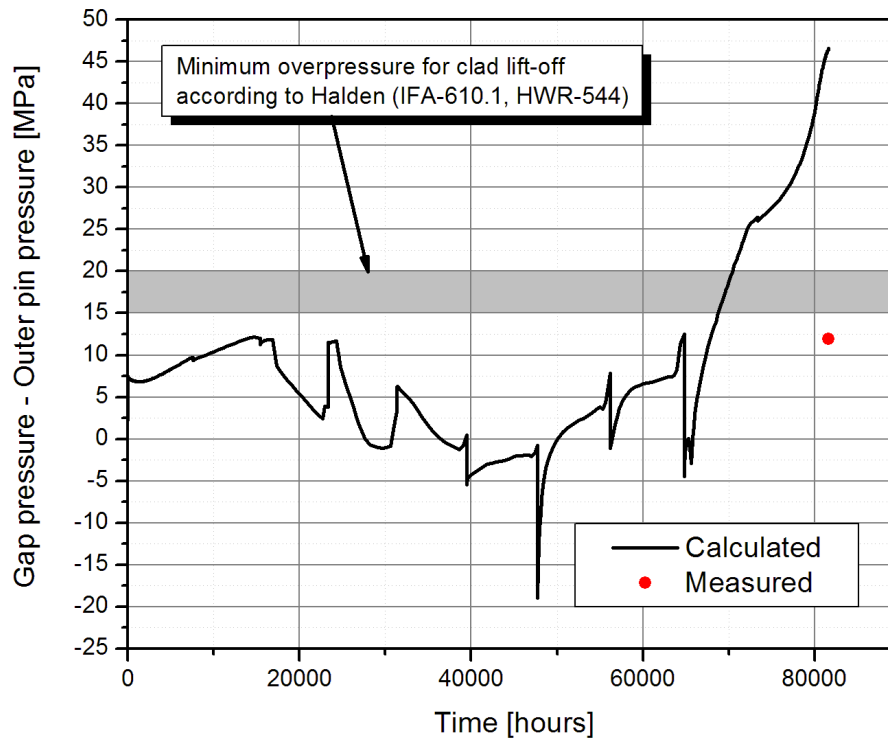


Figure 5.20. Evolution of the calculated gap over-pressure throughout irradiation, the Halden clad lift-off initiation threshold and the measured overpressure from PIE.

Examining the gap width in figure 5.18 and noting that clad lift-off seems to initiate just after 70000 hours we can see in figure 5.20 that this is roughly the point at which the Halden overpressure criterion is observed. While this agreement seems good one cannot use clad lift-off to explain the high fission gas release due to the PIE observations cited for the experimental rod in the previous paragraph. Figure 5.20 also shows the overpressure calculated from the measured pressure obtained during rod puncturing of the rod. It is clear from figure 5.20 that although the overpressure is high (11.91 MPa) it is still below the Halden overpressure criterion and consequently does not indicate that clad lift-off was initiated during irradiation. Moreover, both ceramography and rod diameter measurements indicate that the presence of pellet-clad bonding remained intact.

5.5.3 Athermal fission gas release from the pellet periphery

In the previous section we addressed one potential source for the discrepancy between the calculated and measured fission gas release, viz. uncertainty in the predicted fuel centre temperature and possible clad lift-off inducing a higher gas release from the central regions of the fuel. However we should also consider that there are additional uncertainties associated with the outer regions of the fuel, specifically with the HBS regions.

Athermal release without pellet-clad bonding

To investigate the effect of a possible additional release of fission gas from the periphery an “athermal” release term was added to the release from the HBS porosity, such that there was

good agreement between calculation and experiment for the integral gas release. This “athermal” release was considered to be independent of the temperature and power history of the fuel and was added to the release from the HBS regions once transformation was complete.

Figure 5.21 shows the fuel centre, surface and clad inner temperatures along with the integral fission gas release.

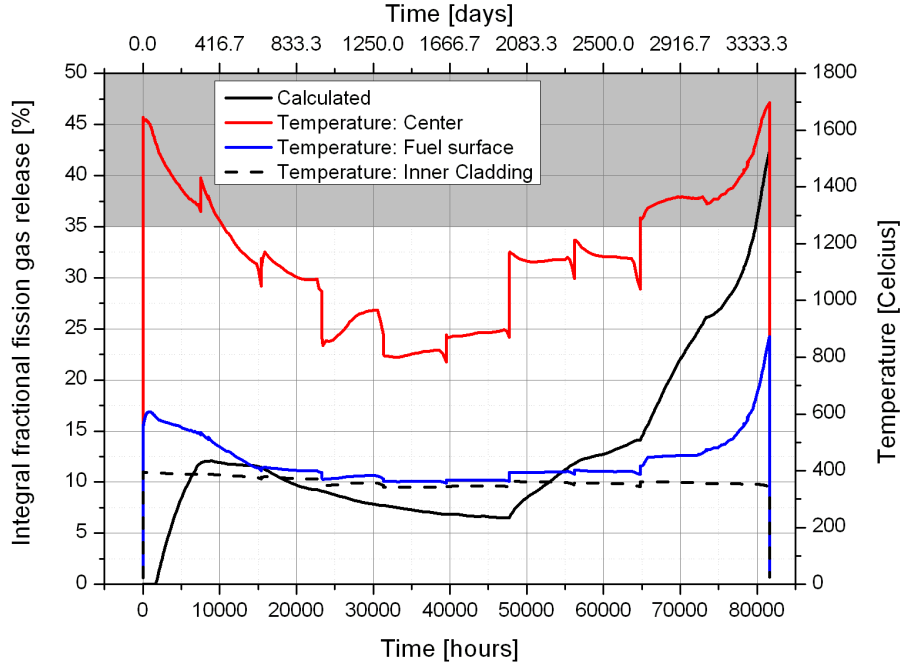


Figure 5.21. Fuel centre, surface and clad inner temperatures and the integral fission gas release. The gray area indicates the region where the measured fission gas release lies.

The situation is seen to be similar to that described in the previous section, viz. with clad lift-off inducing higher fission gas release. If we look at the fuel centre and surface temperatures it is clear that after ≈ 70000 hours the temperatures increase significantly along with the fission gas release. The fuel surface temperature exceeding 800°C is clearly indicative of clad lift-off. However, in this case it is induced by a small additional athermal release from the HBS pores, not by a modified gap conductivity as in section 5.5.2.

Figure 5.22 shows the radial distribution of the created and released concentrations of fission gas for a slice taken at an axial position 3046 mm from the bottom the rod. As should be expected due to the higher centre temperatures, the gas release come predominantly from the central regions of the fuel with high local fission gas releases ($\sim 90\%$). To induce the clad lift-off an athermal contribution of $\approx 17\%$ from the HBS porosity was required. Manzel and Walker [15] have noted that significant increases in the fission gas release at high burnups are likely to come from the central regions of the fuel where thermally activated release dominates. This is particularly clear when one considers that the EPMA of xenon in both this fuel rod and that reported by Manzel and Walker both exhibited a significantly depleted central xenon concentration. However, as in the previous section, the mismatch between the predicted state of the fuel and PIE observations indicates that a clad lift-off scenario is unlikely.

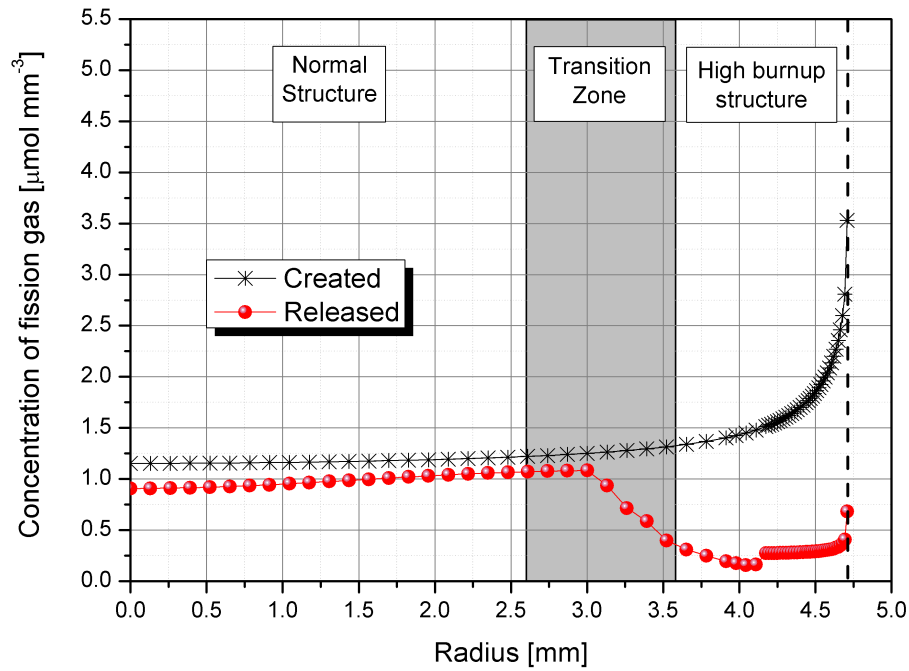


Figure 5.22. Concentrations of created and released fission gas as a function of the radius for an additional athermal release from the HBS.

Athermal release with pellet clad bonding

It is clear that for such a high burnup rod the presence of bonding between the fuel and cladding should mitigate the clad lift-off scenario. Although TRANSURANUS can calculate the effect of fuel-clad contact pressure on axial movement when the gap is closed, there is no treatment of fuel clad bonding. Specifically, even with a closed gap the fuel and cladding are treated as separate entities between which a gap always exists, and where the mechanical behaviour is calculated by considering the surface roughness of the fuel and cladding. Consequently when the overpressure becomes high enough the gap has to open.

To determine exactly how much fission gas release is necessary from the HBS without clad lift-off to match the observed integral fission gas release we need to artificially force TRANSURANUS to maintain a closed gap at power. To do this the coolant pressure and fast neutron flux (which influences the creep rate) were adjusted such that at the point where clad lift-off was observed to occur in the previous sections (sections 5.5.2 and 5.5.3) the fast flux decreases and the coolant pressure increases.

Figure 5.23 shows the time dependence of the pin outer pressure and fast flux both with and without alteration. The alteration to the input was successful in forcing TRANSURANUS to keep the gap closed. We can now calculate the required athermal release from the HBS to produce the measured integral release without initiation of clad lift-off. Figure 5.24 shows the integral fission gas release, the fuel centre temperature, fuel surface temperature and the cladding inner temperature. Figure 5.25 shows the radial distribution of fission gas release for the slice taken at a position of ≈ 3046 mm from the end of the fuel rod. It is seen from figure 5.24 that, in the absence of clad lift-off, it is possible to reach the measured fission gas release without any anomalous effect on the fuel temperatures. However, figure 5.25 shows that the required release

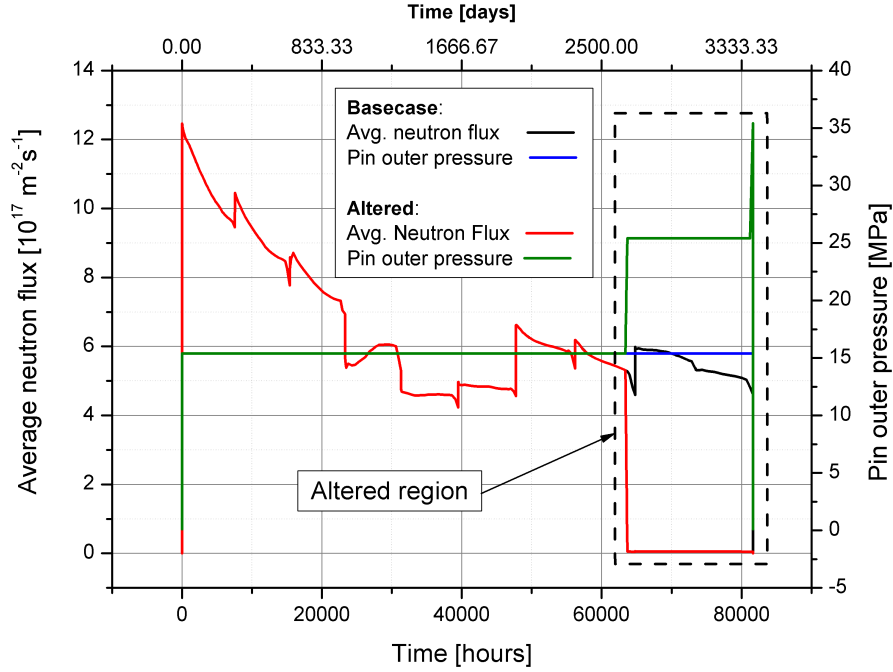


Figure 5.23. Time dependence of the pin outer pressure and fast neutron flux with and without the alterations to force gap closure.

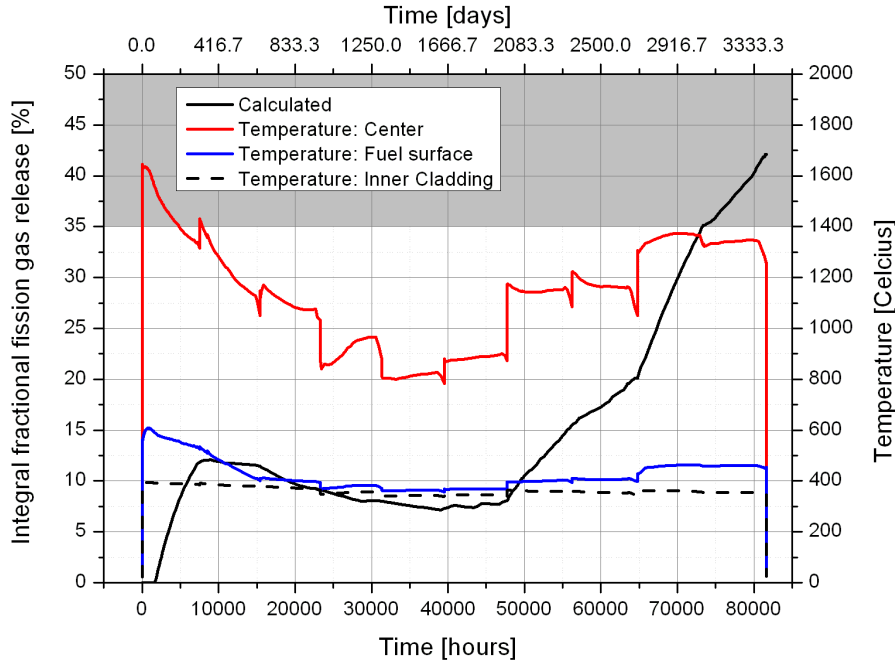


Figure 5.24. Integral fission gas release, the fuel centre temperature, fuel surface temperature and the cladding inner temperature. The gray area indicates the region where the measured fission gas release lies.

of gas from the HBS zone of the fuel is nearly 60 %. This is a significant departure from both the model predictions and the current consensus view on fission gas release in the HBS. For example, the estimations of gas release from the HBS provided by Horvath [10], and also by Manzel and Walker [15], are significantly lower. The question then is as to which other processes could induce such a large release of gas from the periphery of the fuel pellet. More specifically one may ask

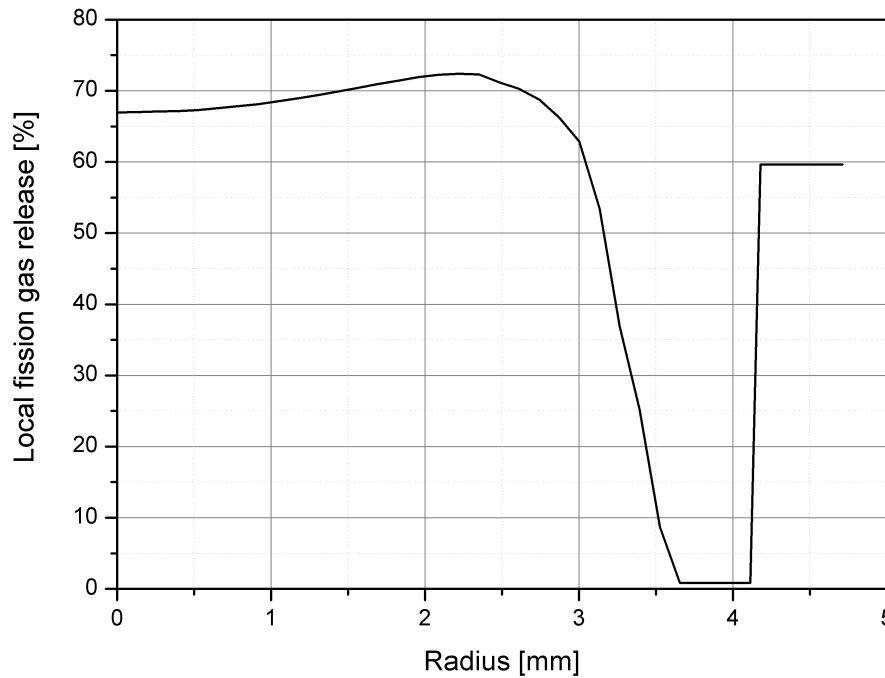


Figure 5.25. Radial distribution of fission gas release at EOL for the slice taken at a position of ≈ 3000 mm from the end of the fuel rod.

whether the transition zone plays a role, or whether there is indeed an underestimation of the fission gas release from the centre.

In the first case we can consider the potential contribution of the transition zone. While most estimations of gas release suggest that release during transition is limited [27] for burnups lower than the rod calculated here, it has yet to be conclusively demonstrated that there is no release from the HBS regions in the transition zone. Manzel and Walker have attributed the large releases at high burnups (>80 MWd/kgHM) to be due to the effect of thermally induced release in the central regions of the fuel pellets and release due to the transition from a normal microstructure to the HBS. We might also expect that because the release from the HBS pores is continuous there would still be some release in the transition zone, regardless of any other processes. Although nearly 60 % of the HBS-generated gas is required to be released for being consistent with the measured result the exact location of the release, be it the HBS spots in the transition zone or in the fully transformed HBS zone, is not important from the point of view of the integral fission gas release. In point of fact it can be considered reasonable in light of the results from Manzel and Walker to consider that there is some release during transformation; this release will transfer over to the HBS zone as this region was also once in transition.

If we assume that any HBS volume releases a constant fraction of the local HBS-created fission gas then we can calculate the radial distribution of release, assuming a component is coming from the transition-zone HBS spots.

First we define a step function such that it is equal to unity only if the HBS transformation is

complete i.e. $F_{HBS} = 1.0$, specifically:

$$h(r) = \begin{cases} 0 & \text{if } F_{HBS}(r) < 1.0 \\ 1 & \text{if } F_{HBS}(r) = 1.0 \end{cases} \quad (5.19)$$

We then consider the total quantity of fission gas released from the HBS zone only, i.e.

$$\sum_r h(r) N_{rel}^{fg}(r) \quad (5.20)$$

where $N_{rel}^{fg}(r)$ is the quantity of fission gas released at a radius of r in the fuel pellet and the summation is performed over the entire pellet radius. In addition we require the total created HBS fission gas, i.e. only the gas created within a HBS volume:

$$\sum_r F_{HBS}(r) N_{crea}^{fg}(r) \quad (5.21)$$

Consequently we can calculate the total fission gas release from the HBS volumes using equations 5.20 and 5.21 as:

$$\sum_r FGR_{HBS}(r) = \frac{\sum_r h(r) N_{rel}^{fg}(r)}{\sum_r F_{HBS}(r) N_{crea}^{fg}(r)} \quad (5.22)$$

If we assume that the fission gas release in any local volume of HBS is constant then we obtain the redistributed athermal contribution to the release from the HBS as:

$$[FGR(r)]_{redist}^{HBS} = F_{HBS}(r) \frac{\sum_r h(r) N_{rel}^{fg}(r)}{\sum_r F_{HBS}(r) N_{crea}^{fg}(r)} \quad (5.23)$$

Finally, there is also the contribution to the fission gas release from the normal structure volumes, which can be calculated as:

$$[FGR(r)]_{redist}^{NS} = (1 - h(r)) \frac{N_{rel}^{fg}(r)}{N_{crea}^{fg}(r)} \quad (5.24)$$

From equations 5.23 and 5.24 we can calculate the redistributed fission gas release that takes into account an athermal release from the HBS spots in the transition zone:

$$[FGR(r)]_{redist} = F_{HBS}(r) \frac{\sum_r h(r) N_{rel}^{fg}(r)}{\sum_r F_{HBS}(r) N_{crea}^{fg}(r)} + (1 - h(r)) \frac{N_{rel}^{fg}(r)}{N_{crea}^{fg}(r)} \quad (5.25)$$

Figure 5.26 shows the redistributed radial fission gas release when applying equation 5.25 to the radial distribution seen in figure 5.25. As can be seen from figure 5.26 the assumption that the athermal contribution to the gas release from the HBS also applies to the transition zone results in a lower local fission gas release in the HBS of <34%. This is consistent with the

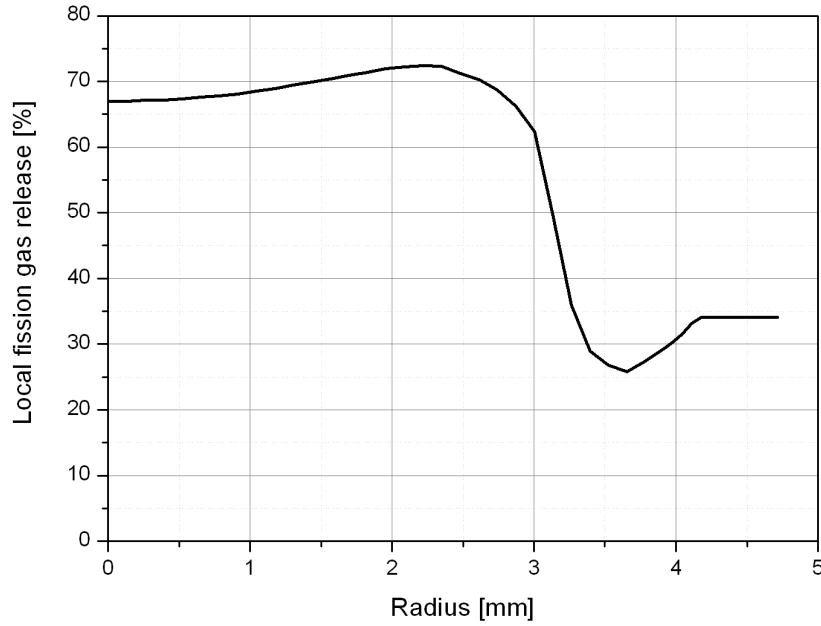


Figure 5.26. Radial distribution of the athermal contribution to the pellet periphery release to take into account HBS volumes present in the transition zone.

estimates of fission gas release provided by Manzel and Walker [15]; however, it is clear that there is a mismatch with the data from Horvath [10]. Care must be taken here though as the HBS is highly heterogeneous and the estimate of the fission gas release in [10] has uncertainties associated with it other than just statistical errors in the measurements.

5.5.4 Effect of changes in the surface-to-volume ratio

The original correlation for gas release was generated upon the assumption that the surface-to-volume ratio is approximately constant and low; however, the possibility of cracking in the outer region of the fuel could raise the surface-to-volume ratio. In order to examine as to whether changes in this parameter could account for the observed high fission gas release, several correlations at different values of the surface-to-volume ratio were generated. Table 5.8 shows the fitting parameters for each surface-to-volume ratio.

Table 5.8. Coefficients for the 5th order polynomial fits to the absolute gas release (see equation 5.17) at different surface-to-volume ratios

Coefficient	Surface-to-volume ratio [m ⁻¹]			
	2×10^4	3×10^4	4×10^4	1×10^5
a_0	-5.0879×10^{30}	-8.06594×10^{30}	-1.01686×10^{31}	-8.24726×10^{31}
a_1	1.7734×10^{32}	2.84698×10^{32}	3.63069×10^{32}	3.10396×10^{33}
a_2	-2.4565×10^{33}	-3.99652×10^{33}	-5.15940×10^{33}	-4.65710×10^{34}
a_3	1.6906×10^{34}	2.78937×10^{34}	3.64796×10^{34}	3.48209×10^{35}
a_4	-5.7823×10^{34}	-9.68317×10^{34}	-1.28381×10^{35}	-1.29764×10^{36}
a_5	7.8742×10^{34}	1.33914×10^{35}	1.80111×10^{35}	1.92883×10^{36}

The above parameters have been used within the gas release correlation in TRANSURANUS and the fission gas release was calculated for the different surface-to-volume ratios. Figure 5.27 shows corresponding results for the integral fission gas release. It is seen that even at a high surface-

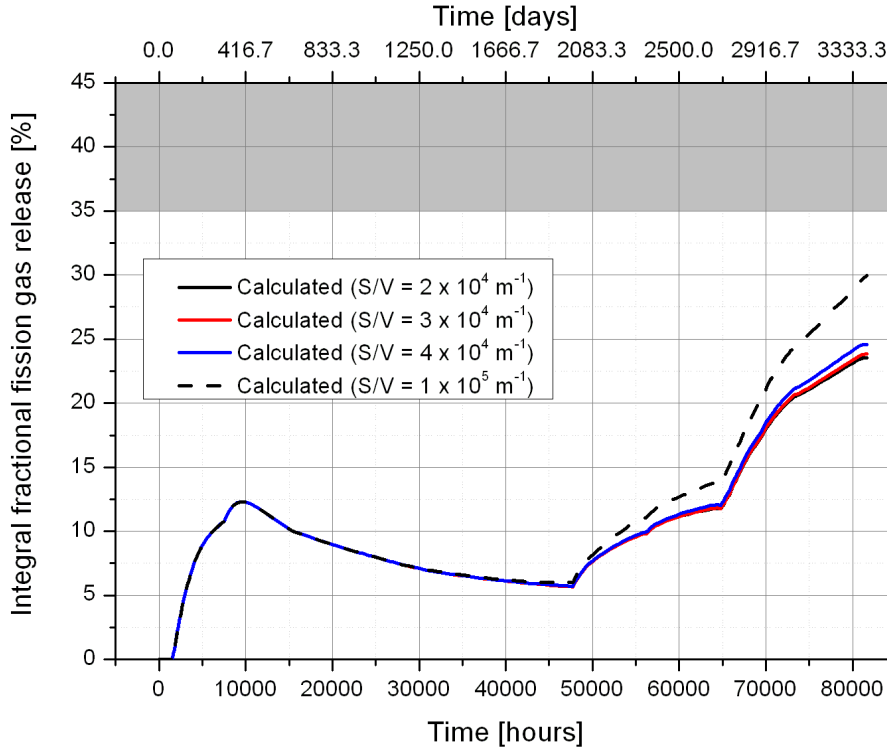


Figure 5.27. Integral fission gas release at different surface-to-volume ratios. The gray area indicates the region where the measured fission gas release lies.

to-volume ratio, which is of the same order as that seen during interlinkage of grain boundary bubbles in the normal structure, the integral gas release still falls short of the measured value. If we examine the radial distribution of the fission gas release (figure 5.28) we can see that the reason is that, although a higher surface-to-volume ratio produces a higher release, this effect is limited to the pellet periphery. Consequently the contribution to the global release is minimal. This is mainly due to the fact that the growth of the HBS porosity is burnup dependent and consequently any release from the porosity will follow the radial burnup profile. In conclusion it seems unlikely that an increase in the surface-to-volume ratio alone could account for the discrepancy between measurement and calculation, although it may still play a role.

5.5.5 Effects of other uncertainties

In the previous sections we have examined the effect of uncertainties in various quantities of significance to the fission gas release, specifically the fuel centre temperatures and the release from the HBS as calculated by the integrated HBS model. Although these are of significant interest there are other uncertainties that cumulatively could account for the discrepancy between measured and calculated fission gas release. For example the release from the central fuel region (i.e. normal fuel microstructure) is primarily controlled by the diffusion behaviour of the fission

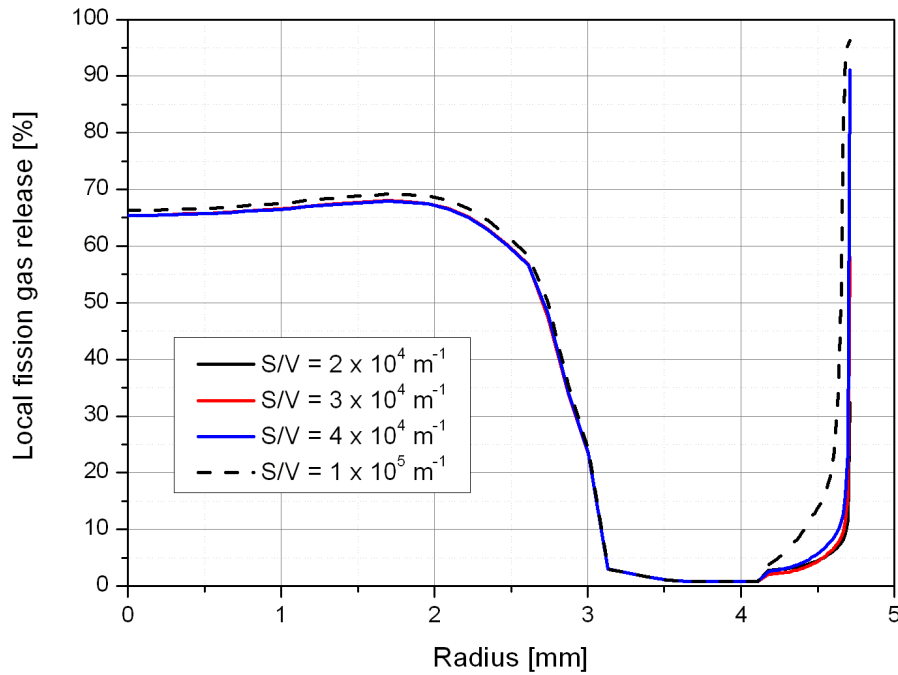


Figure 5.28. Radial distribution of fission gas release at EOL at a position ≈ 3046 mm from the rod end for several different values of the surface to volume ratio.

gas, and consequently uncertainties in the diffusion coefficient could contribute to an increased gas release. We can also examine such effects by considering the uncertainty in the radial fission gas release profile in a general way that will encompass parameters not considered earlier. To do this without considering each process individually we consider the uncertainty in fission gas release for three particular features of the radial fission gas release, specifically:

- Gas release in the centre of the fuel pellet.
- Width of the central region of the fuel where thermally activated release is dominant.
- Gas release in the HBS and transition zones of the pellet.

By considering a change for each of these features we can examine the change in the pellet average fission gas release to see the effect. Figure 5.29 shows schematic diagrams of the various changes considered here.

Table 5.9 shows the change in the pellet average fission gas release for the different types of adjustments of the radial fission gas release profile. In each case we estimate the effect on the pellet average fission gas release for two different values of the change considered. For the case of the shift in the position of the drop from the central high fission gas release we can consider that the width of the central thermal release zone² has an associated uncertainty but would not be expected to vary by more than $100 \mu\text{m}$; however, to see the effect of a major shift we have also considered a shift of $500 \mu\text{m}$.

It is clear that each effect on its own is not significant enough to resolve the discrepancy between the calculated and measured fission gas release, with the exception of the uncertainty in the

²By adjusting this width we are implicitly considering uncertainties in the temperature gradient and the temperature dependence of the diffusion coefficient.

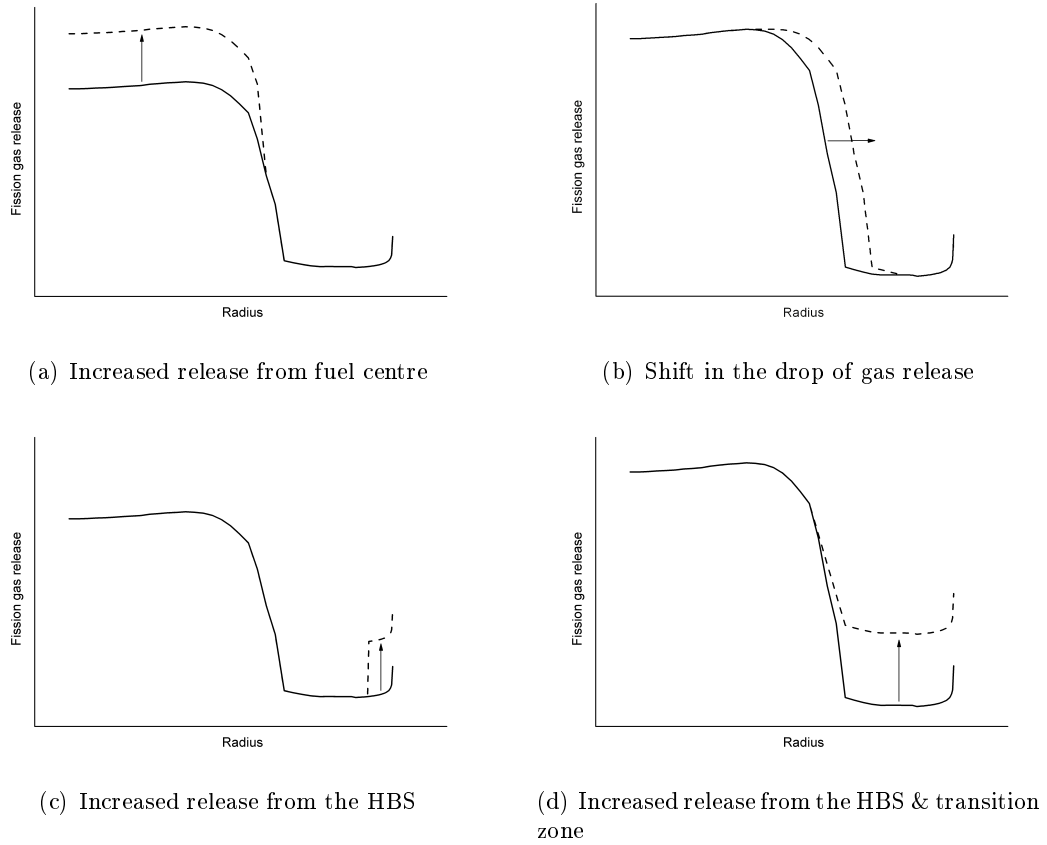


Figure 5.29. Schematic diagrams of adjustments made to the radial fission gas release profile to estimate the effects of other general uncertainties.

Table 5.9. Increase in pellet average fission gas when taking into account increased release from several regions across the pellet radius

Change to the radial release profile	Schematic	Increase in pellet average FGR ^a , $\Delta \langle FGR \rangle$
10 % increase in central release	5.29(a)	3.0 %
20 % increase in central release	5.29(a)	6.0 %
100 μm shift in release drop	5.29(b)	2.0 %
500 μm shift in release drop	5.29(b)	6.4 %
10 % increase in HBS release	5.29(c)	2.1 %
20 % increase in HBS release	5.29(c)	4.2 %
10 % increase in HBS & transition zone release	5.29(d)	7.3 %
20 % increase in HBS & transition zone release	5.29(d)	14.5 %

^a Increase is with respect to the base case value of integral release (see section 5.5.1).

gas release from the HBS and transition zone. In the previous section we considered the effect of athermal release on the integral fission gas release and found that we required a significant release from the HBS ($\sim 60\%$) in order to be consistent with the measured integral fission gas release. In addition we also saw that by taking into account the transition zone HBS volumes we required much less local gas release across the HBS and transition regions ($\approx 34\%$ in the HBS volumes). In table 5.9 we also see that a considerable local increase in the HBS gas release is needed to have a significant increase in the pellet average gas release, whereas considering both

the HBS and transition zone release results in a much stronger effect on the pellet average fission gas release. This is due to the volume over which the increase takes place; specifically, the HBS and transition zones together make up $\approx 2/3$ of the pellet volume and the effect is much greater than when considering the HBS zone alone.

Another point to note is that uncertainties in the central release and width are not enough to provide a significant increase in the pellet gas release; consequently while they might contribute to the discrepancy between measured and calculated gas release, it is unlikely that they provide the main contribution.

It is clear from both this and the previous sections that uncertainties in gas release processes in each of the fuel regions can contribute to the difference between measured and calculated fission gas release. The dominant region is seen to be the HBS volumes in the transition and HBS regions, simply because of the large volume fraction. We would however expect each of the uncertainties (power history, fuel centre temperatures, diffusion coefficients, HBS release, etc.) to contribute to the discrepancy to a greater or lesser degree. Consequently it is perhaps unreasonable to consider any single one uncertainty as an explanation for the difference between measurement and calculation.

5.6 Summary

The model of porosity growth and venting developed in chapter 4 has been extended to take into account the production, annihilation and capture of irradiation induced vacancies and interstitials and the transport of fission gas to the porosity. For steady-state conditions that are typical of the pellet periphery in LWRs we find good agreement with existing data on porosity growth in the HBS. A real irradiation history has been modelled and good agreement is found between the calculation of porosity growth and the PIE results. The model predictions for both steady-state and the real irradiation calculations are consistent with the observations made in chapter 4 regarding the comparison between annealing and in-pile porosity growth, in particular the venting of the porosity results in a local fission gas release from the HBS that is less than 20 % of the gas in the HBS porosity. This is consistent with estimates of fission gas release from Manzel and Walker [15] and Horvath *et al.* [10] .

A gas release and porosity correlation has been developed from the stand-alone modelling of porosity growth and has been implemented into the fuel performance code TRANSURANUS. This correlation controls the gas release due to pore venting. A high burnup irradiation has been modelled using the modified version of TRANSURANUS with the correlation implemented.

The fuel performance analysis has revealed that the effect of venting from the HBS has a small effect on the integral fission gas release with the release increasing towards the pellet periphery. The principle effect of the HBS for this irradiation is the presence of the high porosity, which increases the fuel centre temperatures and therefore the fission gas release from the centre of the rod. The base case, i.e. calculation of fuel performance without adjustment of model parameters, results in 22 % of the integral fission gas being released. However, this is less than that measured by rod puncturing.

Several sensitivity studies have been performed to investigate where the additional fission gas release originates, specifically from the fuel centre and/or the HBS zones in the pellet periphery. The effect of the fuel centre temperature (and therefore release from the fuel centre) has been examined by varying the gap conductivity. It has been found that for a gap conductivity that is reduced by a factor of 0.4 with respect to the TRANSURANUS correlation it is possible to match the integral fission gas released measured during PIE. However, this results in clad lift-off and thermal feedback. The resulting fuel centre temperatures are consistent with temperatures at which restructuring should occur, i.e. grain growth, pore migration and columnar grain formation. Although grain growth has been observed, pore migration and columnar grain formation was not seen during PIE. Moreover, detailed examination of the fuel has revealed pellet-clad bonding that will act to restrict the opening of a gap. Consequently it seems unlikely that temperatures in the fuel centre increased to the high level corresponding to clad lift-off, which would be needed to explain the discrepancy between the calculation and measured results. However, this does not rule out the possibility that fission gas release in the centre is under-predicted by the PSI fission gas model implemented in TRANSURANUS.

To examine the effect of the gas coming from the periphery, i.e. the HBS, an athermal release term was added to the HBS region, such that the integral gas release is approximately the same as that measured during rod puncturing. It was seen that even adding a relatively small athermal release ($\sim 10\%$ local fission gas release) from the HBS induces a clad lift-off scenario similar to that resulting from variation of the centre temperatures. However, as was seen earlier the total release from the centre due to pore migration is unlikely due to the absence of certain microstructural features.

To determine exactly how much fission gas release from the HBS without clad lift-off would be necessary to match the observed integral fission gas release the TRANSURANUS calculation was forced to restrict the opening of the gap by raising the coolant pressure and reducing the fast neutron flux. When this was done it was found that $\sim 60\%$ of the HBS-created gas needs to be released to match the experimental fission gas release. This is significantly larger than gas releases derived from LA-ICP-MS measurements and consequently seems highly unlikely. Based on the assumption that the gas release from the HBS postulated in this work may also apply to the transition zone, the release for both the HBS and transition zones was found to lower the required local fission gas release from HBS volumes to $< 34\%$.

The original correlations were generated upon the assumption that the surface-to-volume ratio is approximately constant. In order to examine changes in this parameter could account for the high observed fission gas releases, several correlations at different values were generated. However, for values in the range that is physically acceptable, agreement with the measured fission gas release could not be achieved.

In general it seems unlikely that the discrepancy between the calculated and measured fission gas release can be accounted for by extra release from the fuel centre alone, and a significant contribution from the pellet periphery seems necessary. The presence of an athermal gas release from within the HBS has been explored and it has been shown that, while significant release should occur, there is still considerable retention. Previous examinations of fuel behaviour have assumed little to no release from the HBS; however, it is clear from the present analysis that at

very high burnups the gas release does have a component coming from the pellet periphery.

Bibliography

- [1] J. M. Griesmeyer, N. M. Ghoniem, and D. Okrent. A dynamic intragranular fission gas behavior model. *Nucl. Eng. Des.*, 55:69–95, 1979.
- [2] A.D. Brailsford and R. Bullough. The theory of sink strengths. *Philos. Trans. Royal Soc. A*, 302(1465):87–137, 1981.
- [3] K. Nogita and K. Une. Thermal recovery of radiation defects and microstructural change in irradiated UO_2 fuels. *J. Nucl. Sci. Technol.*, 30(9):900–910, 1993.
- [4] K. Nogita and K. Une. Radiation-induced microstructural change in high burnup UO_2 fuel pellets. *Nucl. Instrum. Meth. B.*, 91:301–306, 1994.
- [5] K. Nogita and K. Une. High resolution TEM of high burnup UO_2 fuel. *J. Nucl. Mater.*, 250:244–249, 1997.
- [6] D. R. Olander. *Fundamental aspects of nuclear reactor fuel elements*. Energy research and development administration, 1976.
- [7] H. J. Matzke. Atomic transport properties in UO_2 and mixed oxides $(\text{U,Pu})\text{O}_2$. *J. Chem. Soc. Farad. T. 2.*, 83:1121–1142, 1987.
- [8] M. Kinoshita. Towards the mathematical model of rim structure formation. *J. Nucl. Mater.*, 248:185–190, 1997.
- [9] M. S. Veshchunov. On the theory of fission gas bubble evolution in irradiated UO_2 fuel. *J. Nucl. Mater.*, 277:67–81, 2000.
- [10] M. I. Horvath. *Development of a Method for Xenon Determination in the Microstructure of High Burn-up Nuclear Fuel*. PhD thesis, Swiss Federal Institute of Technology Zürich, 2007.
- [11] M. Kinoshita, T. Sonoda, S. Kitajima, A. Sasahara, T. Kameyama, T. Matsumura, E. Kolstad, V. V. Rondinella, C. Ronchi, J. P. Hiernaut, T. Wiss, F. Kinnart, J. Etjon, D. Papaioannou, and H. J. Matzke. High burnup rim project: (III) Properties of Rim-structured fuel. In *Proceedings of the 2004 International Meeting on LWR Fuel Performance*, Orlando, Florida, 2004.
- [12] J. Spino, A. D. Stalios, H. Santa Cruz, and D. Baron. Stereological evolution of the rim structure in PWR-fuels at prolonged irradiation: Dependencies with burn-up and temperature. *J. Nucl. Mater.*, 354:66–84, 2006.
- [13] K. Nogita and K. Une. Irradiation induced recrystallization in high burnup UO_2 fuel. *J. Nucl. Mater.*, 226:302–310, 1995.
- [14] J. Spino, K. Vennix, and M. Coquerelle. Detailed characterisation of the rim microstructure in PWR fuels in the burn-up range 40-67 GWd/tM. *J. Nucl. Mater.*, 231:179–190, 1996.

- [15] R. Manzel and C. T. Walker. EPMA and SEM of fuel samples from PWR rods with an average burn-up of around 100 MWd/kgHM. *J. Nucl. Mater.*, 301:170–182, 2002.
- [16] K. Lassman, C. T. Walker, J. van de Laar, and F. Lindström. Modelling the high burnup UO_2 structure in LWR fuel. *J. Nucl. Mater.*, 226:1–8, 1995.
- [17] H. Wallin, L.Å. Nordström, and Ch. Hellwig. Fission gas model of the fuel code SPHERE–3. In *Proceedings of the IAEA/NEA/CEA International Seminar on Fission Gas behaviour in Water Reactor Fuels*, pages 391–406, Cadarache, France, September 2000.
- [18] C. Hellwig and P. Blair. Final implementation of the SPHERE fission gas model into TRANSURANUS. Technical Report TM-43-03-19, rev.1, Paul Scherrer Institut, apr 2004.
- [19] M. V. Speight. A calculation on the migration of fission gas in material exhibiting precipitation and re-resolution of gas atoms under irradiation. *Nucl. Sci. Eng.*, 37:180–185, 1969.
- [20] J. A. Turnbull, C. A. Friskney, J. R. Findlay, F. A. Johnson, and A. J. Walter. The diffusion coefficients of gaseous and volatile species during the irradiation of uranium dioxide. *J. Nucl. Mater.*, 107:168–184, 1982.
- [21] R.J. White and M.O. Tucker. A new fission-gas release model. *J. Nucl. Mater.*, 118:1–38, 1983.
- [22] M. Kinoshita. Mesoscopic approach to describe high burnup fuel behavior. In *Enlarged Halden Programme Group Meeting 1999*, volume 1. OECD Halden Reactor Project, may 1999.
- [23] M. Avrami. Kinetics of Phase Change. I General Theory. *J. Chem. Phys.*, 7:1103, 1939.
- [24] M. Avrami. Kinetics of Phase Change. II Transformation-Time Relations for Random Distribution of Nuclei. *J. Chem. Phys.*, 8:212, 1940.
- [25] M. Avrami. Granulation, Phase Change, and Microstructure - Kinetics of Phase Change. III. *J. Chem. Phys.*, 9:177, 1941.
- [26] J. Spino, D. Papaioannou, and J.-P. Glatz. Comments on the threshold porosity for fission gas release in high burn-up fuels. *J. Nucl. Mater.*, 328:67–70, 2004.
- [27] L. Noirot, Ph. Garcia, and C. Struzik. A mechanistic fission gas behaviour model for UO_2 and MOX fuels. In *Proceedings of the IAEA/NEA/CEA International Seminar on Fission Gas behaviour in Water Reactor Fuels*, Cadarache, France, September 2000.
- [28] S. Béguin. The lift-off experiment IFA-610.1 – Initial Results. Technical Report HWR-544, OECD Halden Reactor Project, jan 1998.

Chapter 6

Conclusions and recommendations for future work

I am turned into a sort of machine for observing facts and grinding out conclusions.

- C. Darwin

The present study has focussed on the development and evaluation of high burnup structure (HBS) fission gas transport models, with a view to improve upon the current gap in fuel performance modelling. In particular two features of the HBS have been focussed on, viz. (1) the equilibrium xenon concentration in the matrix of the HBS in UO_2 fuel pellets and (2) the growth of the HBS porosity and its effect on fission gas release. In the first phase a steady-state fission gas model was developed to examine the effect of various transport processes on the fission gas migration in the HBS, and in particular the effect on the equilibrium xenon concentration. In the second phase a model describing the evolution of the HBS porosity under annealing and in-pile conditions was developed. The porosity growth model takes into account the growth and coalescence of the HBS porosity and the resulting fission gas release that occurs when the HBS porosity comes into contact with the free surface. The correlation based upon this model has been integrated into a fuel performance code and used to evaluate the effect of the HBS on the integral fission gas release at high burnups.

The following sections summarise the work performed, the main achievements and recommendations for further work.

6.1 Summary

The first chapter of the thesis serves to introduce the reader to the present study by describing the general framework for its realisation. The principal aim of the second chapter is to provide an overview of the current state-of-the-art concerning fission gas behaviour and HBS research.

Chapter 3 focuses on the development and application of a one-dimensional fission gas model describing the steady-state concentrations of xenon in the matrix of the HBS. The results of

a sensitivity study with respect to the principal parameters of the developed equation set are presented and compared with the measured xenon concentration in the HBS matrix. Finally, conclusions are drawn regarding the impact of the results on the modelling of HBS fission gas behaviour in fuel performance codes.

Chapter 4 presents the development of a model describing the growth of the HBS porosity under annealing conditions. A gas release model is developed that takes into account the growth of pores, interactions with the open surface and higher-order compound interactions. A sensitivity analysis is presented evaluating the effect of parameters such as temperature and the surface-to-volume ratio on the fission gas release under static conditions. The model is then applied to a high burnup light water reactor (LWR) UO_2 annealing experiment to assess its predictions. The implications of the results from the annealing case for in-pile behaviour are discussed.

Chapter 5 concerns the extension of the annealing porosity growth model to in-pile conditions. First, this model is used to simulate the local behaviour of the HBS in a pellet taken from a fuel rod irradiated to very high burnup in a Swiss nuclear power plant (NPP). The results are also compared with those from open literature. From the analysis of the in-pile behaviour, a correlation describing the evolution of the fission gas release is developed. This correlation is then implemented into the fuel performance code TRANSURANUS. The code is then used to model the irradiation of the complete experimental fuel rod and evaluate the consequences for fuel performance. In particular the effects of uncertainties in variables such as temperature and HBS release are discussed.

6.2 Main achievements

As sketched above, the principal aspects of the research presented in this thesis are: (i) the development of models to evaluate the impact of the HBS on the fission gas behaviour in nuclear fuel under annealing and in-pile conditions (chapters 3, 4 and 5), and (ii) the analysis of the impact of the HBS on fuel performance using a correlation-based approach in the TRANSURANUS code (section 5.5 in chapter 5).

Steady-state modelling of the HBS

In the first step a steady-state fission gas model was developed to examine the importance of grain boundary diffusion for the gas dynamics in the HBS. A stable solution was achieved for the set of parameters used in common fission gas models combined with parameter values specific to the HBS. With this model it was possible to simulate the 0.2 wt% experimentally observed xenon concentration under certain conditions, i.e. fast grain boundary diffusion and a reduced grain diffusion coefficient.

The sensitivity study conducted has shown that the value of the grain boundary diffusion coefficient is not important for diffusion coefficient ratios above $\sim 10^4$. However, in the limit of “slow” grain boundary diffusion a sizeable effect on the calculated xenon depletion value is obtained. Within the grain boundary diffusion saturation regime the model exhibits a high sensitivity

to three principal parameters: the grain diffusion coefficient, the bubble number density and the re-resolution rate coefficient. A detailed examination of the sensitivity with respect to these parameters has shown that:

1. The grain diffusion coefficient is the crucial parameter in the model due to its high sensitivity and because most of the gas contributing to the averaged xenon concentration is in the grains.
2. At bubble densities below 10^{13} m^{-2} there is a secondary saturation in the averaged xenon concentration with respect to the bubble density, i.e. decreasing the bubble density no longer has any effect on the equilibrium xenon concentration.
3. If the re-resolution rate is high then the sensitivity to the bubble density is severely reduced, whereas at lower re-resolution rates the sensitivity is important. However, the bubble density saturation is still apparent at low re-resolution rates.

All of these observations have been presented within a single “locus” plot, which illustrates the necessary combination of these parameters for the 0.2 wt% concentration. It is clear from this “locus” plot that at low re-resolution rates all three parameters are of relevance. Of particular significance is the relatively small range of required values for the grain diffusion coefficient. In spite of the uncertainties in the input parameters it is clear that this model can reproduce the observed HBS xenon depletion with the assumption that grain boundary diffusion of fission gas is significantly faster than lattice diffusion. Moreover, it is also clear that the reduction of geometrical characteristics such as pore separation and grain size facilitates the maintenance of the xenon depletion. The fact that this can be maintained without considering a new transport process is an indication that gas transport within the HBS is similar to that found in normal structure.

In particular this model demonstrates that the release of produced gas from the grains to the HBS porosity corresponds to a dynamic equilibrium, providing justification for the typical modelling approach used in HBS fuel performance modelling, i.e. fast transport to the porosity. The present work thus suggests that the modelling strategy used in most fuel performance codes is an appropriate approach for describing the transport of fission gas in the HBS, which from a fuel performance modelling point of view greatly simplifies the simulations.

Porosity growth and fission gas release

Although the calculation of equilibrium xenon concentrations suggests that fast transport to the porosity is an adequate description of the fission gas transport in the HBS, it does not address the issue of what happens once the fission gas is in the HBS porosity. This question was addressed by introducing a model that describes the effects of the fission gas accumulation in the porosity. In a first phase we considered the behaviour of the porosity under annealing conditions as this provides a good way to examine the HBS in situations where temperatures are well characterised and the release of fission products can be monitored on-line. A temperature dependent gas release model was developed to examine the release due to porosity growth in the HBS. A stable solution was

achieved for LWR UO_2 fuel with typical stereological parameters for the HBS. The model was applied to a high burnup fuel annealing experiment to assess its predictions in comparison with experimental measurements. Reasonable agreement was found with respect to the experimental release measurements in the temperature range where the release mechanism was considered to be due to grain diffusion of the gaseous fission products. In contrast to the original analysis, this model interprets the release mechanism as being due to pore growth, coalescence and, ultimately, venting. Several general features of the porosity growth were observed to be independent of the model parameters, viz.:

- The porosity increases until it reaches a maximum value, after which it decreases at a slower rate.
- The pore number density continuously decreases.
- The gas release from the porosity is a continuous process and begins as soon as the number density starts to decrease, i.e. as soon as the transition to the HBS is complete.

A comparison of out-of-pile and in-pile release (with respect to porosity) indicates that, for burnups examined to date, the maximum porosity has yet to be reached. Consequently, most of the fission gas is expected to be retained within the HBS porosity. However, while this comparison is certainly conservative, the invariance in the features of the porosity evolution suggests that the main difference between out-of-pile and in-pile porosity growth will simply be a time-scale change.

Although annealing conditions provide a number of advantages for investigating the HBS porosity, the calculation of the evolution during irradiation is of significant interest. The model of porosity growth and venting developed for annealing conditions was extended accordingly to take into account the production, annihilation and capture of irradiation induced vacancies and interstitials. The power history of a high burnup fuel rod from a Swiss NPP has been used to model the local behaviour of the HBS and good agreement was found between the calculation of porosity growth and results from open literature. In addition a comparison between the calculated local gas release is consistent with measurements performed on the same fuel rod using Laser Ablation Inductively Coupled Plasma Mass Spectrometry (LA-ICP-MS). The model predictions for the in-pile conditions are also consistent with the observations made in chapter 4 with respect to the comparison between annealing and in-pile porosity growth, specifically:

- The maximum porosity has yet to be reached for all in-pile irradiations reported so far in open literature.
- The venting of the porosity results in a local fission gas release from the HBS that is less than 20 % of the gas in the HBS porosity.

Model implementation in TRANSURANUS

A gas release correlation for calculating the gas release due to pore venting has been developed from the stand-alone modelling of porosity growth and implemented into the fuel performance

code TRANSURANUS. The examined high burnup rod was modelled using TRANSURANUS with the correlation implemented so that the integral behaviour (rather than just the local HBS behaviour) could be calculated.

The fuel performance analysis has revealed that the effect of venting from the HBS has a small effect on the integral fission gas release with the release increasing towards the pellet periphery. The principal effect of the HBS for this irradiation is the presence of the high porosity, which increases the fuel centre temperatures and therefore the fission gas release from the centre of the rod. For the base case analysis 22 % of the integral fission gas was found to be released. However, this is less than the quantity measured by rod puncturing.

Several sensitivity studies have been performed to determine where the additional fission gas release originates, specifically the fuel centre and/or the HBS zones in the pellet periphery. The effect of the fuel centre temperature (and therefore release from the fuel centre) has been examined by varying the gap conductivity. It has been found that for a gap conductivity that is reduced by a factor of 0.4 with respect to the TRANSURANUS correlation it is possible to match the integral fission gas released measured during post irradiation examination (PIE). However, this high fission gas release was the result of clad lift-off and corresponding thermal feedback.

The calculated peak fuel centre temperatures would have caused fuel restructuring, i.e. grain growth, pore migration and columnar grain formation. Although some grain growth was observed in the PIE of the experimental rod, pore migration and columnar grain formation were not. Moreover, detailed examination of the fuel has revealed pellet-clad bonding that will act to restrict the opening of a gap. Consequently it seems unlikely that such a high sweep-out of fission gas from the pellet centre could be responsible for the discrepancy between the calculated and measured results. However, uncertainties other than those related to the fuel centre temperature could indeed contribute a part of the discrepancy in the integral fission gas release.

To determine how much fission gas release from the HBS (without clad lift-off) would be necessary to match the observed integral release, the TRANSURANUS calculation was forced to restrict the opening of the gap by increasing the coolant pressure and decreasing the fast neutron flux. Under these conditions $\sim 60\%$ of the HBS-created gas needs to be released to match the measured integral fission gas release. This is significantly larger than gas releases derived from LA-ICP-MS measurements and consequently seems highly unlikely. With the assumption that the gas release from the HBS postulated in this work may also apply to the transition zone, the release for both the HBS and transition zones was calculated, lowering the required local fission gas release to $<34\%$.

While determining the necessary quantity of gas released from the HBS to match the measured integral values provides a good indication, the mechanism of release is not made clear from such an analysis alone. We have explored one possibility, viz. changes in the HBS surface-to-volume ratio by events such as cracking, and have shown that while the gas release does increase it is not sufficient to meet the measured release. However, this does not exclude the possibility that changes in the HBS surface-to-volume ratio do play a role.

The investigation of uncertainties in release from the centre of the fuel and the HBS serve to illustrate the difficulty in modelling the extremely high burnup case examined. While the

uncertainties in the fuel centre temperature and the quantification of required release from the HBS were considered explicitly, there are several other types of uncertainties present. To address these we considered the effect of adjusting the fission gas distribution for three particular features of the radial profile, viz. the gas release from the centre of the fuel pellet, the width of the central region of the fuel where thermally activated release is dominant, and the gas release in the HBS and transition zones. It has been shown from this sensitivity analysis that extra release from just one of the fuel pellet regions is unlikely to account for the discrepancy between measured and calculated fission gas release. It is more likely that the uncertainties for each of the regions, when considered together, could account for the observed integral gas release. In particular the presence of an athermal gas release from within the HBS has been explored in detail and it has been shown that while significant release should occur there is still significant retention. Previous examinations of fuel behaviour have assumed little to no release in the HBS; however, it is clear from this work that, at burnups as high as considered currently, the gas release does have a significant component coming from the pellet periphery.

6.3 Recommendations for future work

The present study has focussed on the detailed description of fission gas transport and release in the HBS of LWR UO_2 fuel. While it was successful in clarifying the effect of fission gas transport and porosity growth on the residual fission gas concentrations in the fuel microstructure and on gas release, further work is required to address still open questions. The suggestions and recommendations for possible further work are given below.

Uncertainty in parameters for fission gas modelling

A large number of developed fission gas release models for both the normal structure and HBS feature a wide variety of processes with various degrees of uncertainty. In particular phenomena such as re-solution, lattice and grain boundary diffusion, etc. are understood in the theoretical sense but have significant uncertainties associated with their rates. This was seen in chapter 3 where we were compelled to estimate the equilibrium xenon concentration via a sensitivity study. It is clear that to correctly evaluate the capability and accuracy of a given model the values of parameters controlling the processes should be known with a reasonable accuracy. Consequently future work is needed to address this issue. Specifically, more accurate models of these sub-processes should be developed, e.g. by utilising single-effect tests.

Incorporation of additional processes in porosity growth

The growth of the porosity presents several features not investigated in the present work that would be valuable to study for both validating the modelling approach and understanding the behaviour of the HBS and its impact on fuel performance issues. In particular there are two features that should be explored in future:

1. Direct calculation of the pore growth/shrinkage once a pore has vented.

2. Extension of the modelling approach to include a pore size distribution.

In the first case, the extension of the modelling approach to include growth/shrinkage of the vented pores is necessary to evaluate the impact a vented pore has on the surface-to-volume ratio in the HBS. Measurements to date have indicated that the surface-to-volume ratio remains low up to significant burnups; however whether this remains the case at very high burnups has yet to be demonstrated. This is important because changes in the surface-to-volume ratio will influence the rate of fission gas release from the HBS porosity and consequently could be a factor in safety related considerations.

In the second case, the extension to include a pore size distribution instead of mono-sized pores is important as it will both serve as a validation of the modelling methodology and further bolster the predictions of fission gas release. If the modelling strategy is reasonable we would expect to see features such as multi-modal distributions to appear at ultra-high burnups, a feature that has been observed in a number of detailed PIE examinations of the HBS.

Modelling of other high burnup rods

It needs to be emphasised that we have carried out the detailed modelling of the integral fission gas release for only one particular high burnup fuel irradiation. Further calculations for other irradiations should be performed, although it is clear that experimental data for well characterised irradiations corresponding to burnups as high as in the present case are indeed sparse. It has long been known that there are significant difficulties in reproducing the fission gas releases from mechanistic models of fission gas behaviour, and so the single test considered currently may not be fully representative. Further validation steps could highlight strengths and weakness of the present modelling more clearly.

Application to transient tests

The present work has focussed on the behaviour of fission gas in the HBS under steady-state conditions; however, there is considerable interest in improved understanding of the behaviour during design based accidents, in particular under reactivity initiated accident (RIA) conditions. In particular we can consider two specific avenues for further modelling work in this context, viz. (1) using the models developed here to calculate the state of the fission gas inventory and porosity to serve as an input into a transient code, and (2) the extension of the present models, including the introduction of new mechanisms, to take into account transient behaviour.

6.4 Concluding remarks

In conclusion the present work has contributed to a better understanding of fission gas behaviour in the HBS indicating its impact on the retained/released concentrations of fission gas and the evolution of the HBS porosity under annealing and in-pile conditions. To the author's knowledge mechanistic modelling of both the retained matrix concentration of fission gas and the release

behaviour from the HBS porosity has not previously been explored in detail before. The models presented here provide a platform to further explore the effect of the transition from a normal fuel microstructure to the HBS on the fission gas inventory and the potential for release from the HBS porosity.

The developed models show several interesting features of fission gas and porosity behaviour that seem to be unique to the HBS. The importance of grain boundary diffusion for the maintenance of a stable xenon matrix concentration is of particular note and warrants further examination in the future. Modelling the fission gas release from the porosity has also highlighted the need for accurate measurements of the fission gas inventory in the fuel microstructure. We have predicted that most of the gas should be retained, which is consistent with measurements performed by LA-ICP-MS on the HBS; however, to the author's knowledge the experimental evidence at this point in time for being able to make this statement categorically is still lacking.

Appendix A

Percolation theory

The percolation model was introduced by Broadbent and Hammersley [1] in 1957 as an idealised model of diffusive processes in random media. Since its initial conception the model has been applied to a wide variety of problems including the permeability of porous rocks [2, 3], epidemic processes [4] and the quantum Hall effect [5]. A distinct characteristic of the model is the existence of a very sharp phase transition and in this context it has been extensively studied for a large number of spatial dimensions. The lattice percolation model is also related to several other discrete lattice phase transition models such as the Ising model and q -state Potts model. There are several different types of percolation models which are of immediate interest:

- Site Percolation
- Bond Percolation
- Continuum Percolation

Both site and bond percolation are performed on a lattice structure which in a theoretical treatment is assumed to be infinite in extent. For both these cases each site or bond¹ on the lattice geometry can be occupied with a probability p . This results in a percolation lattice with forms similar to those seen in figure A.1.

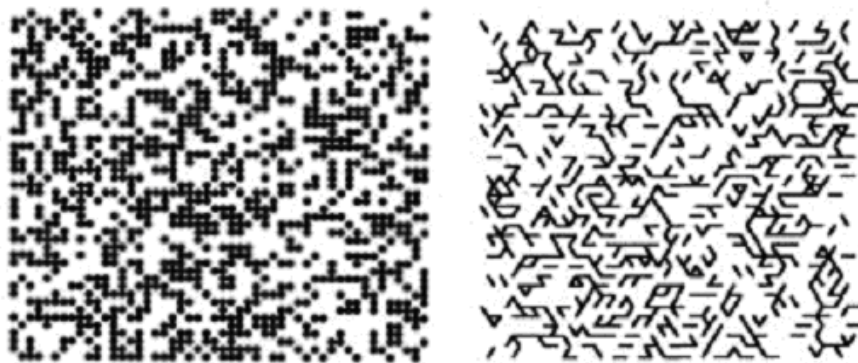


Figure A.1. Percolation lattices for site and bond percolation. Figures 3a and 4a from [6].

The interesting feature of this model, as has already been mentioned, is a sharp phase transition which manifests itself as the appearance of an infinite cluster of sites/bonds. This cluster only

¹Usually the model is either site *or* bond, but hybrid models do exist

appears when the probability of occupation/bond formation is greater than a certain value of the occupation probability which is thus known as the percolation threshold (p_c). It has been shown that for 2-D and 3-D problems there is either 1 (for $p \geq p_c$) or no (for $p < p_c$) infinite cluster [7, 8]. The value of the percolation threshold varies depending on lattice structure and is only known analytically for certain 2-D lattices and not at all in 3-D. Whilst analytical results are hard to come by Scher and Zallen [9] found that for each dimension there is a quantity which is approximately invariant and almost independent of the lattice type. This invariant is the critical fraction of space occupied by spheres and was found to be:

$$\phi_c = f \times p_c, \text{ where } f \text{ is the volume fraction filled by spheres.} \quad (\text{A.1})$$

In 3-D for a cubic structure, $\phi_c = 0.154 \pm 0.005$ and $f = \pi/8$ whilst for a 2-D square lattice, $\phi_c = 0.44 \pm 0.02$ and $f = \pi/4$. Whilst the lattice type can be quite important for the value of p_c , the behaviour of the percolation lattice as a function of p near p_c is universal. This means that only the lattice spatial dimension and not the lattice structure influences the behaviour near to the critical point. It can be shown that several quantities of interest vary like:

$$|p - p_c|^\alpha, \text{ where } \alpha \text{ is some critical and universal exponent.} \quad (\text{A.2})$$

In the case of magnetic phase transitions these important quantities include free energy, susceptibility and magnetisation in an external field.

So far only site and bond percolation has been presented but the third model, continuum percolation, is also of interest. Given the robustness of the critical exponents to lattice change a lattice may not be necessary and thus a continuum model can be used instead. This is also an advantage as a large number of phenomena do not have a perfect lattice structure. Continuum percolation typically falls into three variants:

1. Swiss cheese model [10]
2. Inverted swiss cheese model [11, 12].
3. Potential model

In the "swiss cheese" model a number of spherical voids are placed at random in a uniform transport medium and the spheres are allowed to overlap with each other. At a critical void volume fraction the infinite cluster of the transport medium ceases to exist. As should be apparent this model is essentially the inverse of the typical site and bond percolation models. In the "inverted swiss cheese" model the randomly placed spheres are the transport medium. This model is essentially the old site percolation model without a lattice and exhibits a phase transition above a certain sphere volume fraction.

In the third model (the potential model), a smooth random function, $\psi(x)$, is considered. The regions of interest in this case are those which satisfy the inequality $\psi(x) \leq h = \text{constant}$. For a low value of h the areas which satisfy the inequality are clearly isolated clusters. As h increases these clusters increase until an infinite cluster emerges at a critical value of h (h_c).

Bibliography

- [1] S. R. Broadbent and J. M. Hammersley. Percolation processes I. Crystals and mazes. *P. Camb. Philos. Soc.*, 53:629–641, 1957.
- [2] M. Sahimi. Hydrodynamic dispersion near the percolation threshold: scaling and probability densities. *J. Phys. A-Math. Gen.*, 20(18):L1293–L1298, 1987.

- [3] A. H. Thompson, A. J. Katz, and C. E. Krohn. The microgeometry and transport properties of sedimentary rock. *Adv. Phys.*, 36:625–694, 1987.
- [4] P. Grassberger. On the critical behavior of the general epidemic process and dynamical percolation. *Math. Biosci.*, 62:157, 1983.
- [5] S. A. Trugman. Localization, percolation, and the quantum hall effect. *Phys. Rev. B.*, 27:7539–7546, 1983.
- [6] M. B. Ishichenko. Percolation, statistical topography, and transport in random media. *Rev. Mod. Phys.*, 64:961–1043, 1992.
- [7] R. Kikuchi. Concept of long-range order in percolation problems. *J. Chem. Phys.*, 53(7):2713, 1970.
- [8] C.M. Newman and L.S. Schulman. Number and density of percolating clusters. *J. Phys. A-Math. Gen.*, 14(7):1735–1743, 1981.
- [9] H. Scher and R. Zallen. Critical density in percolation processes. *J. Chem. Phys.*, 53:3759–3761, 1970.
- [10] B.I. Halperin, S. Feng, and P.N. Sen. Differences between lattice and continuum percolation transport exponents. *Phys. Rev. Lett.*, 54(22):2391–2394, 1985.
- [11] A. S. Skal, B. I. Shklovsk, and A. L. Efros. Calculation of percolation level for 2-dimensional random potential. *Fiz. Tverd. Tela.*, 15(5):1423–1426, 1973.
- [12] G. E. Pike and C. H Seager. Percolation and Conductivity - Computer study I. *Phys. Rev. B.*, 10(4):1421–1434, 1974.

Appendix B

Gauss–Seidel method

The Gauss–Seidel method is an iterative technique for solving sets of linear equations that exhibit diagonal dominance in the coefficient matrix. Each simultaneous equation is rewritten so that the variable with diagonal dominance is expressed in terms of all other variables. Starting from a trial solution vector each rewritten equation is evaluated to yield a solution for a given variable. The crucial point with the Gauss–Seidel method is that each time a new value for an iterate is calculated the old value is discarded and the new value is used in all later calculations in the current iteration. The technique has the advantage that if the coefficient matrix is diagonally dominant then the technique is guaranteed to converge, no matter what the choice of the initial solution vector.

B.1 Mathematical formulation

For a system of N simultaneous equations with N unknowns we have:

$$\begin{pmatrix} a_{11} & \dots & a_{1N} \\ \vdots & \ddots & \vdots \\ a_{N1} & \dots & a_{NN} \end{pmatrix} \begin{pmatrix} x_1 \\ \vdots \\ x_N \end{pmatrix} = \begin{pmatrix} b_1 \\ \vdots \\ b_N \end{pmatrix} \quad (\text{B.1})$$

or more simply:

$$\mathbf{Ax} = \mathbf{b} \quad (\text{B.2})$$

Rewriting equation B.2 in terms of the variable with a strong diagonal coefficient:

$$\mathbf{x}^{(k)} = (\mathbf{D} - \mathbf{L})^{-1} (\mathbf{U}\mathbf{x}^{(k-1)} + \mathbf{b}) \quad (\text{B.3})$$

where k is the iteration count, $\mathbf{A} = \mathbf{D} - \mathbf{L} - \mathbf{U}$ and \mathbf{D} , \mathbf{L} , and \mathbf{U} represent the diagonal, lower triangular, and upper triangular parts of the coefficient matrix \mathbf{A} respectively. This matrix expression is not typically used to program the method. Instead an element-based approach is used:

$$x_i^{(k)} = \frac{1}{a_{ii}} \left(b_i - \sum_{j < i} a_{ij} x_j^{(k)} - \sum_{j > i} a_{ij} x_j^{(k-1)} \right), \quad i = 1, 2, \dots, n \quad (\text{B.4})$$

It is important to note that the calculation of $x_i^{(k)}$ only uses the elements of $x^{(k)}$ that have already been calculated and only those elements of $x^{(k)}$ that have yet to be advanced to iteration

$k+1$. Consequently no additional storage is needed and the calculation can be done in place, i.e. ($\mathbf{x}^{(k+1)}$ replaces $\mathbf{x}^{(k-1)}$). This becomes useful for large systems of equations where the storage of every iteration may become expensive. Generally the Gauss–Seidel iteration is continued until the solution satisfies some tolerance criteria.

B.2 Algorithm

The algorithm for calculating the \mathbf{x} in equation B.2 uses equation B.4 as follows:

```

Choose an initial guess  $\mathbf{x}^0$ ;
for  $k = 1$ , step 1 until convergence do
    for  $i = 1$  to  $N$  do
         $\sigma = 0$ ;
        for  $j = 1$  to  $i - 1$  do
             $\sigma + a_{ij}x_j^{(k)}$ ;
        end
        for  $j = i + 1$  to  $N$  do
             $\sigma + a_{ij}x_j^{(k-1)}$ ;
        end
         $x_i^{(k)} = \frac{(b_i - \sigma)}{a_{ii}}$ ;
    end
    check if convergence has been reached;
end

```

Appendix C

Derivation of equation for finding the equilibrium grain boundary bubble radius

C.1 Critical number of atoms per bubble for growth

Bubble growth/shrinkage occurs when there is a departure from mechanical equilibrium, e.g. pore over/under-pressurisation. Mechanical equilibrium occurs when the sum of all the forces acting on the bubble is equal to zero, which for the case of a bubble of size R_{gbb} in UO_2 can be expressed as:

$$p_{gbb} = \frac{2\gamma_{fs}}{R_{gbb}} - p_h \quad (\text{C.1})$$

where p_{gbb} is the internal gas pressure in the grain boundary bubble, γ_{fs} is the surface energy and p_h is the hydrostatic pressure. Equation C.1 is referred to as the capillarity condition and can be used to calculate the equilibrium radius of a grain boundary bubble containing $N_b^{fg}|_{crit}$ atoms of fission gas. First we consider the Van-der-Waals equation of state, i.e.:

$$p_{gbb} (V_{gbb} - \omega_{Xe} N_b^{fg}) = N_b^{fg} k_B T_K \quad (\text{C.2})$$

where ω_{Xe} is the Van-der-Waals constant for Xe gas ($\sim 8.5 \times 10^{-29} \text{ m}^3/\text{atom}$). Taking equations C.1 and C.2 we have:

$$p_{gbb} V_{gbb} - N_b^{fg} \omega_{Xe} p_{gbb} = N_b^{fg} k_B T_K \quad (\text{C.3})$$

$$p_{gbb} V_{gbb} = N_b^{fg} (k_B T_K + \omega_{Xe} p_{gbb}) \quad (\text{C.4})$$

$$N_b^{fg} = \frac{p_{gbb} V_{gbb}}{k_B T_K + \omega_{Xe} p_{gbb}} \quad (\text{C.5})$$

Taking the capillarity condition, equation C.1, and substituting for the pressure, p_{gbb} , in equation C.5 we find that the critical number of atoms for a bubble to be in equilibrium is given by:

$$N_b^{fg}|_{crit}^{tot} = \left(\frac{2\gamma_{fs}}{R_{gbb}} - p_h \right) \frac{V_{gbb}}{k_B T_K + \omega_{Xe} \left(\frac{2\gamma_{fs}}{R_{gbb}} - p_h \right)} \quad (\text{C.6})$$

Equation C.6 describes the critical number of atoms of fission gas per bubble that is required to satisfy the mechanical equilibrium condition, viz. equation C.1. If the quantity of gas per grain boundary bubble is less or more than this then the bubble will shrink or grow, respectively.

C.2 Calculation of the equilibrium radius

The maintenance of mechanical equilibrium, equation C.1 is controlled by a flux of defects to the pore providing the additional volume needed for relaxation of over-pressurisation due to the in-flux of fission gas atoms. Using equation C.6 we can derive an expression to calculate the grain boundary bubble radius for a mono-sized population of grain boundary bubbles where the total quantity of gas in the grain boundary bubbles is $N_b^{fg}|^{tot}$. First we consider that per grain there are $n_{gbb}A_{gr}$ grain boundary bubbles, where n_{gbb} is the surface density of grain boundary bubbles and A_{gr} is the surface area of the grain, which means that the total amount of fission gas on the grain boundary required to maintain mechanical equilibrium is given by:

$$N_{bl}^{fg}|_{crit}^{tot} = \left(\frac{2\gamma_{fs}}{R_{gbb}} - p_h \right) \frac{n_{gbb}A_{gr}V_{gbb}}{k_B T_K + \omega_{Xe} \left(\frac{2\gamma_{fs}}{R_{gbb}} - p_h \right)} \quad (C.7)$$

We want to calculate the grain boundary bubble radius that satisfies the capillarity condition for the total number of atoms of fission gas in the grain boundary bubble population, i.e.

$$N_{bl}^{fg}|_{crit}^{tot} = N_b^{fg}|^{tot} \quad (C.8)$$

or

$$N_b^{fg}|^{tot} = \left(\frac{2\gamma_{fs}}{R_{gbb}} - p_h \right) \frac{n_{gbb}A_{gr}V_{gbb}}{k_B T_K + \omega_{Xe} \left(\frac{2\gamma_{fs}}{R_{gbb}} - p_h \right)} \quad (C.9)$$

Considering that the volume of a grain boundary bubble can be written as:

$$V_{gbb} = \frac{4}{3}\pi R_{gbb}^3 f(\theta) \quad (C.10)$$

Here $f(\theta)$ is the lenticular factor and corrects the volume to take into account the fact that while grain boundary bubbles have a circular projection they are lenticular. Substituting equation C.10 into equation C.9:

$$0 = k_B T_K N_b^{fg}|^{tot} - \omega_{Xe} N_b^{fg}|^{tot} \left(p_h - \frac{2\gamma_{fs}}{R_{gbb}} \right) - \left(p_h - \frac{2\gamma_{fs}}{R_{gbb}} \right) n_{gbb}A_{gr} \frac{4}{3}\pi R_{gbb}^3 f(\theta) \quad (C.11)$$

and solving for the radius we find:

$$\begin{aligned} 0 = & R_{gbb}^4 \left[\frac{4}{3}\pi p_h f(\theta) n_{gbb}A_{gr} \right] - R_{gbb}^3 \left[\frac{8}{3}\pi \gamma_{fs} f(\theta) n_{gbb}A_{gr} \right] + \\ & + R_{gbb} \left[k_B T_K N_b^{fg}|^{tot} - \omega_{Xe} N_b^{fg}|^{tot} p_h \right] - 2\gamma_{fs}\omega_{Xe} N_b^{fg}|^{tot} \end{aligned} \quad (C.12)$$

As the quantity of gas within the grain boundary bubbles increases, equation C.12 is solved at each step to calculate the equilibrium radius of the grain boundary bubbles using the root finding methods described in appendix D.

Appendix D

Root finding

In general any equation with one independent variable (x) can be rearranged such that:

$$f(x) = 0 \tag{D.1}$$

Solving such an equation is generally referred to as “root finding”. If $f(x)$ is linear then the solution is trivial, however if it is nonlinear then one usually needs to employ iterative techniques to calculate the roots. In general there can be multiple roots and consequently some prior knowledge about the form of the function and the required roots is required to proceed. The solution scheme follows a specific pattern regardless of the method employed. First an initial “guess” is provided based upon some insight into the form of the function. This initial guess is input into an iterative algorithm that has the role of successively improving the estimate of the root. The iteration continues until some pre-determined convergence criterion is satisfied.

It should be emphasised that success crucially depends on having a good first guess for the solution; however, if the function is smoothly varying and a good initial “guess” is supplied then convergence can always be guaranteed. If the initial guess is not good enough the algorithm can result in divergence or cyclic behaviour instead of convergence. Consequently it is important to have checks within any algorithm to ensure that such behaviour is identified. One such check for divergence is to ensure that during the iteration the solution remains within a certain “bracket”. We can say that a root is “bracketed” in the interval (a, b) if $f(a)$ and $f(b)$ have opposite signs. According to the *intermediate value theorem*¹ if the function is continuous there should be at least one root in the interval (a, b) . This interval can be used to check that the initial guess does not result in divergence.

Once we know an interval contains at least one root we can use one of several procedures to iteratively improve the solution. Here we summarise two particular methods employed in this work, Bisection and the Newton–Raphson method.

D.1 Bisection

The bisection method is a robust method and is guaranteed to be successful provided the root has previously been bracketed. The idea is simple. Over some interval the function is known to pass through zero because of a change in the sign. The function is evaluated at the midpoint of the interval and the sign examined. This midpoint then replaces the interval endpoint that has the same sign. Consequently the interval reduces in size by half after each iteration. The number

¹The intermediate value theorem basically states that if function $f(x)$ is continuous in the interval (a, b) and N is a number between $f(a)$ and $f(b)$ then there has to be at least one c in the interval (a, b) such that $f(c) = N$.

of iterations required to achieve a certain tolerance (ϵ) when the initial bracketing interval has a size ϵ_0 can therefore be calculated, viz.:

$$n = \log_2 \frac{\epsilon_0}{\epsilon} \quad (\text{D.2})$$

In general bisection must succeed. However if we have multiple roots in the bracketing interval then bisection will find only one of them. In the case that the interval straddles a singularity bisection will converge on the singularity.

D.2 Newton–Raphson method with derivatives

Perhaps the most commonly used root finding algorithm is the Newton–Raphson method. The method relies upon the ability to calculate the value of the function and its derivative at arbitrary points in the bracketed interval. First we consider a Taylor expansion of our function $f(x)$ about the point $x_0 + \delta$, i.e.

$$f(x + \delta) = f(x) + f'(x)\delta + \frac{1}{2}f''(x)\delta^2 + \dots \quad (\text{D.3})$$

For small values of δ and a well behaved function the higher order nonlinear terms can be ignored. Consequently for $f(x + \delta) = 0$ we find

$$\delta = -\frac{f(x)}{f'(x)} \quad (\text{D.4})$$

If an initial guess of the root (x_0) is supplied a better approximation to the root can be obtained, viz.:

$$x_1 = x_0 + \delta \quad (\text{D.5})$$

$$x_1 = x_0 - \frac{f(x)}{f'(x)} \quad (\text{D.6})$$

Obviously this process can be repeated to improve the result further, such that after n applications the approximate value of the root is:

$$x_{n+1} = x_n - \frac{f(x_n)}{f'(x_n)} \quad (\text{D.7})$$

Figure D.1 illustrates the application of the Newton–Raphson method.

The Newton–Raphson method is powerful because of its convergence properties. We can consider that the estimates to the true root, x_i and x_{i+1} differ from the true root by:

$$x_i = r - \epsilon_i \quad (\text{D.8})$$

$$x_{i+1} = r - \epsilon_{i+1} \quad (\text{D.9})$$

Substituting equations D.8 and D.9 into equation D.7 we find:

$$\epsilon_{i+1} = \epsilon_i - \frac{f(r - \epsilon_i)}{f'(r - \epsilon_i)} \quad (\text{D.10})$$

Within a small distance of the true root, r , the function and its derivative can be approximated by Taylor expansions, viz.:

$$f(r - \epsilon) = f(r) - \epsilon f'(r) + \frac{1}{2}\epsilon^2 f''(r) + \dots, \quad (\text{D.11})$$

$$f'(r - \epsilon) = f'(r) - \epsilon f''(r) + \dots \quad (\text{D.12})$$

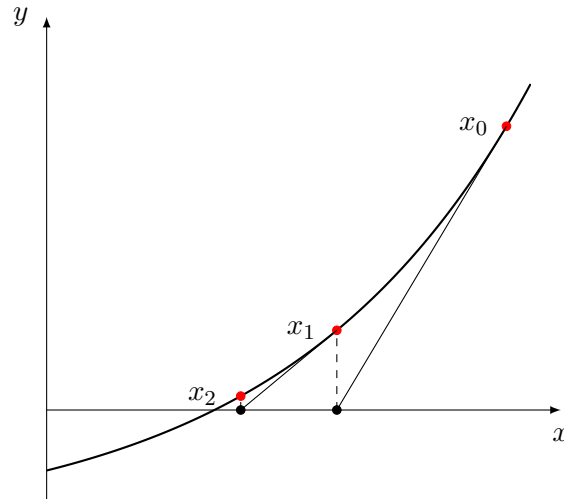


Figure D.1. Schematic showing the progression of the Newton–Raphson method for finding the root of a function of a single variable.

Substituting equations D.11 and D.12 into equation D.10 it can be shown that:

$$\epsilon_{i+1} = -\epsilon_i^2 \frac{f''(x)}{2f'(x)} \quad (\text{D.13})$$

Equation D.13 illustrates that Newton–Raphson converges quadratically and as a result provides a powerful technique for functions whose derivative is continuous and non-zero near the root. However equation D.13 also illustrates that if the initial guess is far enough away from the root such that the search interval contains a minimum or maximum then the method can send the solution to infinity. As was mentioned earlier the choice of the initial guess is vitally important and so care should be exercised. However, although Newton–Raphson suffers from poor global convergence properties, it can still be employed for “polishing” up the root after another more robust method (e.g. Bisection) has been employed.

Appendix E

TRANSURANUS–PSI fission gas release model and the HBS

E.1 The TRANSURANUS–PSI fission gas release model (SPHERE)

The Paul Scherrer Institute (PSI) SPHERE fission gas model [1] was developed in order to model the fission gas transport processes in a more realistic way. The model can calculate the fission gas release from different fuel types irradiated under different reactor conditions and provides an enhanced understanding of post irradiation examination (PIE) results. Several transport processes in the fuel grains and the grain boundaries are considered, viz.:

- Single atom diffusion.
- Grain and grain boundary trapping.
- Irradiation-induced re-solution.
- Grain boundary bubble inter-linkage resulting in fission gas release.

The model is based on work of Speight [2], Turnbull [3], White and Tucker [4] and was originally developed to model sphere-pac fuel [5, 6]. More recently the model has been integrated into the TRANSURANUS fuel performance code as part of the 5th European Union (EU) framework programme, producing the code version TRANSURANUS–PSI (details of the implementation can be found in [7]).

In its original form the SPHERE model divides the fuel into axial segments, which are further divided into radial cylindrical fuel elements (see figure E.1 for a schematic illustration). For the TRANSURANUS implementation of the fission gas model the radial discretisation follows the TRANSURANUS scheme viz.: TRANSURANUS divides the fuel axially into a number of slices. Within each axial slice the fuel and cladding are divided into a number of coarse rings. Each coarse ring is further divided into finer rings each of which is associated with a mesh point. At the boundary of adjacent coarse rings two mesh points with the same radial position exist. The number of fine mesh points in each coarse zone can take different values for each coarse zone allowing a finer discretisation to be specified in areas of interest. Figure E.2 illustrates the radial discretisation scheme in TRANSURANUS.

The TRANSURANUS–PSI fission gas model calculates the concentration of fission gas in the different phases (intra-granular bubbles, dissolved in the matrix, etc.) for each cylindrical fuel

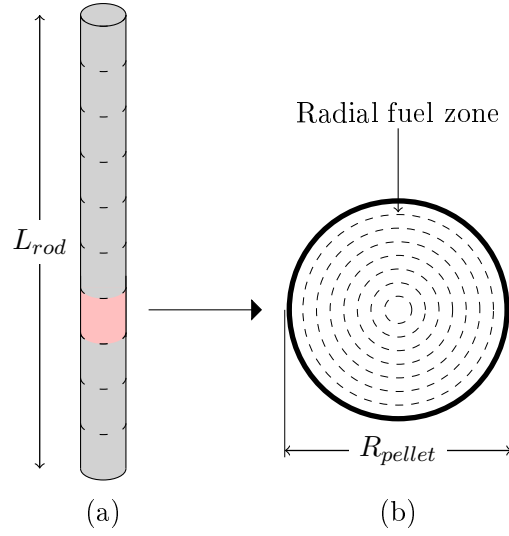


Figure E.1. Schematic showing how a fuel rod is discretised in the SPHERE fission gas release model (a) axially and (b) radially.

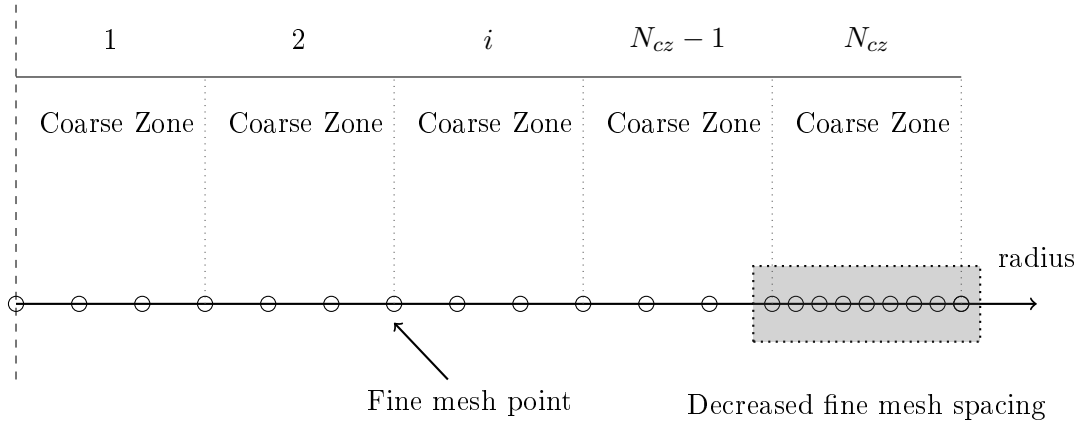


Figure E.2. Schematic illustrating the TRANSURANUS radial discretisation scheme for an axial slice.

element. The transport of the fission gas is calculated at the grain level with the resulting concentrations converted to fission gas quantities for the entire cylindrical fuel element volume. The fuel is considered as a collection of spherical grains of uniform size. Only the stable or long-lived nuclides are included in the model as the shorter ones decay to solid fission products during typical reactor operation histories. Inside the fuel grains gas atoms exist as single, freely diffusing atoms. After a short irradiation period, nanometre sized fission gas bubbles (later referred to as “bubbles”) are formed when gas atoms combine with point defects created by fission fragments. On the way out of the grain, gas atoms may become trapped at these immobile bubbles or at as-fabricated micrometer intra-granular pores (later referred to as “pores”). Bubbles nucleate in the wake of energetic fission fragments, and grow by absorbing single gas atoms before being destroyed by another fission fragment (intra-granular re-solution). Consequently, under steady conditions the bubble sizes and concentrations attain dynamic equilibrium values. After entering a grain boundary, atoms are immediately absorbed into grain boundary bubbles. Grain boundary bubbles grow until they are interlinked and excess gas after interlinkage is vented off, i.e. gas release is initiated. Because of re-solution from the grain boundaries back to the grain, grain boundaries act as an imperfect sink for diffusing gas atoms (inter-granular re-solution). A sketch of the modelled processes is given in figure E.3.

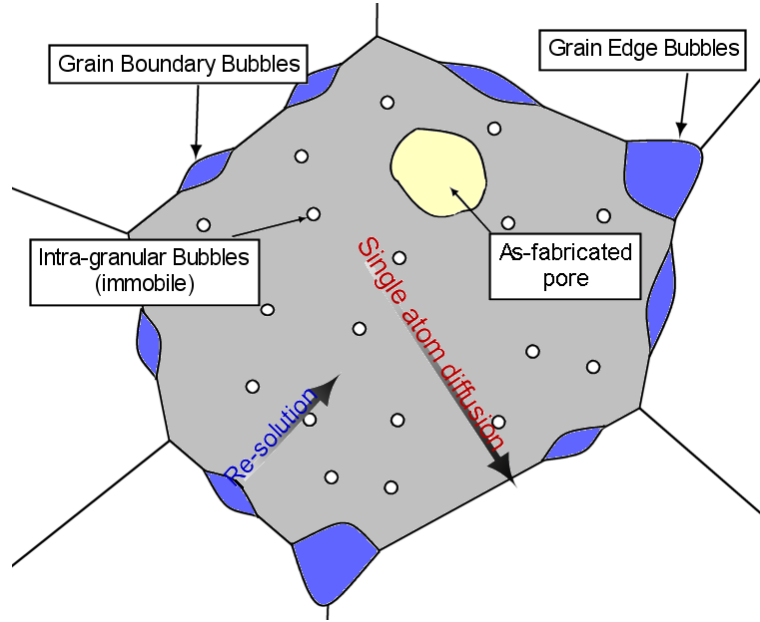


Figure E.3. A schematic of the processes considered in the PSI fission gas model showing the fission gas locations and the transport processes in the fuel grains and the grain boundaries.

The primary controlling factor in the transport of fission gas is single atom diffusion. The model has several options for the diffusion coefficient; however, the recommended equation for UO_2 is the Turnbull three-term equation (cm^2s^{-1}):

$$D = D_1^{fg} + D_2^{fg} + D_3^{fg} \quad (\text{E.1})$$

where:

$$\begin{aligned} D_1^{fg} &= 7.6 \times 10^{-6} \exp\left(\frac{-35000}{T_K}\right) \\ D_2^{fg} &= 4.84 \times 10^{-18} \sqrt{\dot{F}} \exp\left(\frac{-13800}{T_K}\right) \\ D_3^{fg} &= 2 \times 10^{-40} \dot{F} \end{aligned}$$

Here \dot{F} is the local fission rate density and T_K is the local temperature. At the moment it remains open as to whether the last, athermal term in equation E.1 should be zero for stable nuclides. It should be noted though that recent work has suggested that there is an athermal component for the stable fission gas isotopes as for the short-lived isotopes [8]. However, at moderate burnups, there is little release from the colder fuel regions, and consequently this is not significant as D_3^{fg} has an effect only at temperatures below 800°C .

The probability of absorption into bubbles and pores depends on the bubble/pore sizes and concentrations and they must therefore be integrated at the same time as the diffusion equation. In the absorption term the probability that a gas atom is captured by a bubble or an as-fabricated pore is calculated according to [2]. The bubble concentrations have a strong effect on the trapping of fission gas. The number of bubbles generated per fission, the range of influence for the path of fission spike and consequently the intra-granular bubble radius have large uncertainties associated with them. In spite of this it was found that the best results in modelling the Halden-Gösigen experiment IFA-550.9 [9] was achieved with Baker's empirical formula [4, 10]. Consequently this correlation is used for calculating the effect of re-solution on the intra-granular fission gas population. The re-solution of fission gas from intra-granular bubbles back to the matrix is caused either by simple collisional knock-on or through high temperature and pressure shocks created by fission spikes.

In UO_2 fission spikes are able to destroy a single fission bubble completely. As the bubbles are destroyed, the gas they contained is re-solved back to the fuel matrix. The intra-granular re-solution is modelled according to [11] with a correction for the bubble size distribution as shown in [4]. The effect of re-solution and knock-on from the as-fabricated pores is not explicitly considered as it is assumed that their large size prevents a significant loss of gas.

Gas release (interlinkage) occurs when the grain boundary bubbles cover the whole grain surface. Interlinkage (and gas release) can also be established before the grain boundary bubbles cover the whole grain surface, but in light of the IFA-550.9 [10] test results this was not considered necessary. This condition is slightly different than the maximum value of $5 \times 10^{15} \text{ atoms cm}^{-2}$, when the interlinkage and gas release starts [4, 11]; however, the values calculated by the PSI fission gas release model are quite close to that number.

A specific topic of interest is the gas release from the columnar grain area. At high temperatures (1600-1700 °C), fuel evaporates at the hotter side of a pore and condenses at the cooler side resulting in pore movement towards the rod centre. This process leaves behind columnar grains. In the PSI fission gas release model it is assumed that all fission gas (in fuel matrix, pores, on the grain boundary, etc.) is swept into moving pores and released into the rod open volume. If pore movement ceases at a later time then normal fission gas accumulation continues.

A minor shortcoming in this is that the fission gas release model assumes only equiaxed grains and cannot take into account the special shape of the columnar grains. However, this has no effect for normal thermal reactor temperatures, which are too low to create columnar grains. In fast breeder reactor (FBR) conditions this approximation is not important because gas is released from the columnar grains mainly by moving pores and not by gas diffusion. If the temperature decreases later to a lower level the release mechanism in the columnar grain zones would again be diffusional. However, the effect of this is limited, as:

- The characteristic distance that an atom must diffuse to arrive on the grain boundary is the width of the columnar grain, not its length. Therefore, if the columnar grain is approximated as a sphere, the fission gas diffusion to the grain boundary is only slightly overestimated.
- The grains have been “cleaned” of the fission gas by moving pores.
- Uncertainties in the subsequent smaller diffusional release have only a minor effect on total gas release.

E.2 Extension of TRANSURANUS–PSI for the HBS

The TRANSURANUS–PSI fission gas release model, as described above, is only applicable to fuel up to moderate burnups. Consequently to take into account the modified microstructure and fission gas distribution in the high burnup structure (HBS), the PSI model has been extended with respect to the HBS.

The extended model divides the fuel radius into three zones, normal structure, transition zone and HBS. The model considers a threshold in the grain xenon concentration to be the point at which transformation from normal structure to HBS is initiated. This is based on electron probe microanalysis (EPMA) measurements, which show that up to the burnup at which the transformation begins ($\approx 60\text{--}75 \text{ MWd/kg}$) the xenon concentration rises up to $\approx 1 \text{ wt\%}$. Afterwards this drops again until it reaches a stable value of $\approx 0.2 \text{ wt\%}$. Consequently in the present model the fuel microstructure is considered to start transforming once the xenon concentration in the grains has reached a certain threshold concentration. This method has the advantage that both

the local temperature and burnup are consolidated within one parameter. This is important as it has been previously demonstrated that above $1100 \pm 100^\circ\text{C}$ the HBS does not form. By using the xenon concentration the temperature is taken into account as the local concentration will be low if the average temperature at a particular radial point has been higher than this threshold.

To model the transformation once the xenon concentration threshold has been reached we have considered a correlation derived from that proposed by Kinoshita [12]. The correlation utilises a generic phenomenological description for the transformation of a microstructure called Kolmogorov–Johnson–Mehl–Avrami (KJMA) theory [13, 14, 15] to describe the transformation of the HBS. In the form presented by Kinoshita the local volume fraction of HBS in the microstructure, F_{HBS} , can be calculated as:

$$F_{HBS} = 1 - \exp\left(-k \left(\frac{B - B_0}{B_0}\right)^3\right) \quad (\text{E.2})$$

Here B is the local burnup in the fuel, B_0 is the local burnup at which the microstructure is transformed and k is the rate coefficient for the transformation. As was described in section 2.2.1 the transformation is generally accepted to be complete by a local burnup of $\approx 120 \text{ MWd/kg}$. However it should be noted that equation E.2 only asymptotically approaches a complete transformation from normal structure to HBS, i.e.

$$\lim_{B \rightarrow \infty} F_{HBS} = 1 \quad (\text{E.3})$$

As a consequence if we wish to divide the fuel radius into the three zones observable in high burnup fuel, i.e. normal structure, transition zone and HBS, then we require the transformation to HBS to be complete after a certain burnup increment, ΔB . To do this we calculate the rate coefficient such that when a volume of fuel equal to one HBS grain per normal structure grain is left untransformed we consider the transformation to be complete, viz:

$$F_{HBS}|_{\text{complete}} = 1 - \left(\frac{R_{gr}^{HBS}}{R_{gr}^{NS}}\right)^3 \quad (\text{E.4})$$

Here R_{gr}^{NS} is the radius of the unrestructured grain. We consider that at the point that equation E.4 is satisfied we can essentially say that the transformation is complete, i.e. $F_{HBS} = 1$. Using this and assuming that the transformation requires a burnup increment ΔB to be complete we can derive an expression for the rate coefficient, k :

$$k = \left(\frac{B_0}{\Delta B}\right)^3 \ln \left(\left(\frac{R_{gr}^{NS}}{R_{gr}^{HBS}}\right)^3\right) \quad (\text{E.5})$$

Using equations E.2 and E.5 we can calculate for a given burnup how much HBS exists locally. Figure E.4 shows the correlation for a starting burnup, B_0 , of 60 MWd/kg , a normal structure grain size of $R_{gr}^{NS} = 10 \mu\text{m}$, the HBS grain size of $R_{gr}^{HBS} = 0.1 \mu\text{m}$ and several different values of the burnup increment required to complete the transformation, ΔB .

Within each of the three microstructure zones the fission gas transport is calculated using three different submodels (see figure E.5). For the normal structure the PSI fission gas release model (as described in section E.1) is applied. During the transformation (i.e. $0 < F_{HBS} < 1$) the fission gas concentration is redistributed such that in the HBS volumes the concentration in the grains is 0.2 wt\% with the rest of the gas in the HBS porosity, while the normal structure fuel volume is untouched. Within this zone the PSI fission gas release model is only applied to the normal structure volume fraction.

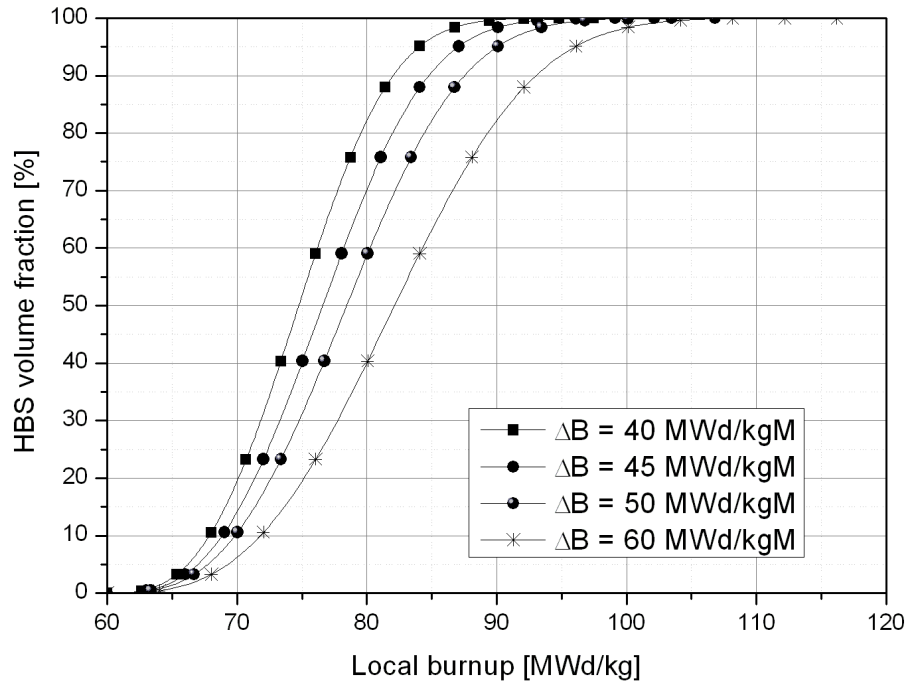


Figure E.4. Variation of the volume fraction of HBS as a function of local burnup for several different values of ΔB according to the correlation specified by equations E.2 and E.5.

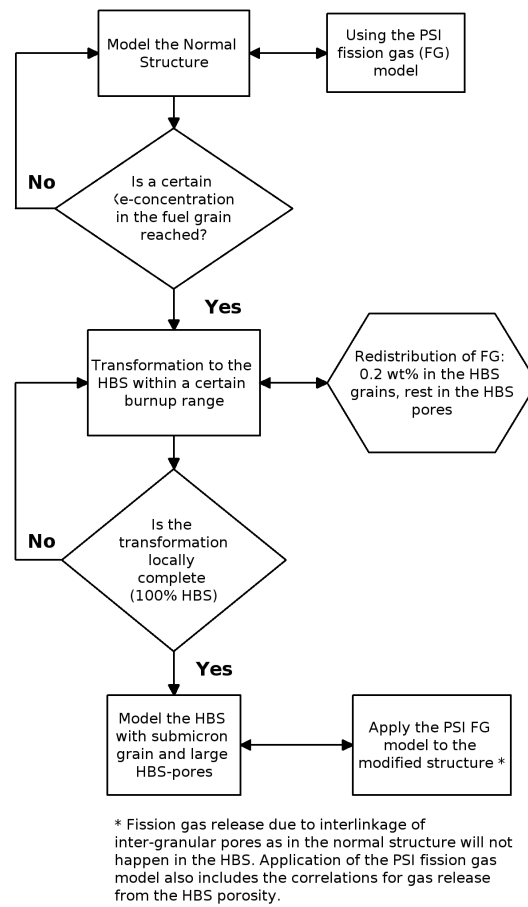


Figure E.5. A flowchart for the PSI HBS extension and its interaction with the PSI FGR model.

Once the microstructure has transformed completely at a particular radial position any generated gas is immediately transported to the HBS porosity (as was shown in chapter 3). In addition we have developed in chapter 5 correlations describing the development of the porosity and release of the fission gas from the HBS porosity. These correlations are used to specify the local porosity and the gas in the porosity for the completely transformed microstructure. TRANSURANUS calculates the fission gas release by summing up all the contributions to the gas inventory and then compares this with the created amount of gas. The difference between the two is then considered to be the fission gas release from the local radial position. By specifying the amount of gas remaining in the porosity the contribution of the HBS to the global fission gas release is calculated naturally as part of the TRANSURANUS calculation.

Bibliography

- [1] H. Wallin, L.Å. Nordström, and Ch. Hellwig. Fission gas model of the fuel code SPHERE-3. In *Proceedings of the IAEA/NEA/CEA International Seminar on Fission Gas behaviour in Water Reactor Fuels*, pages 391–406, Cadarache, France, September 2000.
- [2] M. V. Speight. A calculation on the migration of fission gas in material exhibiting precipitation and re-solution of gas atoms under irradiation. *Nucl. Sci. Eng.*, 37:180–185, 1969.
- [3] J. A. Turnbull, C. A. Friskney, J. R. Findlay, F. A. Johnson, and A. J. Walter. The diffusion coefficients of gaseous and volatile species during the irradiation of uranium dioxide. *J. Nucl. Mater.*, 107:168–184, 1982.
- [4] R.J. White and M.O. Tucker. A new fission-gas release model. *J. Nucl. Mater.*, 118:1–38, 1983.
- [5] R.W. Stratton, G. Ledergerber, F. Ingold, T.W. Latimer, and K.M. Chidester. Fuel fabrication processes, design and experimental conditions for the joint united-states-swiss mixed carbide test in FFTF (AC-3 test). *J. Nucl. Mater.*, 204:39–49, 1993.
- [6] R.W. Stratton. Preliminary-observations on irradiation behavior of hyperstoichiometric mixed-carbide SPHERE-PAC fuel. *T. Am. Nucl. Soc.*, 24:143–144, 1976.
- [7] C. Hellwig and P. Blair. Final implementation of the SPHERE fission gas model into TRANSURANUS. Technical Report TM-43-03-19, rev.1, Paul Scherrer Institut, apr 2004.
- [8] R. J. White. The fractal nature of the surface of uranium dioxide: a resolution of the short-lived/stable gas release dichotomy. *J. Nucl. Mater.*, 295:133–148, 2001.
- [9] L.Å. Nordström, H. Wallin, and Ch. Hellwig. A Comparative Irradiation Test of Pellet and Sphere-Pac Fuel (IFA-550.9). In *Enlarged Halden Programme Group Meeting 1999*, pages HPR-351/25. OECD Halden Reactor Project, 1999.
- [10] C. Baker. The fission gas bubble distribution in uranium dioxide from high temperature irradiated SGHWR fuel pins. *J. Nucl. Mater.*, 66:283, 1977.
- [11] J.A. Turnbull. An assessment of fission gas release and the effect of microstructure at high burn-up. Technical Report HWR-604, OECD Halden Reactor Project, mar 1999.
- [12] M. Kinoshita. Mesoscopic approach to describe high burnup fuel behavior. In *Enlarged Halden Programme Group Meeting 1999*, volume 1. OECD Halden Reactor Project, may 1999.
- [13] M. Avrami. Kinetics of Phase Change. I General Theory. *J. Chem. Phys.*, 7:1103, 1939.
- [14] M. Avrami. Kinetics of Phase Change. II Transformation-Time Relations for Random Distribution of Nuclei. *J. Chem. Phys.*, 8:212, 1940.
- [15] M. Avrami. Granulation, Phase Change, and Microstructure - Kinetics of Phase Change. III. *J. Chem. Phys.*, 9:177, 1941.

Acknowledgements

This research was carried out in the Laboratory for Reactor Physics and Systems Behaviour and the Laboratory for Materials Behaviour of the Paul Scherrer Institut (PSI), in the framework of the collaboration between PSI, EPFL and the Swiss nuclear power plants (*swissnuclear*).

This thesis could not have been achieved without the help and support of a wide variety of people. I am particularly grateful to:

- Prof. R. Chawla, the director of this thesis and head of the Laboratory for Reactor Physics and Systems Behaviour at EPFL and PSI, for giving me the opportunity to carry out this research and for his advice and guidance throughout this doctoral work.
- My supervisors, Dr. Ch. Hellwig, Dr. A. Romano and G. Khvostov; they have contributed significantly to this work and have tirelessly supported me during the doctoral work. Thank you.
- Dr. Y. Guérin, Dr. A. Alam and Dr. M. Marques for the inspired translation of the abstract for this thesis.
- Dr J. Bertsch and M. Zimmermann, who have helped me through the administrative hurdles during this thesis and have been hugely supportive of the work carried out.
- Dr. C.A. Degueldre, for providing many opportunities to present this work to a wider audience.
- Dr. M.I. Horvath, with whom I shared an office for many years as well and had many inspired and illuminating discussions. Thank you for the support and the many good times we spent together.
- L.Å. Nordström for the wonderful collaboration with the TRANSURANUS calculations. Thank you for being there when I needed help.
- R. Restani and H. Wiese; for the many illuminating discussions concerning the practical aspects of Electron Probe Microanalysis (EPMA) and post irradiation examination (PIE) work, you helped ground this work in the practical aspects of fuel PIE investigations.
- Dr. M. Pouchon, whose expertise and love of L^AT_EX helped produce this document. Thank you.
- Dr R. Stoenescu and Dr M. Samaras for always having the door open to talk about both the work and life; your support through the thesis was of immense value to me.
- The Swiss nuclear utilities and *swissnuclear* for supporting this doctoral research and providing valuable suggestions during the course of its execution.
- Dr P. Van Uffelen, Dr. J.P. Hiernaut and Dr. J. Spino of the Institut for Transuranium Elements in Karlsruhe for the illuminating and interesting discussions concerning the high burnup structure and fuel performance.
- All of my friends and colleagues at PSI and elsewhere: Tobe, Stefano, Rosella, Sebastiano, Stefan, Gosha, Ana, Fatima, Gerry, Paolo, Fabio and many more. You have been my rock during the thesis and I will forever be indebted to you for the support and fun times we have shared.
- For Dave, Les and Else whose support during my early education has been invaluable for reaching this point.
- A very special thanks to my family, without whom none of this would ever have been possible. Thank you for your loving support and patience for all the years leading to this point.

Finally I would like to thank Prof. H.B. Püttgen, Prof. R. Chawla, Dr. Y. Guérin, Dr. Ch. Hellwig and Dr. A. Romano for accepting to form the jury.

CURRICULUM VITÆ

Paul Robert Blair

Work contact

Paul Scherrer Institut
CH-5232 Villigen PSI, Switzerland
+41 (0)56 3102285
paul.blair@psi.ch

Home contact

Zürcherstrasse 19a
5400 Baden, Switzerland
+41 (0)76 5688674
aural.blip@gmail.com

Personal details

Date of birth: 10th Aug 1979 **Place of birth:** Liverpool, England **Nationality:** British

Education

2004–2008 *Doctoral student* École Polytechnique Fédérale de Lausanne, 1015 Lausanne, Switzerland
Paul Scherrer Institute, 5232 Villigen PSI, Switzerland

Thesis topic: “Modelling of Fission Gas Behaviour in High Burnup Nuclear Fuel”
Thesis director: Professor Rakesh Chawla

1998–2002 *Masters degree in Theoretical Physics* University of York, York YO10 5DD United Kingdom

Thesis topic: “A fractal model of a polymer adhesive”
Thesis adviser: Professor Peter Main

Professional experience

2004–2008 *Doctoral student* École Polytechnique Fédérale de Lausanne, 1015 Lausanne, Switzerland
Paul Scherrer Institute, 5232 Villigen PSI, Switzerland

Main task: Development of models describing the behaviour of xenon and krypton in the high burnup structure of light water reactor nuclear fuel rods.

2003–2004 *Secondee* OECD Halden Reactor Project, P.O. Box 173, 1751 Halden, Norway

Main task: Responsible for two fuel experiments, specifically an inert–matrix fuel irradiation (IFA-651) and the high burnup disk irradiation experiment (IFA-655). This involved the maintenance of the experiments, checking for errors in the measurements, developing the requirements and documentation for the start of a new loading of the inert–matrix fuel experiment, and analysis of available data for communication/presentation to project members.

2002–2003 *Pre-doctoral student* Paul Scherrer Institute, 5232 Villigen PSI, Switzerland

Main task: Development of a thesis proposal based upon the behaviour of fission gas in the high burnup structure, specifically orientated towards the effect of grain boundaries and the potential for gas release at high burnups.

2001 *Trainee* Paul Scherrer Institute, 5232 Villigen PSI, Switzerland

Main task: Definition of requirements for integrating an in-house developed fission gas release model (SPHERE) with the fuel performance code (TRANSURANUS). This required the identification of differences between the two modelling strategies and developing methods of interfacing the two codes without compromising the benefits of both codes.

Publications

Journal papers

P. Blair, G. Khvostov, A. Romano, Ch. Hellwig, R. Chawla, “A mechanistic model for the interpretation of high-burnup fuel annealing tests”, *Journal of Nuclear Science and Technology*, **45** 7, (2008) *in press*.

P. Blair, A. Romano, Ch. Hellwig, R. Chawla, “Calculations on fission gas behaviour in the high burnup structure”, *Journal of Nuclear Materials*, **350** (2006) 232.

Ch. Hellwig, M. Streit, P. Blair, T. Tverberg, F. C. Klaassen, R. P. C. Schram, F. Vettrano, T. Yamashita, “Inert matrix fuel behaviour in test irradiations”, *Journal of Nuclear Materials*, **352** (2006) 291.

Conference papers

Ch. Hellwig, M.I. Horvath, P.R. Blair, R. Chawla, D. Günther, “Fission gas distribution and behaviour in the high burn-up structure”, in Proceedings of the 2007 international LWR fuel performance meeting, San Francisco, California, (2007).

P. Blair, L.Å. Nordström, Ch. Hellwig, “The PSI mechanistic fission gas release model implemented in the TRANSURANUS fuel behaviour code and applied to some benchmarking cases”, presented at the Enlarged Halden Project Group Meeting, Loen, Norway (2007).

J. Wright, P. Blair, “The IMF/MOX comparative test, IFA-651.1: Results after four cycles of irradiation”, *Halden project work report*, HWR-763, presented at the Enlarged Halden Project Group Meeting, Sandefjord, Norway (2004).

J. Wright, P. Blair, “The high burnup disk irradiation test, IFA-655: Results after three cycles of irradiation”, *Halden project work report*, HWR-766, presented at the Enlarged Halden Project Group Meeting, Sandefjord, Norway (2004).

Presentations and posters

P. Blair, G. Khvostov, “Mechanistic modelling of the high burnup structure porosity evolution under annealing conditions”, presented at the international workshop "Towards nuclear fuel modelling in the various reactor types across Europe", Karlsruhe, Germany (2007)

P. Blair, G. Khvostov, “Fuel performance modelling of the high burnup structure: evolution of porosity and fission gas release”, Karlsruhe, Germany (2007)

L.Å. Nordström, P. Blair, Ch. Hellwig, “A mechanistic fission gas release model implemented in the TRANSURANUS fuel behaviour code and applied on FUMEX-2 benchmarking cases”, presented at TopFuel 2006, Salamanca, Spain (2006).

P. Blair, A. Romano, Ch. Hellwig, R. Chawla, “Modelling fission gas behaviour in the high burnup structure under annealing conditions”, presented at the European Materials Society spring meeting, Nice, France (2006).

P. Blair, A. Romano, Ch. Hellwig, R. Chawla, “Calculations on grain boundary diffusion of Xe in the high burn-up structure”, presented at the European Materials Society spring meeting, Strasbourg, France (2005).